Understanding the behaviour of new low biopersistence high temperature insulation fibre materials

CHRISTOPOULOU, Georgia

Sheffield Hallam University | Materials and Engineering Research Institute

Understanding the Behaviour of New Low Biopersistence High Temperature Insulation Fibre Materials

Georgia Christopoulou

A thesis submitted in partial fulfilment of the requirements of
Sheffield Hallam University
for the degree of Master of Philosophy

Collaborating Organisation: Morgan Advanced Materials

September 2017

Στην Ιάσμη και στον Γιώργο

Abstract

New low-biopersistence glass fibres (Superwool® XT) in the K_2O-MgO-ZrO_2-Al_2O_3-SiO_2 system have been previously developed by compositional reformulation, resulting in a safer, more environmentally-friendly fibre material suitable for applications demanding long-term and high-temperature stability. In this work, heat treatment experiments at 850°C and 1250°C with amorphous and pre-crystallized samples were employed to explore the long-term performance, the crystallization behaviour and the elemental stability of these bio-soluble glass fibres as functions of time, temperature and service conditions.

Superwool® XT requires less than one minute of heating at 1250°C to partially crystallize to form glass-ceramic fibres. Amorphous and pre-crystallized samples of this material have a satisfactory performance at 850°C as no composition alterations or phase transformations occur after kalsilite ($KAlSiO_4$) and zirconium oxide (ZrO_2) completely develop. On the contrary, Superwool® XT samples heat treated at 1250°C revealed the formation of kalsilite at the initial firing stage (168-840 hours) and its transformation to leucite ($KAlSi_2O_6$) from around 800 hours and as crystallization progresses. This phase transformation is accompanied by K_2O evaporation and rough and uneven surface morphology.

To explore the thermal behaviour of Superwool® XT, systematic synthesis and heat treatment experiments were conducted. These resulted in multiphase and single-phase glass-ceramic fibres in the K_2O-Al_2O_3-SiO_2 and the K_2O-ZrO_2-Al_2O_3-SiO_2 system. Heat treated samples at 1250°C showed that leucite is a stable crystalline phase as a function of time (up to 1000 hours) as opposed to kalsilite which is an unstable phase that probably behaves as a precursor of leucite. Samples in which kalsilite is the major

phase lose K_2O after prolonged firing (1000 hours) dissimilarly to those with leucite in which little or no compositional alteration was detected.

The unstable nature of kalsilite will cause loss of K_2O and the development of leucite at 1250°C and after prolonged firing (up to 2000 hours). Two hypotheses have been developed to explain this phenomenon. In the first, unstable kalsilite ejects K_2O and Al_2O_3 and then transforms to leucite. In the second hypothesis, unstable kalsilite reacts with silica from an amorphous phase to form leucite.

Heat treatment experiments demonstrated that the firing atmosphere parameters, such as number of samples inside the furnace and thus atmospheric K_2O concentration and dimensions of the furnace, will affect the crystallization behaviour and the rate of K_2O volatilization. Furthermore, the loss of potassium oxide is strongly connected with the development of leucite as in all the cases where K_2O loss was limited the formation of this phase was also supressed.

Finally, analysis of Cerachem® fibres in the ZrO_2-Al_2O_3-SiO_2 system which is the correct industry standard material for high thermal insulation showed that a loss of silica occurs as a function of temperature and material depth and is observed as a weight loss as gaseous SiO_2 moves away from the hot face of the samples.

Acknowledgements

I would like to thank my academic supervisors Dr. Paul Bingham and Dr. Hywel Jones, and my industrial supervisors Dr. Gary Jubb and Dr. Amanda Quadling for their scientific assistance and invaluable guidance throughout this project.

My sincere thanks also goes to Morgan Advanced Materials, not only for providing the funding which allowed me to undertake this research, but also for giving me the opportunity to share my work by participating in conferences.

I would like to thank Mr Farid Modarresifar for his valuable help and guidance throughout the project and Mr Michael Horobin for his assistance in experiments.

Thanks to all the members of staff at the Materials and Engineering Research Institute of Sheffield Hallam University. I am particularly grateful for the assistance given by Dr. Anthony Bell and Mr Paul Allender.

Thanks to my colleagues in the Glass and Ceramics group for always being willing to help and give their best suggestions. Especially thanks to Cristina Pascual Gonzalez and Benjamin Allsopp for their unreserved help and support and for all the fun we had in the last two years.

Finally, my deepest appreciation goes to my family and my friends for always believing in me and encouraging me to follow my dreams.

Contents

Chapter 1

Introduction

1.Introduction

This chapter provides the underlying rationale and purpose of this research. The aims and the objectives of the investigation will be clearly elucidated and specific research questions will be defined, which take the form of hypotheses that were tested within the study. It is very important to reach an understanding of how aims and objectives each fulfil separate but related functions. Finally, an overview of the following chapters will be presented.

1.1. Rationale

Refractory fibres are a group of diverse types of amorphous or crystalline synthetic mineral fibres that are highly resistant to heat. They are normally used for applications demanding long term and elevated temperature stability such as lining for heat treatment and reheating industrial furnaces, fire-protection applications and in the steelmaking industry. The most commonly used manufacturing process for refractory fibres is melting and fibre-making process (Frydrych, Dziworska, & Bilska, 2002).

Aluminosilicate fibre materials, also known as “refractory ceramic fibres” (RCFs), are fibrous, inorganic, vitreous materials formed by elevated temperature fusion of sources of silica and alumina into a mass which is cooled to a rigid condition without crystallization and formed into fibres. Products made of aluminosilicate wool are commonly used in applications demanding temperatures greater than 900°C and in critical application conditions and intermittently operating equipment (Alper, 1970).

The rapid crystallization of aluminosilicate fibres at temperatures above 1100°C and the formation of mullite ($Al_6Si_2O_{13}$) and cristobalite (SiO_2) have been extensively discussed in many studies (Belyakova, Kutukov, Ustyantsev, & Tretnikova, 1981; Gaodu, Pitak, Volfson, & Drizheruk, 1977; Hickling, Thomas, & Briggs, 1981; Jager, Stadler, & Wernig, 1984; Vine, Young, & Nowell, 1984). Aluminosilicate fibre materials have excellent electrical resistivity (10^{14}-10^{16} Ωm), outstanding resistance to thermal shock, low thermal conductivity and are lightweight.

In recent years RCFs have been used as an alternative to asbestos to protect materials and equipment against elevated temperatures. Nevertheless, they belong to the family of mineral wool fibres and have been categorized as “possible human carcinogen” (category 2B) by the International Agency for Research on Cancer (IARC Working Group on the Evaluation of Carcinogenic Risks to Humans, 2002) .

Two fundamental ways exist for developing safer and environmental-friendly fibre types. The first is to make fibres thicker so as to be non-respirable, but this alteration was not successful as the products lose their desirable insulating properties (Christoph, Nyssen, & Wagner, 2000). The second way is to make fibres with low bio-persistence which has proved to be very promising. Bio-persistence is a complex interaction between fibre solubility and the natural clearance mechanisms in the lung (Stanton & Wrench, 1974). According to theory a fibre with high bio-solubility dissolves on the surface forming micro-cracks, these weaken the fibre and the macrophages in the lung can break the fibre and remove it (Brown et al., 2002).

United States Patent No. 8,088,701 B2 (Jubb, 2012) disclosed potassium aluminosilicate fibres that had a low biopersistence combined with a high thermal stability in which the content of the major oxides SiO_2+Al_2O_3+K_2O is greater than 50

mol% and encompassed fibre compositions in which the percentage of K_2O is greater than 12 mol%. As stated in the patent, these fibres tend to lose potassium. In agreement with this invention, a new safer, environmentally-friendly material suitable for applications demanding long-term and high-temperature stability was developed, Superwool® XT (SWXT®), by the world-leading ceramics manufacturer Morgan Advanced Ceramics. As depicted in Figure 1.1, potassium oxide is important for biosolubility, silica for fiberisation and aluminium oxide for refractoriness. Potassium oxide is an essential compound because fibres with more than 18% alkali metal and alkaline earth oxides avoid the 2B RCF classification (Commission Directive 97/69/EC, 1997).

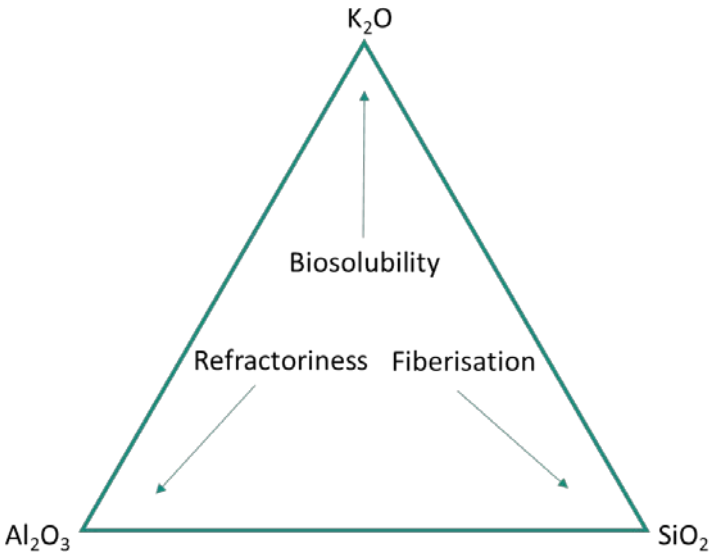

Figure 1.1: Superwool® XT glass fibres chemistry vs performance ternary diagram.

Superwool® XT chemistry is developed from the K_2O-Al_2O_3-SiO_2 phase diagram (Schairer & Bowen, 1955). According to the manufacturer's internal documentation when SWXT® fibres are heat treated at temperatures above 900°C the crystalline phase of potassium aluminium silicate (kalsilite; $KAlSiO_4$) is almost detectable. Kalsilite is an essential crystalline phase because it plays a crucial role in the subsequently forming

crystalline phases and in the stability of the fibres. Moreover, kalsilite is believed to be the precursor of leucite ($KAlSi_2O_6$) (Becerro, Escudero, & Mantovani, 2009; Buljan et al., 2010) and that leucite is a more stable crystalline phase. At the same time potassium oxide volatilizes and K_2O loss begins at 900°C and accelerates at 1100°C. The microstructures of Superwool® XT fibres change at elevated temperature and these changes occur progressively with time, causing grains to grow which reduces the flexibility of the fibres. Eventually the fibres fuse together and the product becomes brittle.

It is argued (Bunsell, 2005) that the shrinkage of glass fibres is due not only to elevated temperatures but also because crystallisation is initiated. There is an absolute need to understand the mechanisms for the loss of K_2O and the loss of mechanical strength with increasing crystallinity and time so that they can be mitigated or reduced. The ambition of this research work is to understand in depth the behaviour and long-term performance of SWXT® under simulated service conditions.

1.2. Aims and objectives

1.2.1. Aims

This project underpins the commercial success of a new safer, environmentally-friendly material, suitable for applications demanding long-term and high-temperature stability, SWXT®. This research topic aims to lead our knowledge one step further regarding the long-term performance of biosoluble glass fibres at elevated temperature. This study aims to determine the current state of the art knowledge in elevated temperature silicate and aluminosilicate fibre insulation materials, and further, to identify the stability of

different chemical species in SWXT® glass fibres in terms of time, temperature and service conditions. This project also aims to build an understanding of the long-term, in-service stability of SWXT® as functions of modifications occurring in service.

1.2.2. Research objectives

The research is intended, in large part, to be a feasibility study: to identify existing literature and practices, and what methodologies might be applied to enable an optimised product strategy to be formed. To address the key aims, the research has five objectives:

- ⇒ Identify literature and theoretical issues related to refractory fibres and their biopersistence, phase relationships and crystallization phenomena in the K_2O-Al_2O_3-SiO_2 ternary system.
- ⇒ Produce glass fibre compositions in the K_2O-Al_2O_3-SiO_2 and the K_2O-ZrO_2-Al_2O_3-SiO_2 system in the compositional field of relevance to Superwool® XT.
- ⇒ Long-term and short-term heat treatment experiments at various temperatures to examine the chemical stability and thermal durability of alkali aluminosilicate glass fibres.
- ⇒ Carry out chemical, structural, microstructural and thermal analysis of alkali aluminosilicate glass fibres.
- ⇒ Extract critical conclusions regarding the in-service stability of Superwool® XT and alkali aluminosilicate glass fibres based from the analysis of heat treated samples.

1.3. Thesis overview

The thesis structure and the presentation of this research work have been selected in a way that can be understood by both specialists in other disciplines and those knowledgeable in this topic. The research topic is addressed in two connected parts: In Chapter 1 the problem statement is presented and a brief review of the research subject, the related theory, and the literature is reported in Chapter 2. Chapter 3 comprises all the experimental procedures used for investigating the research problem. The results of this research are reported in Chapter 4, and the implications of these results will be discussed in Chapter 5. Finally, conclusions and recommendations based on the results of this will be presented.

Chapter 1, the theoretical framework regarding refractory fibres, biosolubility, the K_2O-Al_2O_3-SiO_2 system and Superwool® XT has been introduced. A case has been made regarding the problem under investigation, the purpose of the study, and research questions to be investigated.

Chapter 2, summarizes what is known and identifies what is unknown about the topic of the thesis. The implications of the previous studies for the present work are outlined. The potential contribution of this study to the existing body of knowledge is also identified.

Chapter 3, the research design and the methodology is described in sufficient detail in this chapter that readers come away with a clear understanding of how the study has been conducted. The research questions presented in Chapter 1 have been replicated exactly near the beginning of Chapter 3.

Chapter 4, a factual reporting of the results is presented. Findings are generally organized around the research questions. A summary of the research findings has been presented at the end of this chapter.

Chapter 5, findings are compared and linked to each other and to the existing literature described in Chapter 2. All explanations are supported by the results of Chapter 4.

Chapter 6, conclusions have been presented in this closing chapter and recommendations for future work based on the lines of research that arose from this work.

1.4. References

Alper, A. M. (Ed.). (1970). *High temperature oxides / Part 3, Magnesia, alumina, beryllia ceramics fabrication, characterization and properties* (1st ed.). Cambridge, Massachusetts: Academic Press.

Becerro, A. I., Escudero, A., & Mantovani, M. (2009). The hydrothermal conversion of kaolinite to kalsilite: Influence of time, temperature, and pH. *The American Mineralogist, 94*(11-12), 1672-1678. doi:10.2138/am.2009.3284

Belyakova, N. P., Kutukov, V. F., Ustyantsev, V. M., & Tretnikova, M. G. (1981). Phase-transition in materials based on high-alumina fiber. *Inorganic Materials, 17*(7), 948-951.

Brown, R., Bellmann, B., Muhle, H., Ernst, H., Pohlmann, G., & Sebastien, P. (2002). Subchronic studies on man-made vitreous fibres: Toxicity results. *Annals of Occupational Hygiene, 46*(suppl 1), 102-104.

Buljan, I., Kosanović, C., Subotić, B., Novak Tušar, N., Ristić, A., Gabrovšek, R., . . . Mišić Radić, T. (2010). Kinetic analysis of isothermal crystallization of potassium aluminosilicate ceramics (leucite and kalsilite) from amorphous potassium aluminosilicate precursors. *Crystal Growth & Design, 10*(2), 838-844. doi:10.1021/cg901194k

Bunsell, A. R. (2005). Oxide fibers for high-temperature reinforcement and insulation. *Jom, 57*(2), 48-51. doi:10.1007/s11837-005-0216-9

Christoph, G., Nyssen, P. R., & Wagner, W. (2000). *EP 0399320 B2*. Munich, Germany: European Patent Office.

Commission Directive 97/69/EC, (1997).

Frydrych, I., Dziworska, G., & Bilska, J. (2002). Comparative analysis of the thermal insulation properties of fabrics made of natural and man-made cellulose fibres. *Fibres and Textiles in Eastern Europe, 10*(4), 40-44.

Gaodu, A. N., Pitak, N. V., Volfson, R. E., & Drizheruk, M. E. (1977). Crystallisation in heated aluminosilicate fibers. *Inorganic Materials, 13*(12), 1802-1804.

Hickling, H., Thomas, D. H., & Briggs, J. (1981). High-temperature behaviour of alumino-silicate ceramic fibres. *Science of Ceramics, 11*, 397-403.

IARC Working Group on the Evaluation of Carcinogenic Risks to Humans. (2002). *Man-made vitreous fibres.* (IARC monographs on the evaluation of carcinogenic risks to humans No. 81). Lyon: IARCPress.

Jager, A., Stadler, Z., & Wernig, J. (1984). Investigations on microstructural changes undergone by ceramic fibers at elevated temperatures, particularly as regards the formation of cristobalite. *CFI Ceramic Forum International, 61*(3), 143-147.

Jubb, G. A. (2012). *U.S. Patent No. 8,088,701 B2*. Washington, DC: U.S. Patent and Trademark Office.

Schairer, J. F., & Bowen, N. L. (1955). The system K_2O-Al_2O_3-SiO_2. *American Journal of Science, 253*(12), 681-746. doi:10.2475/ajs.253.12.681

Stanton, M. F., & Wrench, C. (1974). Mechanisms of mesothelioma induction with asbestos and fibrous glass. *Food and Cosmetics Toxicology, 12*(4), 591-592. doi:10.1016/0015-6264(74)90121-7

Vine, G., Young, J., & Nowell, I. W. (1984). Health hazards associated with aluminosilicate fibre products. *The Annals of Occupational Hygiene, 28*(3), 356-359. doi:10.1093/annhyg/28.3.356

Chapter 2

Literature Review

2.Literature Review

A critical review of the literature associated with the subject area of this research study will be presented in this chapter. The strengths and weaknesses of theories of relevance to this subject will be identified and analysed in depth. The contribution of this research to the existing body of knowledge will also be identified.

In this chapter, an effort to build an understanding regarding the thermal behaviour of biosoluble glass fibres has been made. Refractory ceramic fibres will first be presented and how their biological effects have created the need for a new safer, biosoluble material will be discussed. The properties and applications of newly developed biosoluble glass fibres will then be described. Finally, the phase relationships in the systems of interest will be introduced by investigating the experimentally and theoretically calculated relevant phase diagrams.

2.1. Insulation fibres

Insulation fibres are a large group of diverse types of amorphous or crystalline man-made mineral fibres made of alumina, silica and other refractory oxides, such as alkaline earth oxides, and have high resistance to heat. They are masses of disorganized interlocking fibres with variable diameters and lengths, some of which may be inhalable (Wallenberger & Bingham, 2010).

The most commonly used manufacturing process for insulation fibres is melting and fibre-making. A mixture of raw materials is melted at about 2000ºC. As depicted in Figure 2.1 the molten mixture is ejected through a nozzle onto rotors turning at high

speed and made into a bulk (raw fibres) by the centrifugal force of the rotors (spinning method). A stack of bulks is lubricated and subjected to needling, being shaped into a blanket. The lubricant is then removed by heating to create a blanket (Hearle, 2001).

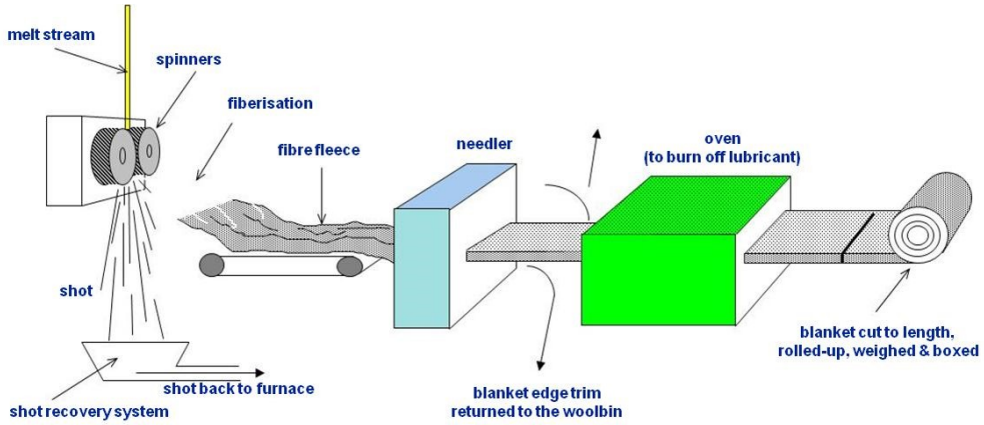

Figure 2.1: Manufacturing process of insulation fibre products (Hearle, 2001).

Insulation fibres are commonly used for applications demanding long-term and elevated temperature stability, and are used to protect equipment, conserve energy and improve process performance in some of the most demanding elevated temperature industrial environments (Bahadori, 2014). Moreover, high temperature insulating fibres provide thermal insulation in processing of metals, petrochemicals, cement, ceramics and glass, and are used by manufacturers of equipment for aerospace, automotive, marine and domestic applications (Hearle, 2001). Typical applications include:

- Chimney and duct insulation in power generation plants
- Pipe insulation in elevated temperature processing plants
- Linings and back-up insulation for all types of furnaces, heaters and kilns
- Insulation of steam turbines and hot boxes
- Exhaust and heat shield cladding
- Vehicle and domestic appliance insulation

2.2. Refractory ceramic fibres

In the first stage of the present work, the study was focused on theoretical and experimental understanding of aluminosilicate ceramic fibres which are also known as "refractory ceramic fibres" (RCFs). Refractory materials from alumino-silicate wool are ordinarily utilized in applications requiring temperatures higher than 900°C and in critical application conditions and intermittently operating equipment.

They are manufactured in the form of wool and typically contain approximately 50% fibre and 50% unfiberised, largely non-respirable material. The fibres do not split longitudinally into thinner fibres as asbestos ones do but rather transversely, ultimately becoming granular dust (Mast, et al., 1995). Table 2.1 shows the composition of the three most widely used RCFs. It indicates that these fibres consist of about 50% each of silicon oxide and aluminium oxide (RCF 1 and 3). In zirconia aluminosilicate fibres (RCF 2) part of the aluminium oxide is substituted by zirconium oxide.

Reported studies (Brown, 2000; Butler & Dyson, 1997; Comodi, Cera, Gatta, Rotiroti, & Garofani, 2010; Dyson, Butler, Hughes, Fisher, & Hicks, 1997; Maxim, Venturin, & Allshouse, 1999) have confirmed that aluminosilicate fibres devitrifiy rapidly at temperatures above 1100°C to form mullite, cristobalite and another silica polymorph. Aluminosilicate fibre materials have great resistance to thermal shock, exceptional acoustical properties, low thermal conductivities, and are lightweight.

A considerable number of studies have examined the crystallization behaviour of refractory ceramic fibres; the outcomes of the most important ones have been summarized in Table 2.2. Most of the studies have focused on the examination of the structure, the biological activity and the composition of as made fibres, and of heat treated fibres for various time periods and temperatures. There is a consensus that the

composition of the untreated fibres will affect the degree of crystallization and the devitrification products of RCFs upon heating at different temperatures. Prolonged heat treatment experiments of RCFs at 1300°C can lead to formation of cristoballite (SiO_2) (CS), mullite ($Al_6Si_2O_{13}$) and various crystalline phases (Gualtieri et al., 2009). In general, firstly mullite will form close to 980°C and cristobalite will then follow close to 1100°C; the level of the crystallization is dependent on the time and temperature of heat treatment.

Table 2.1: Chemical composition of the three mostly used types of RCFs expressed in % weight (Maxim, Allshouse, Kelly, Walters, & Waugh, 1997).

Constituent	**Kaolin aluminosilicate (RCF-1)**	**Zirconia aluminosilicate (RCF-2)**	**High-purity aluminosilicate (RCF-3)**
SiO_2	50-54	48-50	49-54
Al_2O_3	44-47	35-36	46-51
K_2O	<0.01	<0.01	<0.01
Na_2O	0.5	<0.3	0.2
MgO	<0.01	<0.01	<0.01
CaO	<0.01	<0.05	<0.05
TiO_2	2	0.04	0.02
ZrO_2	0.1	15-17	0.2
Fe_2O_3	1	<0.05	<0.2
Cr_2O_3	<0.03	<0.01	<0.01

Table 2.2: Summary of fibre heat treatment conditions and resulting crystallization products, listed in chronological order of publication.

Reference	Type of fibre	Fibre description	Temperature (°C)	Time*	Cristobalite (wt%, unless stated)
Sopicka-Lizer & Pawlowski (1980)	Ceramic fibre	Kaolin-based fibre	1500	Approx. 4 h	mullite
Vine et al. (1984)	ASF	Alumino-silicate fibre	1150	1 w 3 w 5 w	X-ray diffraction peak height ~63mm ~125mm 130mm
Gantner (1986)	Ceramic fibre		315-1315 954-1093 1315 260-1399 1315	471 h 281 h 100 h 130 h 184 h	12 21 20 3
Karlsson et al. (1986)	Cerafiber Cerachrome Fiberfrax Fiberfrax H	Alumino-silicate fibre Alumino-silica-chrome fibre Alumino-silicate fibre Alumino-silicate fibre	1200	600 cycles 500 cycles	X-ray diffraction peak height 9 mm 145 mm 0 45mm
Holroyd et al. (1988)	Standard High duty grade	Standard grade alumino-silicate fibre High duty grade alumino-silicate fibre	1155 1100 950 1270 1155 1100	29 d 33 d	9.1 2.3 0 20 9.1 2

Table 2.2: Summary of fibre heat treatment conditions and resulting crystallization products, listed in chronological order of publication. (Continued)

Reference	Type of fibre	Fibre description	Temperature (°C)	Time*	Cristobalite (wt%, unless stated)
Zhen & Song (1990)	SIF	Alumino-silicate fibre	1100	8/500 h	2.7/19
			1200		14.6/19
			1400		18.2/19
	HPSIF	High purity fibre	1200		1.0/12
			1400		12/16
Brown et al. (1992)	Standard grade		1200	8 w	cristobalite, mullite
			1400	0.5 w	mullite, β-cristobalite (trace)
	High-duty grade		1200	2 w	β-cristobalite, mullite
			1400	2 w	mullite, β-cristobalite (trace)
	Zirconia grade		1200	1 w	mullite, β-cristobalite, zirconia
			1400	8 w	mullite, β-cristobalite, zircon
Laskowski et al. (1994)	Standard	Standard grade™ alumino-silicate fibre	1200	336/7300 h	No/No
			1300	96/7300 h	No/No
			1400	12/336 h	Maybe/Yes
			1500	3/240 h	Yes/Yes
Dyson et al. (1997)	Standard	Alumino-silicate fibre	1100	601 h	
			1200	486 h	α'=19.2
	Cr-fibre	Alumino-silicatic fibre with chromium	1100	601 h	
			1200	486 h	α'=35.2
	Zr-fibre	Alumino-silicatic fibre with zirconium	1100	601 h	
			1200	486 h	α'=37.1

Table 2.2: Summary of fibre heat treatment conditions and resulting crystallization products, listed in chronological order of publication. (Continued)

Reference	Type of fibre	Fibre description	Temperature (°C)	Time*	Cristobalite (wt%, unless stated)
Butler & Dyson (1997)	Standard	Unused ASCF			α'-cristobalite/α-cristobalite
			1050	168 h	0/0
				672 h	0/0
				4004 h	4.4/0
			1200	168 h	6.5/0
			1300	168 h	24.3/0
				708 h	26.0/0
				2706 h	28.5/0
			1500	168 h	22.7/7.5
				768 h	12.2/5.8
				1344 h	19.9/12.2
Binde & Bolender (2002)			900-1200	24 h	Lab 1/Lab 2
	AES: CMS	Calcium magnesium silicate			11/19
	CMZS/HT	Calcium magnesium zirconia silicate			2/2
	CMS/HT	Calcium, magnesium silicate, high temperature			14/19
	MS/HT	Magnesium silicate			35/30
	RCF: RCF1400	Refractory ceramic fibre			Unknown
	$RCF1400_{treat}$	Refractory ceramic fibre, used			Unknown
Bhattacharyya et al. (2005)	ASCF	Alumina-silicate ceramic fibre	1100	1-4 h	Unknown
			1250		
			1350		

Table 2.2: Summary of fibre heat treatment conditions and resulting crystallization products, listed in chronological order of publication. (Continued)

Reference	Type of fibre	Fibre description	Temperature (°C)	Time*	Cristobalite (wt%, unless stated)
Tonnesen & Telle (2007)	RCF1260	Alumino-silicate fibre	1050	250 h	0
				500 h	<1
			1100	100 h	0
				250 h	1.8
				500 h	2.5
			1150	100 h	0
				250 h	1.0
				500 h	3
			1250	100 h	0.7
				250 h	1.2
	RCF1430	Alumino-silicate fibre	1250	100 h	4.2
				250 h	11
				500 h	12.5
	RCF1430Z	Alumino-silicate fibre with zirconia	1250	100 h	11.5
				250 h	12.2
Gualtieri et al. (2009)	Cerafiber	Man-made vitreous fibres	1300	72 h	15.9
	Super wool				3.1
Comodi et al. (2010)	PAT-1	Alumino-silicate fibre	1350	1 d	32.19
			1500		38.2
	Ecofiber	Alkali-silica fibre	1200	7 d	5.84
				2 w	9.40
* h – hours; d – days; w – weeks					

Cerachem®

Morgan Advanced Materials Ltd. has developed Cerachem®, a highly insulating product for applications demanding elevated temperatures (up to 1315°C) for continuous use. Cerachem® composition is based on the alumina-silica-zirconia system (Table 2.3). It is designed for applications where low thermal conductivity, high tensile strength and low shrinkage are needed (Morgan Advanced Materials, 2017).

Table 2.3: Elemental analysis of Cerachem®.

Oxide	Content (wt %)
Al_2O_3	34.90
SiO_2	50.00
ZrO_2	15.20
Fe_2O_3	0.15
$Na_2O + K_2O$	0.10
CaO + MgO	0.09

Cerachem® products exist in five different forms as shown in the following figure (Figure 2.2). Cerachem® is resistant to chemical attack and is classified at 1426°C. It is lightweight, strong and features a low heat storage capacity for effective energy savings and good thermal shock resistance for use in difficult environments. Cerachem® pyro-bloc modules provide easy to use, efficient thermal lining for all types of high temperature processing equipment such as homogenizing furnaces, process heaters, ceramic kilns, annealing furnaces and heat-treating furnaces.

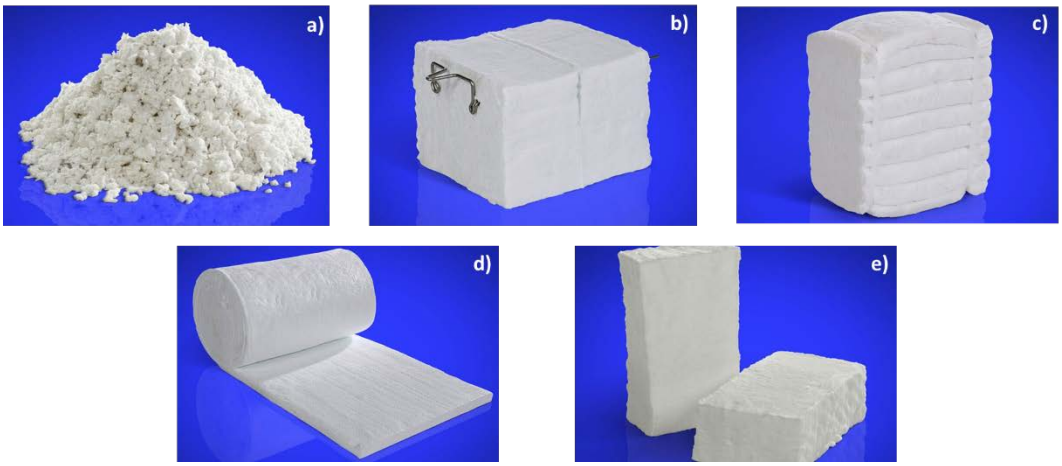

Figure 2.2: Different types of Cerachem®; a) Bulk b) Pyro-Bloc Modules c) Folded and Stacked Blanket Modules d) Blankets e) Pyro-Log.

2.2.1. Biological effects of refractory ceramic fibres

In recent years RCFs have been used as an alternative to asbestos to protect materials and equipment against elevated temperatures. The commercial term “asbestos” includes an entire family of minerals with fibrous-asbestiform habit (Stanton & Wrench, 1972). Chrysotile (serpentine asbestos), actinolite, amosite, anthophyllite, crocidolite, and tremolite (amphibole asbestos) are classified as asbestos minerals (George, Guthrie, & Brooke Mossman, 1994). The fibrous-asbestiform habit, which determines the outstanding technological properties of asbestos, is unfortunately also one of the causes of its toxicity. Fibres released into the air, micrometric in size and with elongated streamlined morphology, can pass through the nasal mucous filter and reach the lungs, lodging in the tissues (Donaldson, Murphy, Duffin, & Poland, 2010). It has been scientifically proven that inhalation of asbestos fibres can cause serious pathologies of the lungs, like mesothelioma (Catherine & Skinner, 2003). For this reason, in many countries asbestos is banned, progressively removed from the environment and eventually substituted with synthetic fibres. It should be pointed out though that asbestos continues to be used in a variety of applications.

The risk of cancer from exposure to asbestos depends mostly on fibre dimensions with long fibres being more dangerous than short for all types of asbestos. Specifically, the ability of the asbestos fibres to split along their length into fine fibres that can reach the furthest part of the lung and the resistance of the fibres to the chemical attack by the lung's defences make asbestos so hazardous to human health (Cugell & Kamp, 2004).

The dimensions (i.e. length, diameter, and length to diameter ratio) of the fibres are also important to rate their potential health hazard and are used to distinguish between continuous fibres, discontinuous fibres, and wools (Gualtieri et al., 2009). The term "discontinuous fibres" includes whiskers and small discrete particles with the appearance of powders but also includes wools and cotton wool-like materials. Fibres with diameters >3 μm are generally regarded as non-breathable and, therefore, cannot present an inhalation hazard.

Devitrification of RCFs can lead to the development of cristobalite that has raised concerns regarding biological effects upon exposure to heat-treated RCFs (Comodi et al., 2010; Gantner, 1986). They belong to the family of mineral wool fibres and have been categorized as "possible human carcinogen" (IARC Working Group on the Evaluation of Carcinogenic Risks to Humans, 2002).

The first in vivo studies on RCFs were conducted with 344 rats that were exposed to heat treated RCFs (1315.6°C, 24 hours) for 24 months (Mast, McConnell, Anderson et al., 1995; Mast, McConnell, Hesterberg et al., 1995; Rossiter & Chase, 1995). These rats were inhaling a 30mg/m^3 of RCFs for 6 hours per day and for 5 days per week. The free CS inside the fibres was observed to be around 27%. This exposure resulted in pleural mesotheliomas in most of the rats for all the as made RCF types (RCF1, RCF2, RCF3) apart from RCF4 (a heat-treated sample simulating the state of the RCF1 fibres

after use in furnace insulation) which has been observed in only one rat. Regarding mesothelioma induction and lung tumour, these studies revealed that unheated RCFs are more toxic than after service RCFs. While the toxicity reduction was a consequence of the alteration in the length of the fibres, there was no evidence that the reason fibres became less toxic is devitrification.

Moreover, experimental studies showed that CS that develops due to devitrification may not be toxicologically active as it is not detected on the fibre surface but escapes from the surface through devitrification (Brown et al., 1992; Harrison & Brown, 2011) and in the case of bulk samples; surface coating with mullite helps CS to be sheltered (Gaodu, Pitak, Volfson, & Drizheruk, 1977). In the latter study, it is indicated that the crystallization process makes the fibres weaker, and leads to fibre structure breakdown (Dietrichs & Kronert, 1981) and this breakdown will probably reduce any potential hazard connected with RCFs.

During the present review, it has been noted that most of the in-vivo studies of heat-treated fibres are not consistent regarding the total firing time and the exact temperatures used. For instance, in the research study of Laskowski et al. (1994) it is not indicated whether the samples have been constantly heat treated for 7300 hours at a specific temperature. In-vitro studies on cells from various species (sheep, hamsters, rat and mice) have demonstrated that after-service fibres have a lesser toxicological impact.

Exposure to refractory ceramic fibres can be increased when removal operations are initiated, but this kind of exposure has been considerably reduced nowadays (ECFIA, 2010; Maxim et al., 1999). The results from industrial measurements while workers are involved with the production, installation and repair/removal of RCFs are contradictory. Some studies reported that these measurements were over exposure limits (Cheng, Mc

Dermott, Gia, Cover, & Duda, 1992; Fairfax & Burmeister, 2001; Gantner, 1986; Shih et al., 2008; Strübel & Faul, 1994; Sweeney & Gilgrist, 1998) while other studies indicated that measurements were under this limit (Groat et al., 1999; Linnainmaa et al., 2007; Maxim et al., 2008; Rice, Lockey, Lemasters, Dimos, & Gartside, 1994; Van Den Bergen, Rocchi, & Boogaard, 1994).

2.3. Biosoluble glass fibres

The biological effects of refractory ceramic fibres created the need for a new and safer material that can be used for refractory applications. Research studies focused on developing safer fibres have proposed two fundamental approaches:

I. Making the fibres thicker
II. Low bio-persistence

The first approach fails because the products then also lose their good insulating properties so the key is low bio-persistence (Maxim, Hadley, Potter, & Niebo, 2006). The term bio-persistence relates to the relative time that fibres remain in the body. A material with low bio-persistence can be removed from the human body quickly so the risk to health is reduced. To this end, the new glass fibres have been based on glass systems that are soluble in lung fluids and lead to low bio-persistence fibres. According to theory a fibre with high bio-solubility dissolves on the surface forming micro cracks – these weaken the fibre and the macrophages in the lung can break the fibre and remove it (Maxim et al., 2006).

Low bio-persistence fibres did not initially have a satisfactory performance for applications demanding high temperature capability. United States Patent No. US

3352746 A (Dunbar, Rademaker, & Williams, 1967) disclosed the first calcium magnesium silicate composition fibres that were biosoluble and also had good thermal performance. A more recent European patent No. 0399320 B2 (Christoph, Nyssen, & Wagner, 2000) reveals a highly biosoluble glass fibre composition (10-20 mol% Na_2O and 0-5 mol% K_2O) but the maximum temperature at which it can be used is not mentioned. Saline soluble fibres based on calcium magnesium silicate glass system with ZrO_2 that can be used up to 1000°C have been introduced by the International Patent Application No. WO 93/15028 A1 (Jubb & Martin, 1993).

The maximum temperature of soluble glass fibres has been elevated according to different patents. Glass fibres with low alkali metal content that can be employed for applications at 1260°C have been introduced by International Patent Application No. WO 94/15883 (Jubb, 1994). In another patent application (WO 03/059835 A1) it is claimed that the addition of lanthanide elements improves the thermal performance of the fibres so they can be used at temperatures higher than 1260°C (Jubb & Freeman, 2003).

Another important fibre property which is an indication of biopersistence, determined by in vitro studies, is the dissolution rate constant K_{dis} (Gualtieri et al., 2009). K_{dis} was extensively studied and it is suggested as one of the candidate parameters for classification of fibre toxicity. Moreover, the correlation between K_{dis} and the time of persistence in a physiological environment was shown to be relatively high (McConnell, 2000). Different parameters such as the content of alkali and alkaline earth oxides, and the distribution of fibre diameter can affect the dissolution rate so for each material in vitro testing is needed to determine the time of degradation in a physiological environment (Maxim et al., 1999). In general, the dissolution rate constant should be

below or around 100 ng cm^{-1} h^{-1} so that the fibres can be characterised as low biopersistence (Eastes & Hadley, 1996).

2.3.1 Superwool XT® and Colloidal silica coated Superwool XT®

Over the past ten years, Morgan Advanced Ceramics has undertaken an extensive research programme that led to the development of a new safer, environmentally-friendly material, Superwool XT® (SWXT), suitable for applications demanding long-term and high-temperature stability (Figure 2.3).

Figure 2.3: Superwool XT® needled blanket (BG-15-P19-7702) with 128kg/m^3 density.

This newly developed material has been designed to replace Cerachem® in high temperature industrial processes (chemical, iron and steel and ceramics) and also to replace standard RCFs in automotive applications. Superwool XT® chemistry is developed from the K_2O-Al_2O_3-SiO_2 phase diagram and is based on the composition depicted with the red circle in Figure 2.4.

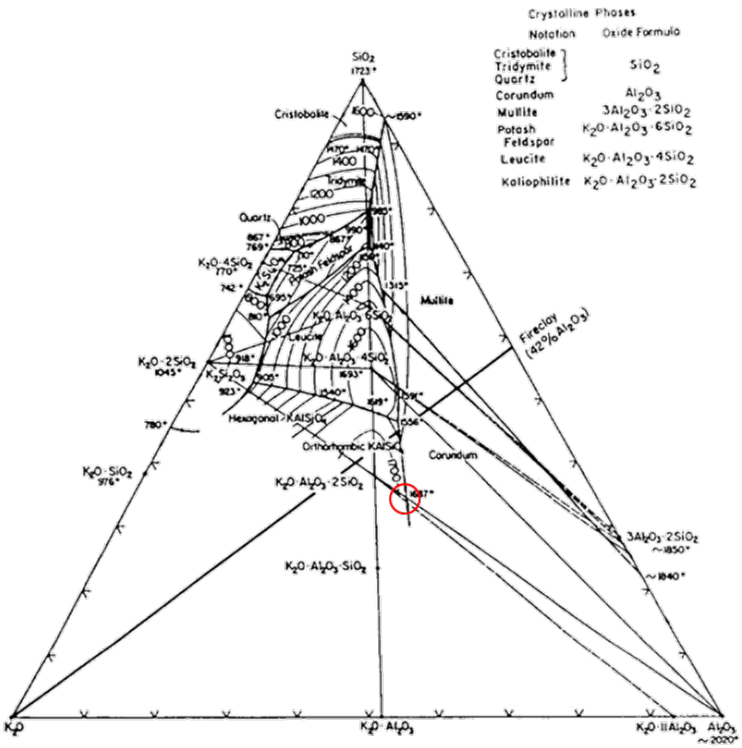

Figure 2.4: Phase diagram of the K_2O-Al_2O_3-SiO_2 system (Schairer & Bowen, 1955) showing the composition Superwool XT® is based on in red circle.

United States Application No. US 8,088,701 B2 (Jubb, 2012) disclosed alternative potassium aluminosilicate fibres that had a low biopersistence combined with a high thermal stability in which the combined mole percentage of the major oxides (SiO_2, Al_2O_3 and K_2O) is greater than 50 mol% and encompassed fibre compositions in which the percentage of K_2O is greater than 12 mol%. Alkali oxide is an essential compound because fibres with more than 18 mol% alkali metal and alkaline earth oxides avoid the category 2 (C2) RCF classification (IARC Working Group on the Evaluation of Carcinogenic Risks to Humans, 2002) - i.e. "a substance to be regarded as if it were carcinogenic to humans". Different agencies around the world have developed standardized protocols to ensure that new refractory fibres are not carcinogenic. For instance, the EU (Commission Directive 97/69/EC, 1997) requires that vitreous silica fibres consist of a minimum of 18 wt% of alkali metal and alkaline earth oxides and animal testing is also needed for complete exoneration (Figure 2.5). The elemental

analysis of as made Superwool XT® obtained by X-ray fluorescence (XRF) spectrometry is shown in Table 2.4. It is very important to note that this patent (Jubb, 2012) reported that fibres tend to lose potassium which may be an obstacle for certain applications.

Table 2.4: Elemental analysis of Superwool XT®.

Oxide	Content (wt %)
Al_2O_3	35.7
K_2O	25.8
SiO_2	30.5
ZrO_2	6.2
MgO	1.2
HfO_2	0.2
Na_2O	0.4
TiO_2	0.0

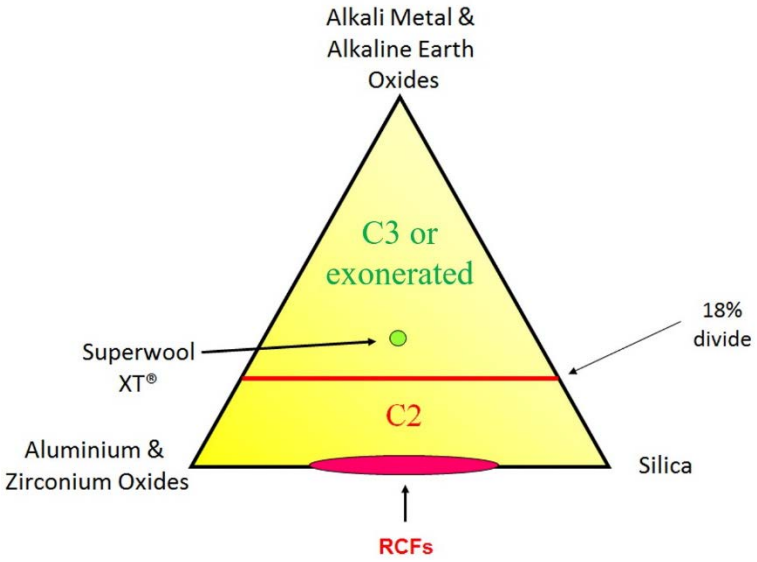

Figure 2.5: RCF and Superwool XT® showing the EU 18% oxides rule for vitreous silica fibres (G. A. Jubb, personal communication, November 16, 2015).

The performance and durability of Superwool XT® is strongly affected by crystallization. Glass fibres change in their microstructures at elevated temperature and as time passes, and their flexibility will be reduced due to grain growth (Bunsell, 2005).

A fundamental problem of aluminium silicate glass fibres is that crystallization and shrinking occur and the fibres become brittle when used at elevated temperatures for a long time. According to the company's internal documentation, when Superwool XT® fibres are heat treated at temperatures above 900°C the crystalline phases of potassium aluminium silicate ($KAlSiO_4$), zirconia (ZrO_2), potassium magnesium silicate ($K_2MgSi_3O_8$) are present (G. A. Jubb, personal communication, November 16, 2015). At higher temperatures (1250°C) for 1000 hours of heat treatment leucite peaks start to appear but are not yet fully formed at this stage. As heat treatment time increases and moving to higher temperatures both leucite and kalsilite phases are detected but as the time passes kalsilite almost completely transforms to leucite.

United States Application No. US WO2004/064996 (Boff, Jubb, & Mottram, 2010) discloses an invention about the effect of partial crystallization of glass fibres on their thermal properties. It is argued that fibres that have first crystallized or at least partly crystallized will have a better performance as their shrinkage resistance will be increased.

Colloidal silica coated Superwool XT®

Colloidal silica consists of non-porous, spherical and fine amorphous silica particles in a liquid phase. To accomplish this, the particles must be small enough so gravity does not affect them. Initially, colloidal silica was used for coatings in a broad range of applications such as investment casting and ingot casting. It was during the late 70's when for the first-time colloidal silica was introduced as a bonding agent in monolithic refractories. United States Patent No. US 4041199 A (Cartwright, 1977) discloses an invention about refractory heat-insulating materials where colloidal silica (2-16 wt%) was used for the first time as a bonding agent.

Refractory materials with colloidal silica were commercially available in gunning, castable and ramming formulations. Colloidal silica offers the perfect functional profile for these purposes thanks to its ability to withstand continuous operating temperatures of 1500°C with little shrinkage, excellent tolerance to thermal shock, and chemical inertness.

Morgan Advanced Ceramics has been exploring the use of colloidal silica on Superwool XT® to supress surface crystallisation. According to the company's internal documentation, addition of 1 wt% of colloidal silica can improve the temperature durability of Superwool XT®. To this end, colloidal silica coated Superwool XT® has been created but further investigation is needed to understand the mechanism behind improved performance and to further develop this material.

Table 2.5: Elemental analysis of colloidal silica coated Superwool XT®.

Oxide	**Content (wt %)**
Al_2O_3	34.4
K_2O	24.7
SiO_2	32.2
ZrO_2	7.2
MgO	1.0
HfO_2	0.1
Na_2O	0.3
TiO_2	0.0

2.4. Quinary system K_2O-MgO-ZrO_2-Al_2O_3-SiO_2

The quinary system of K_2O-MgO-ZrO_2-Al_2O_3-SiO_2 is a very complex and newly developed system so there are not – to the best of the author's knowledge – literature data that directly describe its properties and behaviour in terms of crystallization and phase stability. This review aims to build a theoretical understanding regarding of system by investigating the following subsystems:

- Binary system K_2O-SiO_2
- Binary system K_2O-Al_2O_3
- Binary system Al_2O_3-SiO_2
- Ternary system K_2O-Al_2O_3-SiO_2
- Ternary system ZrO_2-Al_2O_3-SiO_2
- Ternary system MgO-Al_2O_3-SiO_2

2.4.1. Binary system K_2O-SiO_2

Early studies of the K_2O-SiO_2 system involved the preparation of the compound $K_2O{\cdot}2SiO_2$ (Morey, 1914) and of the related ternary system H_2O-K_2SiO_3-SiO_2 by Morey and Fenner (1917) who identified the hydrate, $K_2O{\cdot}4SiO_2{\cdot}H_2O$, but did not report on the anhydrous tetrasilicate. The phase diagram of the system K_2O-SiO_2 and the invariant points as reported by Kracek, Bowen and Morey (1929; 1937) are shown in Figure 2.6 and Table 2.6, respectively.

In the same studies (Kracek et al., 1929; Kracek et al., 1937), the behaviour of compounds in this system is reported as described in this paragraph. Specifically, the melting point of potassium metasilicate ($K_2O{\cdot}SiO_2$) is 976°C and crystallization occurs

very readily. Another compound, potassium disilicate ($K_2O{\cdot}2SiO_2$), will melt at 1045°C, crystallization again occurs very readily, and at 594°C a reversible phase transition is initiated. Potassium tetrasilicate ($K_2O{\cdot}4SiO_2$) has a melting point at 770°C and at 594°C a reversible phase change occurs. Crystallization is more difficult for the K_2O-SiO_2 glasses, with higher SiO_2 content compared with the disilicate, than the Na_2O-SiO_2 glasses.

Table 2.6: Invariant points in the K_2O-SiO_2 system.(Kracek et al., 1929; 1937)

Phase Reaction	**Temperature (°C)**	**Composition (wt%)**	
		K_2O	**SiO_2**
$K_2O \cdot SiO_2 \rightleftharpoons$ L	976	61.07	38.93
$K_2O \cdot SiO_2 + K_2O \cdot 2SiO_2 \rightleftharpoons$ L	780	54.50	45.50
$K_2O \cdot 2SiO_2 \rightleftharpoons$ L	1045	43.95	56.05
$K_2O \cdot 2SiO_2 + K_2O \cdot 4SiO_2 \rightleftharpoons$ L	742	32.40	67.60
$K_2O \cdot 4SiO_2 \rightleftharpoons$ L	770	28.17	71.83
$K_2O \cdot 4SiO_2 + SiO_2$(quartz)$\rightleftharpoons$ L	769	27.50	72.5

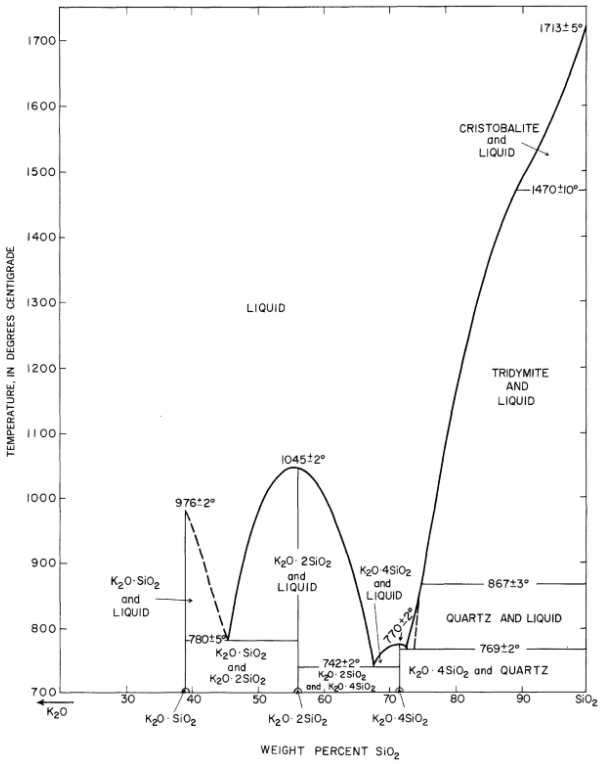

Figure 2.6: Phase diagram of the binary K_2O-SiO_2 system by Kracek, Bowen and Morey (1937).

2.4.2. Binary system K_2O-Al_2O_3

There is only scarce literature data on the binary K_2O-Al_2O_3 system; Brownmiller (1935) demonstrated that the melting temperature of $K_2O{\cdot}Al_2O_3$ is above 1650°C. He also determined that the formation of "β-alumina", an alkali aluminate, is due to mixtures with high alumina content. The reaction between alkali (Na_2O or K_2O) carbonates with Al_2O_3 has been explored by Strokov et al. (1940). According to this study when the molar ratio of K_2CO_3:Al_2O_3 was 1:1 only $K_2O{\cdot}Al_2O_3$ formed on fusion between 900°C and 1100°C and when the ratio was 2:1 or 3:1 the excess K_2O evaporated and only $K_2O{\cdot}Al_2O_3$ was present. Moreover, Kato and Yamauchi (1943) successfully obtained "β-Al_2O_3" by mixing K_2CO_3 and Al_2O_3, heat treating from 1640°C to 1700°C and treating the final products with a 6N solution of HCl.

2.4.3. Binary system Al_2O_3-SiO_2

The binary Al_2O_3-SiO_2 is the most fundamental system that has been used for a broad range of refractory applications and generally to clay industrials. Shepherd, Rankin, and Wright (1909) first reported on this system, without however identifying $3Al_2O_3{\cdot}2SiO_2$ (mullite) until Bowen and Greig (1924) did later. Early studies reported that mullite melts congruently at 1850°C (Budnikov, Tresvyatskii, & Kushakovskii, 1953; Toropov & Galakhov, 1958), and exhibits a eutectic with Al_2O_3 at 1840°C and 78 wt% Al_2O_3 as shown in the Al_2O_3-SiO_2 phase diagram (Figure 2.7) by Aramaki and Roy (1962). According to the authors, mullite is a solid solution, extending from 71.8 to 74.3 wt% Al_2O_3; but under metastable conditions mullite solid solutions can accommodate Al_2O_3 contents up to 77.5 wt%. Some contemporaneous reports observed that mullite melts incongruently (Filonenko & Lavrov, 1953; Horibe & Kuwabara, 1967; Welch, 1960).

Later work by Aksay and Pask (1975) revealed that stable mullite melts incongruently while metastable mullite melts congruently. This is reflected in the phase diagrams produced by Prochazka and Klug (1983) and by Klug, Prochazka and Doremus (1987) . As shown in Figure 2.8, thermodynamically stable mullite does melt incongruently, with the solid solution phase boundaries meeting at 1890°C for 77.2 wt% Al_2O_3 ($2Al_2O_3 \cdot SiO_2$). Al_2O_3 solubility in mullite decreases with decreasing temperature, reaching the nominal mullite composition of 71.6 wt% Al_2O_3 ($3Al_2O_3 \cdot 2SiO_2$) below 1600°C. According to the revised phase diagram, only a single eutectic point exists, that between SiO_2 and mullite at 1587 °C and 7.7 wt% Al_2O_3 (Klug et al., 1987).

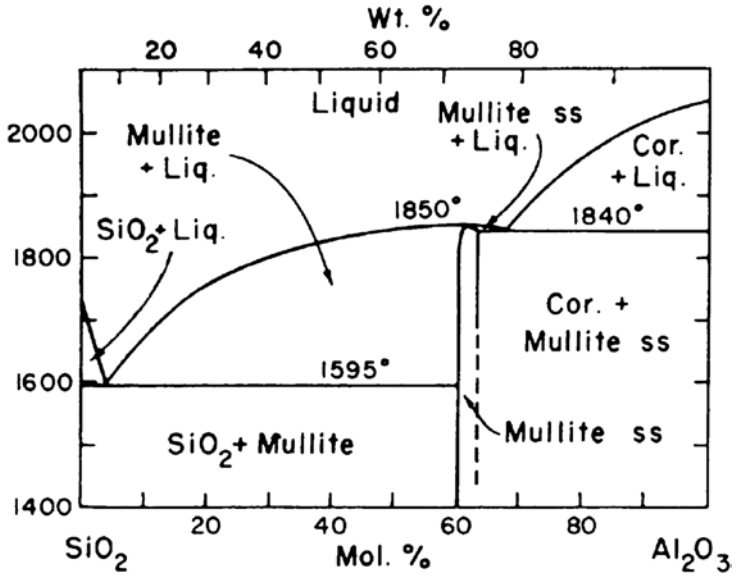

Figure 2.7: The system Al_2O_3-SiO_2. modified by Aramaki and Roy (1959a).

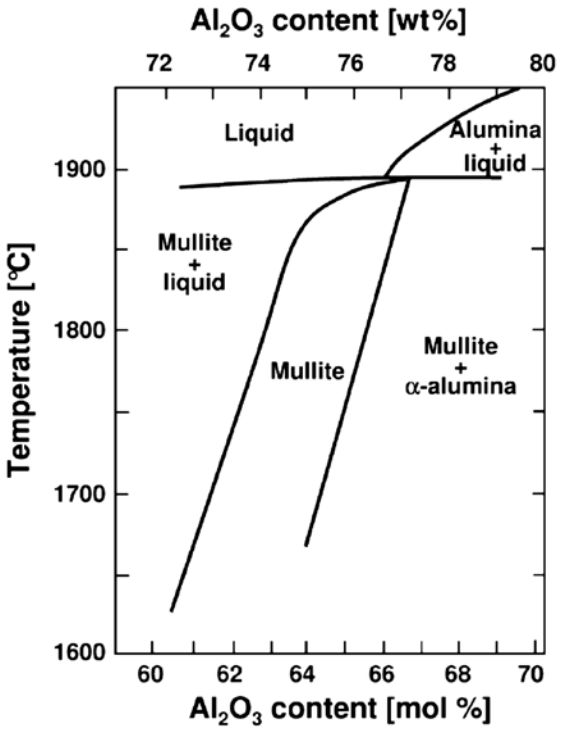

Figure 2.8: The mullite part of the Al_2O_3–SiO_2 phase diagram (Klug et al., 1987).

The excellent mechanical properties ($\sigma = 200\,MPa$), thermal expansion ($\alpha = 4.5 \times 10^{-6}K^{-1}$) and conductivity ($\lambda = 3.5\,W(mK)^{-1}$) at elevated temperatures make mullite a superior candidate for physical, mechanical and thermochemical applications (Ibrahim, Naga, Kader, & Salam, 1995). These compounds are important components in white ware, electrical ceramics and refractories. Mullite refractories are used in a wide range of applications mostly in the metallurgical, furnace lining and glass industries because of their high resistance to glass, molten slags and metal, outstanding load bearing capacity, and volume stability (Kanka & Schneider, 2000). They are also used as thermal insulation mainly in industrial furnaces and refractory ceramic fibres are the most well-known aluminosilicate product for thermal insulation (Butler & Dyson, 1997).

2.4.4. Ternary system K_2O-Al_2O_3-SiO_2

The ternary system K_2O-Al_2O_3-SiO_2 has been investigated because of its fundamental importance to a broad range of disciplines and technologies, like mineralogy, silicate ceramics and refractory applications (Heimann, 2010). This ternary system has high refractoriness which is attributed to the existence of three potassium aluminosilicate compounds ($K_2O.Al_2O_3.2SiO_2$, $K_2O.Al_2O_3.4SiO_2$ and $K_2O.Al_2O_3.6SiO_2$) with congruent melting points higher than 1600°C.

Schairer and Bowen (1955) submitted preliminary data of melting relations in this quasi-ternary system (Figure 2.9). Modifications of this diagram have been made by Aramaki and Roy (1959b).

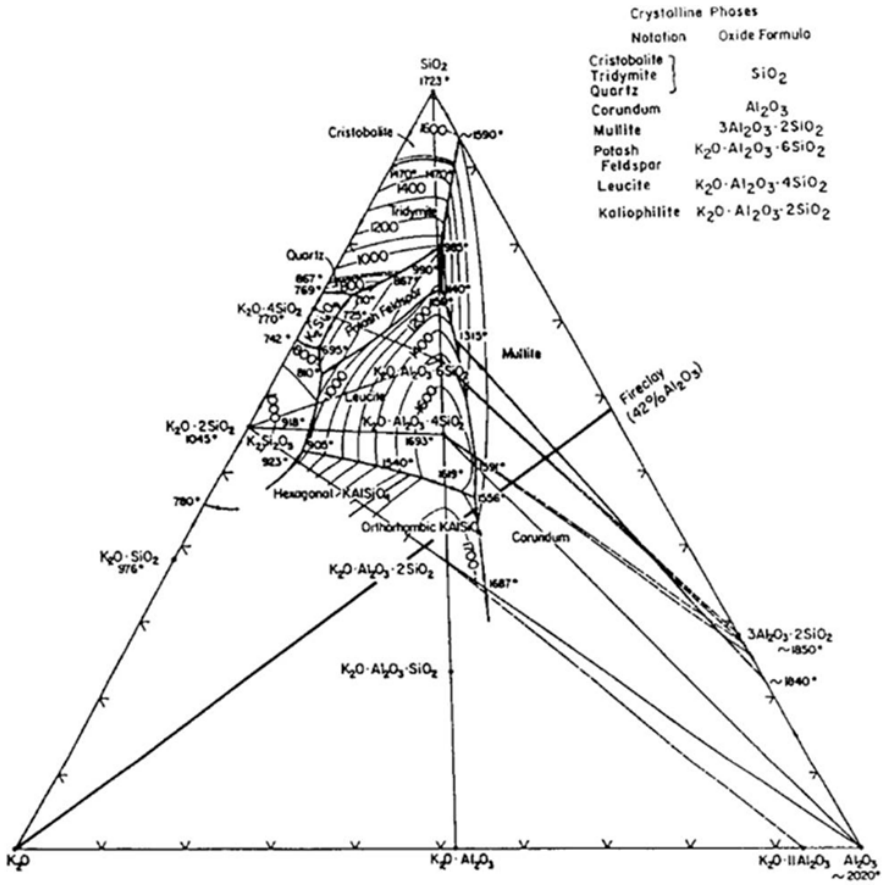

Figure 2.9: Phase diagram of the K_2O-Al_2O_3-SiO_2 system (Schairer & Bowen, 1955).

Moreover, Morey and Bowen (1922) concluded that pure potassium feldspar ($K_2O \cdot Al_2O_3 \cdot 6SiO_2$) which exists as microcline, sanidine, or adularia, has an incongruent melting point at 1150°C and forms leucite ($K_2O \cdot Al_2O_3 \cdot 4SiO_2$) and a more siliceous melt. It is practically very difficult for the compounds on the leucite-SiO_2 line, with lower liquidus temperatures than 1250°C, to crystallize and their viscosity is so high that even at temperatures close to the liquidus powdered glass could not flow. It is believed but not confirmed that the $K_2O \cdot Al_2O_3 \cdot 2SiO_2$ compound melts congruently at temperatures close to 1750°C or higher. Later Osborn and Muan (1960) expanded this system by revising and redrawing the K_2O-Al_2O_3-SiO_2 phase diagram. There are many unexplored regions in this phase diagram that make this system very prominent and interesting for further investigation (Lecomte, Pateyron, & Blanchart, 2004).

Apart from experimental studies that face a lot of difficulties with this system due to the viscous silicate melt, the mixtures being hygroscopic and the volatilization of K_2O, a notable effort has been made to approach this system by modelling (Yazhenskikh et al., 2011). In that paper, the liquidus temperature and the invariant points for the entire compositional range of the K_2O-Al_2O_3-SiO_2 system were calculated (Figure 2.10 & Figure 2.11). The calculated data are in accordance with the existing experimental data of the available phase diagrams.

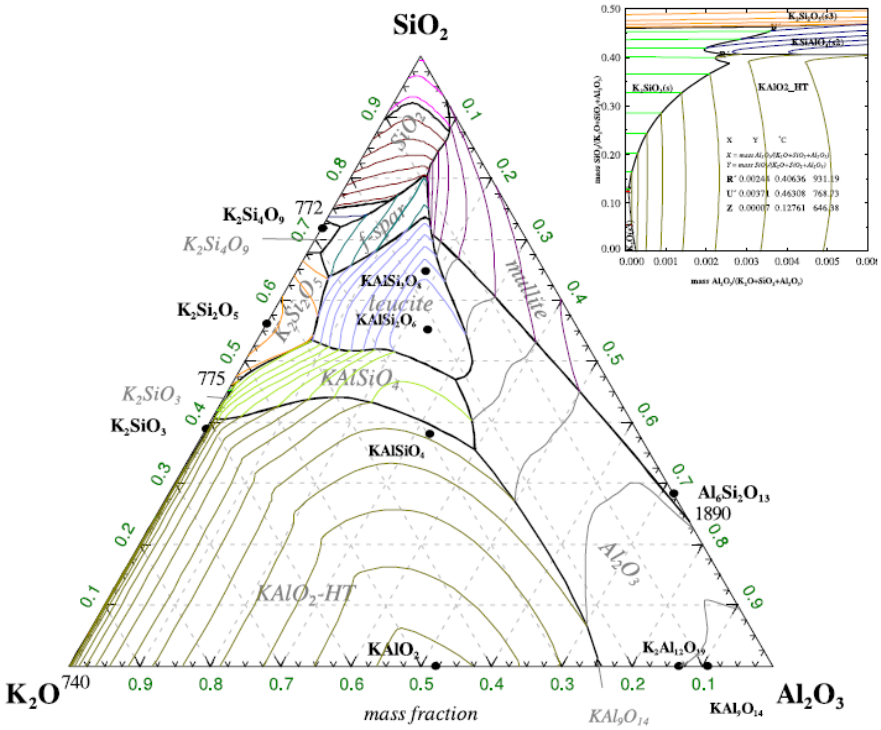

Figure 2.10: Liquidus surface for the K_2O-Al_2O_3-SiO_2 system (Yazhenskikh, Hack, & Müller, 2011).

Binary invariant points:

A = SiO_2, B = K_2O, C = Al_2O_3

	W(A)	W(B)	W(C)	°C
I	0.805	0.094	0.101	990.5
J	0.917	0.040	0.043	1470.0
O	0.737	0.126	0.137	1146.3
Q	0.709	0.267	0.024	725.6
T	0.558	0.371	0.071	905.3
V	0.524	0.411	0.066	896.0
B`	0.483	0.189	0.327	1631.8
D`	0.493	0.244	0.264	1633.0
B	0.502	0.177	0.321	1626.7
F	0.301	0.236	0.463	1776.7
Y	0.681	0.223	0.096	1000.7
W	0.421	0.330	0.248	1727.0
K	0.299	0.014	0.687	1868.8

Ternary invariant points:

A = SiO_2, B = K_2O, C = Al_2O_3

	W(A)	W(B)	W(C)	°C
F	0.010	0.244	0.746	1914.1
E	0.355	0.246	0.398	1725.8
C`	0.470	0.216	0.314	1619.8
L	0.876	0.022	0.102	1470.0
A`	0.707	0.131	0.162	1247.4
N	0.731	0.123	0.146	1139.6
M	0.801	0.092	0.107	984.9
R`	0.406	0.591	0.002	931.2
U	0.534	0.389	0.077	891.4
H	0.764	0.163	0.073	869.8
U`	0.463	0.533	0.004	768.7
R	0.639	0.312	0.049	786.0
P	0.721	0.254	0.025	724.0
S	0.678	0.304	0.018	707.2
Z	0.128	0.872	7.E-5	648.0

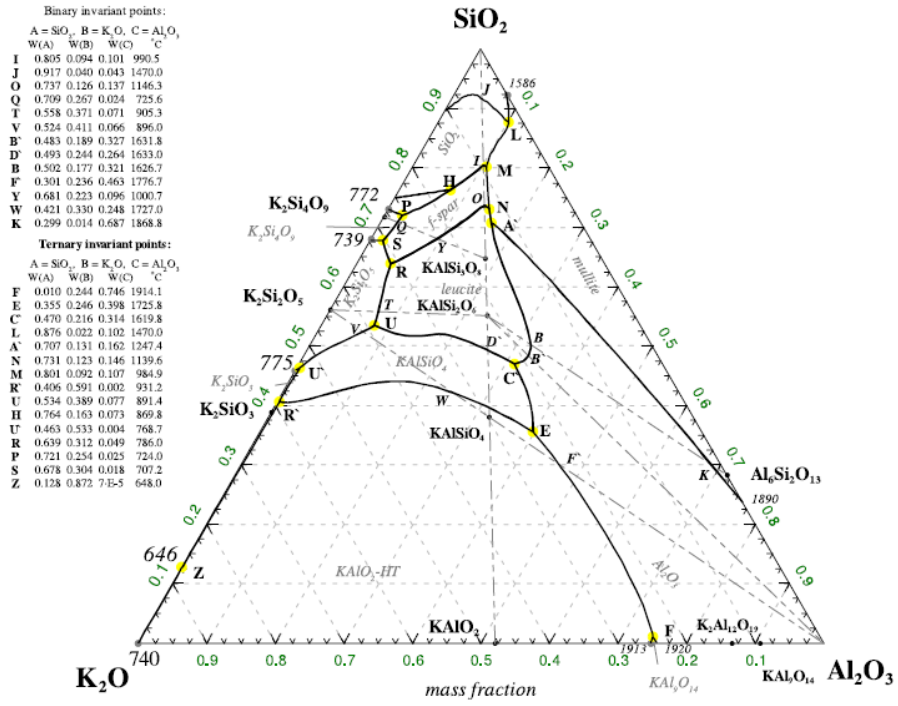

Figure 2.11: Invariant points for the K_2O-Al_2O_3-SiO_2 system (Yazhenskikh et al., 2011)

The most commonly used compound of this ternary system is leucite as its optical properties - the development of leucite inside the glass never hinders translucency - and the ability to retain its crystalline structure up to the melting temperature render it as the perfect candidate for dental applications. Leucite is widely used as a feldspathic veneering ceramic for coating different metals and for resin bonded crowns and veneers (Denry & Holloway, 2010). Kalsilite and leucite due to their high refractoriness are used in geopolymers to make them into refractory castables. Their physical behaviour is very advantageous and they are considered as a possible improvement on cement in respect of acidity, compressive strength, resistance to fire, and as a candidate material for the immobilization of hazardous or low/intermediate level radioactive waste (Kamseu, Rizzuti, Leonelli, & Perera, 2010).

2.4.4.1. Leucite

Leucite ($KAlSi_2O_6$) is a potassium aluminium mineral that is found in volcanic rocks, has a congruent melting point at 1686°C and occurs in two different polymorphs. Peacor (1968) discovered that when natural leucite is heat treated at elevated temperatures it crystallizes in cubic form (Figure 2.13) which has an *Ia3d* space group. Palmer et al. (1997) has found that leucite will form a tetragonal phase at tempertures under 665°C and according to Mazzi, Galli and Gottardi (1976) at room temperature leucite has an $I4_1/a$ space group (Figure 2.12). Later, the above space groups for both polymorphs have been confirmed by Walsh, Harrison and Redfern (2006).

Studies have reached somewhat different results regarding the phase transition temperature and the exact phase sequence for leucite. Peacor (1968) showed that leucite transforms with a single transition from tetragonal which is the low temperature form ($I4_1/a$) to cubic which is the high temperature form (*Ia3d).* Later, X-Ray diffraction

revealed the existence of two transition temperatures (655°C and 675°C) (Ito, Kuehner, & Ghose, 1995); tetragonal leucite (*$I4_1/a$)* will transform to an intermediate phase (*$I4_1/acd$)* before the final transformation to cubic leucite (*Ia3d).*

The transformation of kalsilite to leucite has attracted the attention of many research studies (Erbe & Sapieszko, 1997; Liu, Komarneni, & Roy, 1994; Zhang, Wu, Rao, & Lv, 2006) but the exact mechanism has not been determined. In some experiments where leucite was synthesized, kalsilite was detected as a non-stable reaction product that vanishes with prolonged heat treatment. Zhang et al. (2007) reported that the formation of kalsilite is a transitional stage that leads to crystallization of leucite. In addition, more recent studies are in accordance with the idea that kalsilite is the precursor of leucite (Buljane et al. 2009, Becerro et al. 2009). Moreover, in some studies it is indicated that the prolonged heat treatment of natural or synthesized kalsilite at elevated temperatures will gradually lead to a complete conversion to leucite and this phenomenon is believed to be connected with the high volatility of K_2O (Capobianco & Carpenter, 1989; Gregorkiewitz, Li, White, Withers, & Sobrados, 2008).

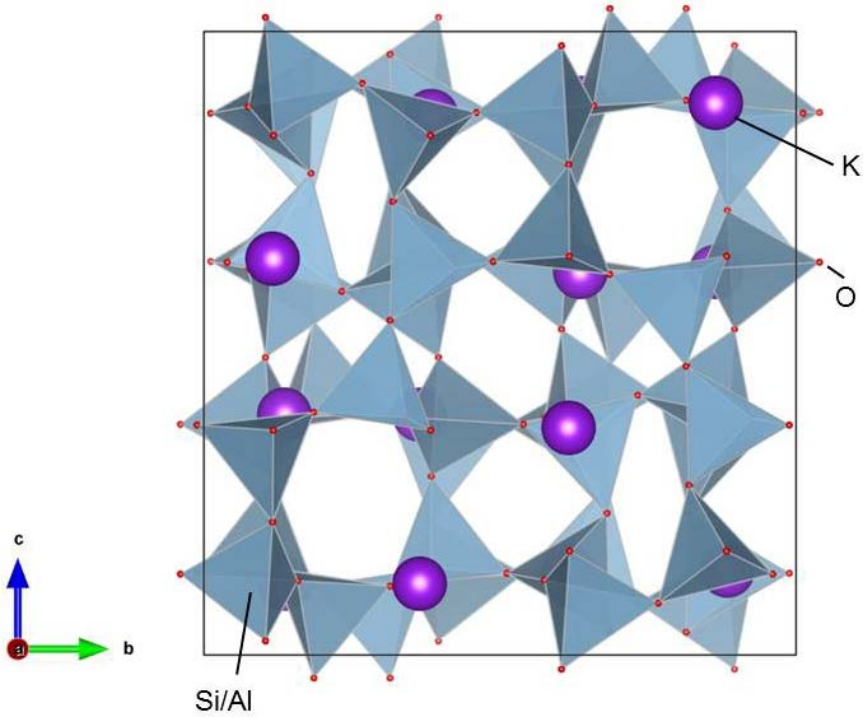

Figure 2.12: Atomic structure of tetragonal $KAlSi_2O_6$ with an $I4_1/a$ space group.

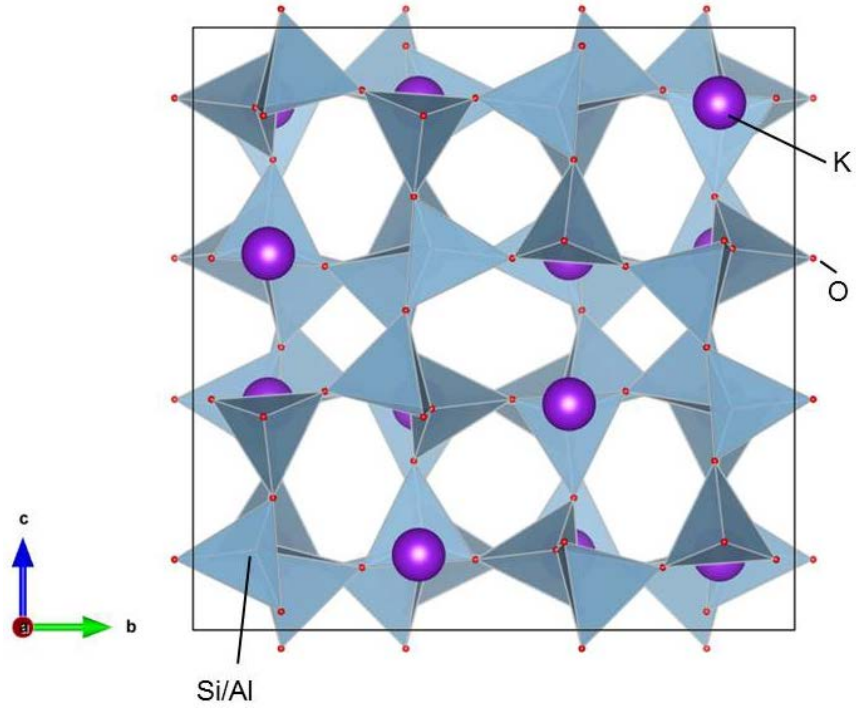

Figure 2.13: Atomic structure of cubic $KAlSi_2O_6$ an Ia3d space group.

2.4.4.2. Potassium aluminium silicate

Potassium aluminium silicate ($KAlSiO_4$) occurs in different crystalline forms; according to Smith and Tuttle (1957) $K_2O{\cdot}Al_2O_3{\cdot}2SiO_2$ compound exists in three different crystal structure families, one orthorhombic (Figure 2.15) and two hexagonal. Kalsilite (Figure 2.14) and kaliophilite minerals correspond to the hexagonal form (Buerger, 1954). Later, six different crystal structures have been confirmed including synthetic and natural forms of kalsilite and kaliophilite (Okamoto, 1997).

Kalsilite is a feldspathoid rock-forming mineral that occurs in potassium rich environment of volcanic rocks (Holmes, 1942). Bannister and Hey (1942) presented the first experimental data by analyzing kalsilite with X-Ray and microscopic methods. The tetrahedral framework structure of kalsilite was discovered by Claringbull and Bannister (1948) and later the first single-crystal X-Ray diffraction pattern for natural kalsilite was presented (Perrotta & Smith, 1965).

Buerger (1954) described the hexagonal crystal structure of kalsilite which is a stuffed derivative of the tridymite structure and was synthetically produced via two methods by Tuttle and Smith (Tuttle & Smith, 1958):

- Hydrothermally by mixing alumina and potassium disilicate at temperatures under 840°C.
- Phase transition by firing the $KAlSiO_4$ orthorhombic polymorph that was first introduced by Bowen (1917).

The crystal structures and phase transitions reported in literature for both synthetic and natural kalsilite forms are quite complex and inconsistent, as the properties and the structure of the modifications are affected by the existence of sodium and the

preparation conditions. $KAlSiO_4$ melts above 1700°C and there are not significant difficulties during the chemical reactions apart from the hygroscopicity of some mixtures and the volatile character of K_2O (Uchida, Downs, & Yang, 2006).

It has been discovered that a reversible transition from hexagonal to orthorhombic (O-form) $KAlSiO_4$ occurs around 840°C under hydrothermal conditions. Probably, this inversion is improved by solid solution of nepheline as kalsilite has been produced under 840°C in mixtures that contain around 10% of $NaAlSiO_4$ (Tuttle & Smith, 1958). However, Bowen (1917) had obtained the O-form of kalsilite from kaliophilite. In that study kaliophilite was heat treated at several temperatures and it was discovered that over 1550°C it will invert to orthorhombic form. Hull (1917) reported as well that an enantiotropic transition from hexagonal to orthorhombic form occurs around 1540°C. Afterwards, orthorhombic was described also as the high-temperature form and kaliophilite as the low-temperature one, although the temperature of the inversion among them was close to 900°C (Rigby & Richardson, 1947).

Orthorhombic kalsilite melts congruently above 1700°C but the exact temperature is unidentified (Schairer & Bowen, 1955). In that study, orthorhombic and hexagonal forms of kalsilite were considered as the high and low temperature modifications, respectively, but a comprehensive structural study was not conducted.

A significant attempt of understanding the interrelation among crystal structure forms of $KAlSiO_4$ has been conducted by Abbot (1984). The phase relationship of Smith and Tuttle has been found to be odd as the high temperature polymorphs (kaliophilite, orthorhombic $KAlSiO_4$) have lower symmetry compared to low temperature polymorphs (kalsilite). According to Abbot orthorhombic $KAlSiO_4$ is more likely to be metastable.

It is important to understand the tetrahedral linkage in $KAlSiO_4$ because it is pertinent to the displasive and reconstructive transitions happening and to further organize its crystalline phases based on the different framework topologies (Capobianco & Carpenter, 1989). The polymorphs of kalsilite share the same structural features, sheets of 6-membered rings (6mR) of tetrahedra. These ordinary structural features give similar parameters for the unit-cell between the polymorphs of kalsilite. The two sheets of tetrahedra are connected by sharing apical oxygens which produce an approximately 8.6 Å length for the c unit-cell parameter. The length of the α unit-cell parameter varies, since it relates to the distance among the 6mR of tetrahedra at about 5.2 Å. Alteration in the framework topology is accomplished by changing the sequence of up and down pointing tetrahedra on the 6mR. This alteration will change the way of linkage through the apical oxygens among the sheets. Stebbins et al. (1986) had examined kalsilite from two groups with different topology and found that silicate and aluminate tetrahedra are all the time ordered in three-dimensional networks.

Capobianco and Carpenter (1989) reported the existence of three temperature ranges for kalsilite:

- 20-850°C, low temperature area, twinned orthorhombic kalsilite (pseudohexagonal)
- 860-910°C, transition temperature area, superstructure $3\sqrt{3}$ kalsilite probably orthorhombic, coexistence of two phases (low temperature and superstructure kalsilite)
- 910-950°C, high temperature area, hexagonal kalsilite, possibly tridymite structure as described by Kawahara et al. (1987).

Hexagonal kalsilite has a tetrahedral open framework which appears to be isotypic with that of nepheline and tridymite and has a topological symmetry $P6_3/mmc$ (Gatta et al., 2011). Kalsilite's framework consists of sheets (001) of ordered SiO_4 and AlO_4 tetrahedra which form 6-membered rings (6mR) pointing alternatively up (U) and down (D); Figure 2.14 shows a single tetrahedral sheet of kalsilite. The stacking of the sheets along the c axis is accomplished by connection by the apical oxygen atoms, which nominally lie on special positions on the threefold rotation axis. The tetrahedral 6mR are additionally di-trigonally distorted as the tetrahedra rotate around [001]. The sense of this rotation will be the same for all the sheets of the *P31c* polymorph but with reversed sense of rotation in the $P6_3$ polymorph among adjacent (001) sheets.

On the other hand, orthorhombic kalsilite ($KAlSiO_4$-01) is disadvantaged by twinning and pseudosymmetry and its crystal symmetry has been reported to be an average orthorhombic structure with *Pnam* and $Pn2_1m$ space groups (Gregorkiewitz & Schäfer, 1980). Gregorkiewitz et al. (2008) successfully produced $KAlSiO_4$-01 via solid state synthesis and concluded that its framework topology is different from tridymite and its stuffed derivatives. It is built of sheets which consist of 6-membered rings of ordered SiO_4 and AlO_4 tetrahedra in the ab plane but these ring topologies are not the UDUDUD sequence of tridymite. In the (001) plane there are two types of six-membered rings, UUDUDD and UUUDDD, in a 2:1 ratio (Figure 2.15). These authors reported that $KAlSiO_4$-01 is actually monoclinic with space group $P12_11$ and has two orthorhombic supergroups, $Pn2_1m$ and $P2_12_12_1$.

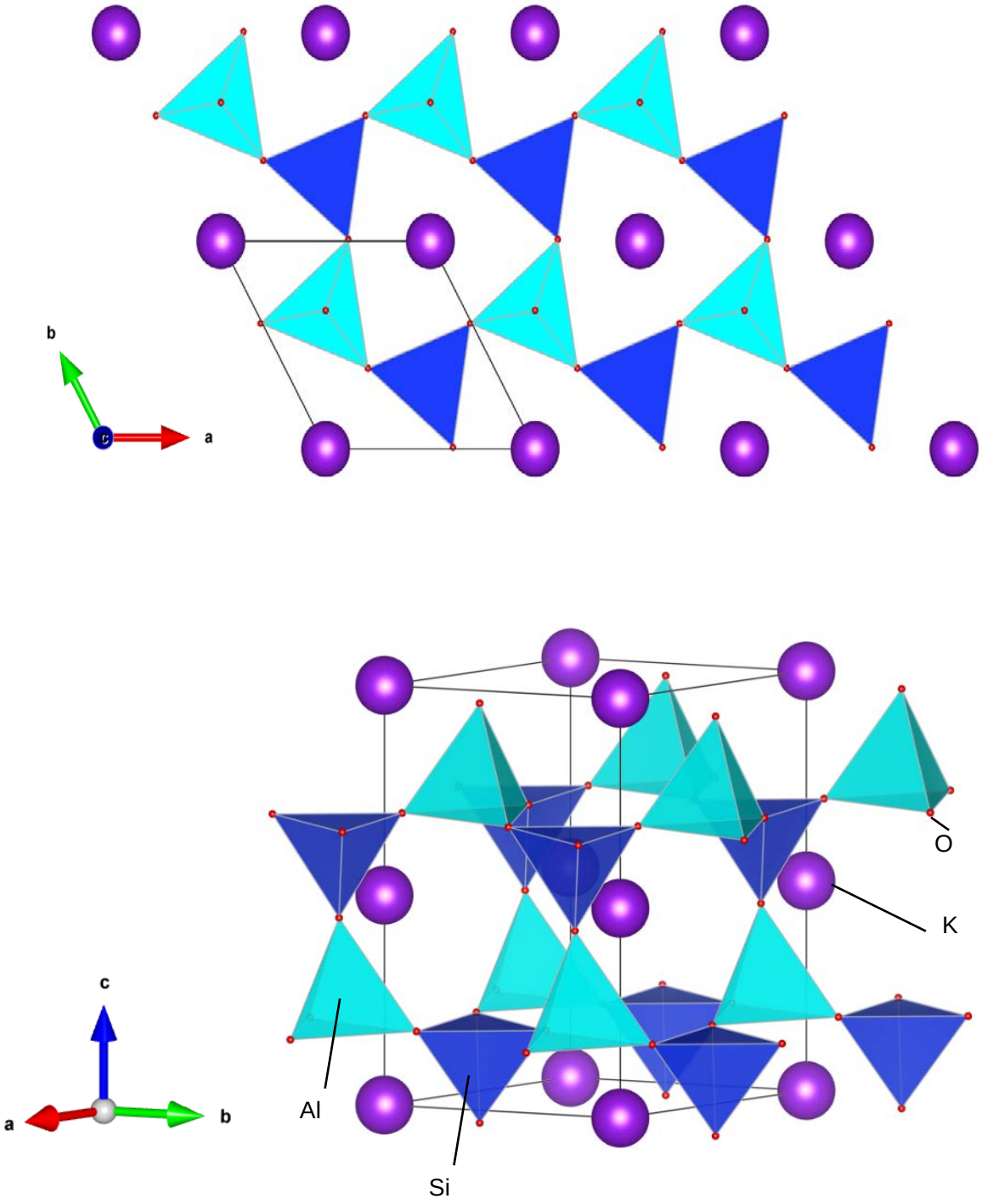

Figure 2.14: 1. Crystal structure of P63 hexagonal $KAlSiO_4$: (top) a single tetrahedral sheet of kalsilite, and (bottom) a view of the three-dimensional framework.

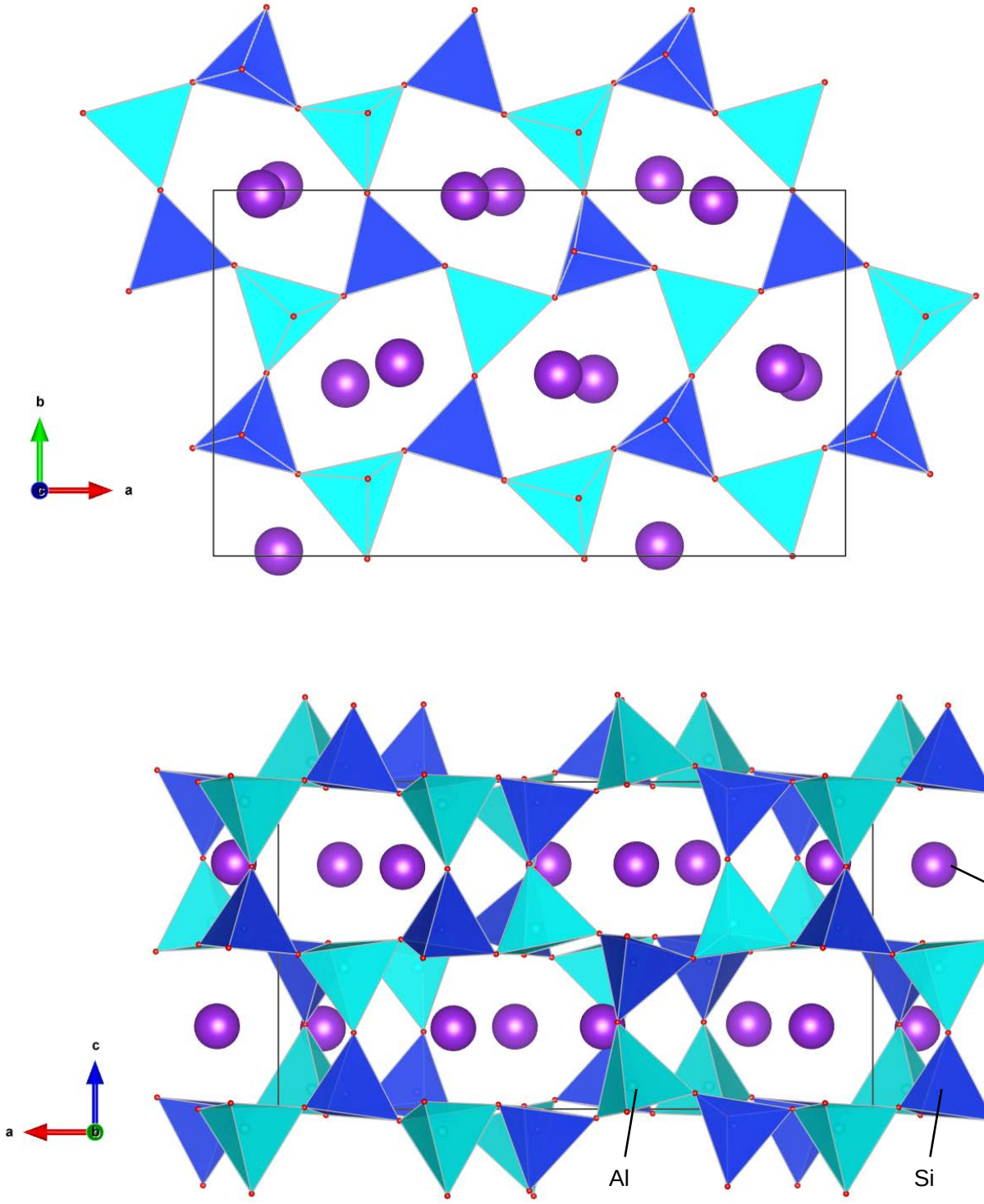

Figure 2.15: Atomic structure of $P12_11$ "orthorhombic" $KAlSiO_4$ (top) a single tetrahedral sheet, and (bottom) projection along the b axis.

2.4.5. Ternary system ZrO_2-Al_2O_3-SiO_2.

The Al_2O_3-SiO_2-ZrO_2 system is broadly used in several applications mainly due to its refractoriness. The high thermal shock resistance, excellent mechanical strength, low creep at elevated temperatures and corrosion resistance over alkaline compounds makes this system ideal for applications demanding high temperature resistance (Gawronski, Patzig, Höche, & Rüssel, 2013).

Adding zirconia to mullite refractories was first employed to improve the manufacturing process (Garvie, Goss, Marshall, & Urbani, 1988). However, it was discovered early on that this also resulted in significant enhancement of the resistance to corrosion by chemicals in the furnace during glass melting, which prompted extensive use of this refractory type after 1940. The reaction-sintering concept suggested by Claussen & Jahn (1980) further established the field of Al_2O_3-ZrO_2 composites. According to this concept, when alumina reacts with zircon ($ZrSiO_4$), at approximately 1450°C, zirconia toughened alumina materials can be produced. Budnikov & Litvakovskii (1953) first produced the phase diagram for this system (Figure 2.16).

More accurate phase diagrams of the binary ZrO_2-SiO_2 and Al_2O_3-ZrO_2 systems were developed by Levin, Robbins and Howard (1964) as depicted in the following figures (Figure 2.17 & Figure 2.18).

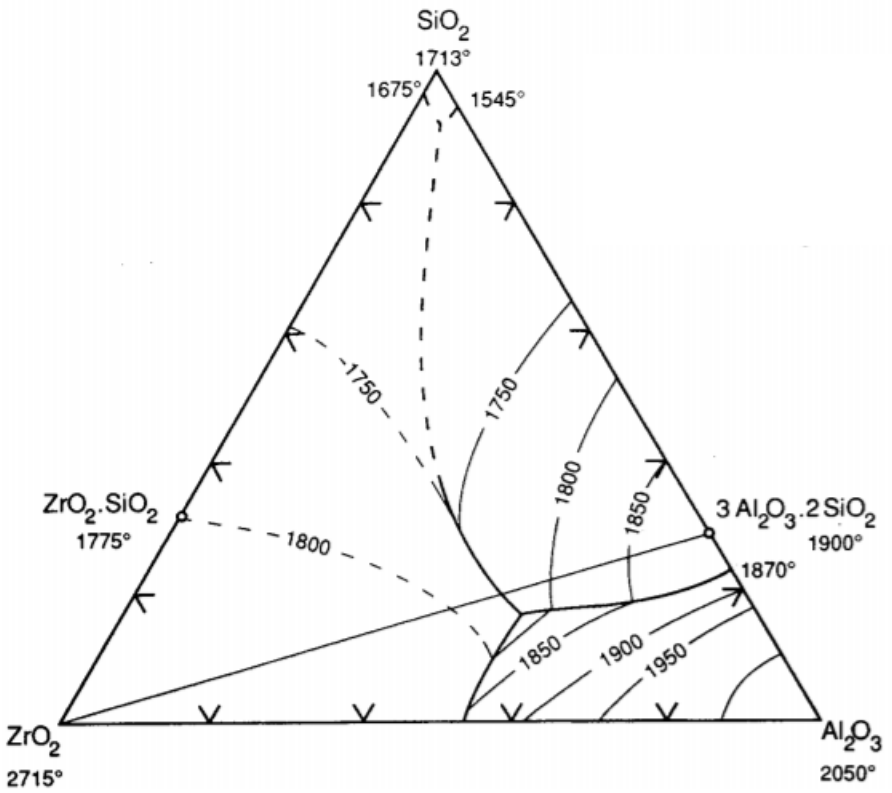

Figure 2.16: Phase diagram of the ZrO_2-Al_2O_3-SiO_2 system (Budnikov et al., 1953).

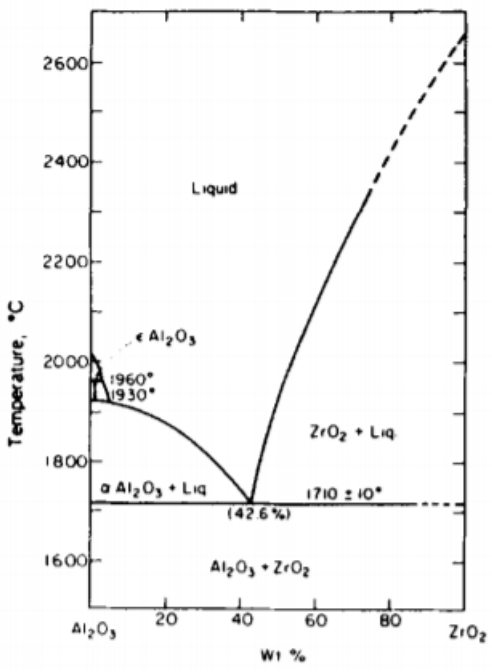

Figure 2.17: Phase diagram of the binary system Al_20_3-ZrO_2 (Levin et al., 1964).

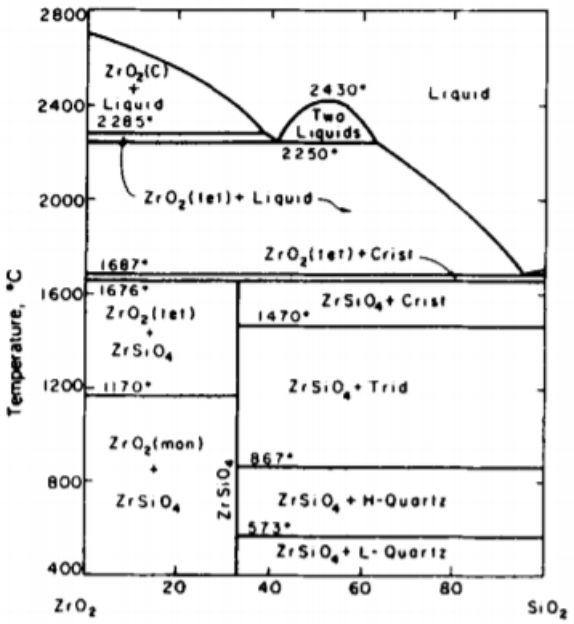

Figure 2.18: Phase diagram of the binary system ZrO_2 -SiO_2 (Levin et al., 1964).

The outstanding thermal shock resistance, low creep, elevated mechanical strength and corrosion resistance in alkaline compounds at high temperature make this system ideal for refractory applications. A principal group of refractories in the Al_2O_3-SiO_2-ZrO_2 system is based on baddeleyite (ZrO_2), mullite ($Al_{4.5}Si_{1.5}O_{9.75}$) and corundum (SiO_2) structures. It is widely employed in glass-melting furnaces, feeders, forehearths, as mantle blocks, plungers, channels, tubes and orifice rings. These materials are broadly used as refractory rollers in fast firing furnaces for the manufacture of sanitary ware, tableware and ceramic tiles (Zanelli, Dondi, Raimondo, & Guarini, 2010).

2.4.6. Ternary system MgO-Al_2O_3-SiO_2

Magnesium aluminium silicate materials are commonly used due to their elevated chemical and thermal stability, low coefficient of thermal expansion, elevated mechanical strength and good dielectric properties (Shamsudin et al., 2011).

The $MgO\text{-}Al_2O_3\text{-}SiO_2$ system was originally explored by Rankin and Merwin (1918). The cordierite $2MgO{\cdot}2Al_2O_3{\cdot}5SiO_2$ mineral was the first compound discovered with a melting temperature of 1460°C where liquid and mullite forms. Later, it was confirmed that a glass with cordierite composition can form the indialite mineral with fast cooling (Miyashiro & Iiyama, 1954). Karkhanavala and Hummel (1953) confirmed the existence of three different polymorphic forms of cordierite, an α-form or high temperature (crystallization above 950°C), an unstable μ-form, (crystallization around 850°C), and a stable β-form or low temperature (hydrothermal crystallization).

Foster (1950) concluded that sapphirine mineral $4MgO{\cdot}5Al_2O_3{\cdot}2SiO_2$ would have a region of stability in the $MgO\text{-}Al_2O_3\text{-}SiO_2$ system. Accodingly, Keith and Schairer (1952) developed a detailed phase-equilibrium diagram including a field of stability for sapphirine (Figure 2.19).

The magnesium-aluminium silicate system is a basis for glass ceramics, cordierite ceramics, metallurgical slags, and rocks and minerals. Moreover, $MgO–Al_2O_3–SiO_2$ is a high quality refractory system because it has excellent thermomechanical, thermo-chemical and physical properties under service conditions (Lee, Zhang, & Karakus, 2004). Cordierite has an outstanding resistance to thermal shock. Thus, cordierite's anisotropic expansion behaviour is used for the manufacture of honey comb catalysts. It is used for burner nozzles, kiln furniture and as insulator in electric hot plates (Camerucci, Urretavizcaya et al. 2001).

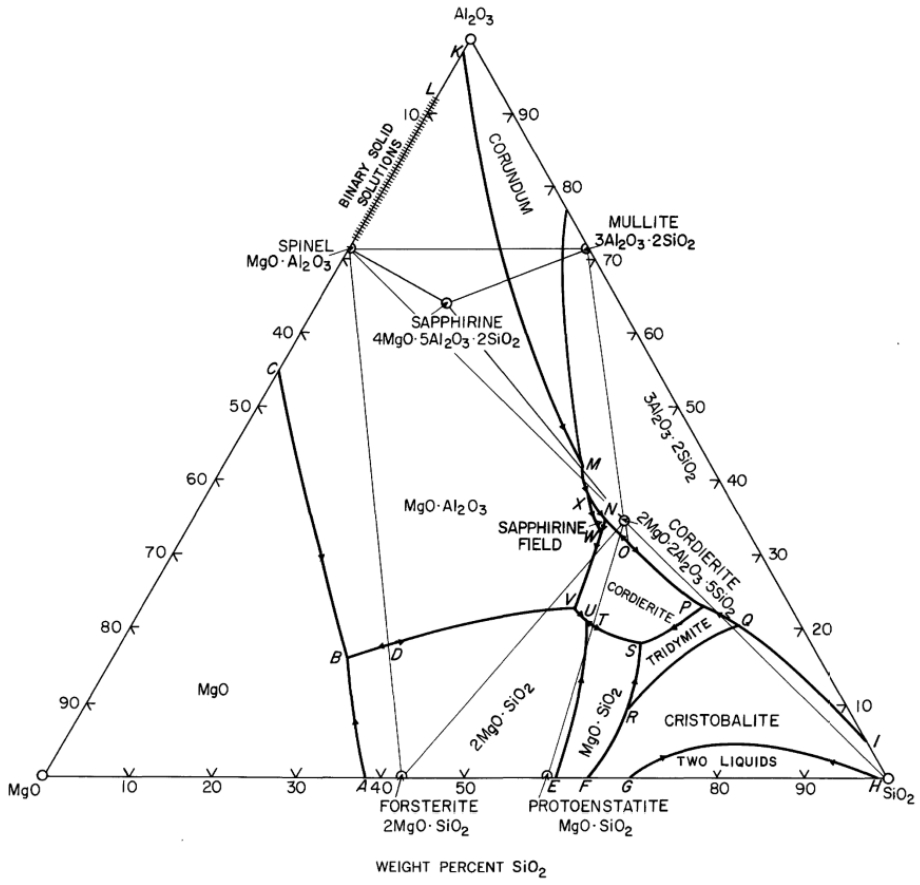

Figure 2.19: Phase diagram of the system MgO-Al_2O_3-SiO_2, modified from Keith and Schairer (1952).

2.4.7 Compositional Modifications

In this section, the effect of adding different chemical compounds on the properties and the chemical stability of alkali aluminosilicate systems is examined.

SnO_2

The role of SnO_2 in aluminosilicate systems and its influence on their crystallization and chemical-physical properties has not been extensively explored. Bobkova and Kuz'menkova (2008) discuss that adding SnO_2 in aluminosilicate glasses has comparable effects with ZrO_2. Their study also indicated that the solubility of SnO_2 in aluminosilicate melts is greater than that of ZrO_2.

Rare Earth Oxides (La_2O_3, Nd_2O_3 and Y_2O_3)

Wang et al. (2016) discuss the challenges faced by the addition of rare earth oxides to alkaline earth aluminosilicate glass fibres. It is debated that a small addition of rare earth oxides has the tendency to increase the crystallization temperature of fibres and as a result affect the thermal performance and crystallization behaviour of glass fibres. However, Wang et al. (2016) assume that this addition will negatively influence the bio-solubility of glass fibres but not in a way that the bio-soluble character could be in doubt.

MgO, ZrO_2 and Y_2O_3

Addition of MgO, Y_2O_3 and ZrO_2 is known to affect the grain growth and densification of alumina (Bunsell, 2005; Galusek, Sedláček, Chovanec, & Michálková, 2015). Addition of dopants changes the microstructure of the samples and decelerates densification and grain growth, particularly regarding ZrO_2 and Y_2O_3. In general, temperatures by about 50-100 °C higher compared with materials without these dopants were required to achieve the same microstructural characteristics.

TiO_2

Titanium dioxide (TiO_2) is an important nucleating agent (Höland, Frank, & Rheinberger, 1995; Rouf, Hermansson, & Carlsson, 1978); elevated (4–8 wt%) TiO_2 content in the K_2O-Al_2O_3-SiO_2 system, is related to the evolution of leucite. Stookey (1959) conducted a research on both theory and practice of catalysed crystallization of glass. The sub-microscopic catalysts promote the growth of the principal crystalline phases and heterogeneous nucleation. Cattell et al. (2005) have used titanium dioxide as a sub-microscopic catalyst in the K_2O-Al_2O_3-SiO_2 system, they have added (0.4 wt%)

TiO_2 to their glass compositions and concluded that amorphous phase separation is a result of this addition.

ZnO

In a recent paper (Smedskjaer, Youngman, & Mauro, 2013) the rheological and physical properties of five series of sodium aluminosilicate glasses with ZnO, CaO, MgO, SrO or BaO and deviating Al_2O_3-to-SiO_2 ratio have been explored. The main aspect of this paper was to examine and compare the effect of ZnO in aluminosilicate glasses. It is indicated that specifically for the glass samples with ZnO or MgO the content of Al_2O_3 in comparison with Na_2O/K_2O will influence most of the property values. Specifically, when the Al_2O_3 content is equal to Na_2O/K_2O content, the coefficient of thermal expansion, liquid fragility index, refractive index and the isoform temperatures display a change in slope. The conclusions of this paper showed that the effect of Zn^{2+} on sodium aluminosilicate glasses is analogous to that of Mg^{2+}. Replacing MgO with ZnO can be very advantageous where the MgO content is limited as it can have a negative effect on the glass-forming ability.

2.5. References

Abbot, R. N. (1984). $KAlSiO_4$ stuffed derivatives of tridymite - phase-relationships. *American Mineralogist, 69*(5-6), 449-457.

Aksay, İ A., & Pask, J. A. (1975). Stable and metastable equilibria in the system SiO_2-Al_2O_3. *Journal of the American Ceramic Society, 58*(11-12), 507-512. doi:10.1111/j.1151-2916.1975.tb18770.x

Aramaki, S., & Roy, R. (1962). Revised phase diagram for the system Al_2O_3-SiO_2. *Journal of the American Ceramic Society, 45*(5), 229-242. doi:10.1111/j.1151-2916.1962.tb11133.x

Aramaki, S., & Roy, R. (1959a). The mullite-corundum boundary in the systems MgO-Al_2O_3-SiO_2 and CaO-Al_2O_3-SiO_2. *Journal of the American Ceramic Society, 42*(12), 644-645. doi:10.1111/j.1151-2916.1959.tb13589.x

Aramaki, S., & Roy, R. (1959b). Revised equilibrium diagram for the system Al_2O_3-SiO_2. *Nature, 184*(4686), 631-632.

Bahadori, A. (2014). *Thermal insulation handbook for the oil, gas, and petrochemical industries.* Amsterdam: Elsevier.

Bannister, F. A., & Hey, M. H. (1942). Kalsilite, a polymorph of $KAlSiO_4$, from Uganda. *Mineralogical Magazine, 26*(177), 218-224. doi:10.1180/minmag.1942.026.177.02

Bhattacharya, A. K., Das, P., & Chakraborti, D. P. (2005). Devitrification characteristics of aluminosilicate ceramic vitreous fibres. *InterCeram: International Ceramic Review, 54*(1), 26-28.

Binde, G., & Bolender, T. (2002). Recrystallisation and formation of cristobalite in alkaline earth silicate fibres (AES) under thermic stress. [Rekristallisation und cristobalitbildung in hochtemperaturglasfasern (AES) nach thermischer belastung] *Gefahrstoffe Reinhaltung Der Luft, 62*(6), 273-278.

Bobkova, N. M., & Kuz'menkova, N. M. (2008). Crystallization of SnO_2-modified K_2O-Li_2O-Al_2O_3-SiO_2 glasses. *Glass and Ceramics, 65*(11), 390-392. doi:10.1007/s10717-009-9096-8

Boff, J. C., Jubb, G. A., & Mottram, R. S. (2010). *European Patent Application EP 2213634 A1*. Munich, Germany: European Patent Office.

Bowen, N. L., & Greig, J. W. (1924). The system: Al_2O_3.SiO_2. *Journal of the American Ceramic Society, 7*(4), 238-254. doi:10.1111/j.1151-2916.1924.tb18190.x

Bowen, N. L. (1917). The sodium-potassium nephelites. *American Journal of Science, 43*(254), 115-132. doi:10.2475/ajs.s4-43.254.115

Brown, R. C. (2000). Activity of crystalline silica formed during use of refractory ceramic fiber products. *Aihc & E,* Orlando, Florida.

Brown, R. C., Sara, E. A., Hoskins, J. A., Evans, C. E., Young, J., Laskowski, J. J., . . . Rood, A. P. (1992). The effects of heating and devitrification on the structure and biological activity of aluminosilicate refractory ceramic fibres. *Annals of Occupational Hygiene, 36*(2), 115-129. doi:10.1093/annhyg/36.2.115

Brownmiller, L. T. (1935). A study of the system lime-potash-alumina. *American Journal of Science, 29*(171), 260-277. doi:10.2475/ajs.s5-29.171.260

Budnikov, P. P., Tresvyatskii, S. G., & Kushakovskii, V. I. (1953). The refinement in the Al_2O_3-SiO_2 phase diagram. *USSR Academy of Sciences, 93*, 281-283.

Buerger, M. J. (1954). The stuffed derivatives of the silica structures. *American Mineralogist, 39*(7-8), 600-614.

Bunsell, A. R. (2005). Oxide fibers for high-temperature reinforcement and insulation. *Jom, 57*(2), 48-51. doi:10.1007/s11837-005-0216-9

Butler, M. A., & Dyson, D. J. (1997). The quantification of different forms of cristobalite in devitrified alumino-silicate ceramic fibres. *Journal of Applied Crystallography, 30*(4), 467-475.

Capobianco, C., & Carpenter, M. (1989). Thermally induced changes in kalsilite ($KAlSiO_4$). *American Mineralogist, 74*(7-8), 797-811.

Cartwright, J. E. (1977). *U.S. Patent No. 4041199 A*. Washington, DC: U.S. Patent and Trademark Office.

Catherine, H., & Skinner, W. (2003). Mineralogy of Asbestos Minerals. *Indoor and Built Environment, 12*(6), 385-389. doi:10.1177/1420326X03037003

Cattell, M. J., Chadwick, T. C., Knowles, J. C., & Clarke, R. L. (2005). The crystallization of an aluminosilicate glass in the $K_2O–Al_2O_3–SiO_2$ system. *Dental Materials, 21*(9), 811-822.

Cheng, R. T., Mc Dermott, H. J., Gia, G. M., Cover, T. L., & Duda, M. M. (1992). Exposures to refractory ceramic fibers in refineries and chemical plants. *Applied Occupational and Environmental Hygiene, 7*(6), 361-367. doi:10.1080/1047322X.1992.10390173

Christoph, G., Nyssen, P. R., & Wagner, W. (2000). *EP 0399320 B2*. Munich, Germany: European Patent Office.

Claringbull, G. F., & Bannister, F. A. (1948). The crystal structure of kalsilite. *Acta Crystallographica, 1*(1), 42-43. doi:10.1107/S0365110X48000089

Claussen, N., & Jahn, J. (1980). Mechanical properties of sintered, in situ-reacted mullite-zirconia composites. *Journal of the American Ceramic Society, 63*(3-4), 228-229. doi:10.1111/j.1151-2916.1980.tb10700.x

Commission Directive 97/69/EC, (1997).

Comodi, P., Cera, F., Gatta, G. D., Rotiroti, N., & Garofani, P. (2010). The devitrification of artificial fibers: A multimethodic approach to quantify the temperature-time onset of cancerogenic crystalline phases. *Annals of Occupational Hygiene, 54*(8), 893-903. doi:10.1093/annhyg/meq056

Cugell, D. W., & Kamp, D. W. (2004). Asbestos and the pleura: a review. *Chest, 125* doi:10.1378/chest.125.3.1103

Denry, I., & Holloway, J. A. (2010). Ceramics for dental applications: a review. *Materials, 3*(1), 351-368.

Dietrichs, P., & Kronert, W. (1981). Properties, high-temperature behaviour and service conditions of ceramic fibres. *Proceedings High Temperature Ceramic Fibres for the Insulation of Industrial Furnaces*, Essen, FRG.

Donaldson, K., Murphy, F. A., Duffin, R., & Poland, C. A. (2010). Asbestos, carbon nanotubes and the pleural mesothelium: a review of the hypothesis regarding the role of long fibre retention in the parietal pleura, inflammation and mesothelioma. *Particle and Fibre Toxicology, 7*(1), 5. doi:10.1186/1743-8977-7-5

Dunbar, R. B., Rademaker, J. C., & Williams, S. E. (1967). *US Patent No. US 3352746 A*. Washington, DC: United States Patent and Trademark Office.

Dyson, D. J., Butler, M. A., Hughes, R. J., Fisher, R., & Hicks, G. W. (1997). The de-vitrification of alumino-silicate ceramic fibre materials - The kinetics of the formation of different crystalline phases. *Annals of Occupational Hygiene, 41*(5), 561-590. doi:10.1016/S0003-4878(97)00013-6

Eastes, W., & Hadley, J. G. (1996). A Mathematical Model of fiber Carcinogenicity and Fibrosis in Inhalation and Intraperitoneal Experiments in Rats. *Inhalation Toxicology, 8*(4), 323-343. doi:10.3109/08958379609052912

ECFIA (Ed.). (2010). *Recognition and control of exposure to alumino silicate wools/refractory ceramic fibres (ASW/RCF).* Paris: ECFIA.

Erbe, E. M., & Sapieszko, R. S. (1997). *US Patent No.5,622,551*. Washington, DC: U.S. Patent and Trademark Office.

Fairfax, R., & Burmeister, S. (2001). Exposure to crystalline silica during a foundry ladle relining process. *Applied Occupational and Environmental Hygiene, 16*(7), 718-720. doi:10.1080/10473220117540

Filonenko, N. E., & Lavrov, I. V. (1953). Fusion of mullite. *Doklady Akademii Nauk SSSR, 89*, 141-142.

Foster, W. R. (1950). Synthetic sapphirine and its stability relations in the system MgO-Al_2O_3-SiO_2. *Journal of the American Ceramic Society, 33*(3), 73-84. doi:10.1111/j.1151-2916.1950.tb12765.x

George, D., Guthrie, J., & Brooke Mossman, T. (1994). Health effects of mineral dusts, mineralogical society of America. *Rev.Mineral., 28*, 584.

Gualtieri, A. F., Foresti, E., Lesci, I. G., Roveri, N., Gualtieri, M. L., Dondi, M., & Zapparoli, M. (2009). The thermal transformation of Man Made Vitreous Fibers

(MMVF) and safe recycling as secondary raw materials (SRM). *Journal of Hazardous Materials, 162*(2-3), 1494-1506. doi:10.1016/j.jhazmat.2008.06.066

Galusek, D., Sedláček, J., Chovanec, J., & Michálková, M. (2015). The influence of MgO, Y_2O_3 and ZrO_2 additions on densification and grain growth of submicrometre alumina sintered by SPS and HIP. *Ceramics International, 41*(8), 9692-9700. doi:10.1016/j.ceramint.2015.04.038

Gantner, B. A. (1986). Respiratory hazard from removal of ceramic fiber insulation from high temperature industrial furnaces. *American Industrial Hygiene Association Journal, 47*(9), 530-534. doi:10.1080/15298668691390179

Gaodu, A. N., Pitak, N. V., Volfson, R. E., & Drizheruk, M. E. (1977). Crystallisation in heated aluminosilicate fibers. *Inorganic Materials, 13*(12), 1802-1804.

Garvie, R. C., Goss, M. F., Marshall, S., & Urbani, C. (1988). Designing advanced refractories with monoclinic zirconia polycrystals. *Materials Science Forum, 34*(36), 681-688.

Gatta, G. D., Angel, R. J., Zhao, J., Alvaro, M., Rotiroti, N., & Carpenter, M. A. (2011). Phase stability, elastic behavior, and pressure-induced structural evolution of kalsilite: A ceramic material and high-T/high-P mineral. *American Mineralogist, 96*(8-9), 1363-1372. doi:10.2138/am.2011.3793

Gawronski, A., Patzig, C., Höche, T., & Rüssel, C. (2013). High-strength glass-ceramics in the system $MgO/Al_2O_3/SiO_2/ZrO_2/Y_2O_3$–microstructure and properties. *CrystEngComm, 15*(31), 6165-6176.

Gregorkiewitz, M., Li, Y., White, T. J., Withers, R. L., & Sobrados, I. (2008). The structure of “orthorhombic” $KAlSiO_4$-O1: evidence for Al–Si order from MAS

NMR data combined with Rietveld refinement and electron microscopy. *The Canadian Mineralogist, 46*(6), 1511-1526.

Gregorkiewitz, M., & Schäfer, H. (1980). The structure of $KAlSiO_4$-kaliophilite-O1: Application of the subgroup-supergroup relations to the quantitative space group determination of pseudosymmetric crystals. *Sixth European Crystallographic Meeting,* Barcelona. 155.

Groat, S., Kauffer, E., Lovett, M., Miller, B. G., Kidd, M. W., Davies, L. S. T., . . . Hurley, J. F. (1999). *Epidemiological research in the European ceramic fibre industry, 1994–8. Vol. 1: Workplace concentrations of airborne dust and fibres.* (IOM Report No. 1). Edinburgh: Institute of Occupational Medicine.

Gualtieri, A. F., Foresti, E., Lesci, I. G., Roveri, N., Gualtieri, M. L., Dondi, M., & Zapparoli, M. (2009). The thermal transformation of Man Made Vitreous Fibers (MMVF) and safe recycling as secondary raw materials (SRM). *Journal of Hazardous Materials, 162*(2-3), 1494-1506. doi:10.1016/j.jhazmat.2008.06.066

Harrison, P. T. C., & Brown, R. C. (2011). Devitrification of artificial fibres. *Annals of Occupational Hygiene, 55*(7), 823-824. doi:10.1093/annhyg/mer061

Hearle, J. W. S. (Ed.). (2001). *High-performance fibres* (1st ed.). Cambridge, England: Woodhead Publishing.

Heimann, R. B. (2010). *Classic and advanced ceramics: from fundamentals to applications*. Weinheim: John Wiley & Sons.

Höland, W., Frank, M., & Rheinberger, V. (1995). Surface crystallization of leucite in glasses. *Journal of Non-Crystalline Solids, 180*(2-3), 292-307. doi:10.1016/0022-3093(94)00464-1

Holmes, A. (1942). A suite of volcanic rocks from south-west Uganda containing kalsilite (a polymorph of $KAlSiO_4$). *Mineralogical Magazine, 26*(19), 217.

Holroyd, D., Rea, M. S., Young, J., & Briggs, G. (1988). Health-related aspects of the devitrification of aluminosilicate refractory fibres during use as a high-temperature furnace insulant. *Annals of Occupational Hygiene, 32*(2), 171-178. doi:10.1093/annhyg/32.2.171

Horibe, T., & Kuwabara, S. (1967). Thermo-analytical investigation in the Al_2O_3-SiO_2 system. *Bulletin of the Chemical Society of Japan, 40*(4), 972-982.

Hull., A. W. (1917). A new method of x-ray crystal analysis. *Physical Review, 10*(6), 661-696. doi:10.1103/PhysRev.10.661

IARC Working Group on the Evaluation of Carcinogenic Risks to Humans. (2002). *Man-made vitreous fibres.* (IARC monographs on the evaluation of carcinogenic risks to humans No. 81). Lyon: IARCPress.

Ibrahim, D., Naga, S., Kader, Z. A., & Salam, E. A. (1995). Cordierite-mullite refractories. *Ceramics International, 21*(4), 265-269.

Ito, Y., Kuehner, S., & Ghose, S. (1995). The structure of a high temperature phase in a cationic conductor, $KAlSi_2O_6$. *Solid State Ionics, 79*, 120-123.

Jubb, G. A. (2012). *U.S. Patent No. 8,088,701 B2*. Washington, DC: U.S. Patent and Trademark Office.

Jubb, G. A. (1994). *International Patent Application No. WO 94/15883*. Geneva, Switzerland: World Intellectual Property Organization.

Jubb, G. A., & Freeman, C. J. (2003). *WO 03/059835 A1*. Geneva, Switzerland: World Intellectual Property Organization.

Jubb, G. A., & Martin, J. L. (1993). *International Patent Application No. WO 93/15028 A1*. Geneva, Switzerland: World Intellectual Property Oganization.

Kamseu, E., Rizzuti, A., Leonelli, C., & Perera, D. (2010). Enhanced thermal stability in K_2O-metakaolin-based geopolymer concretes by Al_2O_3 and SiO_2 fillers addition. *Journal of Materials Science, 45*(7), 1715-1724.

Kanka, B., & Schneider, H. (2000). Aluminosilicate fiber/mullite matrix composites with favorable high-temperature properties. *Journal of the European Ceramic Society, 20*(5), 619-623.

Karkhanavala, M. D., & Hummel, F. A. (1953). The polymorphism of cordierite. *Journal of the American Ceramic Society, 36*(12), 389-392. doi:10.1111/j.1151-2916.1953.tb12825.x

Karlsson, S., Lundberg, R., & Carlsson, R. (1986). Thermal and environmental effects on ceramic fibres. *Journal De Physique, Colloque, 47*(C1), C1-587-C1-591.

Kato, S., & Yamauchi, T. (1943). Untersuchungen über den β·Korund. (2) Synthese im System Na_2O-Al_2O_3. *Journal of the Ceramic Association, Japan, 51*(609), 543-550. doi:10.2109/jcersj1892.51.609_543

Kawahara, A., Andou, Y., Marumo, F., & Okuno, M. (1987). The crystal structure of high temperature form of kalsilite ($KAlSiO_4$) at 950 ^oC. *Mineralogical Journal, 13*(5), 260-270. doi:10.2465/minerj.13.260

Keith, M., & Schairer, J. (1952). The stability Field of sapphirine in the system MgO-Al_2O_3-SiO_2. *The Journal of Geology, 60*(2), 181-186.

Klug, F. J., Prochazka, S., & Doremus, R. H. (1987). Alumina-silica phase diagram in the mullite region. *Journal of the American Ceramic Society, 70*(10), 750-759. doi:10.1111/j.1151-2916.1987.tb04875.x

Kracek, F. C., Bowen, N. L., & Morey, G. W. (1929). The system potassium metasilicate-silica. *The Journal of Physical Chemistry, 33*(12), 1857-1879.

Kracek, F. C., Brown, N. L., & Morey, G. W. (1937). Equilibrium relations and factors influencing their determination in the system K_2SiO_3–SiO_2. *Journal of Physical Chemistry, 41*(9), 1183-1193.

Laskowski, J. J., Young, J., Gray, R., Acheson, R., & Forder, S. D. (1994). The identity, development and quantification of phases in devitrified, commercial-grade, aluminosilicate, refractory ceramic fibres: an x-ray powder diffractometry study. *Analytica Chimica Acta, 286*(1), 9-23. doi:10.1016/0003-2670(94)80172-X

Lecomte, G., Pateyron, B., & Blanchart, P. (2004). Experimental study and simulation of a vertical section mullite-ternary eutectic (985°C) in the SiO_2–Al_2O_3–K_2O. *Materials Research Bulletin, 39*, 1469-1478.

Lee, W., Zhang, S., & Karakus, M. (2004). Refractories: controlled microstructure composites for extreme environments. *Journal of Materials Science, 39*(22), 6675-6685.

Levin, E. M., Robbins, C. R., McMurdie, H. F., & American Ceramic Society. (1964). *Phase diagrams for ceramists*. Columbus, Ohio: American Ceramic Society.

Linnainmaa, M., Kangas, J., Mäkinen, M., Metsärinne, S., Tossavainen, A., Säntti, J., . . . Kalliokoski, P. (2007). Exposure to refractory ceramic fibres in the metal

industry. *Annals of Occupational Hygiene, 51*(6), 509-516. doi:10.1093/annhyg/mem027

Liu, C., Komarneni, S., & Roy, R. (1994). Seeding effects on crystallization of $KAlSi_3O_8$, $RbAlSi_3O_8$, and $CsAlSi_3O_8$ gels and glasses. *Journal of the American Ceramic Society, 77*(12), 3105-3112. doi:10.1111/j.1151-2916.1994.tb04556.x

Mast, R. W., McConnell, E. E., Anderson, R., Chevalier, J., Kotin, P., Bernstein, D. M., . . . Hesterberg, T. W. (1995). Studies on the chronic toxicity (inhalation) of 4 types of refractory ceramic fiber in male fischer-344 rats. *Inhalation Toxicology, 7*(4), 425-467. doi:10.3109/08958379509015208

Mast, R. W., McConnell, E. E., Hesterberg, T. W., Chevalier, J., Kotin, P., Thevenaz, P., . . . Anderson, R. (1995). Multiple-dose chronic inhalation toxicity study of size-separated kaolin refractory ceramic fiber in Male fischer 344 rats. *Inhalation Toxicology, 7*(4), 469-502. doi:10.3109/08958379509015209

Maxim, L. D., Hadley, J. G., Potter, R. M., & Niebo, R. (2006). The role of fiber durability/biopersistence of silica-based synthetic vitreous fibers and their influence on toxicology. *Regulatory Toxicology and Pharmacology, 46*(1), 42-62.

Maxim, L. D., Allshouse, J. N., Kelly, W. P., Walters, T., & Waugh, R. (1997). A multiyear workplace-monitoring program for refractory ceramic fibers: findings and conclusions. *Regulatory Toxicology and Pharmacology, 26*(2), 156-171.

Maxim, L. D., Allshouse, J., Fairfax, R. E., Lentz, T. J., Venturin, D., & Walters, T. E. (2008). Workplace monitoring of occupational exposure to refractory ceramic fiber - A 17-year retrospective. *Inhalation Toxicology, 20*(3), 289-309. doi:10.1080/08958370701866040

Maxim, L. D., Venturin, D., & Allshouse, J. N. (1999). Respirable crystalline silica exposure associated with the installation and removal of RCF and conventional silica-containing refractories in industrial furnaces. *Regulatory Toxicology and Pharmacology, 29*(1), 44-63. doi:10.1006/rtph.1998.1268

Maxim, L. D., Mast, R. W., Utell, M. J., Yu, C. P., Boymel, P. M., Zoitos, B. K., & Cason, J. E. (1999). Hazard assessment and risk analysis of two new synthetic vitreous fibers. *Regulatory Toxicology and Pharmacology, 30*(1), 54-74. doi:10.1006/rtph.1999.1314

Mazzi, F., Galli, E., & Gottardi, G. (1976). The crystal structure of tetragonal leucite. *American Mineralogist, 61*(1-2), 108-115.

McConnell, E. E. (2000). A science-based paradigm for the classification of synthetic vitreous fibers. *Regulatory Toxicology and Pharmacology, 32*(1), 14-21. doi:10.1006/rtph.2000.1409

Miyashiro, A., & Iiyama, T. (1954). Mineral indialite, polymorphic with cordierite. *Japan Academy Proceedings, 30*, 746-751.

Morey, G. W., & Bowen, N. L. (1922). The melting of potash feldspar. *American Journal of Science, 4*, 1-21.

Morey, G. W. (1914). New crystalline silicates of potassium and sodium, their preparation and general properties. *Journal of the American Chemical Society, 36*(2), 215-230.

Morey, G. W. (1917). The ternary system H_2O-K_2SiO_3-SiO_2. *Journal of the American Chemical Society, 39*(6), 1173-1229. doi:10.1021/ja02251a008

Morgan Advanced Materials. (2017). *Thermal ceramics products from Morgan Advanced Materials*. Winsdor, UK: Morgan Advanced Materials.

Okamoto, Y. (1997). Structural modification of $KAlSiO_4$ minerals. *Earth Science Reports, 4*(1), 41-72.

Palmer, D. C., Dove, M. T., Ibberson, R. M., & Powell, B. M. (1997). Structural behavior, crystal chemistry, and phase transitions in substituted leucite: High-resolution neutron powder diffraction studies. *American Mineralogist, 82*(1-2), 16-29.

Peacor, D. R. (1968). A high temperature single crystal diffractometer study of leucite, $(K,Na)AlSi_2O_6$. *Zeitschrift Fur Kristallographie - New Crystal Structures, 127*(1-4), 213-224. doi:10.1524/zkri.1968.127.1-4.213

Perrotta, A., & Smith, J. (1965). The crystal structure of kalsilite, $KAlSiO_4$. *Mineralogical Magazine, 35*(272), 588-595.

Prochazka, S., & Klug, F. J. (1983). Infrared-Transparent Mullite Ceramic. *Journal of the American Ceramic Society, 66*(12), 874-880. doi:10.1111/j.1151-2916.1983.tb11004.x

Rankin, G. A., & Merwin, H. W. (1918). The ternary system MgO-Al_2O_3-SiO_2. *American Journal of Science, 45*, 301-325.

Rice, C., Lockey, J., Lemasters, G., Dimos, J., & Gartside, P. (1994). Assessment of current fibre and silica exposure in the U.S. refractory ceramic fibre manufacturing industry. *Annals of Occupational Hygiene, 38*(inhaled_particles_VII), 739-744. doi:10.1093/annhyg/38.inhaled_particles_VII.739

Rigby, G. R., & Richardson, H. M. (1947). The occurrence of artificial kalsilite and allied potassium aluminum silicates in blast-furnace linings. *Mineralogical Magazine, 28*, 75-88.

Rossiter, C. E., & Chase, J. R. (1995). Statistical analysis of results of carcinogemcity studies of synthetic vitreous fibres at research and consulting company, Geneva. *Annals of Occupational Hygiene, 39*(5), 759-769. doi:10.1093/annhyg/39.5.759

Rouf, M. A., Hermansson, L., & Carlsson, R. (1978). Crystallisation of glasses in the primary phase field of leucite in the K_2O–Al_2O_3–SiO_2 system. *Transactions of the British Ceramic Society, 77*, 36-39.

Schairer, J. F., & Bowen, N. L. (1955). The system K_2O-Al_2O_3-SiO_2. *American Journal of Science, 253*(12), 681-746. doi:10.2475/ajs.253.12.681

Shamsudin, Z., Hodzic, A., Soutis, C., Hand, R., Hayes, S., & Bond, I. (2011). Characterisation of thermo-mechanical properties of MgO–Al_2O_3–SiO_2 glass ceramic with different heat treatment temperatures. *Journal of Materials Science, 46*(17), 5822.

Shepherd, E. W., Rankin, G. A., & Wright, F. E. (1909). The binary systems of alumina and silica, lime, and magnesia. *American Journal of Science, 28*(4), 293-333.

Shih, T. S., Lu, P. Y., Chen, C. H., Soo, J. C., Tsai, C. L., & Tsai, P. J. (2008). Exposure profiles and source identifications for workers exposed to crystalline silica during a municipal waste incinerator relining period. *Journal of Hazardous Materials, 154*(1-3), 469-475. doi:10.1016/j.jhazmat.2007.10.047

Smedskjaer, M. M., Youngman, R. E., & Mauro, J. C. (2013). Impact of ZnO on the structure and properties of sodium aluminosilicate glasses: Comparison with

alkaline earth oxides. *Journal of Non-Crystalline Solids, 381*, 58-64. doi:10.1016/j.jnoncrysol.2013.09.019

Smith, J. V., & Tuttle, O. F. (1957). The nepheline-kalsilite system; Part I, X-ray data for the crystalline phases. *American Journal of Science, 255*(4), 282-305.

Sopicka-Lizer, M., & Pawlowski, S. (1980). The applicability of DTA to the study of the crystallisation process of ceramic fibres. *Thermochimica Acta, 38*(3), 293-297. doi:10.1016/0040-6031(80)85036-2

Stanton, M. F., & Wrench, C. (1972). Mechanisms of mesothelioma induction with asbestos and fibrous glass. *Journal of the National Cancer Institute, 48*(3), 797-821. doi:10.1093/jnci/48.3.797

Stebbins, J. F., Murdoch, J. B., Carmichael, I. S. E., & Pines, A. (1986). Defects and short-range order in nepheline group minerals: a silicon-29 nuclear magnetic resonance study. *Physics and Chemistry of Minerals, 13*(6), 371-381. doi:10.1007/BF00309182

Stookey, S. D. (1959). Catalyzed crystallization of glass in theory and practice. *Industrial & Engineering Chemistry, 51*(7), 805-808. doi:10.1021/ie50595a022

Strokov, F. N., Musyakov, V. A., Volkov, V. S., & Katsenelenbogen, P. D. (1940). Reaction of alkali carbonates with alumina and with silica, on fusion. *Sbornik Rabot Gossudarstwennyi Institut Prikladnoi Khimii, 32*, 4-15.

Strübel, G., & Faul, L. (1994). Pollutant load caused by ceramic fibres and new results about their behaviour of recrystallization. *Annals of Occupational Hygiene, 38*(inhaled_particles_VII), 713-722. doi:10.1093/annhyg/38.inhaled_particles_VII.713

Sweeney, J., & Gilgrist, D. (1998). Exposures to respirable silica during relining of furnaces for molten metals. *Applied Occupational and Environmental Hygiene, 13*(7), 508-510.

Tonnesen, T., & Telle, R. (2007). *Influence of firing temperature and time on the quantitative phase formation and recrystallization behaviour of high temperature glass fibres (AES) and refractory ceramic fibres (RCF).* (German Association of Manufacturers and Processors of High Temperature Wool).

Toropov, N. A., & Galakhov, F. I. (1958). Solid solutions in the system Al_2O_3-SiO_2. *Bulletin of the Academy of Sciences of the USSR, Division of Chemical Science, 7*(1), 5-9. doi:10.1007/BF01170853

Tuttle, O. F., & Smith, J. V. (1958). The nepheline-kalsilite system: II. Phase relations. *American Journal of Science, 256*(10), 571-589.

Uchida, H., Downs, R. T., & Yang, H. (2006). Crystal-chemical investigation of kalsilite from San Venanzo, Italy, using single-crystal X-ray diffraction and Raman spectroscopy. *Geochimica Et Cosmochimica Acta, 70*(18), A677-A680. doi:10.1016/j.gca.2006.06.1267

Van Den Bergen, A., Rocchi, P. S., & Boogaard, P. J. (1994). Ceramic fibers and other respiratory hazards during the renewal of the refractory lining in a large industrial furnace. *Applied Occupational and Environmental Hygiene, 9*(1), 32-35. doi:10.1080/1047322X.1994.10388260

Vine, G., Young, J., & Nowell, I. W. (1984). Health hazards associated with aluminosilicate fibre products. *The Annals of Occupational Hygiene, 28*(3), 356-359. doi:10.1093/annhyg/28.3.356

Wallenberger, F. T., & Bingham, P. A. (Eds.). (2010). *Fiberglass and glass technology*. Boston, MA: Springer.

Walsh, J., Harrison, R., & Redfern, S. (2006). Anelastic behaviour of leucite $KAlSi_2O_6$. *Materials Science and Engineering: A, 442*(1), 208-211.

Wang, X., Liu, H., Wang, Z., Ma, Y., & Kale, G. M. (2016). Effect of rare earth oxides on the properties of bio-soluble alkaline earth silicate fibers. *Journal of Rare Earths, 34*(2), 203-207. doi:10.1016/S1002-0721(16)60015-7

Welch, J. H. (1960). A new interpretation of the mullite problem. *Nature, 186*(4724), 545-546.

Yazhenskikh, E., Hack, K., & Müller, M. (2011). Critical thermodynamic evaluation of oxide systems relevant to fuel ashes and slags, Part 5: Potassium oxide–alumina–silica. *CALPHAD: Computer Coupling of Phase Diagrams and Thermochemistry, 35*(1), 6-19. doi:10.1016/j.calphad.2010.10.010

Zanelli, C., Dondi, M., Raimondo, M., & Guarini, G. (2010). Phase composition of alumina–mullite–zirconia refractory materials. *Journal of the European Ceramic Society, 30*(1), 29-35.

Zhang, Y., Lv, M., Chen, D., & Wu, J. (2007). Leucite crystallization kinetics with kalsilite as a transition phase. *Materials Letters, 61*(14-15), 2978-2981.

Zhang, Y., Wu, J., Rao, P., & Lv, M. (2006). Low temperature synthesis of high purity leucite. *Materials Letters, 60*(23), 2819-2823. doi:10.1016/j.matlet.2006.01.098

Zhen, A., & Song, S. (1990). Study of the thermal degradation of ceramic fibres of the Al_2O_3-SiO_2 system. *Refractories, 39*(4-5), 19-22.

Chapter 3

Experimental Procedure

3.Experimental Procedure

This chapter describes the techniques and methods used to prepare and study the materials under investigation in this work. Different techniques were applied for each task, two in the case of the sample preparation: heat treatment of as made glass fibres and glass fibre synthesis through melt processing; two techniques for elemental analysis: X-Ray fluorescence energy-dispersive and X-Ray spectroscopy; four techniques for the structural characterisation: X-Ray powder diffraction, Rietveld refinement, Raman spectroscopy and scanning electron microscopy; and one technique to study the thermal behaviour: differential thermal analysis;.

3.1. Sample preparation

3.1.1. Melt processing

In order to explore the K_2O-Al_2O_3-SiO_2 system, series of glass fibres with increasing amounts of K_2O were prepared based on existing phase diagrams through melt processing. This process can be broken down into three basic steps: batching, melting and fiberisation.

3.1.1.1 Batching

In this initial stage of glass fibre manufacture, all the inorganic raw materials (Table 3.5) were weighed with an electronic balance with an accuracy of ± 0.01 Kg in exact quantities according to the batch calculations as listed in Table 3.1 and Table 3.3 to produce glass fibres with the compositions shown in Table 3.2 and Table 3.4. The raw

materials were then thoroughly mixed in a cement mixer for at least 30 minutes (batching).

Table 3.1: Batches used for production of 16 kg of glass fibres in the K_2O-Al_2O_3-SiO_2 system.

	Al_2O_3 (kg)	**SiO_2 (kg)**	**K_2CO_3 (kg)**	**Total (kg)**
KAS-1	3.75	8.82	5.09	17.66
KAS-2	3.85	8.49	5.43	17.77
KAS-3	4.33	7.72	5.85	17.90
KAS-4	4.65	6.97	6.49	18.11
KAS-5	5.17	6.08	7.03	18.283
KAS-6	6.05	5.59	6.46	18.10
KAS-7	6.41	5.47	6.11	17.99
KAS-8	6.23	5.31	6.61	18.15
KAS-9	7.35	6.26	3.56	17.17

Table 3.2: Nominal glass fibre compositions in the K_2O-Al_2O_3-SiO_2 system.

	Al_2O_3 (wt%)	**SiO_2 (wt%)**	**K_2O (wt%)**
KAS-1	23.4	55.1	21.6
KAS-2	24.0	53.0	23.0
KAS-3	27.0	48.2	27.5
KAS-4	29.0	43.5	27.5
KAS-5	32.2	38.0	29.8
KAS-6	37.7	34.9	27.4
KAS-7	42.8	36.6	20.6
KAS-8	38.8	33.2	28.0
KAS-9	45.8	39.1	15.1

Table 3.3: Batches used for production of 16 kg of glass fibres in the K_2O-Al_2O_3-ZrO_2-SiO_2 system.

	Al_2O_3 (kg)	**SiO_2 (kg)**	**K_2O (kg)**	**ZrO_2 (kg)**	**Total (kg)**
KASZ-1	5.79	4.40	6.13	1.68	18.00
KASZ-2	6.68	5.41	3.28	1.73	17.10

Table 3.4: Nominal glass fibre compositions in the K_2O-Al_2O_3-ZrO_2-SiO_2 system.

	Al_2O_3 (wt%)	**SiO_2 (wt%)**	**K_2O (wt%)**	**ZrO_2 (wt%)**
KASZ-1	36.1	30.9	26.0	7.0
KASZ-2	41.6	37.3	13.9	7.2

Table 3.5: Raw materials used for glass fibre production.

Raw Material	**Purity**	**Supplier**
Al_2O_3	99.0 ± 0.5	Richard Baker Harrison Ltd
K_2CO_3	99.5 ± 0.2	Norkem
SiO_2	99.6 ± 0.2	Sibelco UK
$ZrSiO_2$	99.0 ± 0.5	Richards Bay Minerals

3.1.1.2. Melting

The melt furnace was heated by two molybdenum glass melting electrodes (Figure 3.1). Glass melting electrodes must withstand extremely elevated temperatures and aggressive glass melts. Molybdenum is the right material for these challenging conditions. A smooth flow of glass is achieved by careful temperature control.

Figure 3.1: Melt furnace (344 mm interior Ø and 160 mm height) and molybdenum glass melting electrodes (52 mm outer Ø and 200 mm long).

It is very important to avoid any contamination with remaining materials from previous uses so the first step was to clean the melt furnace and the surface of molybdenum electrodes. The two electrodes were placed in the melt rig with a 5-mm starting distance between their flat surface and an alumina plate with an opening of 10 mm in the middle was used to cover the furnace orifice and the opening was sealed with a ceramic cylinder. Part of the starting material was added to the furnace to cover the orifice and the electrodes. The melting process was initiated by adding a small amount of the batch between electrodes and melting the mixture using an oxy-acetylene torch while applying electric current between the 2 electrodes.

After the melting process was started, the milled powder was gradually added to the furnace while slowly increasing the distance of the 2 electrodes. This allowed to gradually grow the melt pool. The melt was covered by the starting material powder throughout the process (Figure 3.2). Once the melt flowed, the ceramic cylinder was removed from the plate's opening allowing a melt stream of glass to flow down (Figure 3.3).

Figure 3.2: Melting process in progress.

Figure 3.3: Melt stream of glass (700 mm distance).

3.1.1.3. Fiberization

The last step of this process was to fiberize the melt by blowing with compressed air, which divides the melt into drops thus subsequently extracting the fibres. The fraction

of these particles (so-called shots) is approximately between 40 and 60 %. The final product was a glass fibre blanket in most of the cases, as depicted in Figure 3.4.

Figure 3.4: Glass fibre blanket (1100 mm width and length).

3.1.2. Heat treatment processing

Heat treatment was employed to examine the chemical stability and thermal durability at elevated temperature of alkali aluminosilicate fibre insulation materials. In the first stage of the present work, the study was focused on heat treatment experiments of Cerachem® and Superwool® XT samples. Subsequently, the broader scope of this study enabled us to conduct heat treatment experiments with colloidal SiO_2 coated Superwool® XT, which were followed by studies of K_2O-Al_2O_3-SiO_2 glass fibre samples.

During heat treatment experiments two different furnace arrangements were used as shown in the following figures. Initially, in the old furnace arrangement, a structure was built from RCF boards and silicon carbide (SiC) to accommodate more than 12 samples in 3 levels (Figure 3.5). For the new furnace arrangement one RCF board was used to hold a maximum of 5 samples on one level (Figure 3.6).

During the initial heat treatment experiments only the old arrangement was used but the results from comparative experiments revealed the new furnace arrangement to be more accurate.

Figure 3.5: Old sample arrangement inside the furnace.

Figure 3.6: New sample arrangement inside the furnace.

Depending on the different scientific focus during this project, multiple heat treatment conditions have been used for the samples (Table 3.6, Table 3.7 and Table 3.8). During the long-term heat treatment experiments the samples were placed into the furnace at room temperature and then the furnace was ramped to the selected temperature at a rate of 5°C per minute. Samples were then taken out of the furnace at the maximum

temperature, at set time intervals with an accuracy of ±1h. Additionally, during short-term experiments the samples were placed into the furnace and then taken out at the maximum temperature.

Table 3.6: Long-term heat treatment conditions for SWXT® samples at 1250°C using the two furnace arrangements.

Heat Treatment Time (h)	Old Furnace Arrangement	New Furnace Arrangement
168	✓	✓
336	✓	
504	✓	✓
672	✓	✓
840	✓	✓
1008	✓	
1176	✓	✓
1224	✓	
1296	✓	
1344	✓	✓
1392	✓	
1464	✓	
1512	✓	✓
1560	✓	
1632	✓	
1680	✓	✓
1728	✓	
1800	✓	
1848	✓	✓
2160	✓	✓

In the beginning of this study, some of the SWXT® samples were first heat treated at 1200°C for five minutes and then fired at 850°C for long time periods. According to X-ray Powder Diffraction results, SWXT® crystalizes very quickly at elevated temperature and the glass fibres turn into ceramic fibres. The purpose of this pre-

crystallization procedure was to examine whether the ceramic fibres will have a different response in the long-term heat treatment experiments compared with glass fibres.

Table 3.7: Heat treatment conditions for melt-rig samples using the new furnace arrangement.

Sample	**Heat Treatment Time**							
	1min	5min	15min	30min	1h	24h	500h	1000h
KAS-1	✓	✓	✓	✓	✓*	✓	✓	✓
KAS-2		✓	✓		✓	✓		
KAS-3		✓	✓	✓	✓	✓	✓	✓
KAS-4		✓	✓	✓	✓	✓	✓	✓
KAS-5		✓	✓	✓	✓	✓	✓	✓
KAS-8							✓	✓
KAS-9							✓	✓
KASZ-1							✓	✓
KASZ-2							✓	✓

Table 3.8: Short-term heat treatment conditions for industrial samples using the new furnace arrangement.

Sample	**T (°C)**	**Heat Treatment Time**									
		30sec	45sec	1min	5min	10min	30min	1h	24h	48h	72h
Superwool® XT	850								✓	✓	✓
	1250	✓	✓	✓	✓	✓	✓	✓	✓	✓	✓
	1500							✓	✓	✓	✓
Colloidal SiO_2 Coated SWXT®	1250							✓	✓	✓	✓
	1500							✓	✓	✓	✓
Cerachem®	1250								✓	✓	

* Additional heat treatments at 850°C and 950°C.

Table 3.9: Long-term heat treatment conditions for SWXT® and pre-crystallized SWXT® samples at 850°C using the old furnace arrangement.

Heat Treatment Time (h)	SWXT®	Pre-crystallized SWXT®
168	✓	
336	✓	✓
504	✓	
672	✓	✓
840	✓	
1008	✓	✓
1176	✓	
1344	✓	✓
1512	✓	
1680	✓	✓
1848	✓	
2160	✓	✓

All furnaces require a periodic temperature recalibration due to the effluents given off by the materials fired, including alloys, ceramics, investments, stains and glazes. It is very important to examine the temperature stability and uniformity inside the furnace before starting the heat treatment experiments. In some cases, where the furnace calibration shows a remarkable temperature difference the space that can be used inside the furnace is limited. In this study, only the hot zone of the furnace was used where the temperature variation was within ±1°C based on thermocouple measurements. Also, in all heat treatment experiments in this work furnace calibration has affected the furnace settings regarding temperature.

3.2. Elemental analysis

3.2.1. X-Ray fluorescence

X-ray fluorescence (XRF) is one of the most important techniques used for this research project to determine the compositional stability. XRF is a non-destructive technique used to analyse the composition of a sample excited by an X-ray source, by measuring the emitted fluorescent X-rays. When a high energy X-ray beam (incident beam) interacts with a sample, some of its energy is lost, and some is absorbed within the sample depending on the sample chemistry (Goulding & Jaklevic, 1977). The sample excited by the X-ray beam emits X-rays whose wavelengths are characteristic of the atoms present in the sample. As shown in Figure 3.7, incident X-rays eject electrons from the lower energy levels of atoms (ionizing); these are replaced by electrons from higher energy orbitals. This is accompanied by release of energy due to the binding energy difference between the inner and outer electron orbital. Thus, X-rays characteristic of the type of atoms present are emitted (Van Espen, Nullens, & Adams, 1977). In a multi-element sample, a complex X-ray spectrum is emitted and is separated into characteristic wavelengths for each element present with the use of a wavelength dispersive spectrometer (Figure 3.8).

The measurements were performed with a PANalytical - Axios Advanced at Morgan Technical Ceramics which is shown in Figure 3.9. Full quantitative elemental analysis was carried out by XRF analysis of samples in form of fused beads; 1.000 ± 0.002g of sample was carefully weighted and mixed with 10.000 ± 0.002g di-lithium tetraborate and formed into a transparent glass disk using an automatic bead making instrument (Figure 3.10).

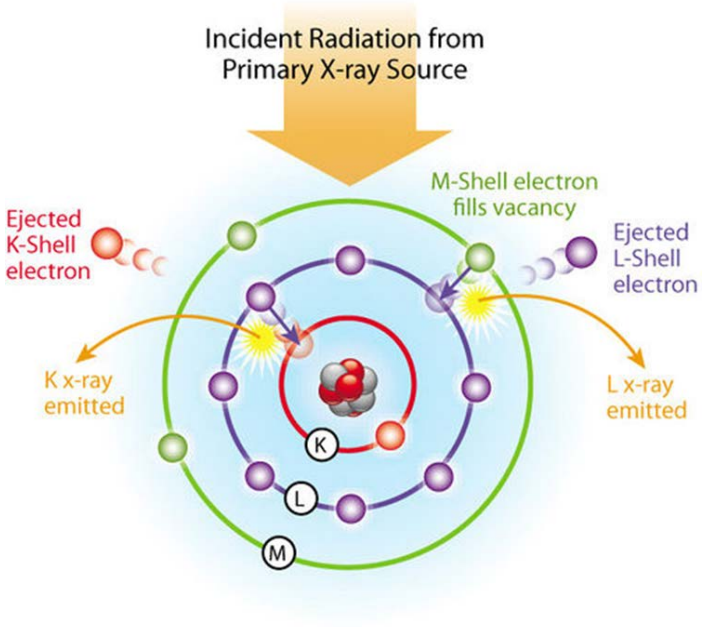

Figure 3.7: The principle of X-Ray Fluorescence (Klockenkämper & von Bohlen, 2014).

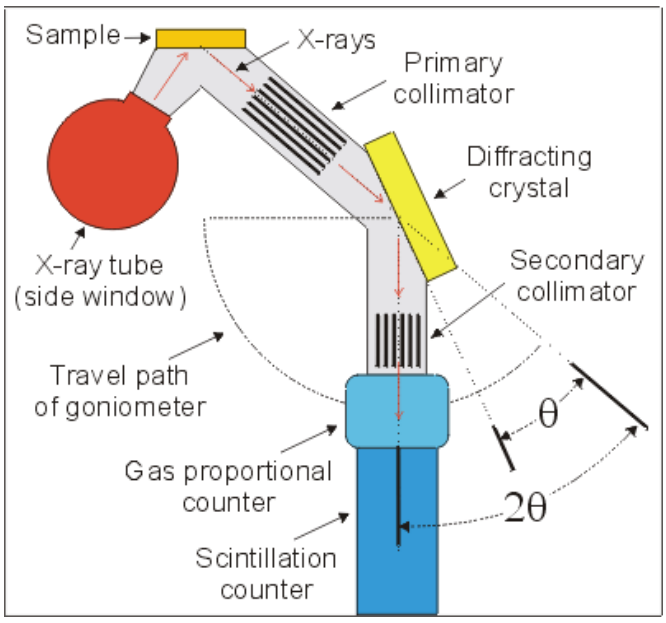

Figure 3.8: Schematic arrangement of wavelength dispersive spectrometer (Klockenkämper & von Bohlen, 2014).

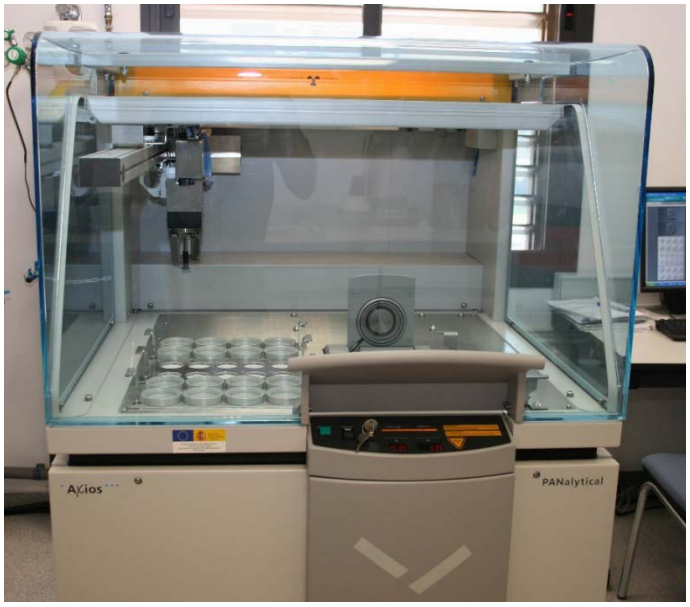

Figure 3.9: PANalytical - Axios Advanced instrument.

Figure 3.10: XRF automatic bead making instrument.

3.3. Structural characterisation

3.3.1. X-Ray diffraction

X-ray diffraction (XRD) analysis was used to identify and study the crystal structure of the glass fibres. This technique is based on Bragg's law, which predicts the angles of peaks in a diffraction pattern from a crystal lattice. Geometrically, it is possible to think of a crystal as families of lattice planes as Figure 3.11 shows (Cullity & Stock, 2001). So, if an incident X-ray beam of wavelength λ (in the order of atomic spacing), interacts with a family of crystal planes, with interplanar spacing d_{hkl}, it is possible to detect a diffraction beam of sufficient intensity, when the incident beam and the detector are placed in a Bragg angle, θ_{hkl} (angle at which reflections from these planes are observed). The Bragg equation (Eq. 3.1) is based on the assumption that the angles of incidence and reflection are equal (Waseda, Matsubara, & Shinoda, 2011).

$$n\lambda = 2d_{hkl}sin\theta_{hkl} \quad 3.1$$

where λ is the X-ray wavelength, d is the interplanar spacing, θ is the angle of incidence, and n is taken as unity and hkl are the Miller indices.

From the powder X-ray diffraction pattern, it is possible to extract useful information about the crystalline structure, such as the symmetry and the dimensions of the unit cell. Furthermore, the intensity of the peaks in the diffraction pattern is related with the atoms' nature and their position in the crystalline system, so it is also possible to obtain information about the internal structure of the crystal from this parameter (Compton & Allison, 1935).

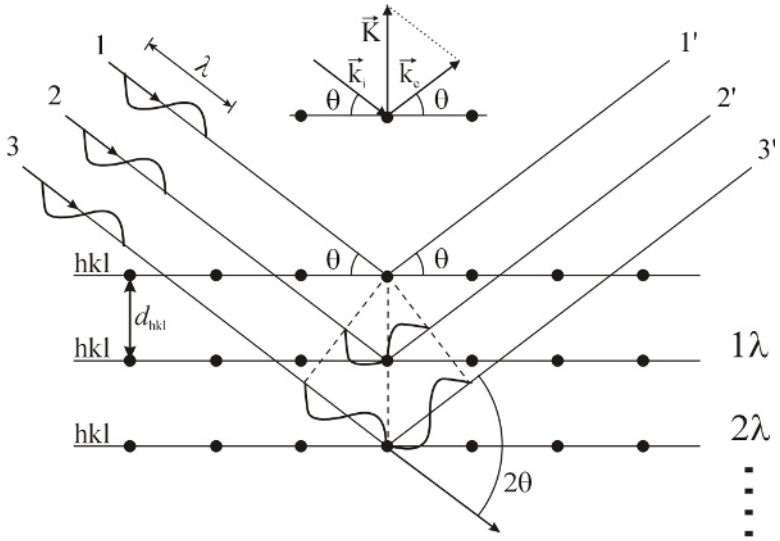

Figure 3.11: Diffraction condition for a given set of atomic planes, `d´ is the spacing between atomic planes (Cullity & Stock, 2001).

The powder diffraction pattern of a sample is characteristic of that sample, like a fingerprint. The measured powder pattern is quite likely to be reproduced by the simple sum of the isolated phases, if the sample contains two or more phases. So, the angles and intensities of a set of obtained peaks in the powder XRD pattern can be matched to those of known materials, to determine the presence or absence of any particular phase (Santra, 2009). The standard diffraction patterns are found in the database of the Joint Committee on Powder Diffraction Standards, known as JCPDS-ICDD cards.

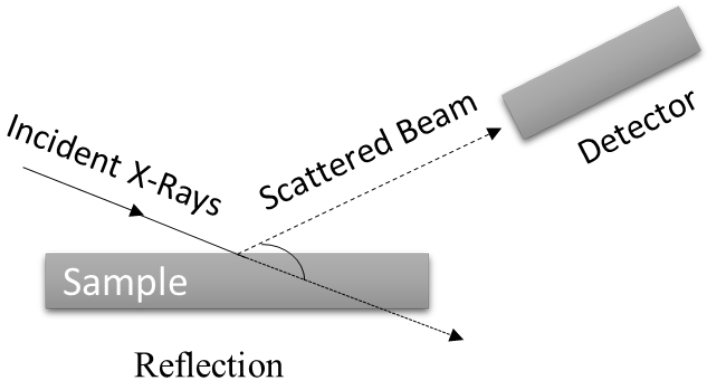

Figure 3.12: Diffraction in Bragg reflection.

The crystallographic evolution after variable heat treatment experiments was investigated by XRD at room temperature, with a diffractometer (model: Empyrean XRD, PANalytical™, Almelo, The Netherlands) equipped with a Cu or Co tube operated at 40 kV and 40 mA, normally in the 2θ range between 5 and 100°, with 2θ increments of 0.013° and counting time of ~70 s per step (Figure 3.13). All the samples were analysed using the reflection spinner sample holder, which spins at 0.25 Hz. All samples were crushed to fine powders using a mortar and pestle.

Figure 3.13: Image of PANalytical Empyrean diffractometer.

3.3.2. Rietveld refinement

Quantitative phase analysis was used to ascertain the presence of an amorphous phase after long-term heat treatment at elevated temperature. This method is a least-square fitting of the experimental diffraction data with a mathematical model of a crystal structure which can provide additional information, such as atomic displacement and site occupancy, apart from precise lattice parameters. It is important to note that this method is a refinement, not a solution method: the structure of the model must be known in advance (Rietveld, 1988).

The purpose of the fitting is to minimize the following residual function S_y (Eq. 3.2):

$$S_y = \sum_{i=1}^{n} \frac{1}{y_{i,obs}} \left(y_{i,obs} - y_{i,calc}\right)^2 \quad 3.2$$

where $y_{i,obs}$ is the intensity of each point in the experimental pattern and $y_{i,calc}$ is the intensity of every point of a calculated pattern using the space group of the crystal, the lattice parameters and the position of each atom in the unit cell.

The best way to assess the quality of the fitting is the visual check of the difference between the calculated and the experimental pattern; however, there are also quantitative indicators: the weighted-profile R value (R_{wp}) (Eq. 3.3) and the expected residual value (R_{exp}) (Eq. 3.4):

$$R_{wp} = \sqrt{\frac{\sum_i w_i \left(y_{i,obs} - y_{i,calc}\right)^2}{\sum_i w_i \left(y_{i,obs}\right)^2}} \quad 3.3$$

$$R_{exp} = \sqrt{\frac{N-P}{\sum_i w_i \left(y_{i,obs}\right)^2}} \quad 3.4$$

where N is the number of observations and P the number of parameters. R_{wp} is therefore the ratio of the difference between the two patterns to the observed pattern, whereas R_{exp} is a measure of the quality of the data (statistically). The ratio (Eq. 3.5):

$$\chi^2 = \left(\frac{R_{wp}}{R_{exp}}\right)^2 \quad 3.5$$

is often given as a measure of the goodness of fit (GOF, or χ^2). If the experimental pattern contains more data points than needed, χ^2 can be much larger than 1, whereas if the data points are not sufficient (i.e. low sensitivity of the detector or scan time too short), χ^2 can be even smaller than 1, which is an indication that the data acquisition

should be repeated (Will, 2006). However, as for every empirical manipulation of data, the results must make physical sense, no matter how good the fitting is.

In addition, the amorphous phase content was determined with the internal standard method (Madsen & Scarlett, 2008). Samples under investigation were mixed with silicon standard in a ratio of 4:1 by weight and the XRD patterns were obtained. The weight fractions of the crystalline phases present in each sample are estimated using the Rietveld methodology. Concentrations to be corrected proportionately according to Eq. 3.6:

$$Corr(W_j) = W_j \frac{STD_{known}}{STD_{measured}} \quad 3.6$$

where Corr(Wj) is the corrected weight percent of phase j, STD_{known} the weighed concentration of the standard in the sample and $STD_{measured}$ the analysed concentration.

The amount of amorphous material $W_{amorphous}$ can then be derived from Eq. 3.7:

$$W_{amorphous} = 1 - \sum_{j=1}^{n} Corr(W_j) \quad 3.7$$

3.3.3. Raman spectroscopy

Raman spectroscopy of glass fibre materials was carried out to study slight changes in material structure and to determine the crystal structure. Raman spectroscopy permits the measurements of vibrational transitions by observing inelastically scattered radiation. This technique is based on the inelastic scattering of light by matter. The incident radiation induces transitions in the atoms that change the scattering medium, showing the variation in the Raman scattering (Truchet, Merlin, & Turrell, 1996). Raman spectroscopy can determine crystal symmetry, the degree of crystallinity, the

effects of temperature on phase transformations, and the strength of interatomic bonds (Turrell, Delhaye, & Dhamelincourt, 1996).

Raman spectra were recorded with a Thermo Scientific™ DXR™2 microscope spectrometer (Figure 3.14) equipped with a laser beam emitting at 520 nm, at 300 mW output power. The photons scattered by the sample were dispersed by a 1200 lines/mm grating monochromator and simultaneously collected on a CCD camera; the collection optic was set at 50× objective. The spectral resolution is 1 cm^{-1} and the measurement range of Raman shift for glass fibres was 100 to 1300 cm^{-1}.

Figure 3.14: Thermo Scientific™ DXR™2 microscope Raman spectrometer.

3.3.5. Scanning electron microscopy

Scanning electron microscopy (SEM) is a micro-analytical technique, able to analyse materials that cannot generally be observed with the resolution offered by optical techniques, thus allowing a detailed analysis of the grain size and morphology of the studied material. It allows the study of phase distribution, sample topography and differences in crystal orientation (Reichelt, 2007).

SEM measures the secondary electrons emitted from a conductive substrate whose number depends on local surface slope and composition. Its spatial resolution is a function of the secondary electron diffusion within the sample and of the electron beam spot size.

Energy Dispersive X-Ray Spectroscopy (EDS or EDX) is a quantitative chemical microanalysis technique used for elemental analysis and chemical characterization of a sample. The EDX technique has been used in conjunction with XRF to identify the different chemical species stability in Superwool® XT glass fibres in terms of time, temperature and service conditions. The elemental composition of the sample bombarded by an electron beam is determined by detecting the characteristic X-rays emitted. Quite small (≤ 1 µm) phases or features can be analyzed (Johansson, Campbell, & Malmqvist, 1995).

All the samples were examined by field emission scanning electron microscopy (model: Nova Nano 200, FEI, Brno, Czech Republic, which is shown in Figure 3.15) equipped with an ultra-high-resolution retro-dispersed secondary electron detector to solid state and an OXFORD INCA 250 electron dispersive X-ray detector (EDX). During an EDX measurement, the theoretical detection limits is approximately 0.08 wt% but there are limitations as this technique has low sensitivity to elements lighter that Na and to trace elements.

Figure 3.15: FEI Nova Nano- SEM/EDX 200 microscope.

Before SEM characterization a suitable sample preparation method must be followed depending on the information sought during the SEM evaluation. All the samples were coated to be conductive. Carbon coating was used because it is almost invisible to most X-rays and it is more suitable for compositional analysis. Coating was applied at a thickness of about 20 nm, which is too thin to interfere with dimensions of surface features

3.4. Thermal analysis

3.4.1. Differential thermal analysis

The thermal behaviour of the samples was investigated by differential thermal analysis (DTA). The measurements were performed with a NETZSCH STA 409 PG Luxx instrument., with α-Al_2O_3 as the inert reference material, between room temperature and 1400ºC, with heating rates between 5ºC.min^{-1} and 50ºC.min^{-1}, depending on the composition (Figure 3.16).

Figure 3.16: NETZSCH STA 409 PG Luxx DTA instrument.

In DTA, while the sample under study and a reference material experience the same heating profile, their temperature difference (ΔT) (Eq. 3.8) in terms of temperature is recorded. The record is the DTA curve; the temperature difference is plotted on the ordinate, and the temperature is on the abscissa. The temperature difference is negative in endothermic processes such as melting, and positive in exothermic processes such as crystallization (Gaisford, Kett, & Haines, 2016). Using DTA, changes taking place such as sublimation, melting, volatilization, phase transition, glass transition can be detected. (Haines, 1995).

$$\Delta T = T_s - T_r \quad 3.8$$

T_r – temperature of reference sample

T_s – temperature of sample.

3.5. References

Compton, A. H., & Allison, S. K. (1935). *X-rays in theory and experiment*. New York: D. Van Nostrand Company, Inc.

Cullity, B. D., & Stock, S. R. (2001). *Elements of x-ray diffraction* (3rd ed.). Upper Saddle River, NJ: Prentice Hall.

Gaisford, S., Kett, V., & Haines, P. (Eds.). (2016). *Principles of thermal analysis and calorimetry*. Cambridge: Royal society of chemistry.

Goulding, F., & Jaklevic, J. (1977). XRF analysis-some sensitivity comparisons between charged-particle and photon excitation. *Nuclear Instruments and Methods, 142*(1-2), 323-332.

Haines, P. J. (1995). *Thermal methods of analysis: principles, applications and problems*. Netherlands: Springer.

Johansson, S. A., Campbell, J. L., & Malmqvist, K. G. (1995). *Particle-induced X-ray emission spectrometry (PIXE)*. Hoboken, NJ: John Wiley & Sons.

Klockenkämper, R., & von Bohlen, A. (2014). *Total-reflection X-ray fluorescence analysis and related methods*. Hoboken, NJ: John Wiley & Sons.

Madsen, I. C., & Scarlett, N. V. Y. (2008). Quantitative Phase Analysis. In R. E. Dinnebier, & S. J. L. Billinge (Eds.), *Powder Diffraction: Theory and Practice* (pp. 298-331). Cambridge, UK: The Royal Society of Chemistry. doi:10.1039/9781847558237-00298

Reichelt, R. (2007). Scanning electron microscopy. In P. Hawkes, & J. C. H. Spence (Eds.), *Science of microscopy* (1st ed., pp. 133-272). New York: Springer-Verlag.

Rietveld, H. M. (1988). The Rietveld method - A historical perspective. *Australian Journal of Physics, 41*(2), 113-116.

Santra, R. (2009). Concepts in x-ray physics. *Journal of Physics B: Atomic, Molecular and Optical Physics, 42*(2), 023001.

Truchet, M., Merlin, J., & Turrell, G. (1996). Raman microscopy and other local analysis techniques. In G. Turrell, & J. Corset (Eds.), *Raman Microscopy* (pp. 201-242). London: Academic Press. doi:10.1016/B978-012189690-4/50025-9

Turrell, G., Delhaye, M., & Dhamelincourt, P. (1996). Characteristics of Raman microscopy. In G. Turrell, & J. Corset (Eds.), *Raman Microscopy* (pp. 27-49). London: Academic Press. doi:10.1016/B978-012189690-4/50022-3

Van Espen, P., Nullens, H., & Adams, F. (1977). A computer analysis of X-ray fluorescence spectra. *Nuclear Instruments and Methods*, *142*(1), 243-250.

Waseda, Y., Matsubara, E., & Shinoda, K. (2011). *X-ray diffraction crystallography introduction, examples and solved problems*. Heidelberg; New York: Springer.

Will, G. (2006). *Powder Diffraction: The Rietveld Method and the Two Stage Method to Determine and Refine Crystal Structures from Powder Diffraction Data*. Berlin, Heidelberg: Springer-Verlag. doi:10.1007/3-540-27986-5

Chapter 4

Results

4.Results

This chapter includes detailed results concerning different aluminosilicate and alkali aluminosilicate glass fibre systems, starting from the most investigated material, Superwool® XT, to the laboratory produced glass fibres, and to the less explored Cerachem® fibres. The heat treatment and structural, thermal and elemental characterization of these glass fibre systems, described in Chapter 3, have allowed detailed studies to be developed, which were not previously described in literature, and that can help clarify the main problems and solutions of biosoluble glass fibres.

4.1. Commercially produced Superwool® XT fibres

The performance and durability of Superwool® XT glass fibres in terms of time and temperature was examined in depth by changing the thermal and furnace conditions. As previously described (Chapter 2) several analytical techniques were employed to determine the properties of this complex material.

4.1.1. Heat treatment experiments

As described in detail in Chapter 3, heat treatment was employed to explore the crystallization behaviour and compositional stability of SWXT®. To this end, SWXT® samples have been heat treated at 850°C and 1250°C for prolonged periods as shown in Table 4.1 and Table 4.3.

After the 1st experiment (expr) at 1250°C that was mainly to investigate the performance of SWXT® under elevated temperature and for long periods, the results

obtained lead this research to new paths and the conduction of three additional long-term heat treatment experiments to understand in depth the complex behaviour of this material. Moreover, during this study the effect of furnace arrangement (3rd and 4th experiments) was also examined to obtain a full picture of all the factors that play a crucial role on the performance of this material. In addition, to investigate SWXT® in more detail short-term experiments with heating times between 30 seconds and 72 hours were also carried out and in some cases colloidal silica SWXT® was also studied. Details of all long-term experiments for SWXT® are listed in Table 4.2.

Table 4.1: Long-term heat treatment conditions for SWXT® samples at 1250°C using the two furnace arrangements.

Heat Treatment Time (h)	**Old Furnace Arrangement**		**New Furnace Arrangement**	
	1st Expr	**2nd Expr**	**3rd Expr**	**4th Expr**
168	✓			✓
336	✓			
504	✓			✓
672	✓			
840	✓			✓
1008	✓			✓
1176	✓	✓	✓	
1224		✓		
1296		✓		
1344	✓	✓	✓	
1392		✓		
1464		✓		
1512	✓	✓	✓	
1560		✓		
1632		✓		
1680	✓	✓	✓	
1728		✓		
1800		✓		
1848	✓	✓	✓	
2160	✓			

Table 4.2: Details of long-term heat treatment experiments of SWXT® at 1250°C.

Experiment	Furnace Arrangement	Heat Treatment Time until Removal of 1st Sample (h)	Heat Treatment Time Range (h)
1st	Old:12 samples	168	168-2160
2nd	Old:13 samples	1176	1176-1848
3rd	New:5 samples	1176	1176-1848
4th	New:4 samples	168	168-1008

Table 4.3: Long-term heat treatment conditions for SWXT® and pre-crystallized SWXT® samples at 850°C using the 1st furnace arrangement.

Heat Treatment Time (h)	SWXT®	Pre-crystallized SWXT®
168	✓	
336	✓	✓
504	✓	
672	✓	✓
840	✓	
1008	✓	✓
1176	✓	
1344	✓	✓
1512	✓	
1680	✓	✓
1848	✓	
2160	✓	✓

4.1.2. Chemical characterization

X-ray fluorescence (XRF) and energy-dispersive X-ray spectroscopy (EDX), have been employed for elemental analysis of SWXT® compounds. Table 4.4 to Table 4.8 show the compositional stability of the key elements of SWXT® compared to the as made one for the main heat treatment experiments.

Table 4.4: XRF analysis (wt% with ±1% relative error) of Superwool® XT fibres, heat treated at 850°C.

Oxide	Unfired	168 h	336 h	504 h	672 h	840 h	1008 h	1176 h	1344 h	1512 h	1680 h	1848 h	2160 h
Al_2O_3	35.7	35.9	35.8	35.8	35.8	35.9	35.8	35.8	35.9	35.9	35.9	35.8	35.9
K_2O	25.8	25.5	25.7	25.7	25.6	25.5	25.6	25.7	25.5	25.5	25.6	25.5	25.5
SiO_2	30.5	30.5	30.5	30.5	30.5	30.6	30.6	30.5	30.6	30.5	30.5	30.6	30.5
ZrO_2	6.2	6.2	6.2	6.2	6.2	6.2	6.2	6.2	6.2	6.2	6.2	6.2	6.2
MgO	1.2	1.2	1.2	1.2	1.2	1.2	1.2	1.2	1.2	1.2	1.2	1.3	1.2
HfO_2	0.2	0.2	0.2	0.2	0.2	0.2	0.2	0.2	0.2	0.2	0.2	0.2	0.2
Na_2O	0.4	0.4	0.4	0.4	0.4	0.4	0.4	0.4	0.4	0.4	0.4	0.4	0.4
TiO_2	0.0	0.0	0.0	0.0	0.0	0.0	0.0	0.0	0.0	0.0	0.0	0.0	0.0
Total	100.0	100.0	100.0	100.0	100.0	100.0	100.0	100.0	100.0	100.0	100.0	100.0	100.0
K_2O Loss	0.0	0.2	0.1	0.1	0.2	0.3	0.2	0.1	0.3	0.3	0.2	0.3	0.3
New Total	100.0	99.8	99.9	99.9	99.8	99.7	99.8	99.9	99.7	99.7	99.8	99.7	99.7

Table 4.5: XRF analysis (wt% with ±1% relative error) of pre-crystallized Superwool® XT fibres (5min, 1200°C), heat treated at 850°C.

Oxide	Unfired	5 min (1200°C)	336 h	672 h	1008 h	1344 h	1680 h	2160 h
Al_2O_3	35.7	35.8	35.8	35.8	35.7	35.8	35.7	35.7
K_2O	25.8	25.6	25.6	25.7	25.7	25.7	25.7	25.7
SiO_2	30.5	30.5	30.5	30.5	30.5	30.5	30.5	30.5
ZrO_2	6.2	6.2	6.2	6.2	6.2	6.2	6.2	6.2
MgO	1.2	1.2	1.2	1.2	1.2	1.2	1.2	1.2
HfO_2	0.2	0.2	0.2	0.2	0.2	0.2	0.2	0.2
Na_2O	0.4	0.4	0.4	0.4	0.4	0.4	0.4	0.4
Total	100.0	100.0	100.0	100.0	100.0	100.0	100.0	100.0
K_2O Loss	0.0	0.1	0.1	0.1	0.1	0.1	0.1	0.0
New Total	100.0	99.9	99.9	99.9	99.9	99.9	99.9	100.0

Table 4.6: XRF analysis (wt% with ±1% relative error) of Superwool® XT fibres, heat treated at 1250°C, 1st experiment.

Oxide	Unfired	168 h	336 h	504 h	672 h	840 h	1008 h	1176 h	1344 h	1512 h	1680 h	1848 h	2160 h
Al_2O_3	35.7	36.5	36.6	36.7	36.9	36.8	36.7	36.9	37.4	38.5	37.6	38.0	39.1
K_2O	25.8	24.2	24.0	23.9	23.6	23.6	23.8	23.5	22.5	20.1	21.8	21.1	18.8
SiO_2	30.5	31.1	31.2	31.2	31.3	31.4	31.4	31.4	31.8	32.8	32.2	32.4	33.4
ZrO_2	6.2	6.3	6.3	6.4	6.4	6.4	6.3	6.4	6.4	6.7	6.5	6.6	6.8
MgO	1.2	1.2	1.2	1.2	1.2	1.3	1.2	1.2	1.2	1.3	1.3	1.3	1.3
HfO_2	0.2	0.2	0.2	0.2	0.2	0.2	0.2	0.2	0.2	0.2	0.2	0.2	0.2
Na_2O	0.4	0.4	0.4	0.4	0.4	0.4	0.4	0.4	0.4	0.4	0.4	0.4	0.3
Total	100.0	100.0	100.0	100.0	100.0	100.0	100.0	100.0	100.0	100.0	100.0	100.0	100.0
K_2O Loss	0.0	1.6	1.8	1.9	2.2	2.2	2.0	2.3	3.2	5.7	4.0	4.7	7.0
New Total	100.0	98.4	98.2	98.1	97.8	97.8	98.0	97.7	96.8	94.3	96.0	95.3	93.0

Table 4.7: XRF analysis (wt% with ±1% relative error) of Superwool® XT fibres, heat treated at 1250°C, 2nd experiment.

Oxide	Unfired	1176 h	1224 h	1296 h	1344 h	1392 h	1464 h	1512 h	1560 h	1632 h	1680	1728 h	1800 h	1848 h
Al_2O_3	35.7	36.8	36.6	36.7	36.8	36.7	36.8	37.2	36.7	36.9	37.5	37.2	37.1	37.5
K_2O	25.8	23.1	23.1	23.3	23.1	23.3	23.2	22.3	23.1	22.8	21.7	22.2	22.4	21.5
SiO_2	30.5	31.5	31.8	31.4	31.5	31.4	31.5	31.8	31.6	31.6	32.0	31.9	31.7	32.1
ZrO_2	6.2	6.9	6.9	6.9	6.9	6.9	6.9	7.0	6.9	7.0	7.1	7.0	7.0	7.1
MgO	1.2	1.1	1.1	1.1	1.1	1.1	1.1	1.1	1.1	1.1	1.1	1.1	1.1	1.1
HfO_2	0.2	0.1	0.1	0.1	0.1	0.1	0.1	0.1	0.1	0.1	0.1	0.1	0.1	0.1
Na_2O	0.4	0.4	0.4	0.3	0.3	0.3	0.3	0.3	0.3	0.3	0.4	0.5	0.5	0.5
Total	100.0	100.0	100.0	100.0	100.0	100.0	100.0	100.0	100.0	100.0	100.0	100.0	100.0	100.0
K_2O Loss	0.0	2.7	2.7	2.5	2.7	2.5	2.6	3.5	2.7	2.9	4.1	3.6	3.3	4.3
New Total	100.0	97.3	97.3	97.5	97.3	97.5	97.4	96.5	97.3	97.1	95.9	96.4	96.7	95.7

Table 4.8: XRF analysis (wt% with ±1% relative error) of Superwool® XT fibres, heat treated at 1250°C, 3rd and 4th experiments.

Oxide	Unfired	168 h	504 h	840 h	1008 h	1176 h	1344 h	1512 h	1680 h	1848 h
Al_2O_3	35.7	36.4	37.0	37.4	38.4	37.5	37.6	37.6	38.7	38.9
K_2O	25.8	23.7	22.6	21.9	19.0	21.5	21.4	21.4	19.2	18.8
SiO_2	30.5	31.3	31.6	32.0	33.3	32.1	32.2	32.2	33.1	33.2
ZrO_2	6.2	6.9	7.0	7.0	7.3	7.1	7.1	7.1	7.3	7.3
MgO	1.2	1.1	1.1	1.1	1.2	1.2	1.2	1.2	1.2	1.2
HfO_2	0.2	0.1	0.1	0.1	0.1	0.1	0.1	0.1	0.1	0.1
Na_2O	0.4	0.4	0.5	0.6	0.7	0.4	0.4	0.4	0.4	0.4
Total	100.0	100.0	100.0	100.0	100.0	100.0	100.0	100.0	100.0	100.0
K_2O Loss	0.0	2.1	3.1	3.9	6.8	4.3	4.4	4.4	6.6	7.0
New Total	100.0	97.9	96.9	96.1	93.2	95.7	95.6	95.6	93.4	93.0

As depicted in Figure 4.1 and Figure 4.2 all the compounds are almost stable when the SWXT® samples are heat treated at 850°C. These experiments at 850°C proved that SWXT® glass fibres have high compositional stability as a function of time.

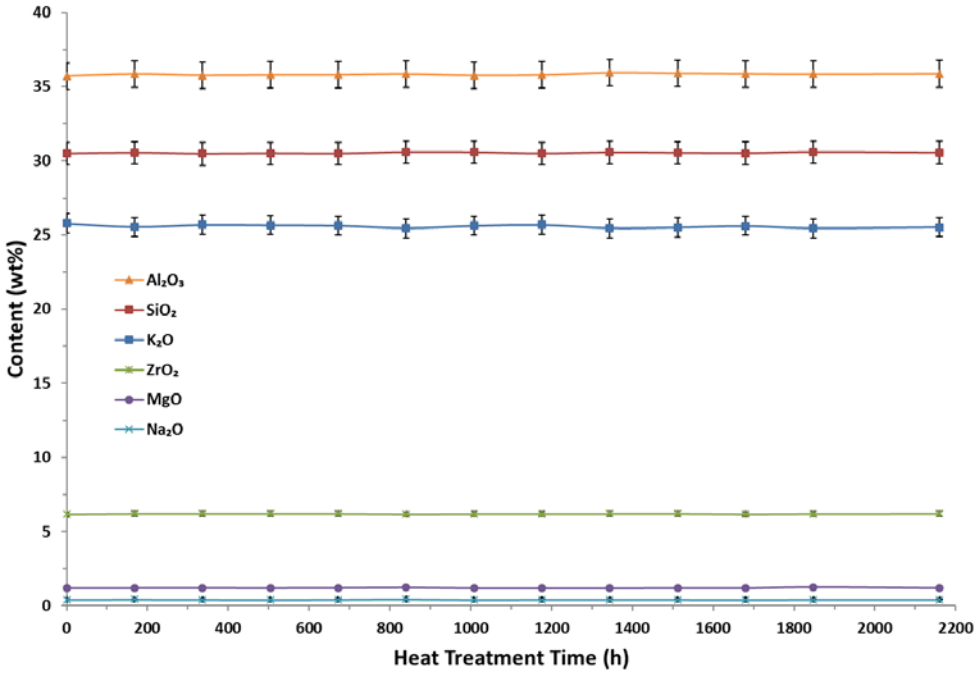

Figure 4.1: Analysed composition of Superwool® XT fibres, heat treated at 850°C as a function of time.

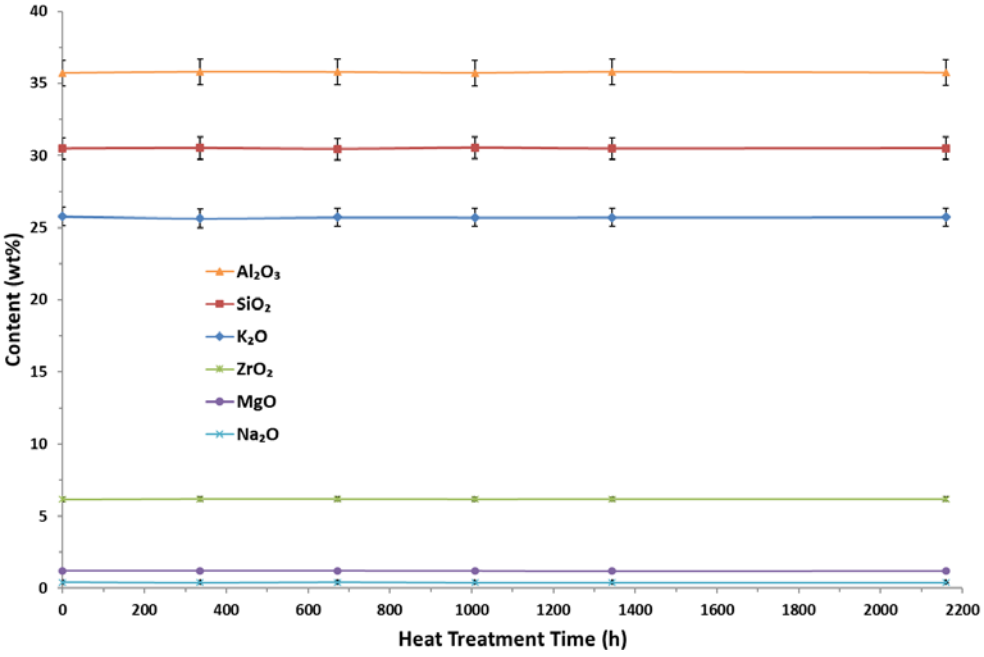

Figure 4.2: Analysed composition of pre-crystallized Superwool® XT fibres (5min, 1200°C), heat treated at 850°C as a function of time.

Figure 4.3 shows that there is a significant reduction in the potassium oxide, K_2O, content at 1250°C and this loss is affected by heat treatment time. Potassium oxide is known for its volatile character especially at elevated temperatures but apart from this apparent reason an effort to understand additional whys and wherefores of this elemental loss will be made. XRF data show a peculiar behaviour of SWXT® around 1500 hours of continuous heat treatment at 1250°C. It appears that SWXT® is gaining potassium oxide after a considerable loss, which is unexpected; this will be explored and discussed later (Figure 4.10).

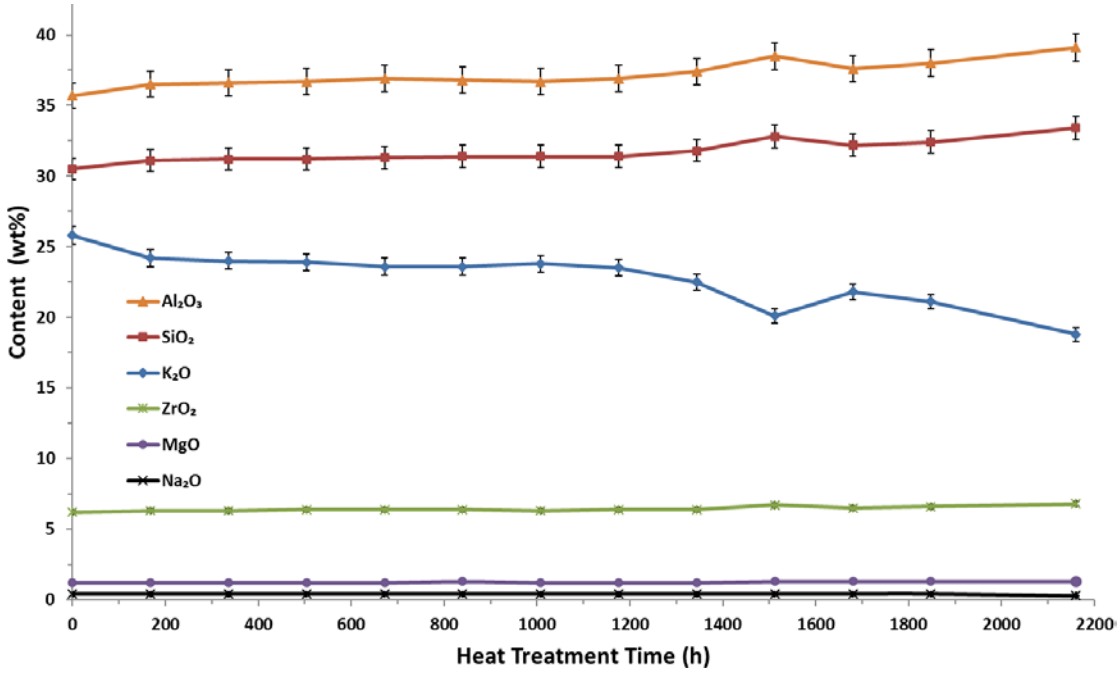

Figure 4.3: Analysed composition of Superwool® XT fibres, heat treated at 1250°C as a function of time (1st expr).

Apart from K_2O loss, Figure 4.3 shows that the other three main compounds (Al_2O_3, SiO_2 and ZrO_2) will increase in relation to their starting amount. To prove this compositional change of K_2O all the other compounds have been normalized excluding the potassium oxide content and the results are presented in Figure 4.4.

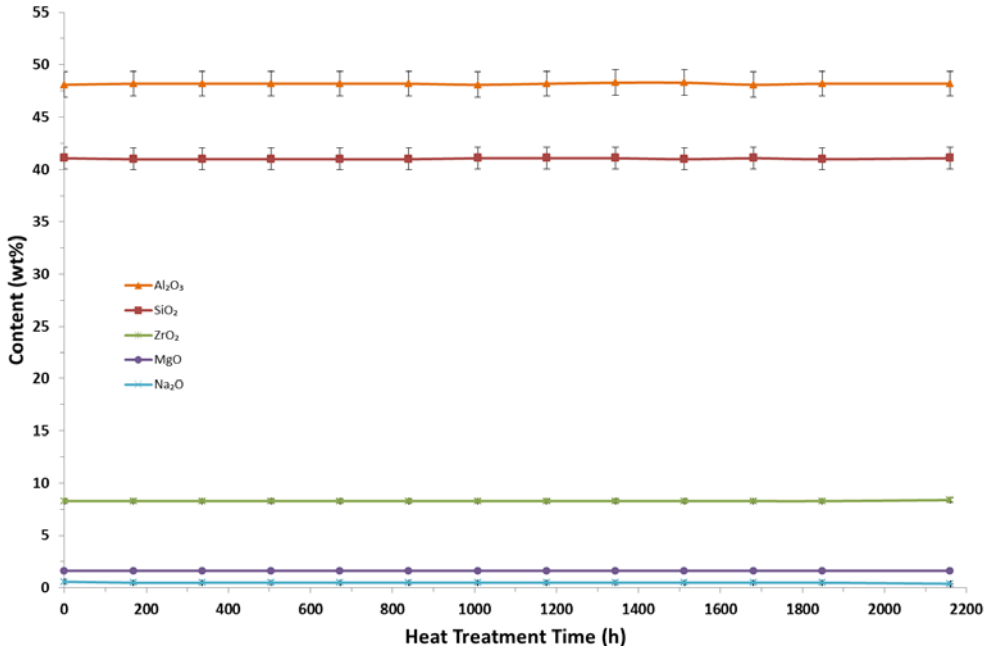

Figure 4.4: Analysed composition of Superwool® XT fibres (excluding K_2O), heat treated at 1250°C as a function of time (1st expr).

As depicted in Figure 4.5 temperature is a very important factor that plays a crucial role in the performance of SWXT®, since for the same heat treatment time it has been confirmed that the loss of potassium is occurring only for the samples that have exposure to elevated temperatures (1250°C). Regarding the samples at 850°C for both experiments up to 2168 hours (precrystallized and amorphous samples), it is evident that, after a small initial loss (0-200 hours), the K_2O content remained stable.

The graph indicates that the behaviour of K_2O content of SWXT® samples that were heat treated at 1250°C is significantly different compared with the samples at 850°C. After a large initial loss (0-200 hours), the K_2O content is relatively stable and further large loss occurs at longer times and continues up to 2168 hours.

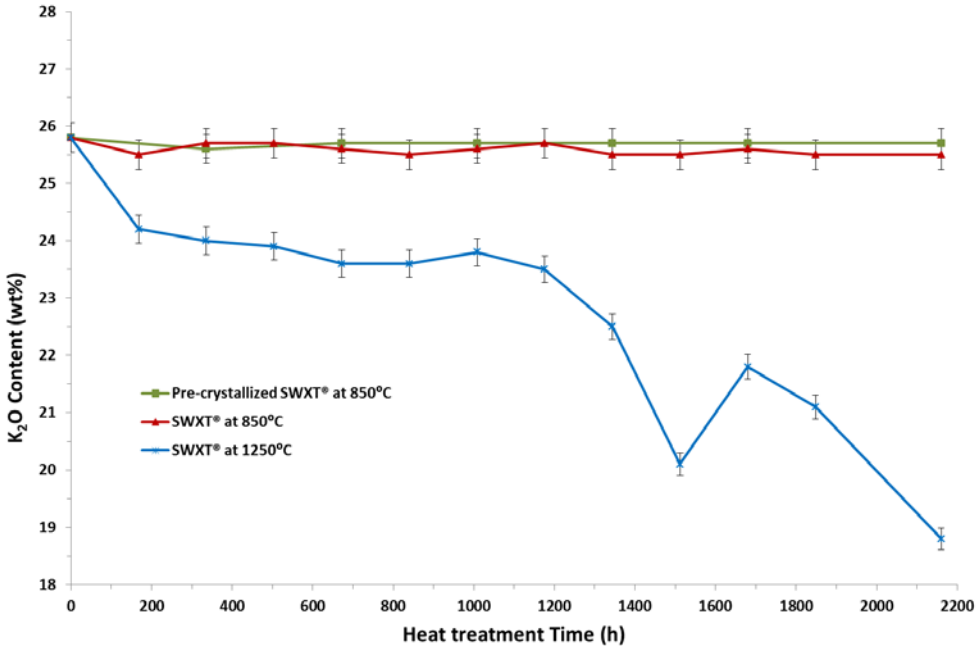

Figure 4.5: Analysed K_2O content as a function of firing time for different temperatures.

Furthermore, EDX analysis has been also used to examine the chemical stability of heat treated SWXT® at 1250°C as a function of time. The chemical composition derived from EDX is listed in Table 4.9 for different firing times.

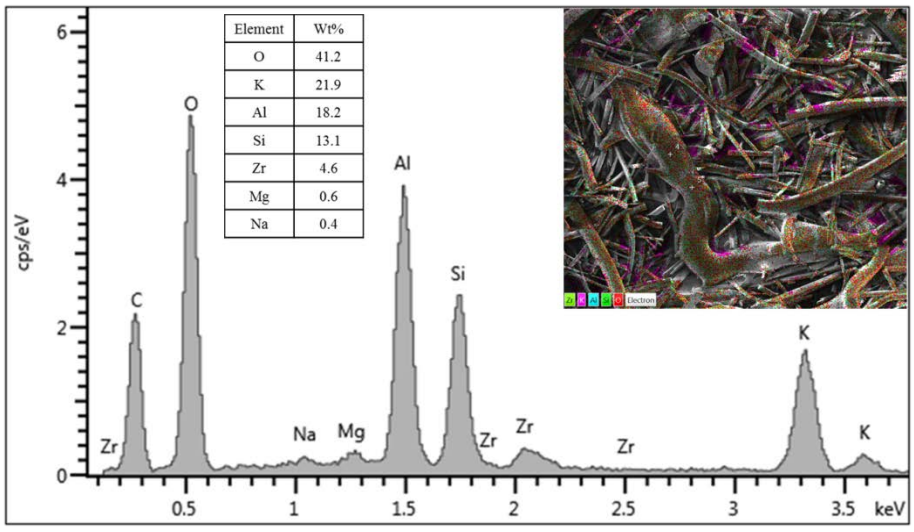

Figure 4.6: EDX spectrum (×500) of fired SWXT® fibres at 1250°C (1st expr) for 1344 hours.

Table 4.9: EDX analysis (wt% with ±2% relative error) of SWXT® fibres heat treated at 1250°C for various firing times.

Firing Time (h)	K_2O	SiO_2	Al_2O_3	ZrO_2	MgO	Na_2O
0	30.63	28.31	33.37	6.24	0.95	0.51
168	27.35	29.10	35.53	6.48	1.03	0.52
1344	26.68	29.80	35.19	6.90	0.95	0.49
2160	22.99	31.56	36.98	6.82	1.02	0.62

The potassium oxide content determined by XRF and EDX is plotted in Figure 4.7. The loss in potassium oxide follows the same trend for both techniques, although there is a difference in the absolute values measured due to EDX sensitivity limitations.

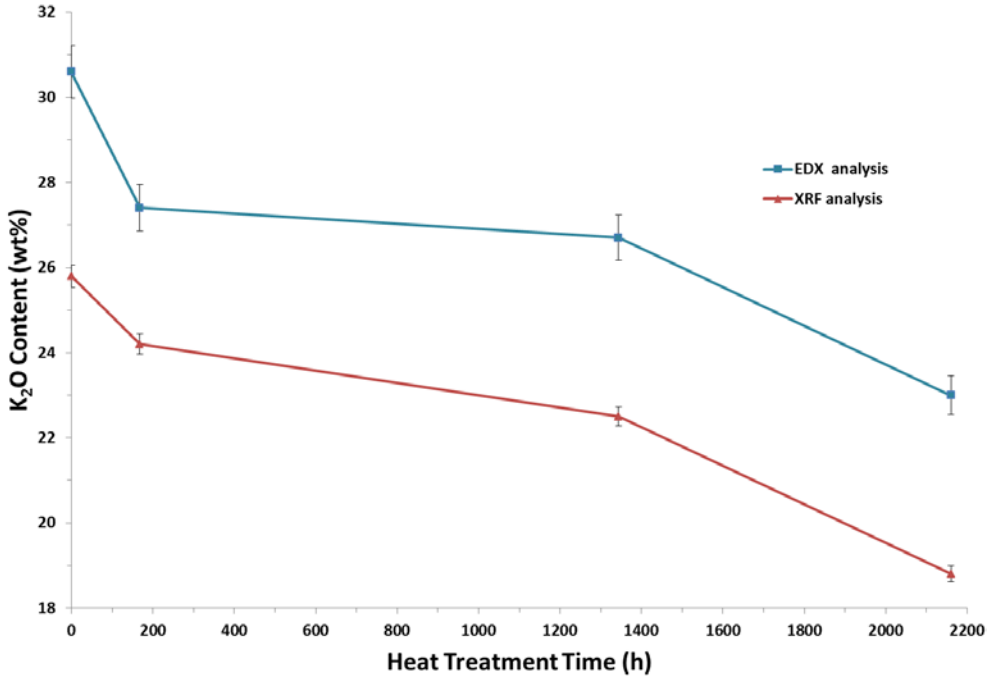

Figure 4.7: EDX and XRF spectra of heat treated SWXT® fibres at 1250°C, showing the K_2O content as a function of time (1st expr).

In order to understand this odd phenomenon happening around 1500 hours at 1250°C, a second experiment was designed, with firing times between 1176 and 1848 h, to obtain more data around 1500 hours by using the same furnace and thermal conditions.

As depicted in Figure 4.8 the new XRF data are not in accordance with old data which suggests that experimental or measurement errors affected the previous result. The K_2O content remains relatively constant up to 1464 h firing time, and then drops for 1512 h, then gradually decreases and remains fairly constant until 1848 hours (experimental limit). All the other components remain constant throughout the long-term heat treatment at 1250°C.

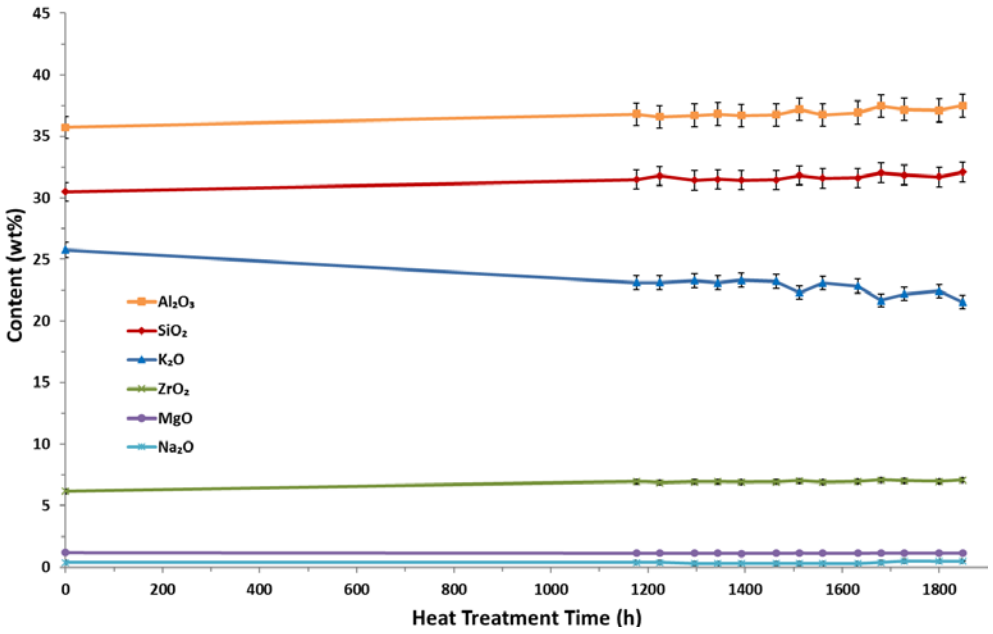

Figure 4.8: Analysed composition of Superwool® XT fibres, heat treated at 1250°C (2nd expr).

Further experiments were designed (3rd and 4th experiment) to investigate whether Superwool® XT samples are affected by the K_2O emissions from nearby samples inside the furnace. To this end, a new furnace arrangement was employed as described in Chapter 3 (3.1.2.).

As illustrated in Figure 4.9, for the 4th experiment after a steep decrease (0-200 hours), the K_2O content gradually declines (200-800 hours) and then it sharply drops again up to 1008 hours. For the 3rd experiment starting at 1176 hours, the K_2O content slightly decreases (1176-1512 hours) and then it steeply declines until 1848 hours. XRF patterns

follow the same trend for both experiments, although variations exist due to furnace arrangement alterations. Apart from the K_2O loss, the above figure shows that the other two main compounds (Al_2O_3 and ZrO_2) will increase in relation to their starting content as expected in tandem with the K_2O loss. The first four data points (168-1008 hours) are from the 4th experiment that was conducted in a bigger furnace and the samples were affected by the regular opening of the furnace compared to 3rd experiment that the door was closed until 1176 hours and which explains why at 1008 hours the K_2O loss is greater than at 1176 hours.

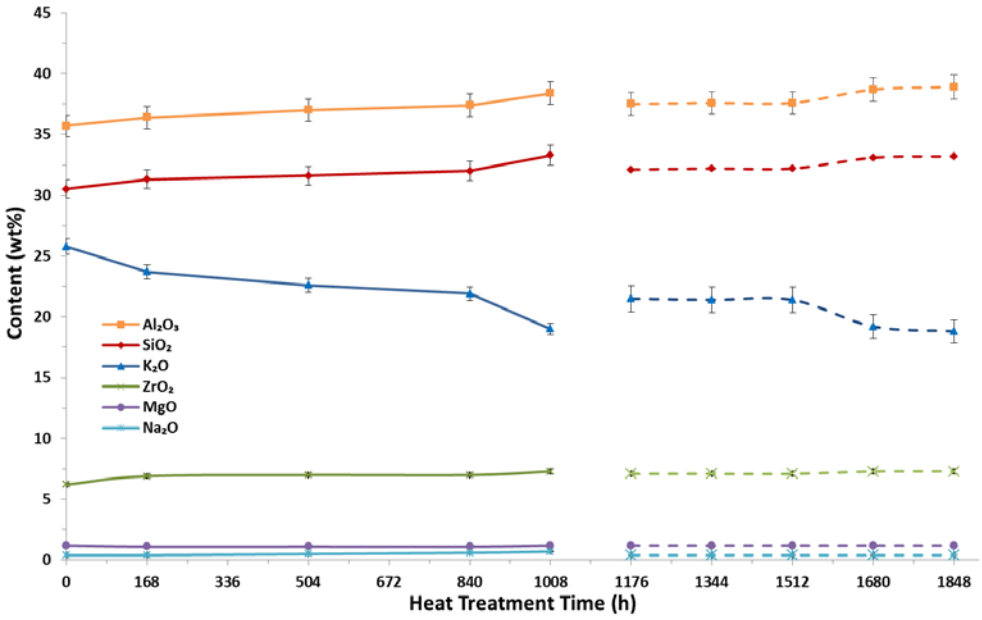

Figure 4.9: Analysed compositions of Superwool® XT fibres (dashed line: 3rd and continuous line: 4th expr), heat treated at 1250°C as a function of time.

Table 4.10 demonstrates a comparison of K_2O content under different furnace conditions. The data from the first two experiments are quite close apart from the 1512 hours, in contrast with the results from the two subsequent experiments. The difference between these experiments is the arrangement inside the furnace.

Table 4.10: XRF analysis of potassium oxide content of SWXT® at 1250°C as a function of furnace arrangement.

Heat Treatment Time (h)	Old arrangement 1st expr K_2O (wt%)	Old arrangement 2nd expr K_2O (wt%)	New arrangement 3rd expr K_2O (wt%)
0	25.8	25.8	25.8
1176	23.5	23.1	21.5
1344	22.5	23.1	21.4
1512	20.1	22.3	21.4
1680	21.8	21.7	19.2
1848	21.1	21.5	18.8

Figure 4.10 shows the K_2O content for the four different long-term experiments. Comparing the results from the first two experiments a difference can be observed especially for 1512 hours of heat treatment. During the 1st experiment the furnace was opened every 168 hours to take one sample out in contrast with the 2nd experiment where the first sample came out after 1176 hours. Each time that the furnace opens, K_2O vapours, due to thermal difference with the outside temperature, will go out of the furnace. Hence, the atmosphere inside the furnace at the 2nd experiment is richer in K_2O than at the 1st experiment which explains why the samples of this experiment lost less K_2O. This also explains the sharp decrease of K_2O content at 1008 hours for the 4th experiment.

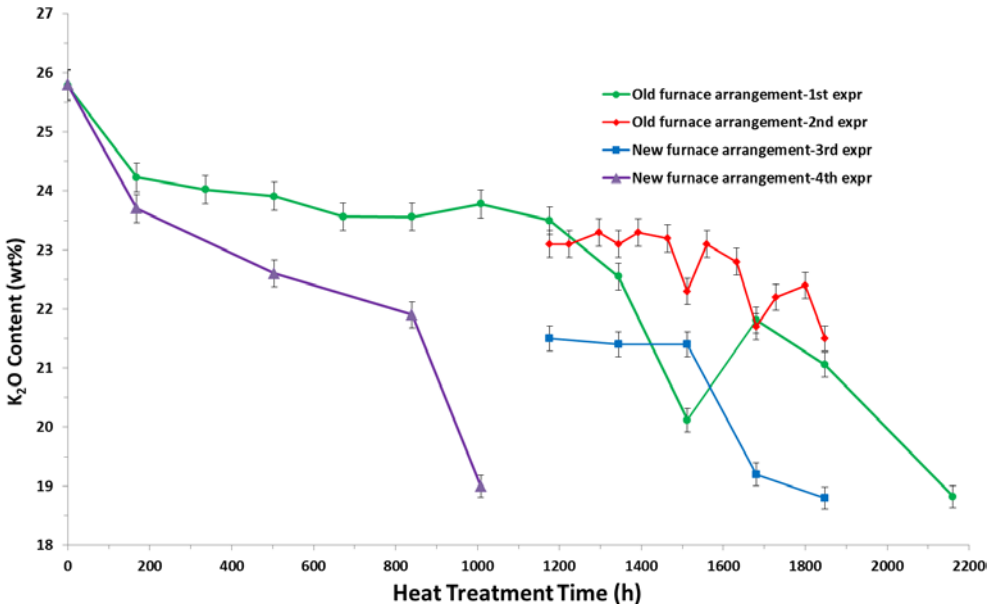

Figure 4.10: Potassium oxide content of SWXT® at 1250°C as a function of heat treatment time, for different furnace arrangements.

Another key factor to consider is the position of each sample inside the furnace. Regarding the sample at 1512 hours the difference of K_2O content for the first two experiments relates to the position of the sample, which was close to the door for the 1st experiment (less K_2O) and close to the back of the furnace for the 2nd experiment (more K_2O). Again, this phenomenon suggests that K_2O vapours from nearby SWXT® samples, the position of the samples and the number of times a furnace will be opened will affect the rate of further losses of the remaining samples.

On the other hand, results from 3rd and 4th experiments whose arrangement is as similar as possible to those of commercial use of SWXT® show that all the samples will lose significantly more K_2O than in previous experiments. The irregular behaviour of K_2O content around 1500 h for 1st and 2nd experiment and around 1000 hours for the 4th experiment suggest that probably this is also connected with the furnace arrangement and the K_2O content inside the furnace. Summarizing, these results disclosed that a

K_2O-rich atmosphere inside the heating environment will significantly limit the rate of potassium oxide evaporation.

As listed in Table 4.11, the loss of K_2O from SWXT® samples is affected by the concentration of potassium oxide vapours inside the furnace. Both experiments had the same amount of SWXT® samples but the size of the two furnaces is different so the concertation of K_2O inside the big furnace is less than for the small one. The volume of the big furnace (Furnace 2) is 34.0×10^{-3} m^3 and 9.1×10^{-3} m^3 for the small furnace (Furnace 1). Potassium oxide vapours, as suggested from a number of experiments in this study, will supress the rate of K_2O loss of the remaining samples.

Table 4.11: XRF analysis (wt% with ±1% relative error) of Superwool® XT fibres, heat treated at 1250°C for 1000 hours at different size furnaces.

Oxide	Unfired	Furnace 1	Furnace 2
Al_2O_3	35.7	38.2	38.5
K_2O	25.8	20.1	19.5
SiO_2	30.5	32.7	33.0
ZrO_2	6.2	7.2	7.2
MgO	1.2	1.1	1.1
HfO_2	0.2	0.1	0.1
Na_2O	0.4	0.6	0.5
TiO_2	0.0	0.0	0.0
Total	100.0	100.0	100.0
K_2O Loss	0.0	5.7	6.3
New Total	100.0	94.3	93.7

4.1.3. Structural characterization

X-ray diffraction analysis of short term heating experiments (Figure 4.11) revealed that SWXT® rapidly crystallizes, within less than 1 minute, when heat treated at elevated temperatures (above 1200°C) with multiple phases developing simultaneously. XRD

patterns demonstrate the appearance of three crystalline phases. The major crystalline phase detected is hexagonal kalsilite (ICDD 00-012-0134) that gives a powder pattern whose strong reflections resemble those of natural kaliophilite (Smith & Tuttle, 1957); other crystalline phases detected is hexagonal potassium magnesium silicate (ICDD 04-010-0020) with the chemical formula $K_2MgSi_3O_8$ (Collin, Comes, Boilot, & Colomban, 1980) and tetragonal zirconium oxide (ICDD 04-014-2971) (Bhagwat & Ramaswamy, 2004). Once these phases form after 1 min firing, there are no major changes observed in the XRD patterns for firing times of up to 60 min.

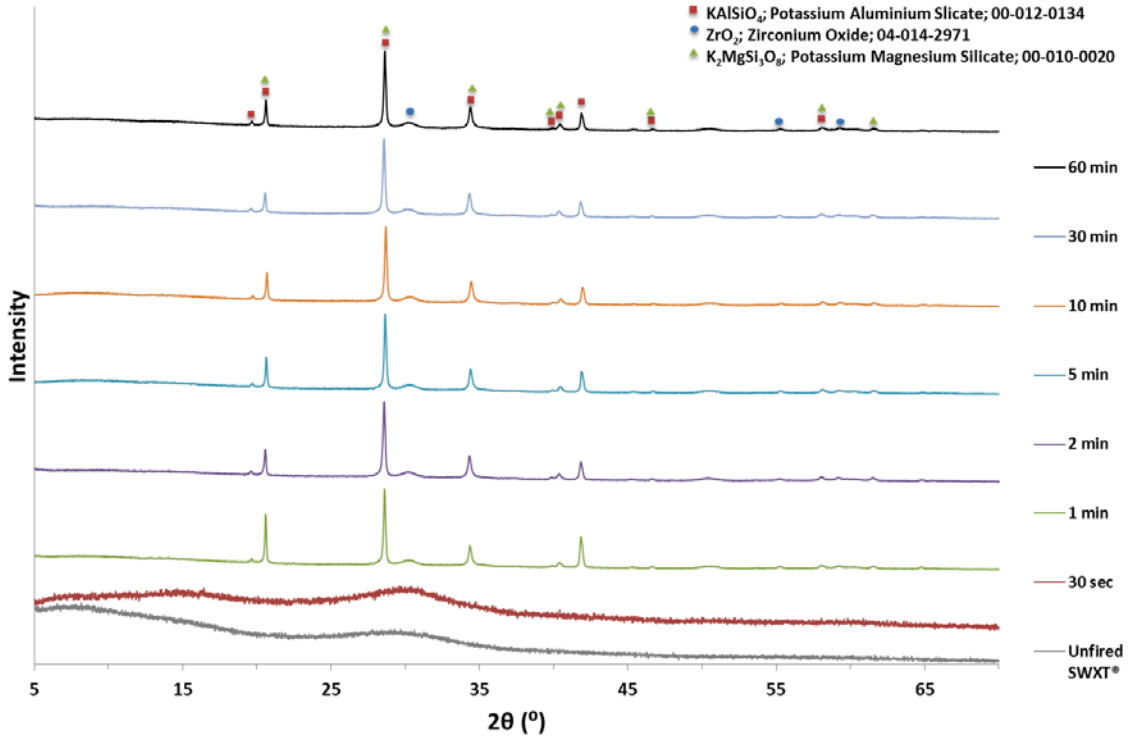

Figure 4.11: XRD patterns of heat treated SWXT® at 1250°C as a function of firing time.

It is important to note here that potassium magnesium silicate is isostructural to kalsilite with lattice parameters that are quite close, and thus shows a similar XRD pattern (Collin et al., 1980 and Smith & Tuttle, 1957). Given the very small magnesium oxide content of SWXT® fibres (1.2 wt%), it appears likely that $K_2MgSi_3O_8$ could exist only in trace amounts, if it does exist at all as a separate crystalline phase. It is more likely

that Mg is substituted in the kalsilite structure for some of the K and thus only a single kalsilite phase is present (Ma, Ma, & Yang, 2016). Therefore, in all the instances in this chapter where $K_2MgSi_3O_8$ is identified as a phase present, it is to be construed to exist in trace amounts only, if it does exist at all.

Figure 4.12 illustrates the XRD patterns from crashed SWXT® samples heat treated at 850°C. Peaks corresponding to crystalline phases start appearing after 336 h of heat treatment. Hexagonal kalsilite and hexagonal potassium magnesium silicate are clearly detectable after 840 h of constant firing. There are no further changes in the phases present for longer times (up to 2160 h).

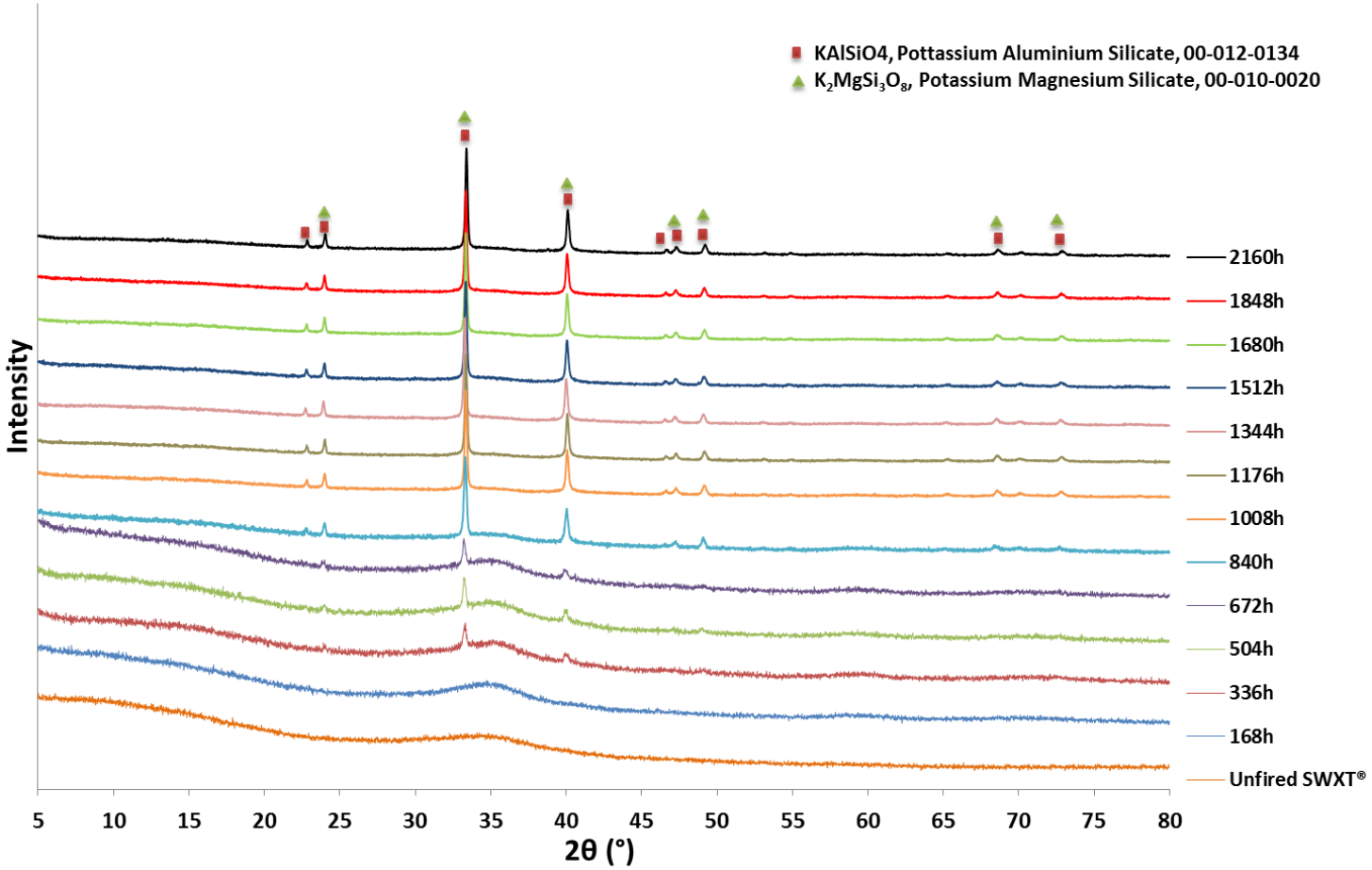

Figure 4.12: XRD patterns of heat treated SWXT® at 850°C as a function of firing time.

On the other hand, when SWXT® was first precrystallized at 1200°C for 5 minutes and then heat treated at 850°C for up to 2160 hours the crystallization behaviour is different. As shown in Figure 4.13 zirconium oxide peaks are now detectable – though with very small intensities – whereas hexagonal kalsilite and potassium magnesium silicate peaks are clearly detectable from the beginning. There is a peak shoulder at the left of the main peak (around 33°) which is not expected for hexagonal kalsilite but is expected for orthorhombic kalsilite. Thus, this indicates the transition from hexagonal to orthorhombic kalsilite (Gregorkiewitz, Li, White, Withers, & Sobrados, 2008) over time at 850°C, which is only observed for the pre-crystallized samples. The crystalline phase of zirconium oxide has been formed since SWXT® samples have been pre-crystallized at elevated temperature and at this temperature there is no further zirconium oxide crystal growth as crystallization process is evolving.

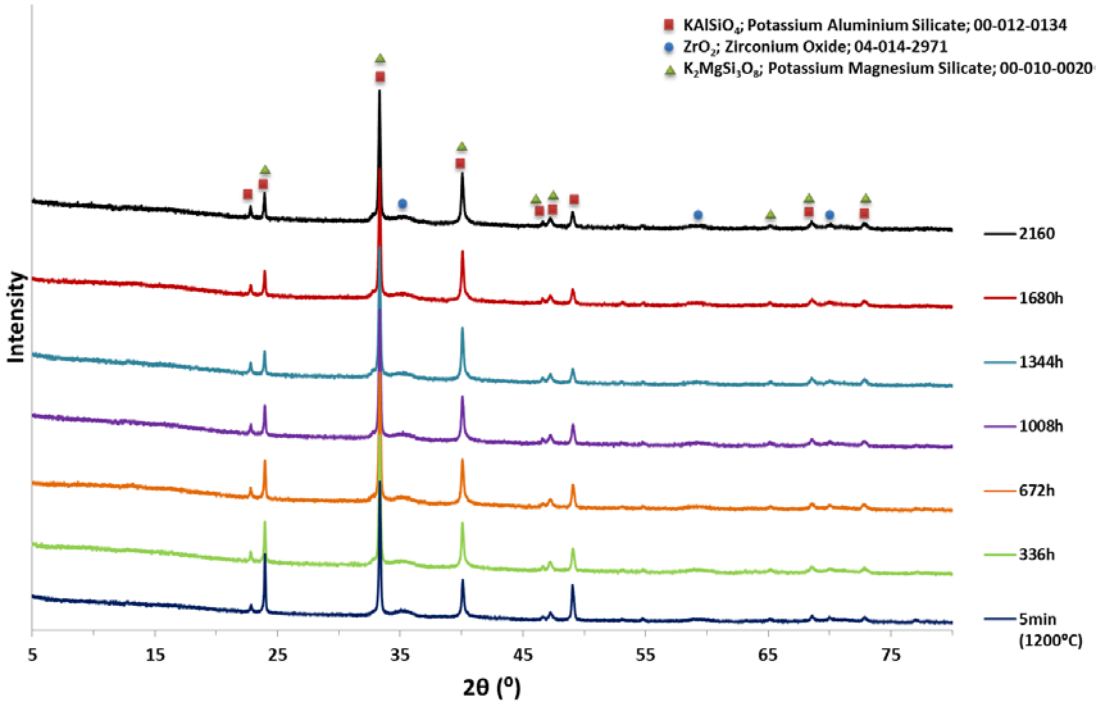

Figure 4.13: XRD patterns of heat treated pre-crystallized SWXT® at 850°C as a function of firing time.

For higher heat treatment temperatures, namely 1250°C, the crystallization behaviour of Superwool® XT differs significantly as depicted in Figure 4.14. Zirconia crystals are nucleating in the initial stages of heat treatment and continue to grow as SWXT® is fired for longer periods of time. Orthorhombic potassium aluminium silicate (ICDD 00-033-0988) is formed but the quantity of the phase keeps reducing for longer firing times (Cook, Roth, Parker, & Negas, 1977). After 1000 hours of heat treatment leucite phase (ICDD 01-076-8737) starts to form and after 2000 hours is clearly detectable (Gatta, Rotiroti, Ballaran, & Pavese, 2008). Moreover, around 300 hours hexagonal potassium aluminium oxide (ICDD 04-010-8954) which is known as potassium doped alumina ($KAl_{11}O_{17}$) peaks are barely detectable (Dernier & Remeika, 1976). This crystalline phase has a characteristic single high intensity peak at around 9°, for Co Kα radiation, and as heat treatment time passes is clearly observed.

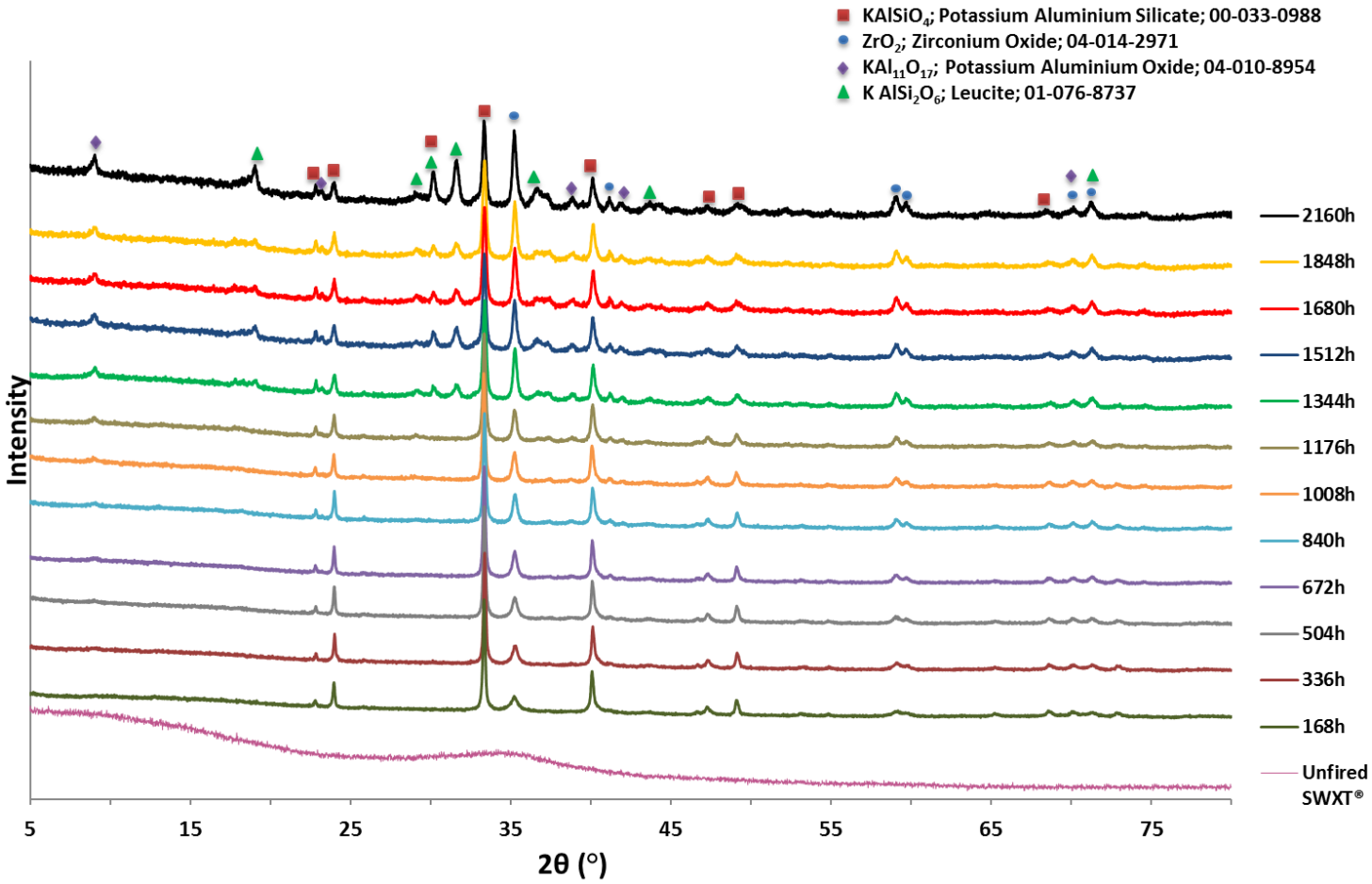

Figure 4.14: XRD patterns of heat treated SWXT® at 1250°C as a function of firing time (1^s expr).

As previously mentioned, XRD has revealed that kalsilite is disappearing as a function of time. To confirm this, peak area and full width at half maximum (FWHM) have been taken into consideration (Table 4.11). All the data presented below have been taken from XRD analysis of the heat treated SWXT samples at 1250°C.

Table 4.12: Peak shape parameters of the main $KAlSiO_4$ matched peak for Superwool® XT fibres, heat treated at 1250°C (1st expr).

Heat Treatment Time (h)	Position (°2th.)	FWHM (±0.01) (°2Th.)	Area (cts*°2Th.)	Relative Intensity (%)
168	33.32	0.10	2334 (±239)	100
336	33.36	0.16	1772 (±114)	100
504	33.34	0.14	1936 (±140)	100
672	33.33	0.13	1853 (±137)	100
840	33.35	0.15	1703 (±111)	100
1008	33.30	0.17	1590 (±96)	100
1176	33.33	0.19	1628 (±84)	100
1344	33.35	0.22	1341 (±60)	100
1512	33.33	0.21	1223 (±59)	100
1848	33.34	0.24	973 (±41)	100
2160	33.33	0.24	656 (±27)	100

Figure 4.15 shows the FWHM for the main peak matched by kalsilite as a function of firing hours. Normally FWHM will decrease as a function of time as it is associated with the crystal growth. The graph is probably affected by chemical formula changes and by lattice strains. In addition, as kalsilite peak gets broader (after 1000 hours of heat treatment) with time it is merged with other peaks that are starting to grow but are not yet detectable.

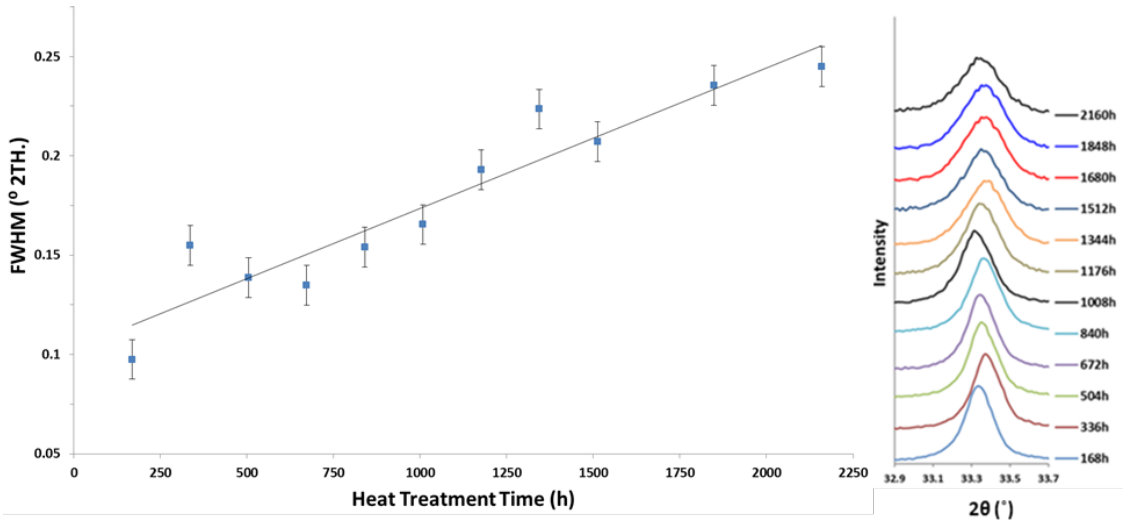

Figure 4.15: FWHM of kalsilite peak at 33.3° for SWXT® fibres, heat treated at 1250°C.

As revealed in Figure 4.16 the peak area decreases with increasing time. The way the area behaves indicates that kalsilite is disappearing and transforming into another crystalline phase.

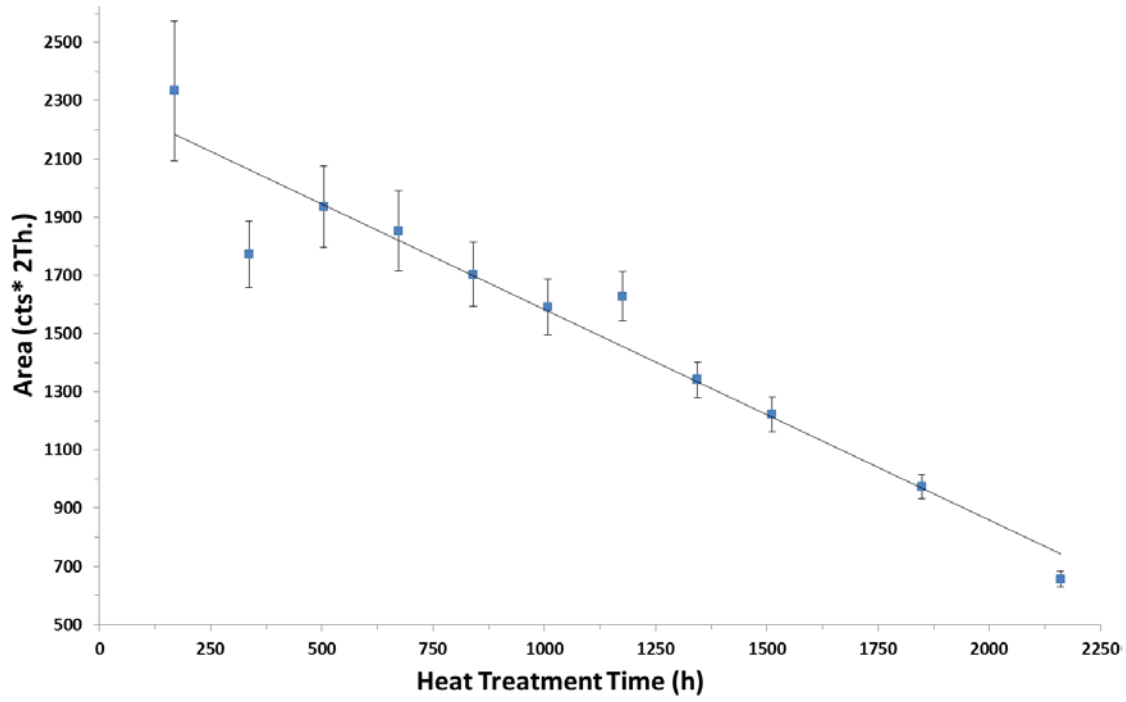

Figure 4.16: Area of kalsilite peak at 33.3° for SWXT® fibres, heat treated at 1250°C.

The nucleation and the crystal growth of zirconium oxide have also been studied with the aid of peak area and FWHM (Table 4.13). All the data presented below have been taken from XRD analysis of the heat treated SWXT® samples at 1250°C.

Table 4.13: Peak shape parameters of ZrO_2 matched peaks of SWXT® fibres, heat treated at 1250°C (1st expr).

Heat Treatment Time (h)	Position (°2th.)	FWHM (±0.01) (°2Th.)	Area (cts*°2Th.)	Relative Intensity (%)
168	35.20	0.34	929.0 (±28)	11.53
336	35.25	0.45	698.3 (±16)	15.54
504	35.23	0.35	764.4 (±22)	18.23
672	35.22	0.31	712.1 (±23)	22.33
840	35.24	0.32	713.9 (±23)	25.77
1008	35.20	0.29	619.6 (±21)	26.35
1176	35.22	0.26	601.8 (±23)	28.46
1344	35.24	0.25	754.9 (±30)	52.73
1512	35.22	0.27	724.7 (±27)	51.30
1848	35.24	0.26	569.8 (±22)	56.64
2160	35.22	0.26	737.3 (±28)	88.24

Figure 4.17 shows that after a gradual decline (0-1000 h) FWHM remains relatively constant in terms of time. The crystal size and strain of ZrO_2 increase significantly at 1000 hours. Moreover, after a substantial change between 168 and 336 hours, the peak area seems to be fairly constant as a function of firing time within acceptable errors (Figure 4.18).

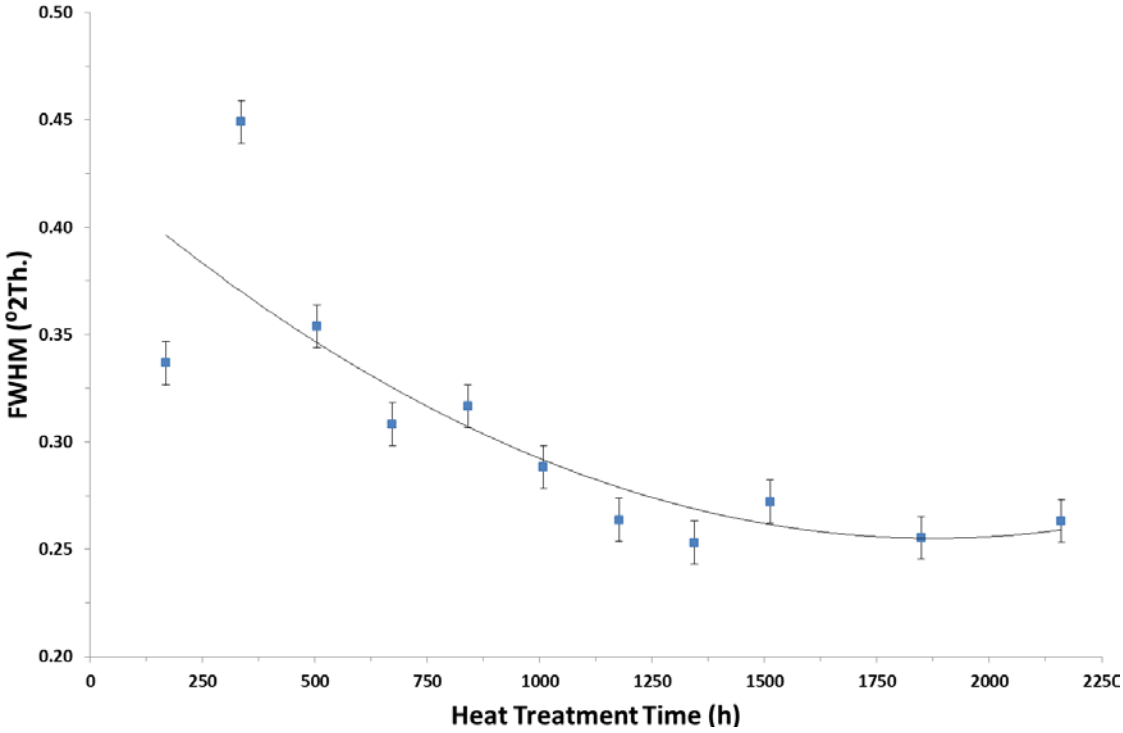

Figure 4.17: FWHM of zirconia peak at 35.2° for SWXT® fibres, heat treated at 1250°C.

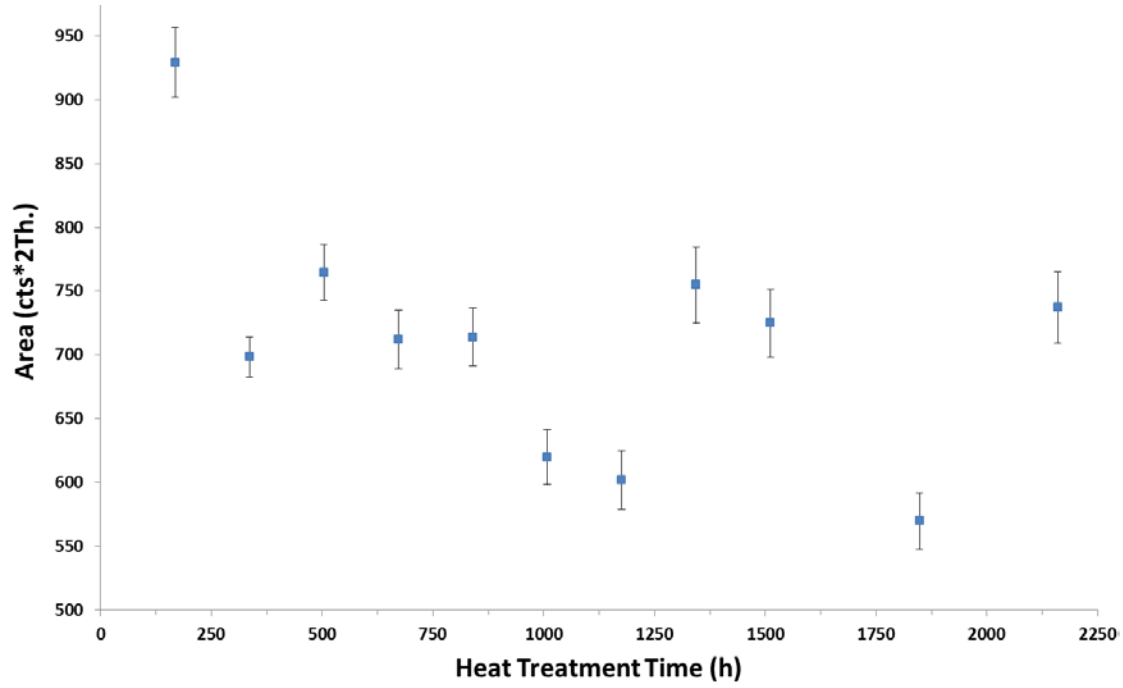

Figure 4.18 Area of zirconia peak at 35.2° for SWXT® fibres, heat treated at 1250°C.

Reitveld refinement was used to identify the percentage of amorphous and crystalline phase and to further identify the percentage of the various crystalline phases as a function of heat treatment hours (Table 4.14).

Table 4.14: Phase content (wt%) obtained from Rietveld analysis of heat treated SWXT® at 1250°C (1st expr).

Heat Treatment Time (h)	Kalsilite	Zirconium Oxide	Leucite	Potassium Aluminium Oxide	Amorphous
168	57	3	0	0	40
336	57	2	0	0	40
504	65	3	0	0	32
672	66	3	0	1	29
1008	57	5	6	2	29
1176	44	5	15	10	25
1512	42	5	17	11	26
1848	41	5	29	11	14
2160	38	5	33	12	12

As demonstrated in Figure 4.19 the percentage of amorphous phase decreases significantly as a function of time. The fairly linear pattern this graph follows is expected as crystal growth is occurring.

Figure 4.20 shows that the ZrO_2 phase content remains almost stable after nucleation has occurred (after 672 hours). The percentage of leucite seems to increase at a similar rate that the percentage of kalsilite is decreasing, indicating that kalsilite is disappearing with time and transforming into leucite. Moreover, potassium aluminium oxide content rises after 1008 hours. All these phase changes happen at the point that the kalsilite content decreases and a massive K_2O loss is occurring.

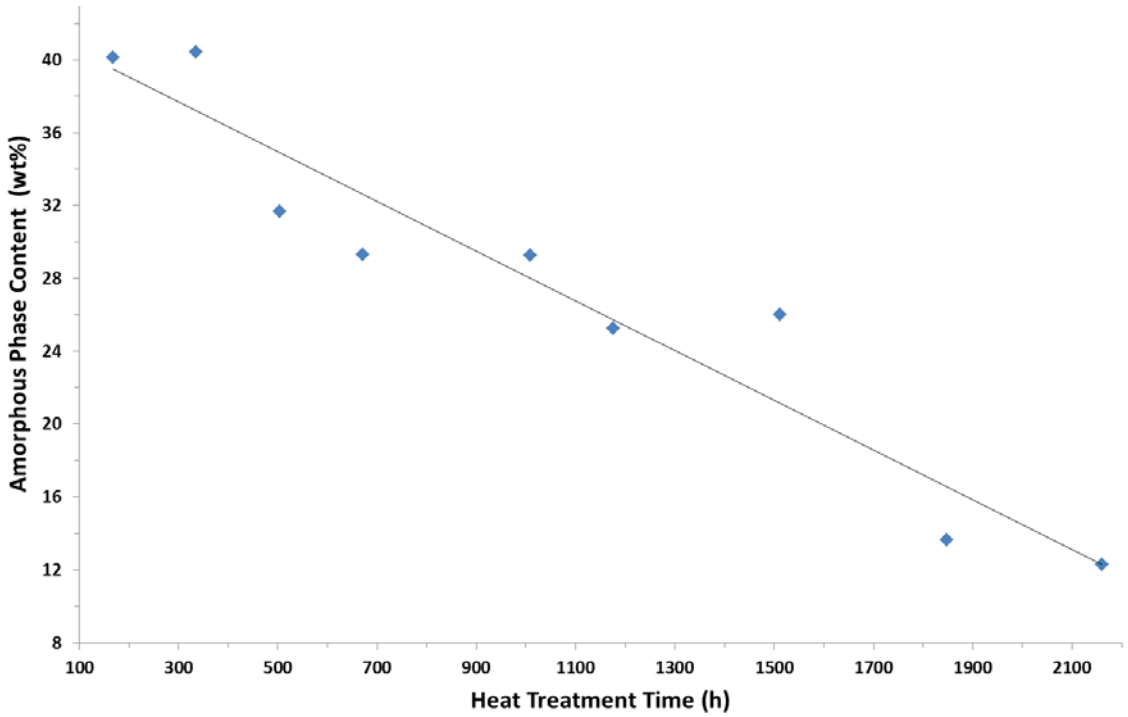

Figure 4.19: Amorphous phase content in SWXT® heat treated at 1250°C as a function of time.

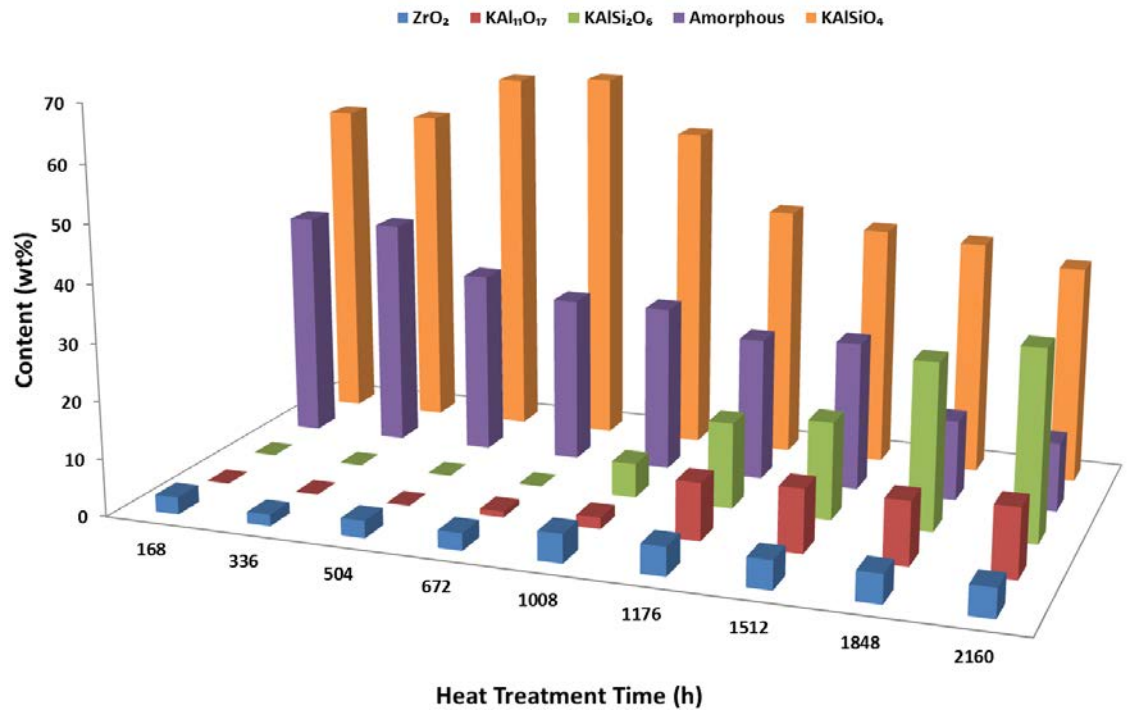

Figure 4.20: Content of amorphous and crystalline phases in heat treated SWXT® at 1250°C as a function of firing time (1st expr).

Heat treatment experiments with Superwool® XT, pre-crystallized Superwool® XT at 1200°C for five minutes and colloidal silica coated SWXT® were performed. All the samples were heat treated at 1500°C for 72 hours to study the different crystallization behaviour. During these experiments, SWXT® has been used as a crucible for the samples to avoid any reaction with alumina crucible.

As depicted in Figure 4.21 there are differences in the phase assemblage, except for ZrO_2 that seems to equally develop for all the samples. Regarding $KAl_{11}O_{17}$, the peak at 7° 2θ is clearly detectable for SWXT® and it is stronger and sharper for the pre-crystallized SWXT® sample in contrast with the colloidal silica coated SWXT® where this phase has not formed. These XRD patterns are a characteristic example to understand the thermal behaviour of biosoluble glass fibres. SWXT® fibres are directly affected by time and temperature because as shown in Figure 4.21 when the fibres are heat treated at higher temperatures less time is needed to reach the same crystallization stage with samples that were heat treated at lower temperature. Finally, at 1500°C leucite needs less than 72 hours to develop in considerable amount.

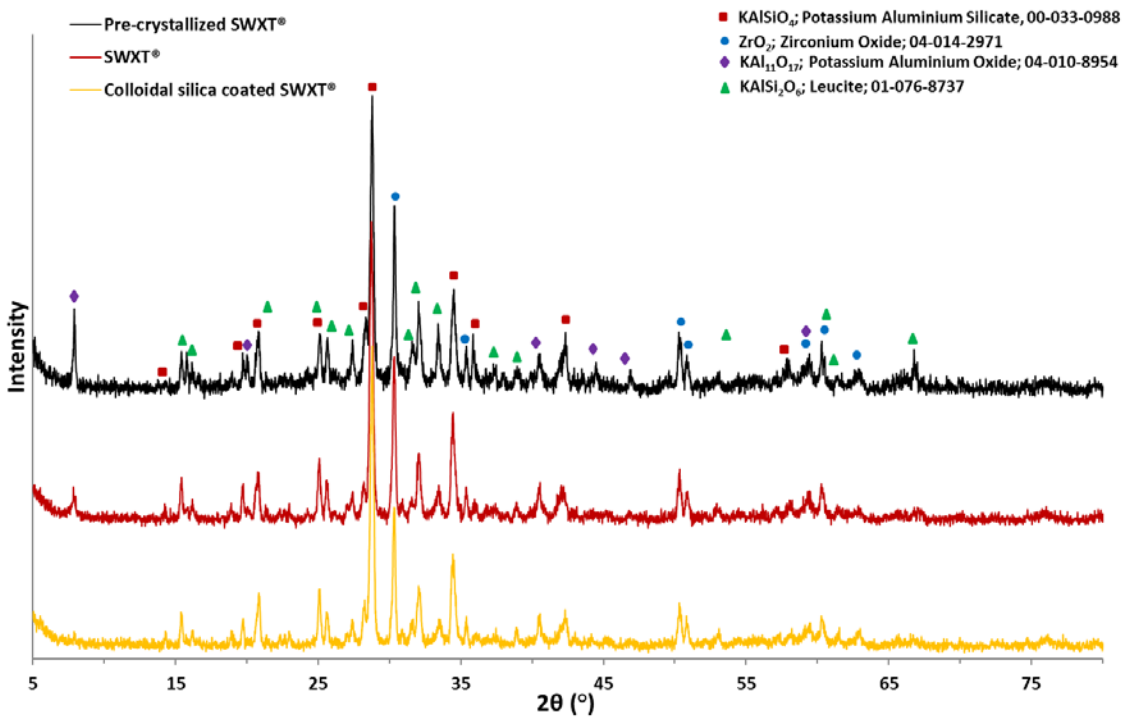

Figure 4.21: XRD patterns of samples heat treated at 1500°C for 72 hours.

XRD patterns (Figure 4.22) of SWXT® fibres heat treated at 1250°C from the 2nd experiment illustrate that potassium aluminium silicate, zirconium oxide and potassium aluminium oxide are clearly detectable after 1176 hours of constant firing, with the latter phase being present in small amounts only. With increasing firing time, leucite peaks start to appear albeit with very low intensities.

Figure 4.23 shows the crystallization behaviour of SWXT® with the new furnace arrangement. The first four patterns (168-1008 hours) are from the 4th experiment that was conducted in a big furnace and as it has been already explained the samples were affected by the regular opening of the furnace and by furnace dimensions which explains why the 1008 hours pattern has more prominent leucite peaks than the 1176 hours pattern. On the other hand, the next five XRD patterns (1176-1848 hours) are from the 3rd experiment conducted in a small furnace and the furnace was not opened till 1176 hours when the first sample was removed.

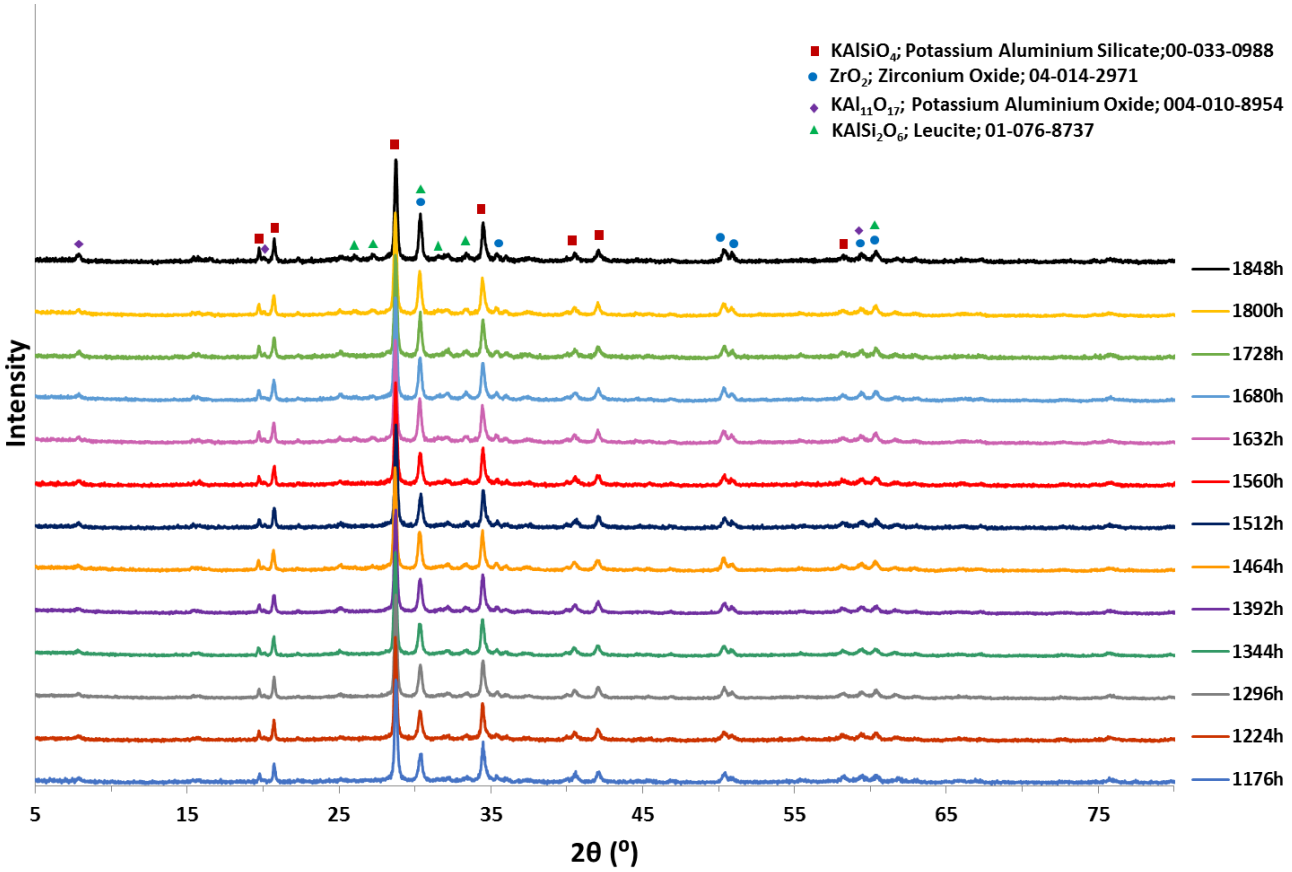

Figure 4.22: XRD patterns of heat treated SWXT® at 1250°C as a function of time (2nd expr).

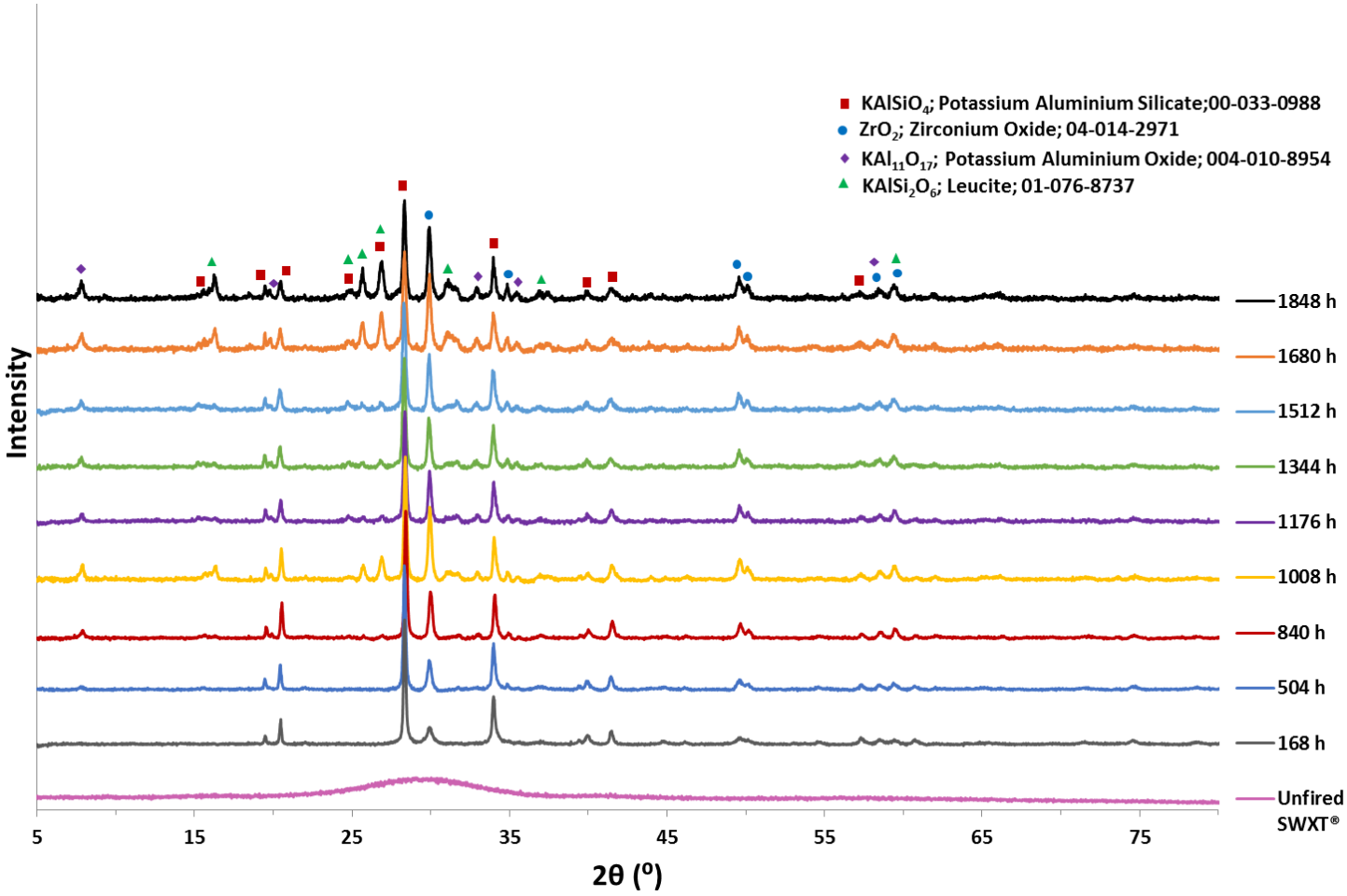

Figure 4.23: XRD patterns of heat treated SWXT® at 1250°C as a function of time (3rd and 4th expr).

Results show that the furnace arrangement is a very important factor that affects the crystallization evolution of SWXT® samples. Figure 4.24 suggests that there is a significant difference in the crystallization process because of K_2O vapours. Potassium aluminium silicate and zirconia phases have already developed below 1000 hours as evidenced in this study so there is not any detectable difference. In contrast, the development of leucite and potassium aluminium oxide crystalline phases is substantially dissimilar for the two furnace arrangements. These XRD patterns prove the starting hypothesis that the presence of K_2O vapours delays the development of the aforementioned phases.

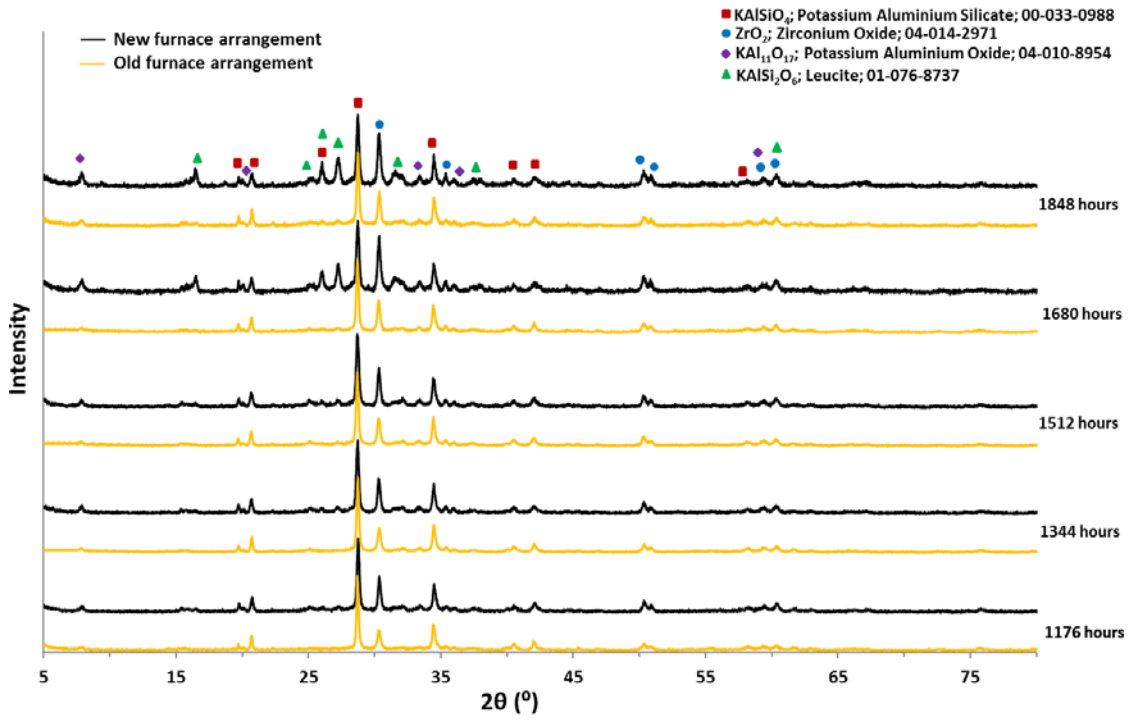

Figure 4.24: XRD patterns comparing the crystallization behaviour of heat treated SWXT® glass fibres at 1250°C as a function of time and different furnace arrangement (Old: 2nd expr and New: 3rd expr).

Figure 4.25 shows the difference between two furnaces with different dimensions where furnace 1 is smaller than furnace 2. Inside these furnaces with the same arrangement a similar amount of SWXT® has been placed and heat treated at 1250°C so the same

amount of K_2O vapours will be in different sized furnaces. As a result, furnace 2 will have the same amount of K_2O in the heat-treating atmosphere but it will have less concertation. XRD patterns specify that samples heat treated in furnace 2, which has less potassium vapours concertation, have greater amount of leucite and potassium aluminium oxide.

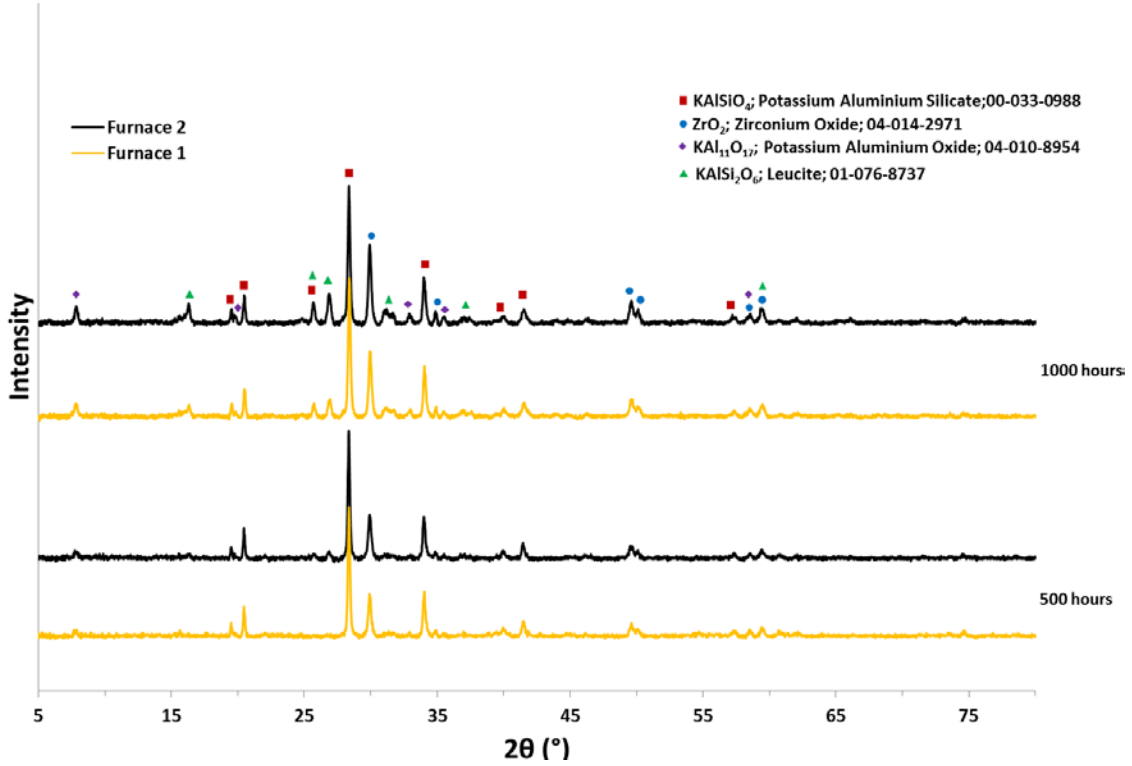

Figure 4.25: XRD patterns comparing the crystallization behaviour of heat treated SWXT® at 1250°C for up to 1000 hours under different experimental conditions; Furnace 2 is bigger than Furnace 1.

4.1.4. Microstructural characterization

Scanning electron microscopy was used to analyse the surface morphology and microstructure of SWXT® samples. Figure 4.26 demonstrates the surface of the unfired SWXT®; both secondary and backscattered imaging revealed that fibres have a featureless and smooth fracture surface as they are completely amorphous. The

observed pinholes (Figure 4.26 b) and c) could be caused – according to the manufacturer – by existence of trapped CO_2 gas during the production of fibres.

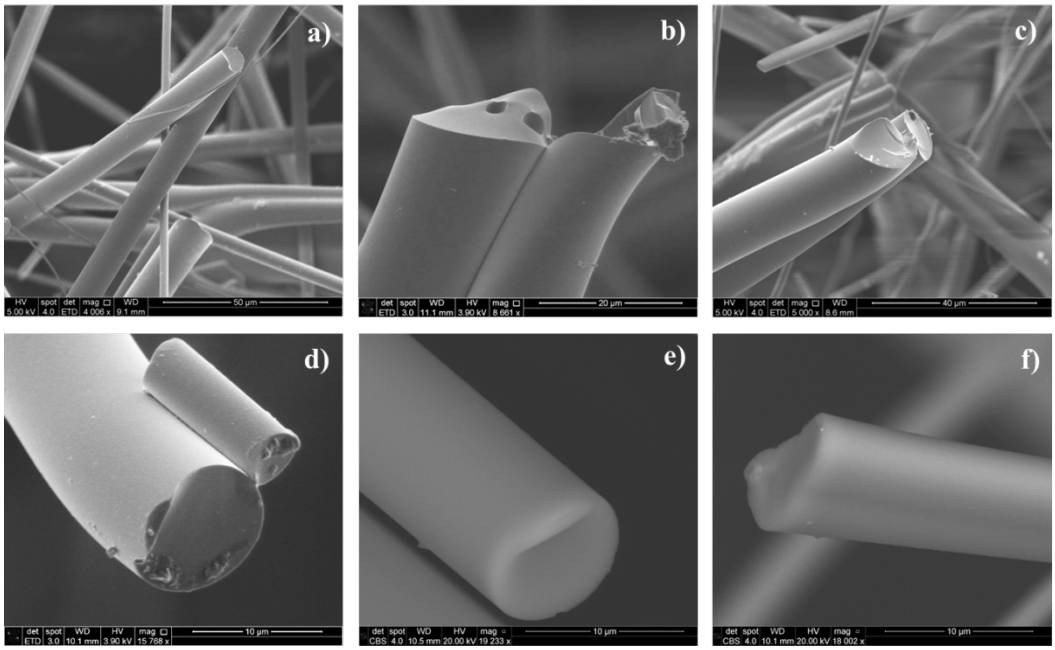

Figure 4.26: Secondary a), b), c), and d) and backscatter e) and f), SEM imaging of unfired SWXT® fibres.

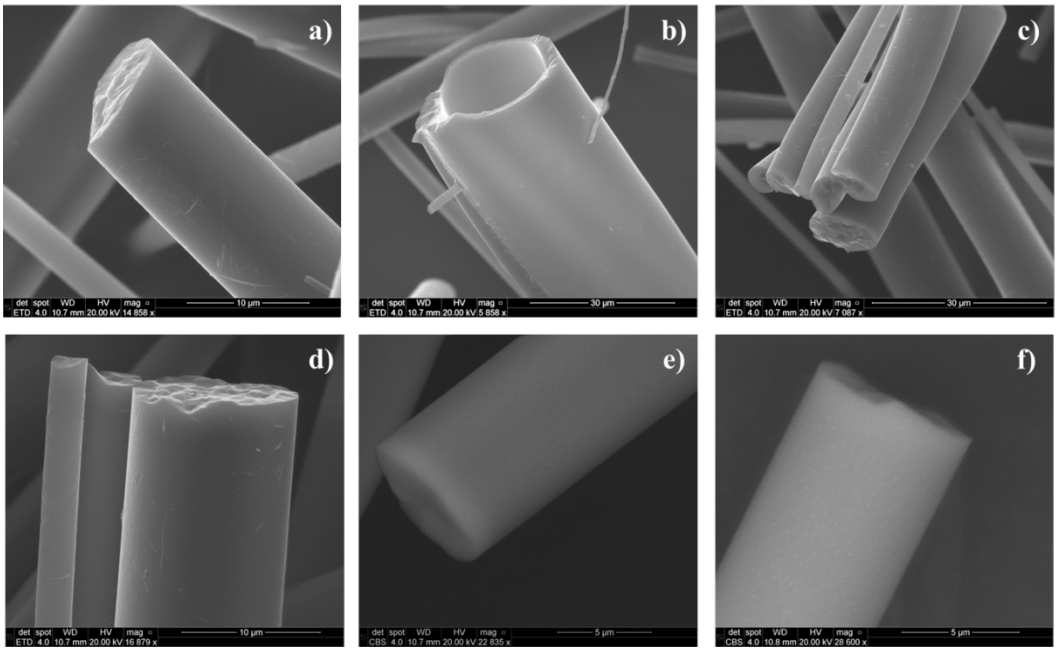

Figure 4.27: Secondary a), b), c), and d) and backscatter e) and f), SEM imaging of heat treated SWXT® fibres at 1250°C for 672 hours.

Figure 4.27 shows that even at initial stages of heat treatment the fracture surface has become already rough and coarse which designates crystallization through the fibre diameter. Backscatter imaging revealed the existence of several bright spots but their size and the phase cannot be detected at this stage. Possibly these spots relate to ZrO_2 crystalline phase because Zr – heaviest element in SWXT® – nuclei are more effective electron scatterers than the lighter nuclei like Si, Al, Mg, K and O; hence Zr appears brighter.

The fracture surface of SWXT® after 1176 hours of constant firing at 1250°C with different furnace conditions as imaged by SEM is shown in Figure 4.28 to Figure 4.30. Secondary imaging revealed that SWXT® fibres are now interconnected and bonded together. The fracture surface is uneven and rough due to crystallization evolution. Moreover, SWXT® samples from the new furnace arrangement that are losing more K_2O will have a greater degree of crystallization compared to the SWXT® samples with the old furnace arrangement. SWXT® glass fibres shown in Figure 4.30 have a very rough surface morphology with scratch-like features on the surface and the earlier observed spots are also larger compared to the samples in Figure 4.28 and Figure 4.29.

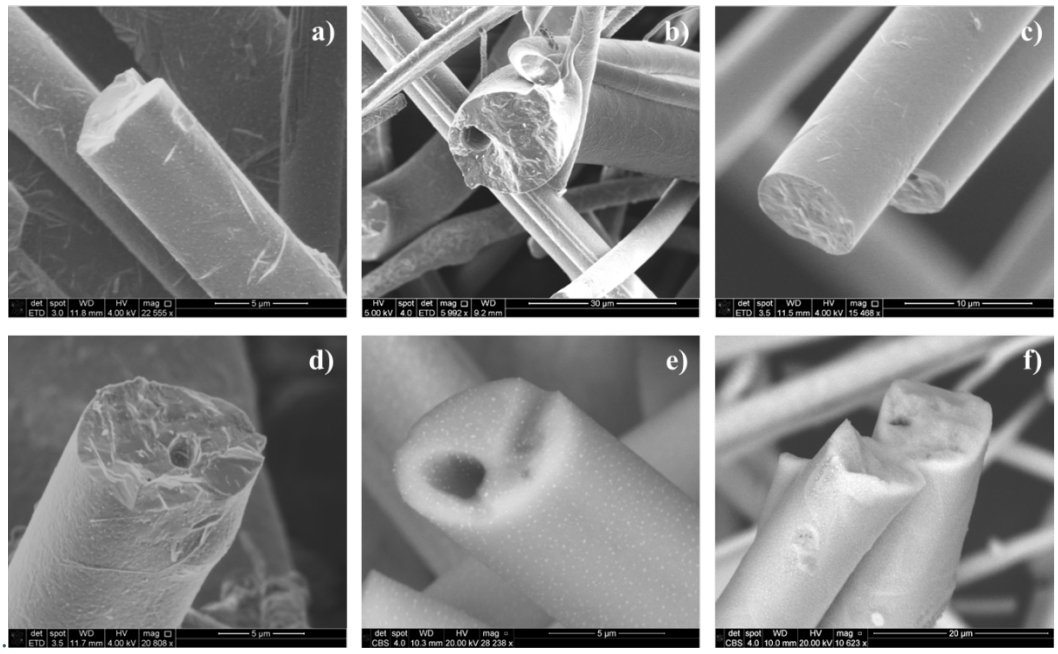

Figure 4.28: Secondary a), b), c), and d) and backscatter e) and f), SEM imaging of heat treated SWXT® fibres at 1250°C (1st expr) for 1176 hours

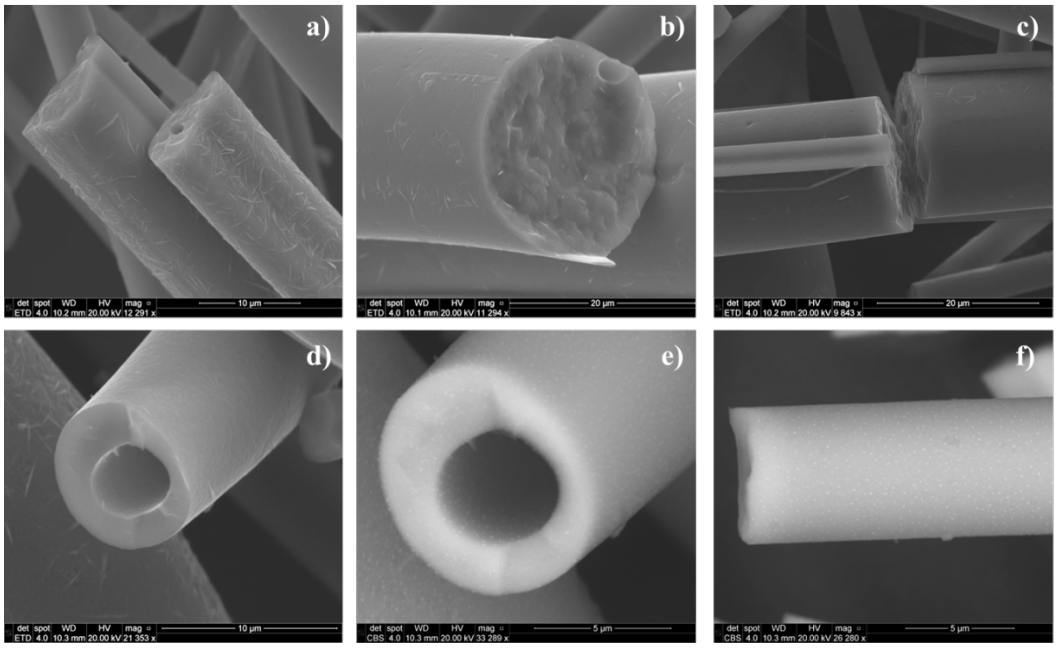

Figure 4.29: Secondary a), b), c), and d) and backscatter e) and f), SEM imaging of heat treated SWXT® fibres at 1250°C (2nd expr) for 1176 hours.

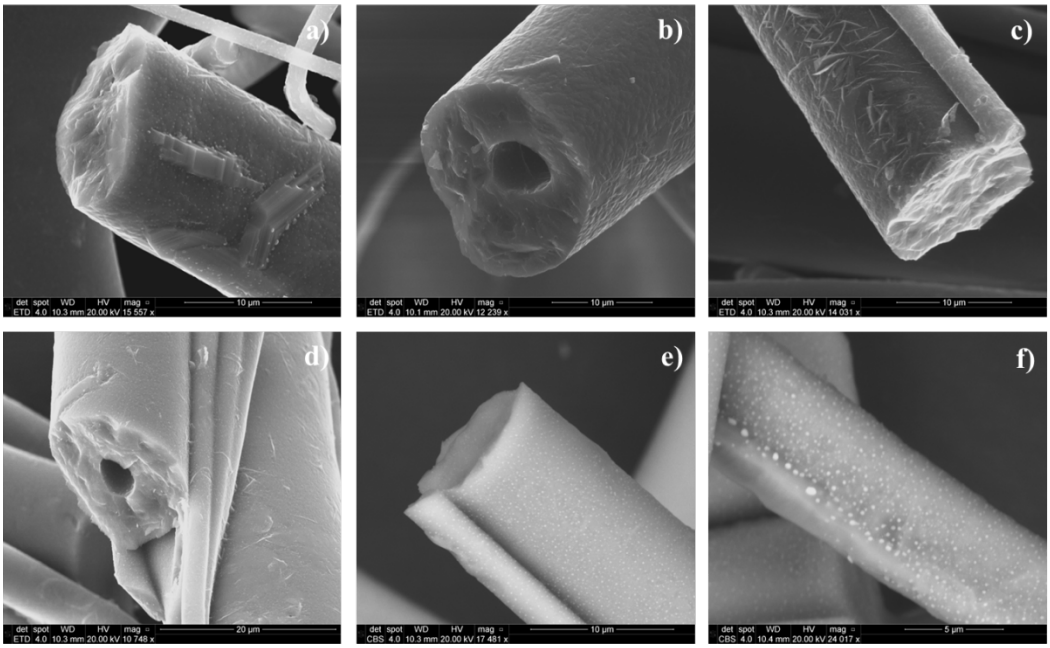

Figure 4.30: Secondary a), b), c), and d) and backscatter e) and f), SEM imaging of heat treated SWXT® fibres at 1250°C (3rd expr) for 1176 hours.

Figure 4.31 shows that for even longer firing times some fibres have a very rough surface morphology with scratch-like features on the surface. The roughness of fracture surfaces suggests that the fibres are crystallized through the diameter.

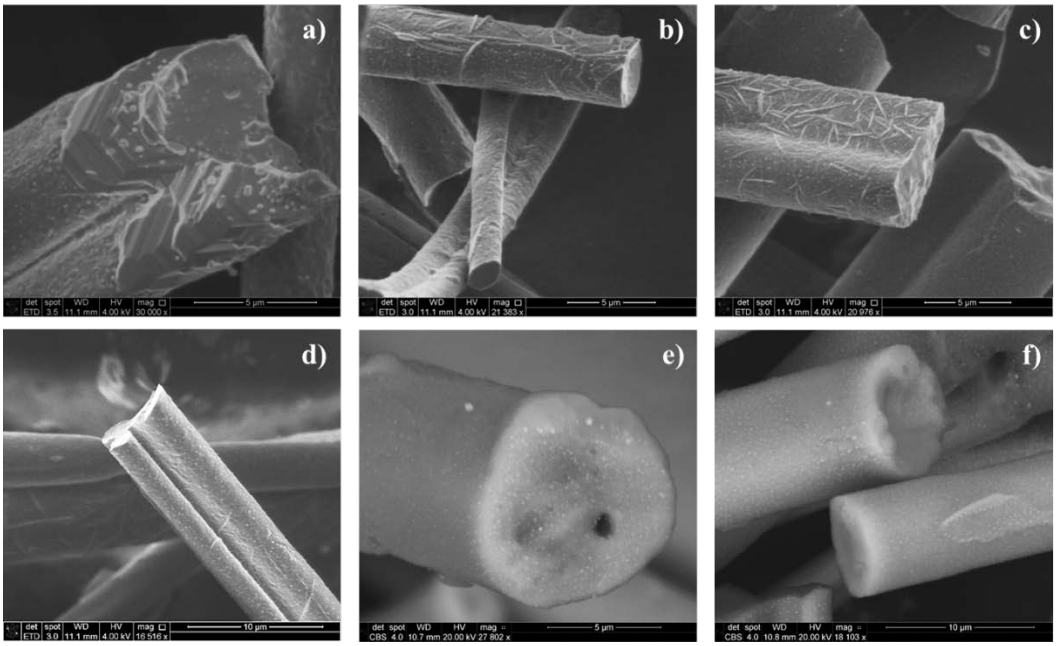

Figure 4.31: Secondary a), b), c), and d) and backscatter e) and f), SEM imaging of heat treated SWXT® fibres at 1250°C for 1512 hours (1st expr).

As depicted in the following SEM figures (Figure 4.32, Figure 4.33 & Figure 4.34), again the SWXT® samples from the new furnace arrangement have a greater degree of crystallization compared to the SWXT® samples with the old furnace arrangement. SWXT® samples (Figure 4.34) have very big hexagonal plate-shaped features; these plates seem to have grown out of the fibres and are more likely to be alumina plates. The zirconia crystals appear to be forming around the boundaries of these plate features and they appear to be larger than the crystals formed in the other areas of the fibres.

Figure 4.35 shows that for the longest firing time (2160 hours) all the fibres have a very coarse and rough surface morphology and plate-shaped features have formed. The zirconia crystals appear to be forming around the boundaries of these plate features and are larger than the crystals formed in the other areas of the fibres. Backscatter imaging showed considerable growth of the previously observed spots.

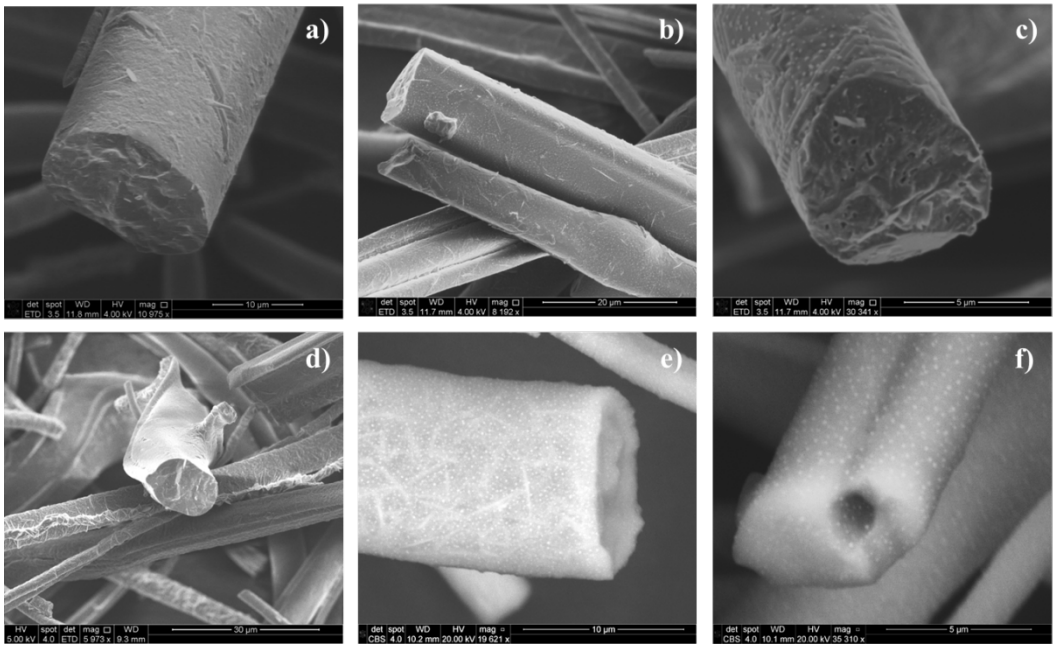

Figure 4.32: Secondary a), b), c), and d) and backscatter e) and f), SEM imaging of heat treated SWXT® fibres at 1250°C (1st expr) for 1848 hours.

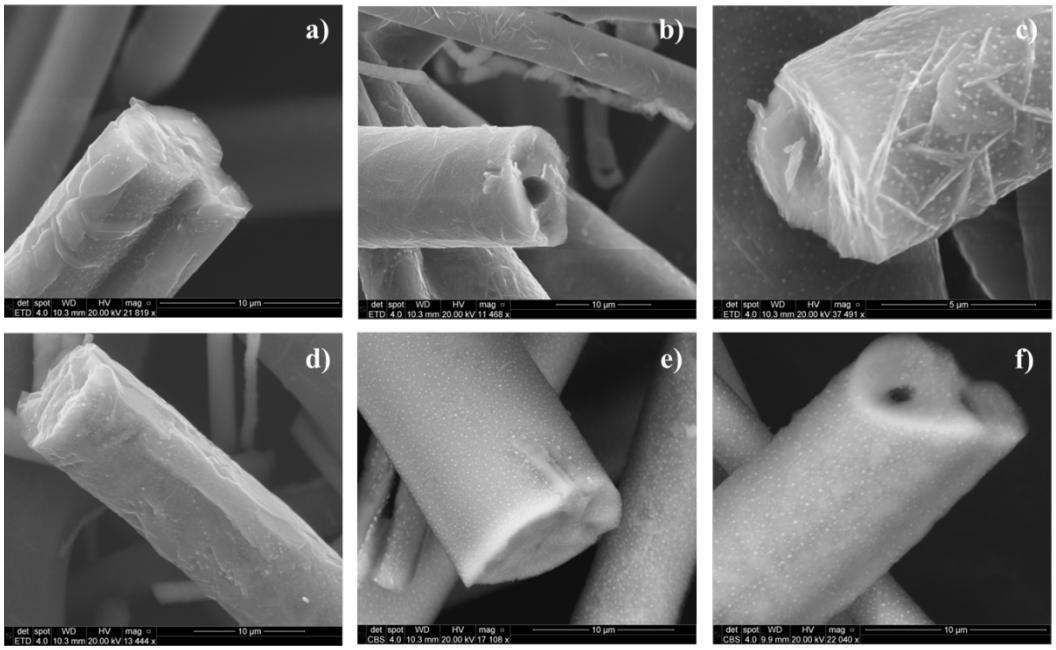

Figure 4.33: Secondary a), b), c), and d) and backscatter e) and f), SEM imaging of heat treated SWXT® fibres at 1250°C (2nd expr) for 1848 hours.

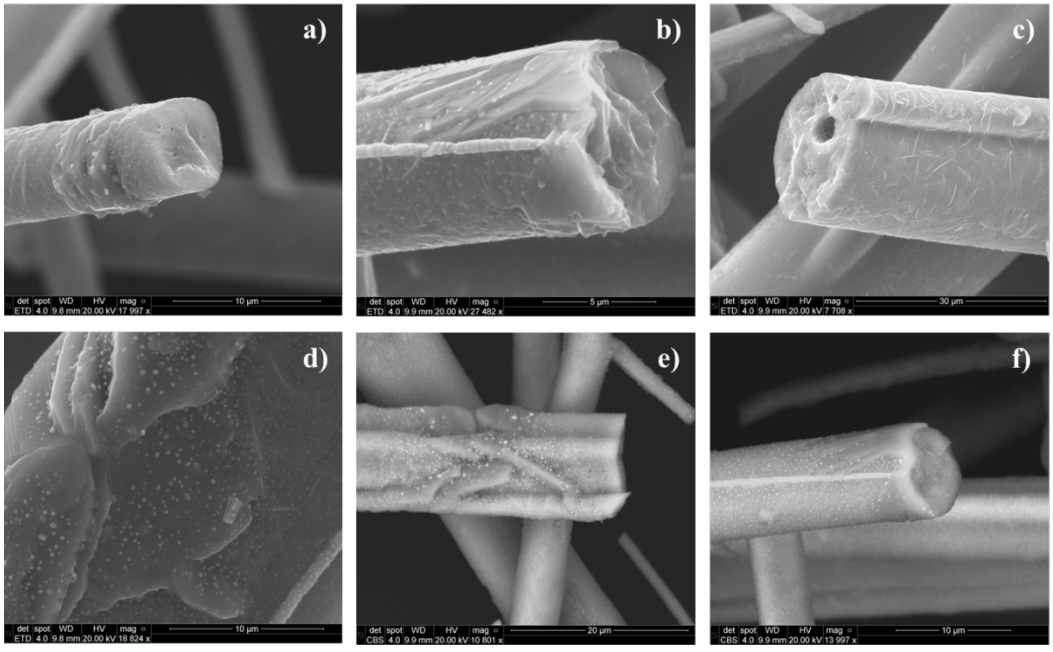

Figure 4.34: Secondary a), b), c), and d) and backscatter e) and f), SEM imaging of heat treated SWXT® fibres at 1250°C (3rd expr) for 1848 hours.

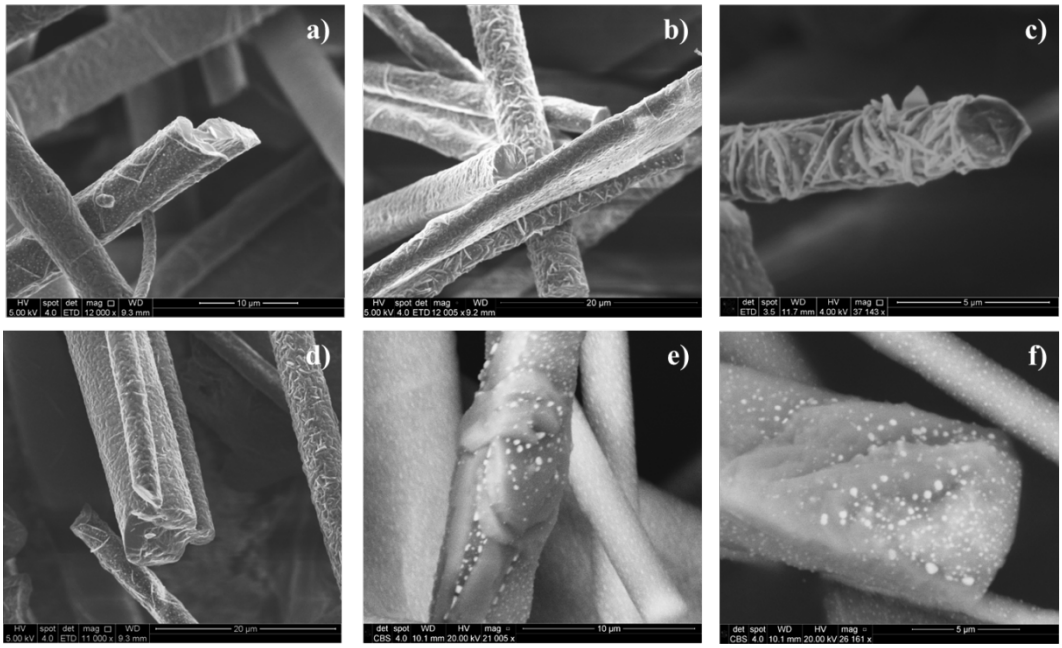

Figure 4.35: Secondary a), b), c), and d) and backscatter e) and f), SEM imaging of heat treated SWXT® fibres at 1250°C for 2160 hours 1st (expr).

The SEM imaging presented here clearly demonstrates that Superwool® XT fibres develop microstructural changes at elevated temperature and with increasing heat treatment time, these changes will occur gradually, provoking growth of grains which reduces fibres' flexibility. Finally, heat-treated fibres fuse together and SWXT® becomes brittle. The observed changes in surface morphology of glass fibres occur not only due to high temperature but also because crystallisation is initiated (Shelby, 2005).

Secondary SEM imaging of SWXT® heat treated at 1500°C (Figure 4.36) demonstrate a very rough morphology, it appears that distinct crystal shaped areas have been formed throughout the fibres for all the different samples.

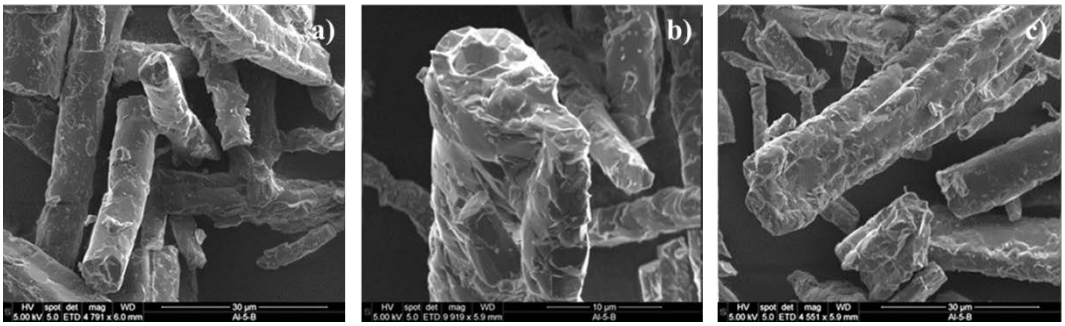

Figure 4.36: Secondary SEM imaging of a) pre-crystallized SWXT® (1200°C, 5min) b) SWXT® c) colloidal silica coated SWXT® glass fibres heat treated at 1500°C for 72 hours.

4.1.5. Thermal analysis

Differential thermal analysis was carried out to study the thermal behaviour of SWXT®. In these patterns (Figure 4.37), a strong exothermic peak is visible which is related to the main crystallization event. In some of the results, a shallow feature peak appears to exist at around 950°C and before the main crystallization peak which may relate to the glass transition temperature of SWXT®.

As depicted, all the exothermic peaks increase in intensity, get broader and shift to higher temperature with the increase of heating rate. According to Kissinger (1957) and Speil et al. (1945) the heating rate ($\Phi = dT/dt$), affects the temperature and shape of DTA peaks. The peaks get wider because at higher heating rates the spacious gradient of temperature in the sample will get greater. At an accelerated Φ, the reactions in the sample needs less time. According to XRD data when SWXT® is heat treated at 1250°C the formation of potassium aluminium silicate occurs quite soon and then leucite appears at longer firing times. In contrast with XRD, DTA is showing only one crystallization event for this material which relates to $KAlSiO_4$.

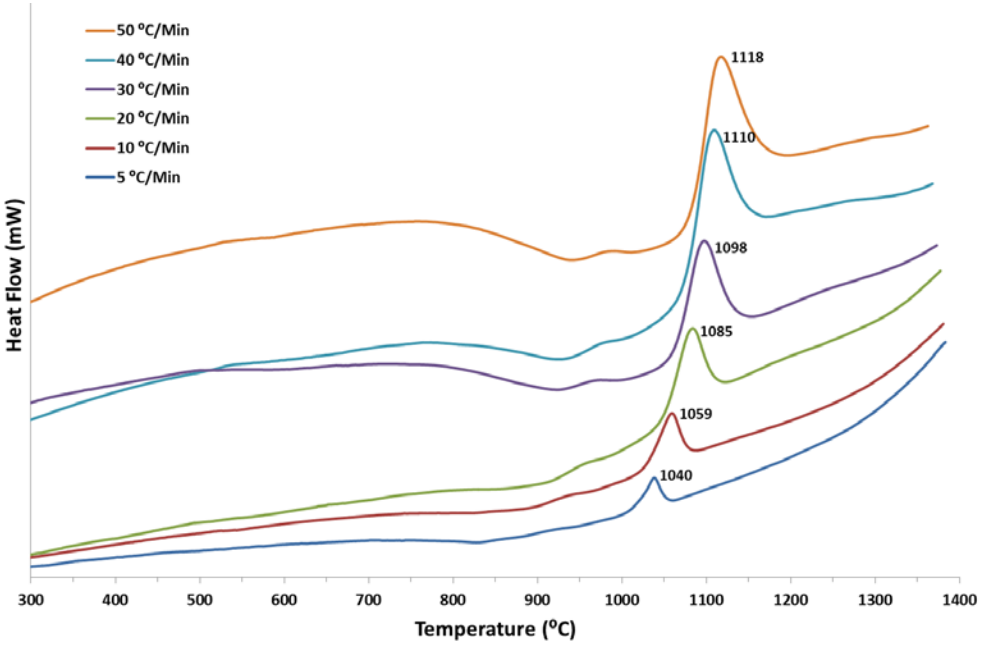

Figure 4.37: DTA curves of unfired SWXT® (100mg) with various heating rates.

The activation energy for SWXT® was determined by the Kissinger method (Eq. 4.1) (Kissinger, 1957).

$$\ln\frac{a}{T_0^2} = -\frac{E_a}{RT_0} + C \quad 4.1$$

where a is the heating rate, E_a is the activation energy, R is the gas constant, T_0 is the exothermic peak temperature and C is a constant. The activation energy is calculated from the slope of the line of $\ln(a/T_0^2)$ vs $1/T_0$.

The shape factor (n) of the exothermic peak is calculated by Eq. 4.2:

$$n = \frac{2.5}{\Delta T} \cdot \frac{T_0^2}{(E_a/R)} \quad 4.2$$

where n is the Avrami constant and ΔT is the full width at half maximum of the exothermic peak.

As Figure 4.38 shows, the activation energy for SWXT® is 420 kJ/mol which is correlated with the first exothermic peak in DTA and corresponds to the crystallization

of kalsilite. The activation energy of crystallization may actually vary with different starting materials. Okada, Kaneda, Kameshima, Yasumori, and Takei (2003) reported the activation energy of mullite for different starting materials (glass, glass fibres, hybrid gel, diphasic gel and single-phase gel) to range from 800 to 1300 kJ/mol.

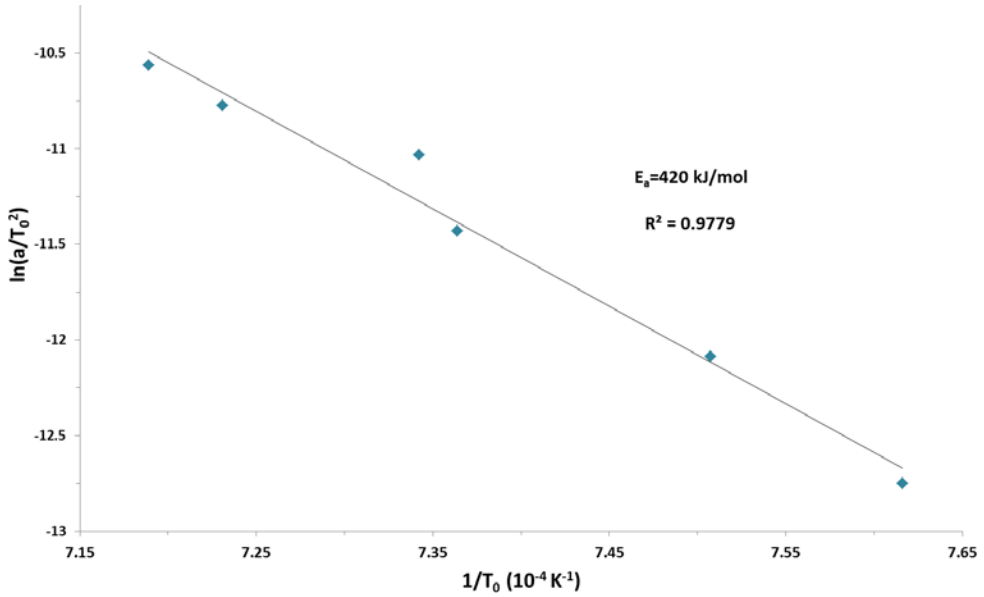

Figure 4.38: Kissinger plot for non-isothermal crystallization of SWXT®.

The value of the Avrami exponent provides information regarding the morphology of the growing crystals (Johnson, Kriven, & Schneider, 2001). The value of n reflects the mechanism dominating the crystallization. Smaller n values indicate that the crystallization is dominated by a surface crystallization mechanism rather than by volume crystallization, and that the crystallization dimension is low. On the other hand, larger n values are expected only in case of increasing nucleation rates, i.e. > 2.5 in diffusion-controlled reaction or > 4 in polymorphic transformation (Takei et al., 2001). The combined average shape factor for SWXT® was 3.3±0.1 (calculated by Fit Multi-Peaks function in Origin) which indicates that the formation process for this material is nucleation and three-dimensional growth that follows the diffusion-controlled

mechanism with increasing nucleation rate (Okada, Kaneda, Kameshima, Yasumori, & Takei, 2003).

DTA analysis (Figure 4.39) shows that for SWXT® the first crystallization event occurs at lower temperature compared with colloidal silica coated SWXT® which is an expected result because as made SWXT® sample has lower silica content (by approximately 2 wt%).

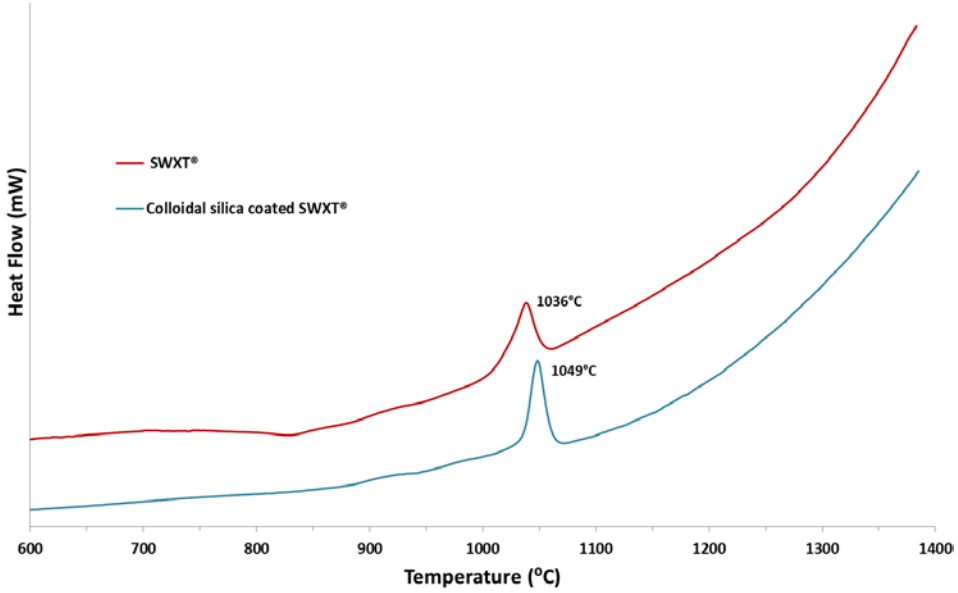

Figure 4.39: DTA curves of unfired colloidal silica coated SWXT® and SWXT® (100mg) with a 5°C/min heating rate.

4.1.6. Summary

Loss of K_2O upon prolonged heat treatment at 1250°C, it is believed by volatilization, has been confirmed with XRF analysis. As time passes and crystallization is initiated the loss of K_2O increases. XRD analysis revealed that SWXT® will crystallize very quickly (< 1 minute) and Rietveld analysis showed that it will transform into a glass-ceramic since after 2000 hours of constant firing there is still some amorphous phase. Kalsilite is the first nucleation product but will transform into leucite with the

concurrent development of potassium aluminium oxide. The K_2O losses, the transformation of kalsilite to leucite and the formation of potassium aluminium oxide are happening simultaneously, with the fracture surface of SWXT® becoming uneven and rough. Finally, K_2O vapours inside the furnace are affecting the performance of SWXT® samples. A combination of XRD and XRF analysis proved that the presence of K_2O vapours inside the furnace delays the development of leucite and potassium aluminium oxide phases and supresses the rate at which glass fibres are losing K_2O.

4.2. Laboratory-produced glass fibres

As described in Chapter 3, glass fibres in the K_2O-Al_2O_3-SiO_2 and the K_2O-ZrO_2-Al_2O_3-SiO_2 systems have been produced via melt processing. Subsequently the investigation of Superwool® XT behaviour in terms of time and temperature, a need for further exploration was created. The idea was to simplify the study of a very complex material like SWXT® by investigating samples with more simple chemistry but with common – according to the phase diagrams – crystalline phases. These experiments aimed to build an understanding of the stability of leucite and potassium aluminium silicate crystalline phases in terms of time and temperature.

4.2.1. Heat treatment experiments

As described in Chapter 3, all the melt-rig samples were heat treated at 1250°C for various periods (Table 4.15Table 4.15: Heat treatment conditions for melt-rig samples using new furnace arrangement at 1250°C.). In all these heat treatment experiments the new furnace arrangement was used and the same thermal conditions.

Table 4.15: Heat treatment conditions for melt-rig samples using new furnace arrangement at 1250°C.

Sample	Heat Treatment Time							
	1min	5min	15min	30min	1h	24h	500h	1000h
KAS-1	✓	✓	✓	✓	✓ †	✓	✓	✓
KAS-2		✓	✓		✓	✓		
KAS-3		✓	✓	✓	✓	✓	✓	✓
KAS-4		✓	✓	✓	✓	✓	✓	✓
KAS-5		✓	✓	✓	✓	✓	✓	✓
KAS-8							✓	✓
KAS-9							✓	✓
KASZ-1							✓	✓
KASZ-2							✓	✓

4.2.2. Chemical characterization

XRF analysis has been carried out to study the compositional variations of melt-rig samples compared to target compositions and to heat treated samples. Apart from KAS-6 and KAS-7 samples that have a significant difference compared to the respective target compositions, all the other glass compositions have been successfully produced with minor variations (Table 4.16 and Table 4.17).

Table 4.16: XRF analysis (wt% with ±1% relative error) of glass fibre compositions of K_2O-ZrO_2-Al_2O_3-SiO_2 quaternary system.

		Target Content (wt%)	Content by XRF (wt%)	Variation (wt%)	Content by XRF (mol%)
KASZ-1	**Al_2O_3**	36.1	34.8	-1.3	28.2
	SiO_2	30.9	32.1	+1.2	44.2
	K_2O	26.0	25.7	-0.3	22.6
	ZrO_2	7.0	7.4	+0.4	5.0
	Total	100.0	100.0		100.0
KASZ-2	**Al_2O_3**	41.6	41.8	+0.2	33.2
	SiO_2	37.3	37.3	+0.0	50.3
	K_2O	13.9	13.8	-0.1	11.9
	ZrO_2	7.2	7.1	-0.1	4.7
	Total	100.0	100.0		100.0

† Additional heat treatments at 850°C and 950°C.

Table 4.17: XRF analysis (wt% with ±1% relative error) of glass fibre compositions of K_2O-Al_2O_3-SiO_2 ternary system.

		Target Content (wt%)	Content by XRF (wt%)	Variation (wt%)	Content by XRF (mol%)
KAS-1	**Al_2O_3**	23.4	22.4	-0.96	15.8
	SiO_2	55.1	57.6	+2.54	68.9
	K_2O	21.6	20.0	-1.58	15.3
	Total	100.0	100.0		100.0
KAS-2	**Al_2O_3**	24.0	23.9	-0.10	17.1
	SiO_2	53.0	54.6	+1.60	66.3
	K_2O	23.0	21.5	-1.50	16.6
	Total	100.0	100.0		100.0
KAS-3	**Al_2O_3**	27.0	26.4	-0.6	19.4
	SiO_2	48.2	49.4	+1.2	61.4
	K_2O	24.8	24.2	-0.6	19.2
	Total	100.0	100.0		100.0
KAS-4	**Al_2O_3**	29.0	28.4	-0.6	21.3
	SiO_2	43.5	45.1	+1.6	57.3
	K_2O	27.5	26.5	-1.0	21.5
	Total	100.0	100.0		100.0
KAS-5	**Al_2O_3**	32.2	33.0	-0.6	25.5
	SiO_2	38.0	38.9	+1.6	51.0
	K_2O	29.8	28.1	-1.0	23.5
	Total	100.0	100.0		100.0
KAS-6	**Al_2O_3**	37.7	33.3	-4.4	25.8
	SiO_2	34.9	38.3	+3.4	50.4
	K_2O	27.4	28.4	+1.0	23.8
	Total	100.0	100.0		100.0
KAS-7	**Al_2O_3**	42.8	35.8	-7.0	27.3
	SiO_2	36.6	42.0	+5.4	54.4
	K_2O	20.6	22.2	+1.6	18.3
	Total	100.0	100.0		100.0
KAS-8	**Al_2O_3**	38.8	37.4	-1.4	29.3
	SiO_2	33.2	34.7	+1.5	46.6
	K_2O	28.0	27.9	-0.1	23.9
	Total	100.0	100.0		100.0
KAS-9	**Al_2O_3**	45.8	45.7	-0.1	35.4
	SiO_2	39.1	39.8	+0.7	52.4
	K_2O	15.1	14.5	-0.6	12.2
	Total	100.0	100.0		100.0

As depicted in the ternary phase diagram (Figure 4.40), the idea was to create five compositions (KAS-1 to KAS-5) from leucite to kalsilite that will result – upon firing – in single-phase and multi-phase glass fibre materials of both phases. KAS-8 is the normalized SWXT® composition by considering only these three compounds and KAS-9 is, according to the company's internal documentation, the normalized heat treated SWXT® (1250°C, 7450 hours) composition by considering again only these three compounds. Finally, only thermal analysis was conducted on KAS-6 and KAS-7 as the great variation from the target compositions put them out of the area of interest of this study.

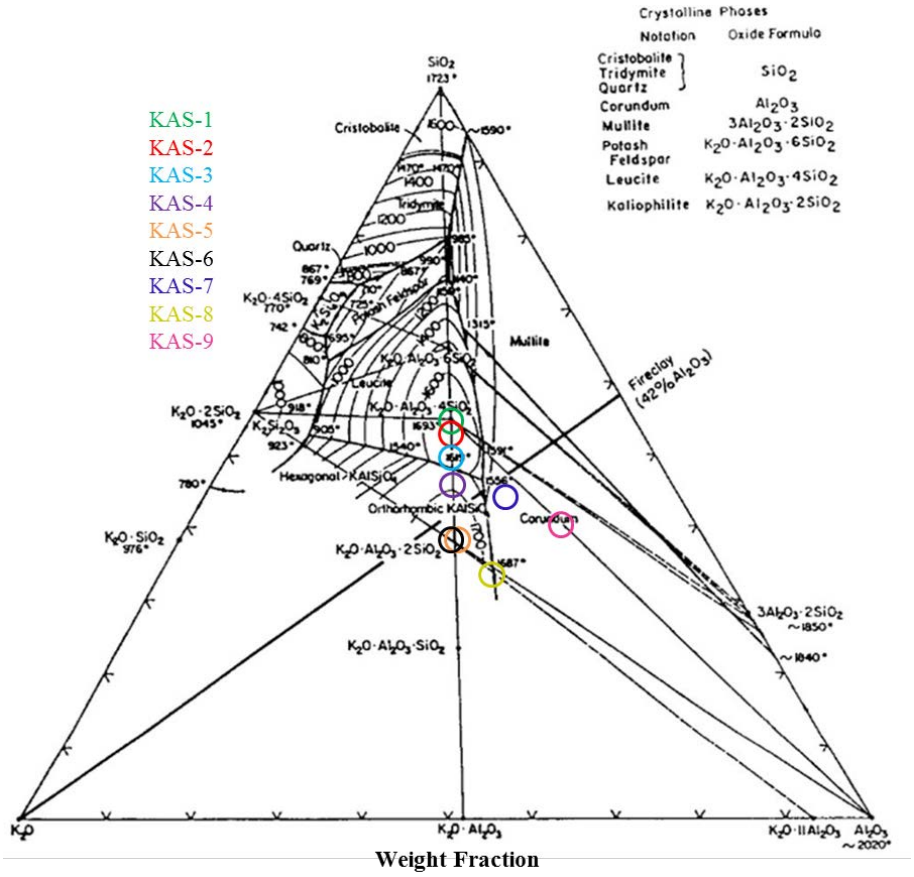

Figure 4.40: The ternary K_2O-Al_2O_3-SiO_2 diagram showing the produced glass fibre compositions. Image modified from Osborn and Muan (1960).

Likewise, the compositions of KASZ-1 and KASZ-2 are based on KAS-8 and KAS-9 respectively. The idea was to add the same weight percentage of ZrO_2 as is contained in

SWXT® and then examine the effect of this addition on the crystallization evolution and chemical stability of glass fibres. The addition of ZrO_2 is expected to decelerate nucleation and crystal growth (Seidel et al., 2016). As listed in Table 4.18 chemical stability is strongly connected with the starting composition. KAS-1, KA-9 and KASZ-2 are the only compositions where all the elements remain stable in terms of firing time. The remaining materials have a similar behaviour with SWXT®; as time passes K_2O loss increases. Samples KAS-8 and KASZ-1 have a difference in K_2O loss probably related to ZrO_2 addition.

Table 4.18: XRF analysis (wt% with ±1% relative error) of heat treated glass fibres at 1250°C for 500 and 1000 hours.

	Heat Treatment Time (h)	**Al_2O_3 (wt%)**	**K_2O (wt%)**	**SiO_2 (wt%)**	**ZrO_2 (wt%)**	**Total (wt%)**	**K_2O Change (wt%)**
KAS-1	0	22.4	20.0	57.6	0.0	100.0	
	500	22.4	20.0	57.6	0.0	100.0	0.0
	1000	22.4	20.0	57.6	0.0	100.0	0.0
KAS-3	0	26.4	24.2	49.4	0.0	100.0	
	500	26.8	23.0	50.2	0.0	100.0	-1.2
	1000	26.9	22.7	50.4	0.0	100.0	-1.5
KAS-4	0	28.4	26.5	45.1	0.0	100.0	
	500	29.0	24.7	46.3	0.0	100.0	-1.8
	1000	29.7	22.8	47.5	0.0	100.0	-3.6
KAS-5	0	33.0	28.1	38.9	0.0	100.0	
	500	33.3	27.1	39.6	0.0	100.0	-1.0
	1000	34.1	25.4	40.5	0.0	100.0	-2.7
KAS-8	0	37.4	27.9	37.4	0.0	100.0	
	500	38.5	25.7	35.8	0.0	100.0	-2.2
	1000	38.8	25.0	36.2	0.0	100.0	-2.9
KAS-9	0	45.7	14.5	39.8	0.0	100.0	
	500	44.6	14.8	40.6	0.0	100.0	+0.3
	1000	45.1	14.4	40.5	0.0	100.0	-0.1
KASZ-1	0	34.8	25.7	32.1	7.4	100.0	
	500	35.5	23.9	32.9	7.7	100.0	-1.7
	1000	36.3	22.2	33.7	7.8	100.0	-3.5
KASZ-2	0	41.8	13.8	37.3	7.1	100.0	
	500	41.0	14.0	38.0	7.1	100.0	+0.2
	1000	41.4	13.8	37.7	7.1	100.0	0.0

4.2.3. Structural characterization

Figure 4.41 and Figure 4.42 show the crystallization behaviour of KAS-1 and KAS-2 as a function of time at 1250°C. All peaks are matched by tetragonal leucite and no second phase peaks were observed which suggests that this crystalline phase is very stable in terms of time. Crystallization of leucite occurs very rapidly, in less than 5 minutes for KAS-1 and less than 15 minutes for KAS-2.

Figure 4.43 shows the crystallization behaviour of KAS-1 as a function of temperature for 1 hour of heat treatment. At 850°C kalsilite peaks are stronger compared to those of leucite. At higher temperature (950°C) the proportion of leucite increases and kalsilite is still present. At even more elevated temperatures (1250°C), kalsilite is not detectable and leucite is the sole crystalline phase.

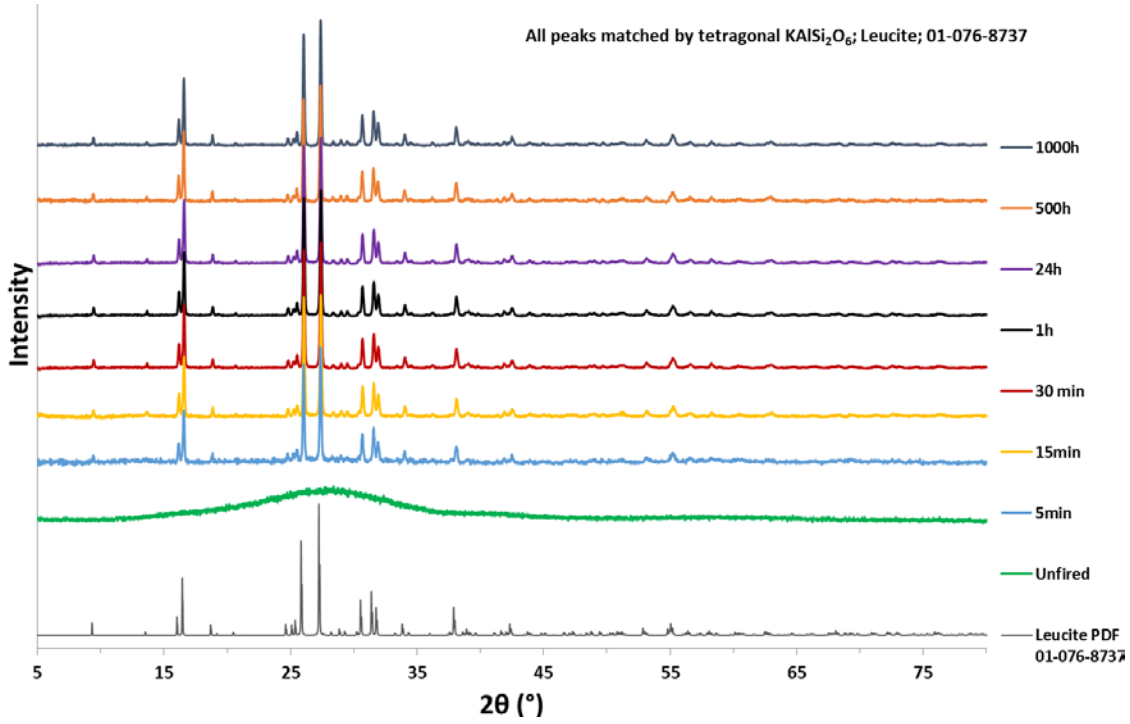

Figure 4.41: XRD patterns of heat treated KAS-1 glass fibres at 1250°C as a function of time.

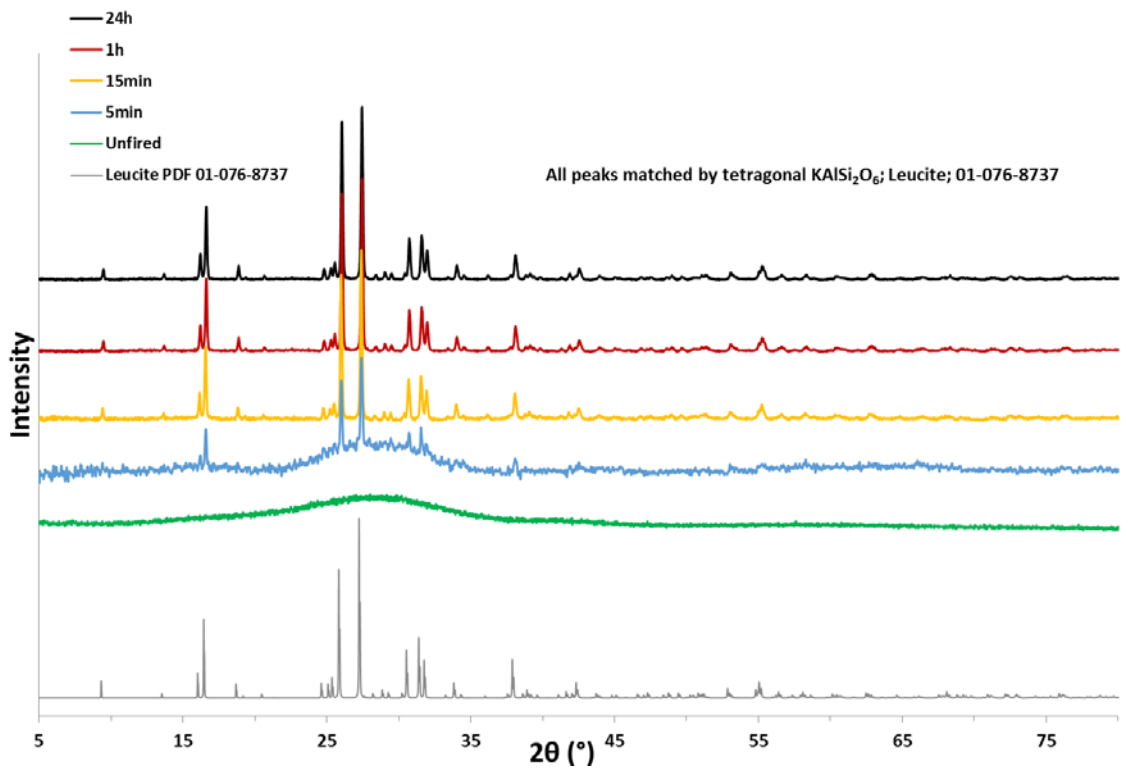

Figure 4.42: XRD patterns of heat treated KAS-2 glass fibres at 1250°C as a function of time.

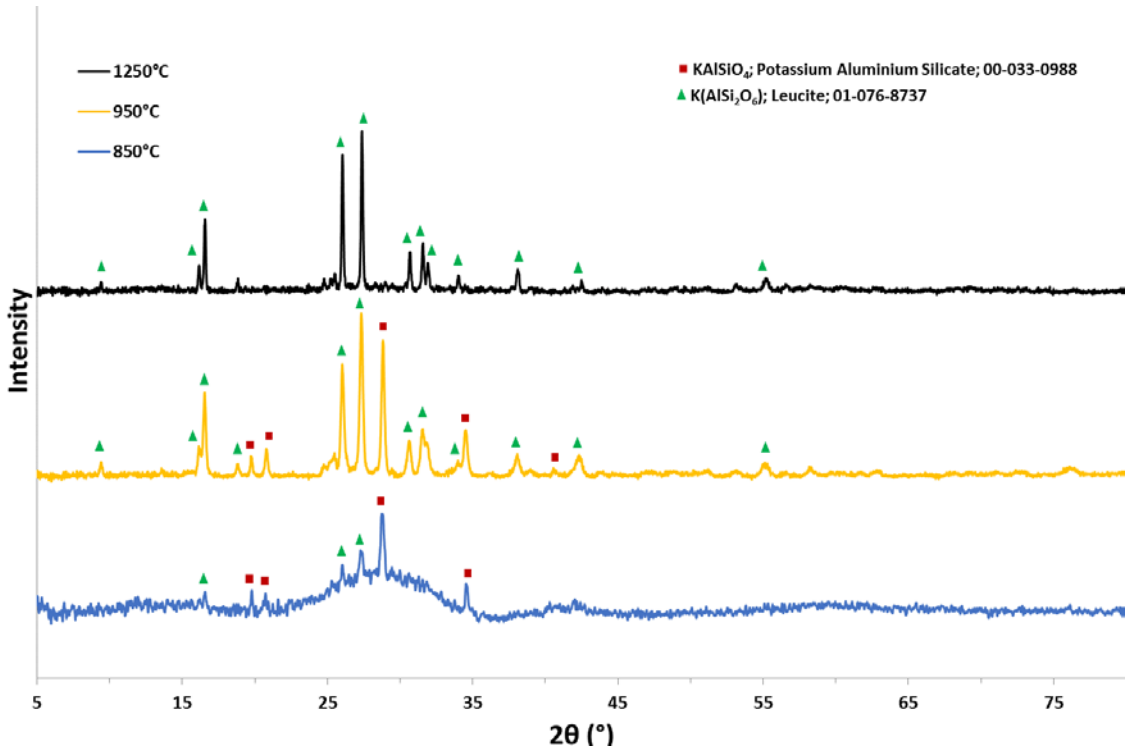

Figure 4.43: XRD patterns of heat treated KAS-1 glass fibres for 1 hour as a function of temperature.

As shown in Figure 4.44 for KAS-3, peaks are matched by kalsilite and leucite. Both phases seem to develop simultaneously but the crystallization process takes longer (< 30 min) compared to the previous samples.

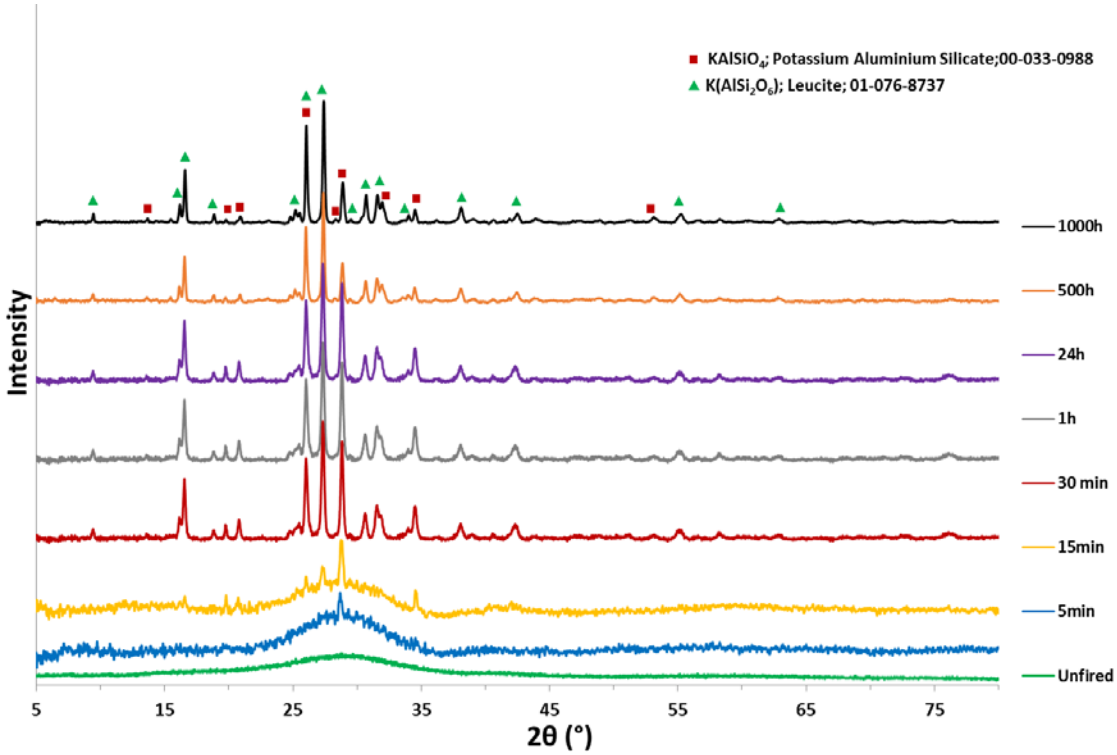

Figure 4.44: XRD patterns of heat treated KAS-3 glass fibres at 1250°C as a function of time.

For KAS-4, Figure 4.45 illustrates that at the beginning of the crystallization most of the peaks are matched by kalsilite. After 24 hours of constant heat treatment at 1250°C tetragonal leucite is fully formed. Moreover, crystallization occurs rapidly in less than 15 minutes.

Figure 4.46 shows XRD patterns of KAS-5, which is closer to kalsilite stoichiometry, heat treated at 1250°C in terms of time. Initially, only kalsilite is present (<15 min) and then at 500 hours of prolonged firing at elevated temperature potassium aluminium oxide and leucite develop.

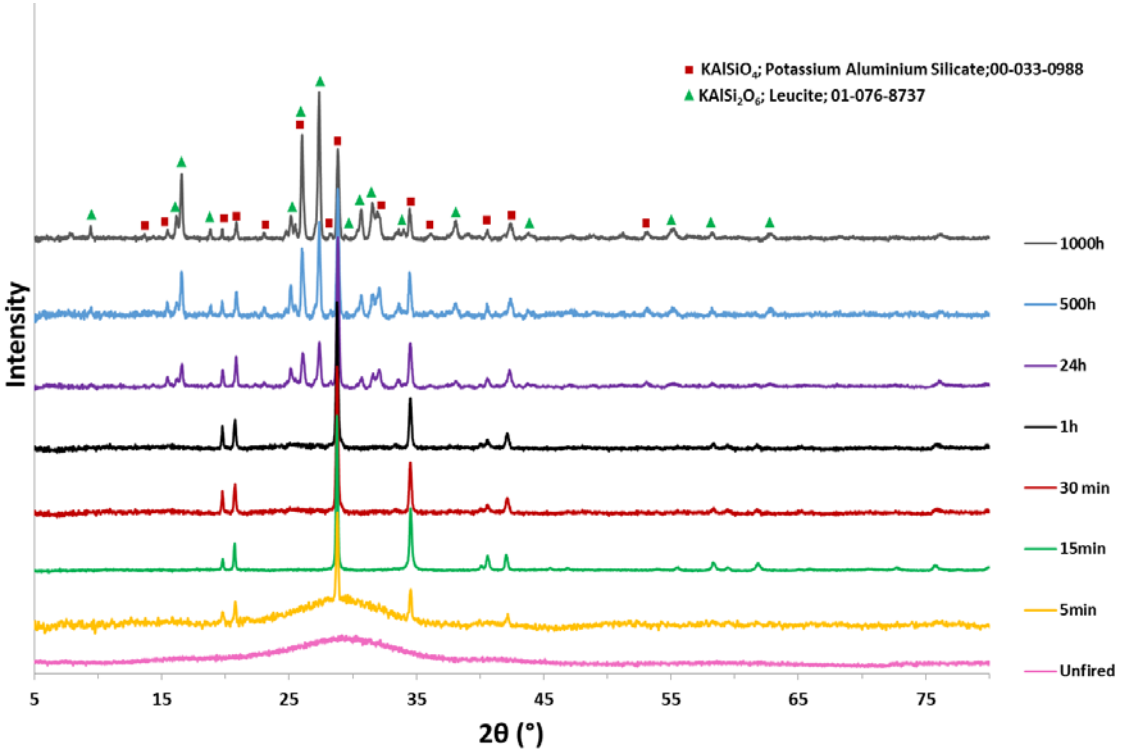

Figure 4.45: XRD patterns of heat treated KAS-4 glass fibres at 1250°C as a function of time.

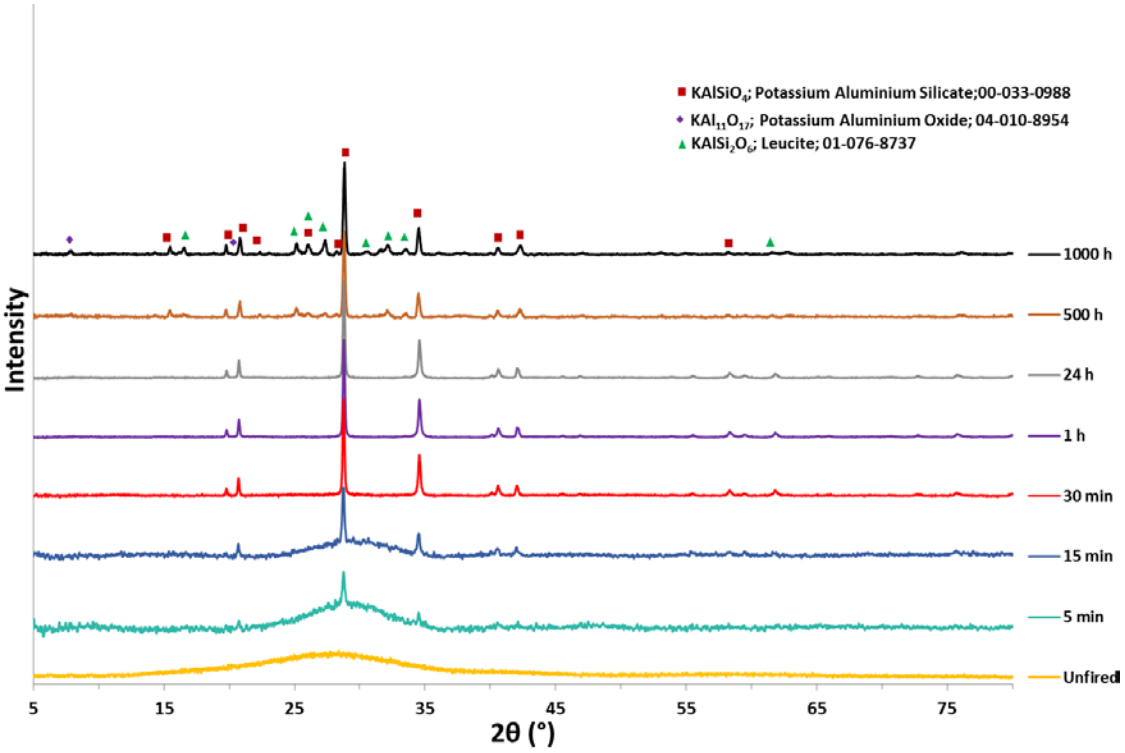

Figure 4.46: XRD patterns of heat treated KAS-5 glass fibres at 1250°C as a function of time.

Figure 4.47 and Figure 4.48 show XRD patterns for KAS-8 and KASZ-1, respectively, which are the melt-rig glass fibres with compositions as close as possible to SWXT®. KAS-8 peaks are matched by kalsilite, leucite and potassium aluminium oxide phase. Regarding the XRD patterns of KASZ-1, the only difference with KAS-8 is the formation of tetragonal zirconium oxide phase.

Figure 4.49 and Figure 4.50 demonstrate the crystallization behaviour of KAS-9 and KASZ-2, respectively, at 1250°C. No second phases are observed for KAS-9 and all peaks are matched by tetragonal leucite. Apart from leucite, tetragonal zirconium oxide is also present for KASZ-2.

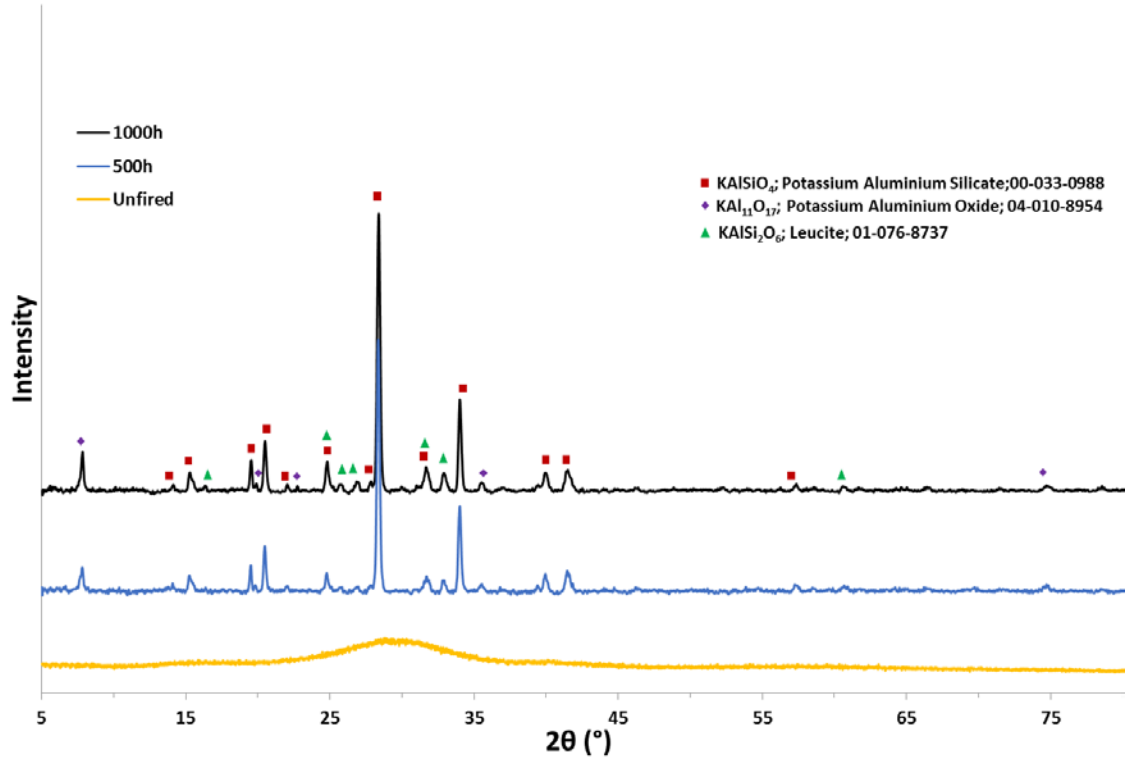

Figure 4.47: XRD patterns of heat treated KAS-8 glass fibres at 1250°C as a function of time.

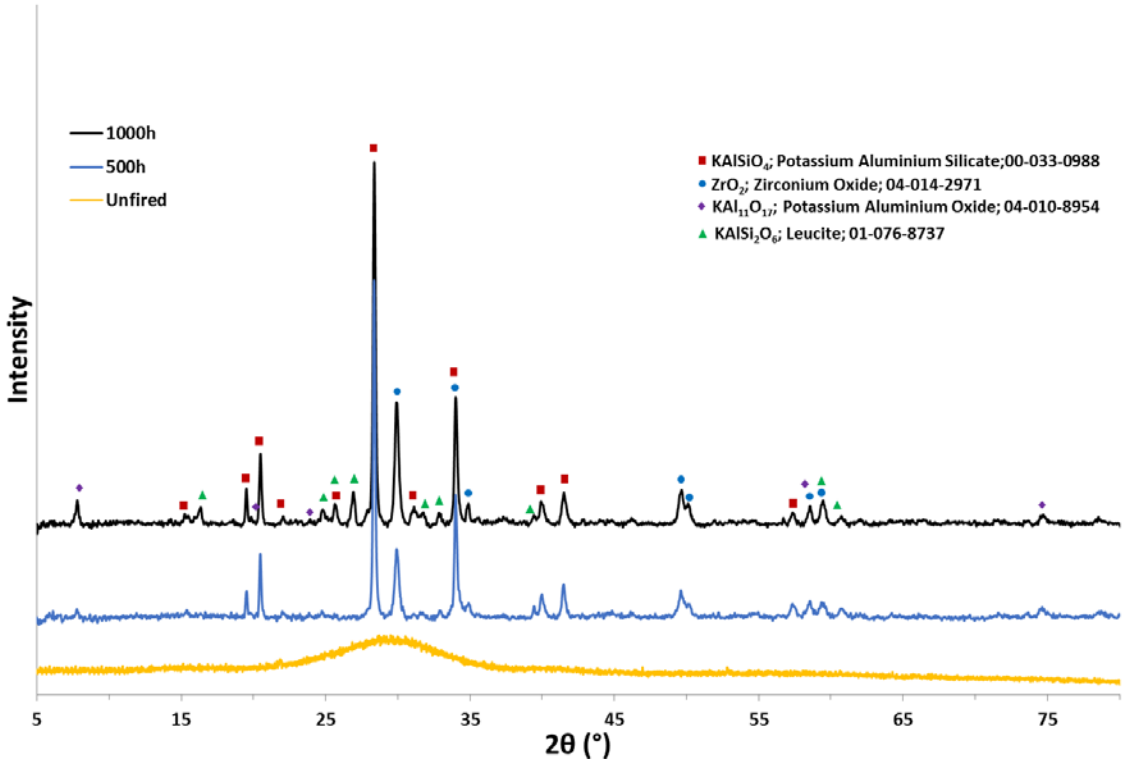

Figure 4.48: XRD patterns of heat treated KASZ-1 glass fibres at 1250°C as a function of time.

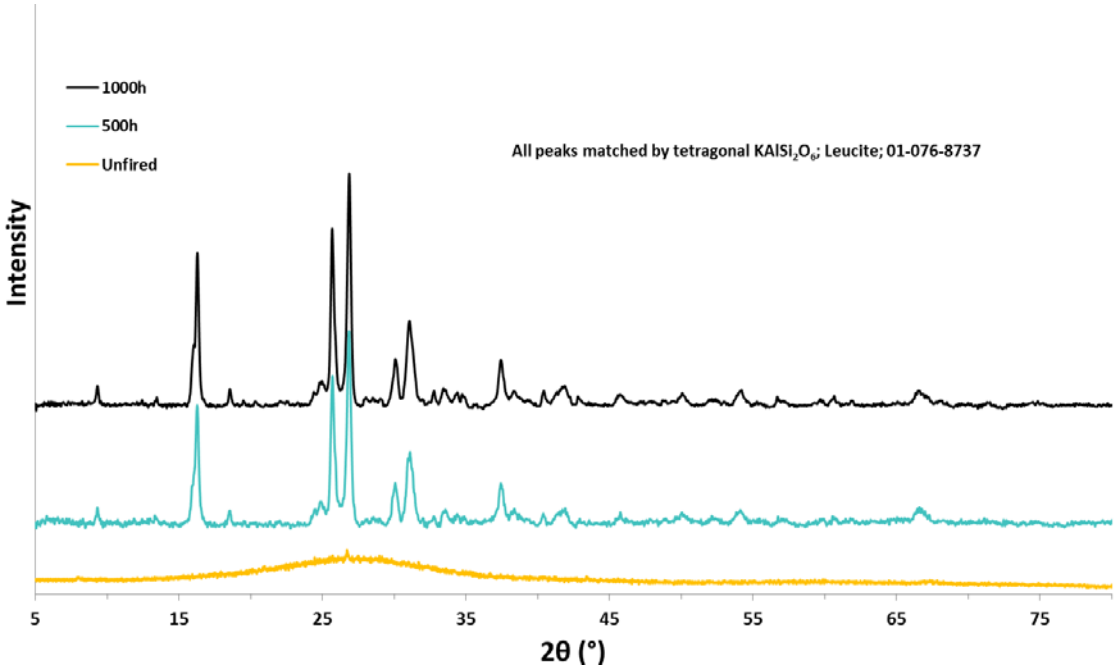

Figure 4.49: XRD patterns of heat treated KAS-9 glass fibres at 1250°C as a function of time.

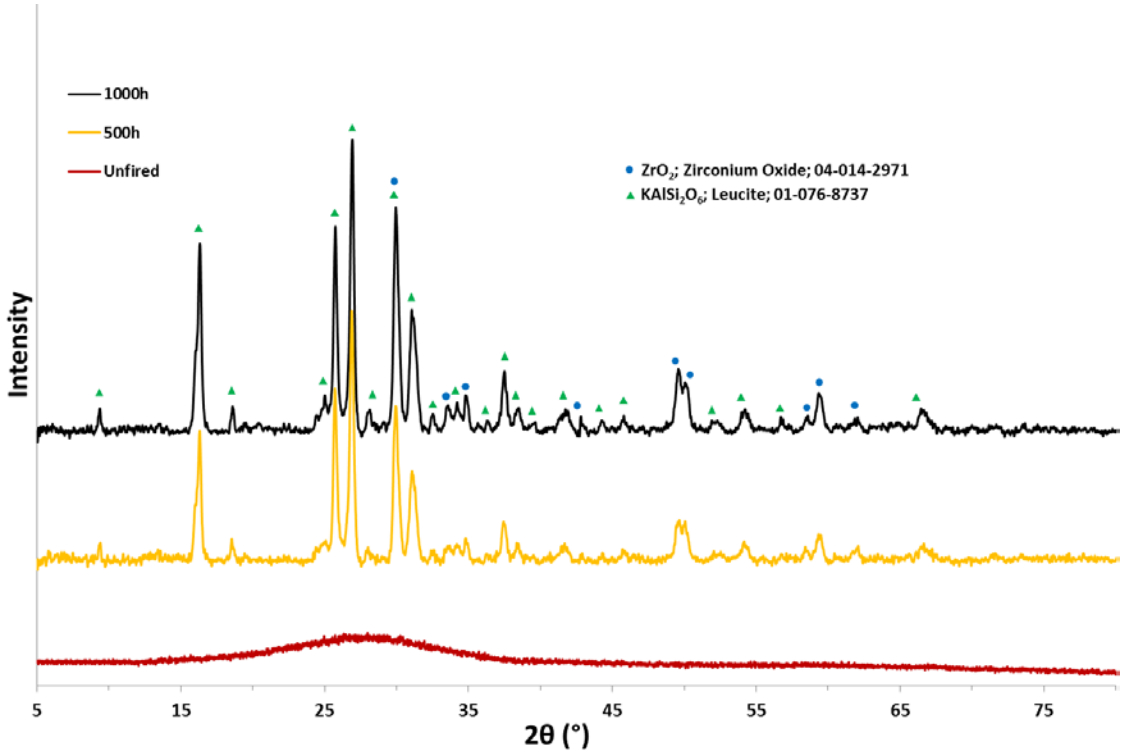

Figure 4.50: XRD patterns of heat treated KASZ-2 glass fibres at 1250°C as a function of time.

Raman spectroscopy was used to locally characterize the structure of the five melt-rig compositions. Raman spectra (Figure 4.51) of unfired melt-rig glass fibres (KAS-1 to KAS-5) show the presence of three sets of bands which are located in the ranges of about 400-500 cm^{-1}, 550-570 cm^{-1}, and 950-1150 cm^{-1}. The large width of these bands confirms the high presence of amorphous phase in the examined materials. A peak around 1020 cm^{-1} which is present for KAS-5 and KAS-4 and is more prominent for KAS-3 is due to impurities of the materials and more specifically carbon (Ferrari & Robertson, 2000). Glasses with high K_2O content have the tendency to react with the atmosphere and form K_2CO_3.

Figure 4.52 shows the effect of heat treatment on the melt-rig samples which have now sharper bands confirming the existence of crystalline phases. All samples were fired at 1250°C for 24 hours before being tested. KAS-1, KAS-2, and KAS-3 have Raman spectra corresponding to leucite. Moreover, some modes are labelled as 1 to 7 because at this stage their origin is purely speculative. They are in the ranges of about 240-260 cm^{-1} (1), 275-325 cm^{-1} (2), 350-370 cm^{-1} (3), 380-400 cm^{-1} (4), 450-470 cm^{-1} (5), 900-950 cm^{-1} (6), 1000-1050 cm^{-1} (7) and 1070-1120 cm^{-1} (8).

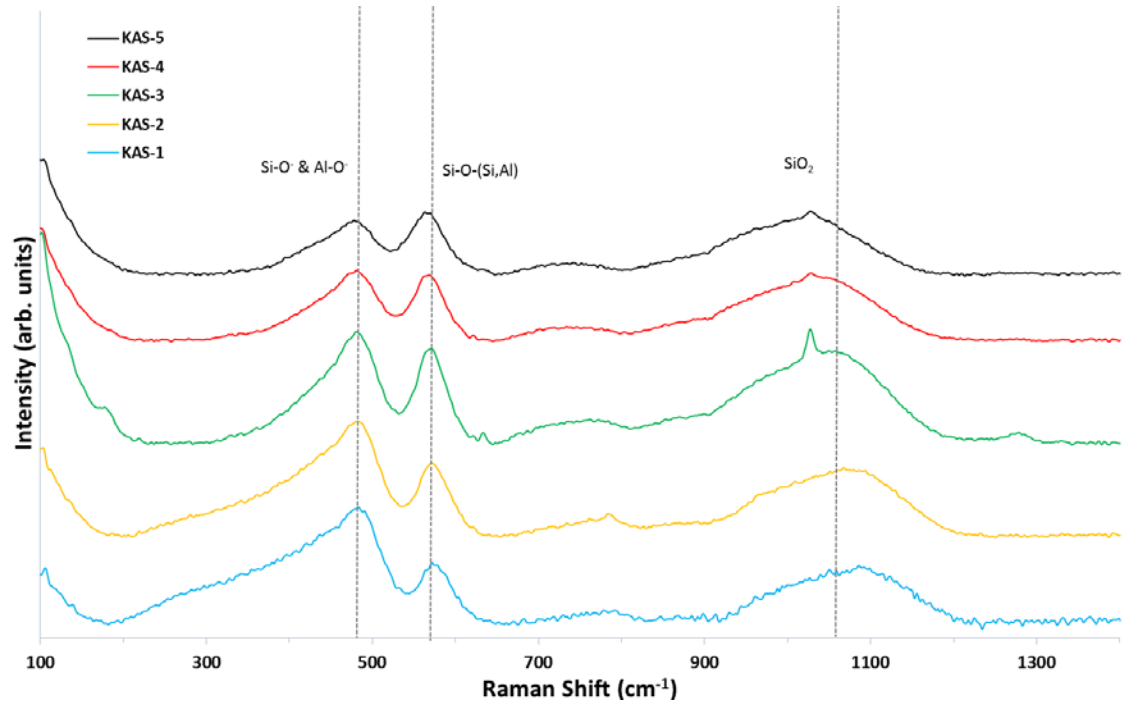

Figure 4.51: Raman spectra of unfired glass fibres.

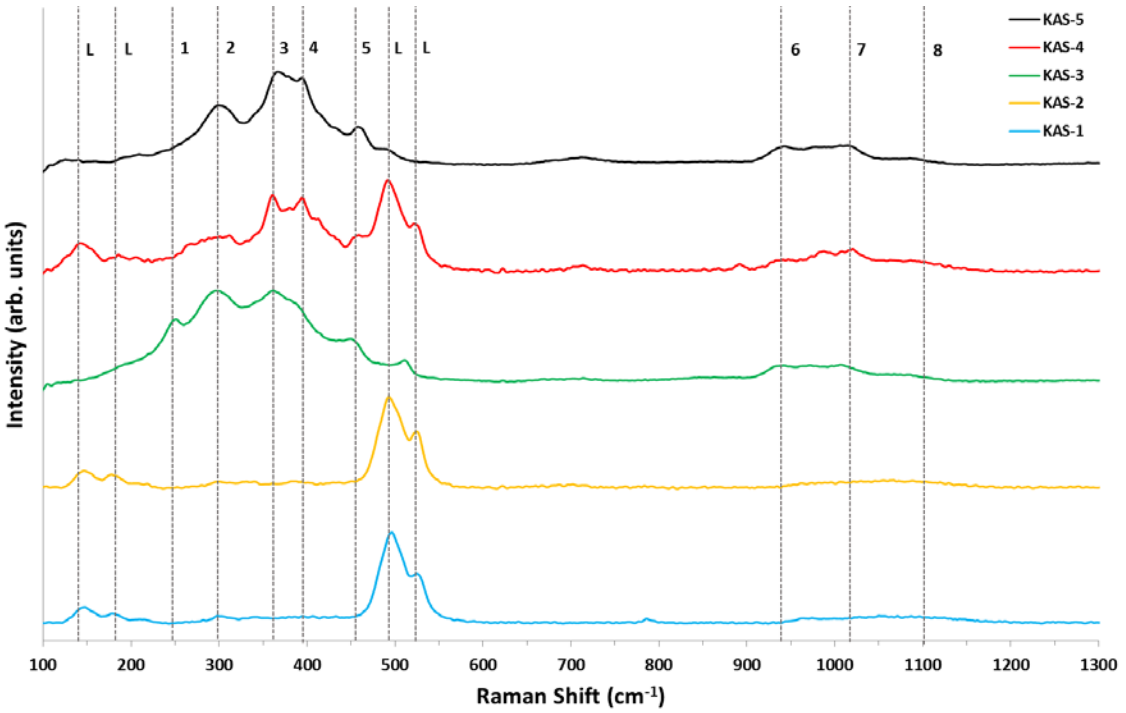

Figure 4.52: Raman spectra of heat treated glass fibres at 1250°C for 24 hours.

4.2.4. Thermal analysis

Differential thermal analysis was employed to explore the crystallization behaviour of unfired melt-rig samples and to understand the effect of altering the content of K_2O, Al_2O_3 and SiO_2 on the thermal behaviour. Figure 4.53 and Figure 4.54 present the DTA patterns gathered at a 5°C/min heating rate.

As depicted in Figure 4.53, DTA patterns show one strong exothermic peak related to the main crystallization event. The main exothermic peak for KAS-1, KAS-2 and KAS-3 relates to the development of leucite. In these three patterns, a strong anomaly is observed just before the first crystallization event which may relate to an endothermic event, probably a rearrangement of the structure of the amorphous phase. Also, moving from KAS-1 to KAS-3 the first crystallization exotherm moves to higher temperatures contrary to the kalsilite glass ceramics, KAS-4 to KAS-7 where it moves to lower temperatures. In KAS-4 a second shallow feature peak appears to exist at around 1183°C which relates to the formation of leucite as a second phase.

Additionally, Figure 4.54 illustrates that both KAS-8 and KASZ-1 have a main crystallization peak that is associated with kalsilite development. As it is expected the addition of ZrO_2 hinders the formation of $KAlSiO_4$ so the first exothermic moves to higher temperature.

At around 993°C (KAS-9) and 965°C (KASZ-2) a strong exothermic peak is visible which is related with kalsilite. A second crystallization peak at 1293°C and 1280°C, respectively that relates to the leucite development and again an anomaly is observed before this peak. Similarly, the addition of zirconia moves the crystallization exotherm to higher temperatures.

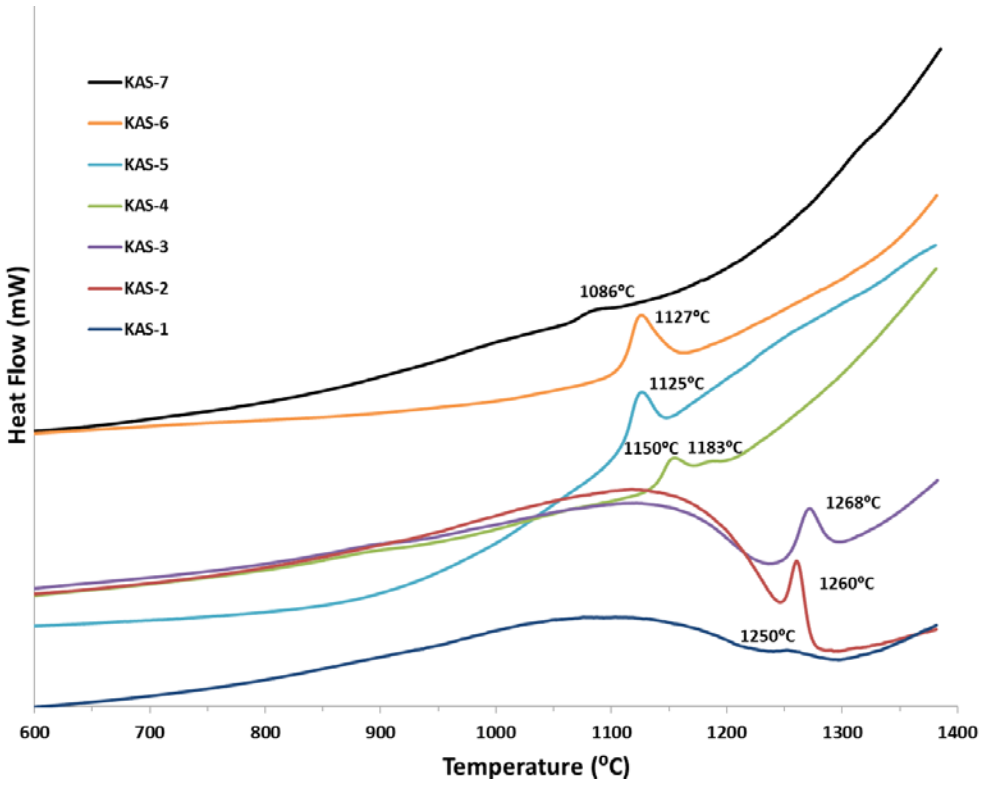

Figure 4.53: DTA curves of unfired K_2O-Al_2O_3-SiO_3 glass fibres (100mg) with a 5°C/min heating rate.

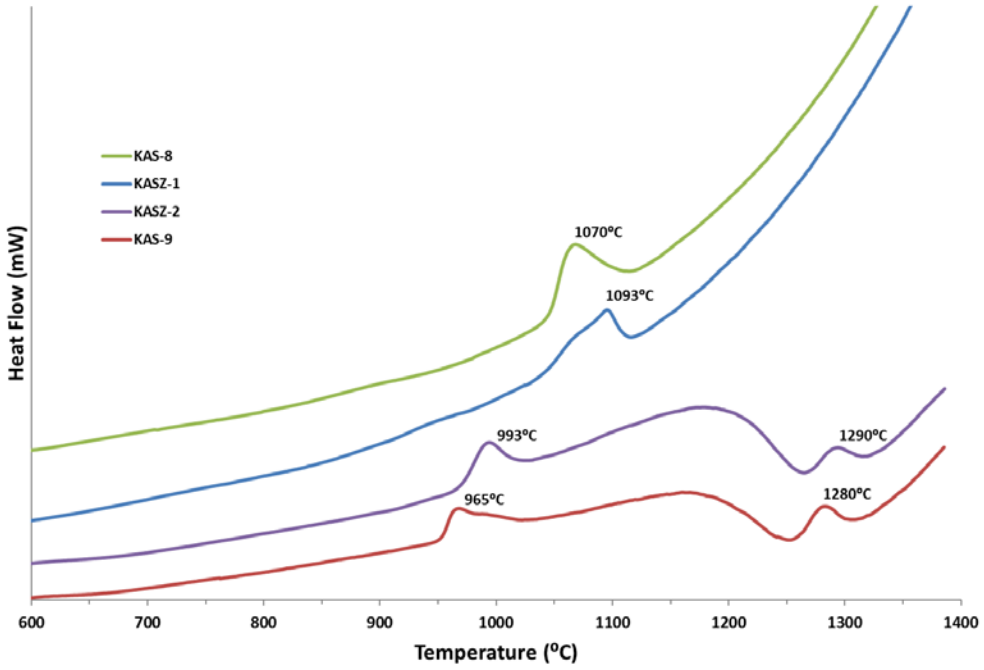

Figure 4.54: DTA curves of unfired K_2O-ZrO_2-Al_2O_3-SiO_3 and K_2O-Al_2O_3-SiO_3 glass fibres (100mg) with a 5°C/min heating rate.

4.2.5. Summary

Systematic synthesis experiments to produce glass fibres in the ternary K_2O-Al_2O_3-SiO_2 and the quaternary K_2O-ZrO_2-Al_2O_3-SiO_2 systems were conducted. Heat treatment experiments resulted in multiphase and single-phase reaction products in the kalsilite-leucite region. Elemental analysis (XRF) revealed that the high volatility of K_2O is related to the stoichiometry of the starting composition and crystallization behaviour as in some samples in which leucite is the major phase (SiO_2-rich and Al_2O_3-rich samples) no loss is observed. Moreover, XRD analysis suggests that kalsilite is an unstable phase which probably works as a precursor of leucite as even for samples with the exact kalsilite stoichiometry, leucite will form after prolonged firing. The XRD results suggest that after long-term (> 500 h) heat treatment all the samples will form leucite – at least in part – but the key difference is that when the starting composition is close to kalsilite this transformation will include K_2O losses.

4.3. Commercially produced Cerachem® fibres

All the Cerachem® samples that have been used in this study are heat treated pyro-block modules that customers have send back to Morgan Advanced Materials for testing. As depicted in Figure 4.55, Cerachem® modules were stacked in the wall of a furnace as insulation. These modules had a hot face, which is the inner surface exposed to heat, and a cold face which is the outer surface. Two pyro-block modules were taken from different sides inside the furnace, one from the west wall (module 1) and the other from the east wall (module 2). Unfortunately, the exact temperature and the hours of prolonged firing were not specified.

Figure 4.55: Hot and cold face of Cerachem® modules.

4.3.1. Chemical characterization

Cerachem® samples were chemically characterized to determine the compositional stability of the two samples moving from the hot face to the cold one. To this end, XRF analysis was carried out and the results are presented in Table 4.19 and

Table 4.20. There is a significant reduction in the wt% of silicon dioxide, SiO_2, closer to the hot face. In all the analysed samples, very small amounts of impurities were detected (Fe_2O_3, HfO_2, K_2O, MgO and TiO_2).

Table 4.19: XRF analysis (wt% with ±1% relative error) of module 1 as a function of depth from the hot face.

Compound	Unfired	0-2.5 mm	2.5-5 mm	5-7.5 mm	7.5-10 mm
Al_2O_3	34.8	41.6	35.0	34.7	34.8
SiO_2	49.8	40.7	49.6	49.9	49.9
ZrO_2	15.1	16.8	14.6	14.6	14.6
Fe_2O_3	0.1	0.1	0.1	0.2	0.1
HfO_2	0.0	0.5	0.4	0.4	0.4
MgO	0.1	0.1	0.1	0.1	0.1
TiO_2	0.0	0.1	0.1	0.1	0.1

Table 4.20: XRF analysis (wt% with ±1% relative error) of module 2 as a function of depth from the hot face.

Compound	Unfired	0-2.5 mm	2.5-5 mm	5-7.5 mm	7.5-10 mm
Al_2O_3	34.8	38.6	35.0	34.7	34.7
SiO_2	49.8	44.6	49.4	49.7	49.9
ZrO_2	15.1	15.9	14.8	14.7	14.7
Fe_2O_3	0.1	0.2	0.2	0.2	0.1
HfO_2	0.0	0.4	0.4	0.4	0.4
MgO	0.1	0.1	0.1	0.1	0.1
TiO_2	0.0	0.1	0.1	0.1	0.1

The loss of silica occurs as a function of material depth and is observed as a weight loss as gaseous SiO_2 moves away from the hot face of the module samples. This can involve reduction of SiO_2 to SiO, or with water vapour or stream present they form silicic acid hydrates such as $Si(OH)_4$ or $Si_2O(OH)_6$. The vaporization of SiO_2 increases with increasing H_2 content, with increased free SiO_2, and with increased temperature (Thermal Ceramics, 1995).

As depicted in Figure 4.56, the SiO_2 content decreases closer to the hot face (0-2.5mm) for both Cerachem® samples. Module 1 sample has lost a higher amount of SiO_2 compared with Module 2 but it is likely that the Module 1 sample was in a position inside the furnace that was more affected by temperature and reduction atmospheres which cause the loss of silica – considering the temperature variations inside the furnace.

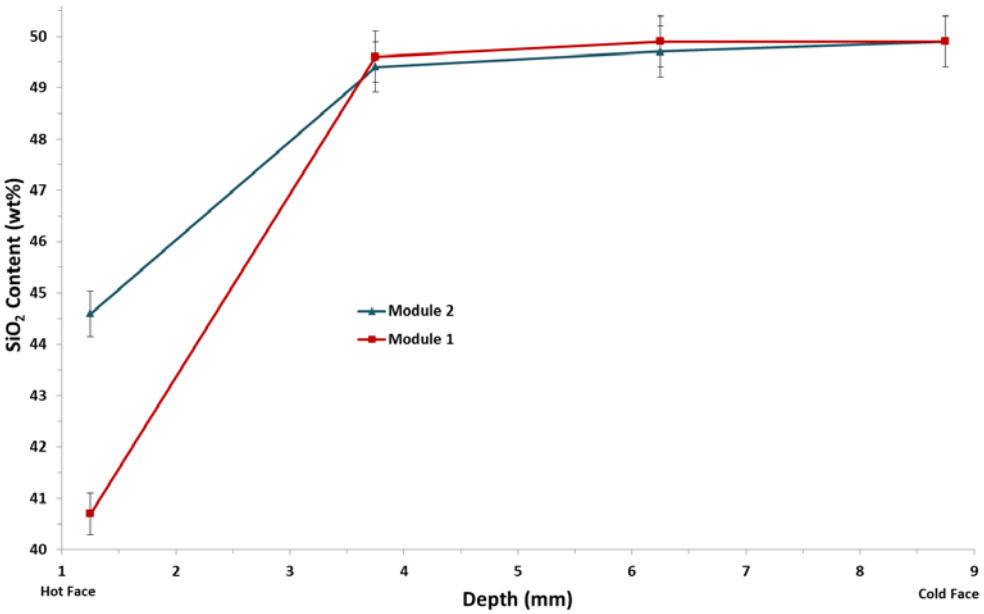

Figure 4.56: Silica content of Cerachem® module 1 and module 2 as a function of depth.

Figure 4.57 and Figure 4.58, apart from the SiO_2 loss, show that the other two main compounds (Al_2O_3 and ZrO_2) will increase in relation to their starting amount. As it has been done in previous cases in this chapter where compositional change is observed all the other compounds have been normalized excluding the silica content and the results are presented in Table 4.21 and Table 4.22.

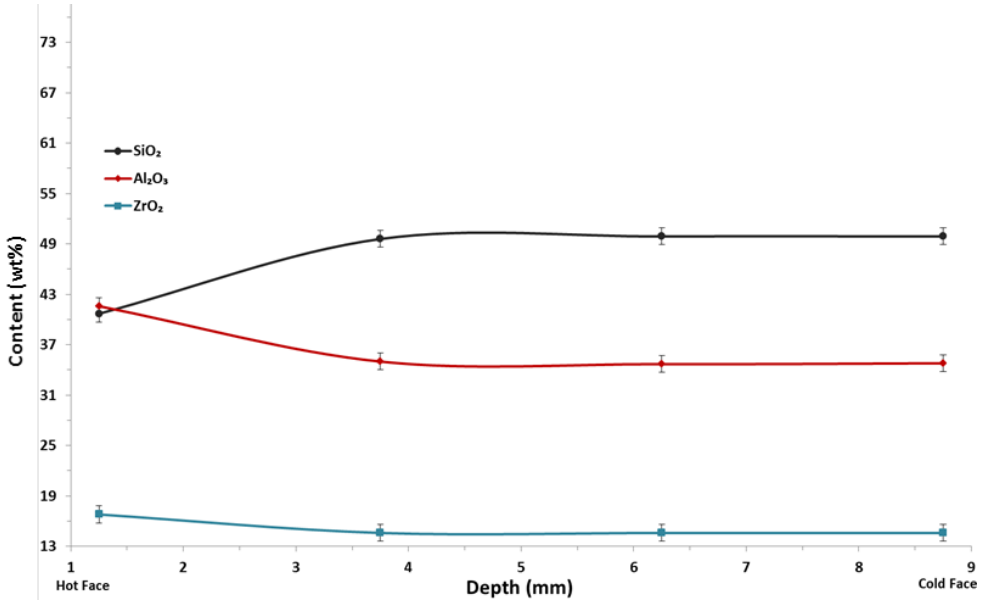

Figure 4.57: SiO_2, Al_2O_3, and K_2O contents of Cerachem® module 1 as a function of depth.

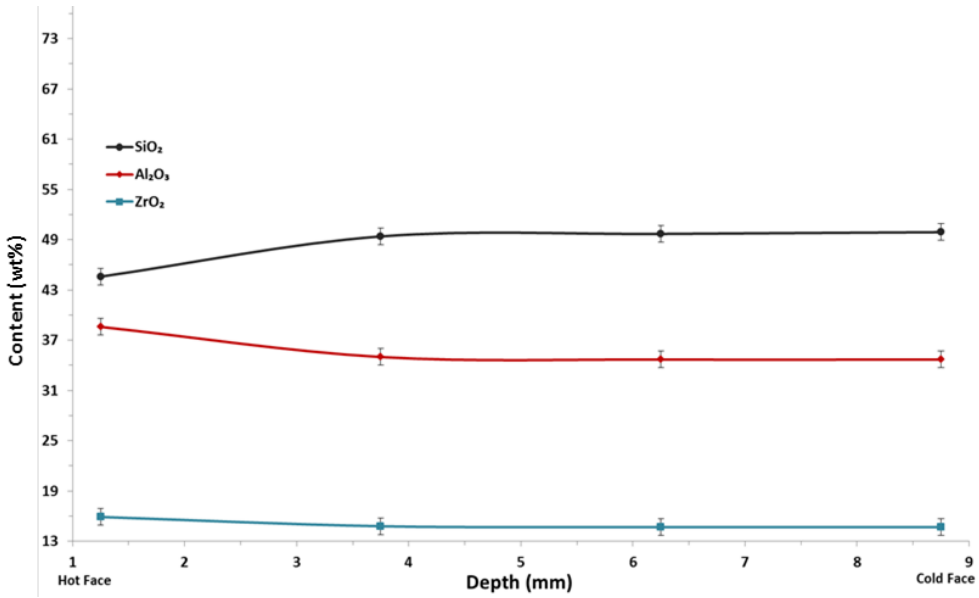

Figure 4.58: SiO_2, Al_2O_3, and K_2O contents of Cerachem® module 2 as a function of depth.

As shown in the tables below (Table 4.21 and Table 4.22), if the volatilization of silica is taken into account, the weight% of all other compounds remains fairly constant as a function of depth. This result confirms the starting hypothesis that silica loss is occurring in the hot face of both modules.

Table 4.21: Normalized XRF results (wt% with ±1% relative error) of module 1, excluding the wt% of silica.

Compound	Unfired	0-2.5 mm	2.5-5 mm	5-7.5 mm	7.5-10 mm
Al_2O_3	69.3	70.3	69.5	69.4	69.5
ZrO_2	30.2	28.3	29	29.1	29.1
Fe_2O_3	0.3	0.2	0.3	0.3	0.2
HfO_2	0	0.8	0.8	0.8	0.8
MgO	0.2	0.2	0.2	0.2	0.2
TiO_2	0	0.2	0.2	0.2	0.2

Table 4.22: Normalized XRF results (wt% with ±1% relative error) of module 2, excluding the wt% of silica.

Compound	Unfired	0-2.5 mm	2.5-5 mm	5-7.5 mm	7.5-10 mm
Al_2O_3	69.3	69.7	69.1	69.2	69.2
ZrO_2	30.2	28.8	29.2	29.3	29.3
Fe_2O_3	0.3	0.3	0.4	0.3	0.2
HfO_2	0	0.8	0.8	0.8	0.8
MgO	0.2	0.2	0.2	0.2	0.2
TiO_2	0	0.2	0.2	0.2	0.2

4.3.2. Structural characterization

To investigate the crystal structure of Cerachem® modules, X-ray diffraction patterns were measured for various depths. As illustrated in Figure 4.59 and Figure 4.60, the major crystalline phase detected is orthorhombic mullite with the chemical formula $Al_{4.54}O_{9.73}Si_{1.46}$ (ICDD 01-079-1456) (Ban & Okada, 1992); other crystalline phases detected is tetragonal cristobalite (ICDD 01-082-0512) with the chemical formula SiO_2 (Lacks & Gordon, 1993) and two tetragonal zirconium oxide phases with the chemical formula ZrO_2, one stable (ICDD 01-079-1771) (Bondars et al., 1995) and one unstable (ICDD 01-078-0047) (Igawa & Ishii, 2001). The presence of the latter is more evident at the hot face.

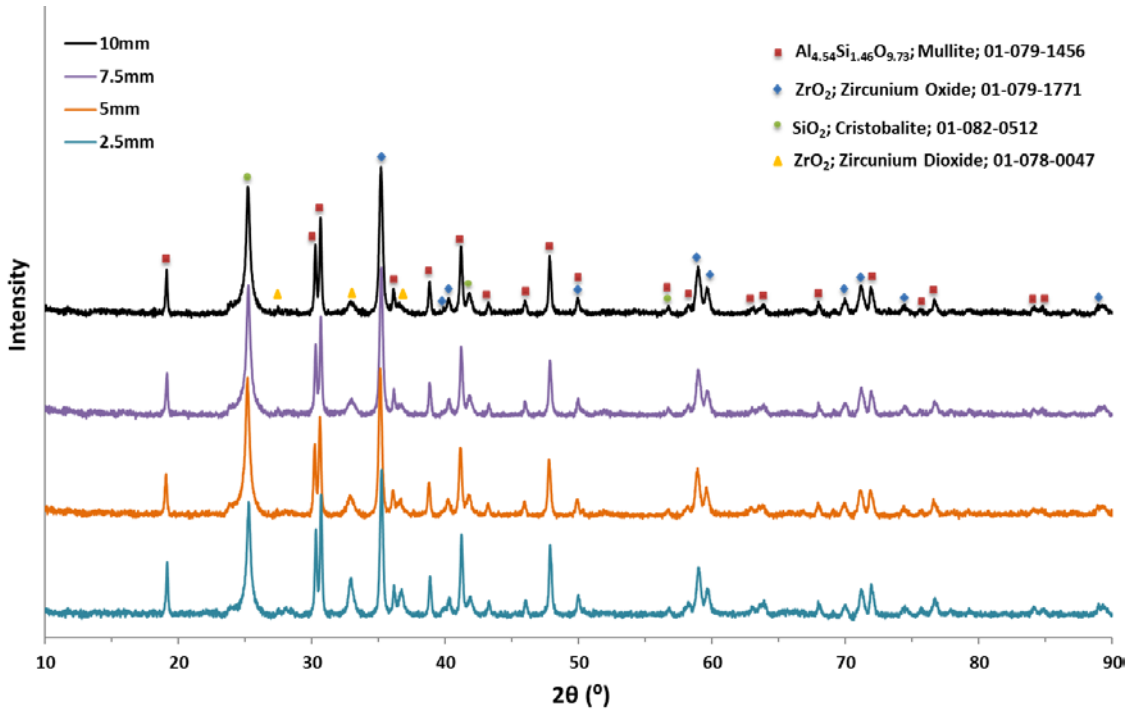

Figure 4.59: XRD patterns from Cerachem®, module 1 showing the crystallization as a function of depth.

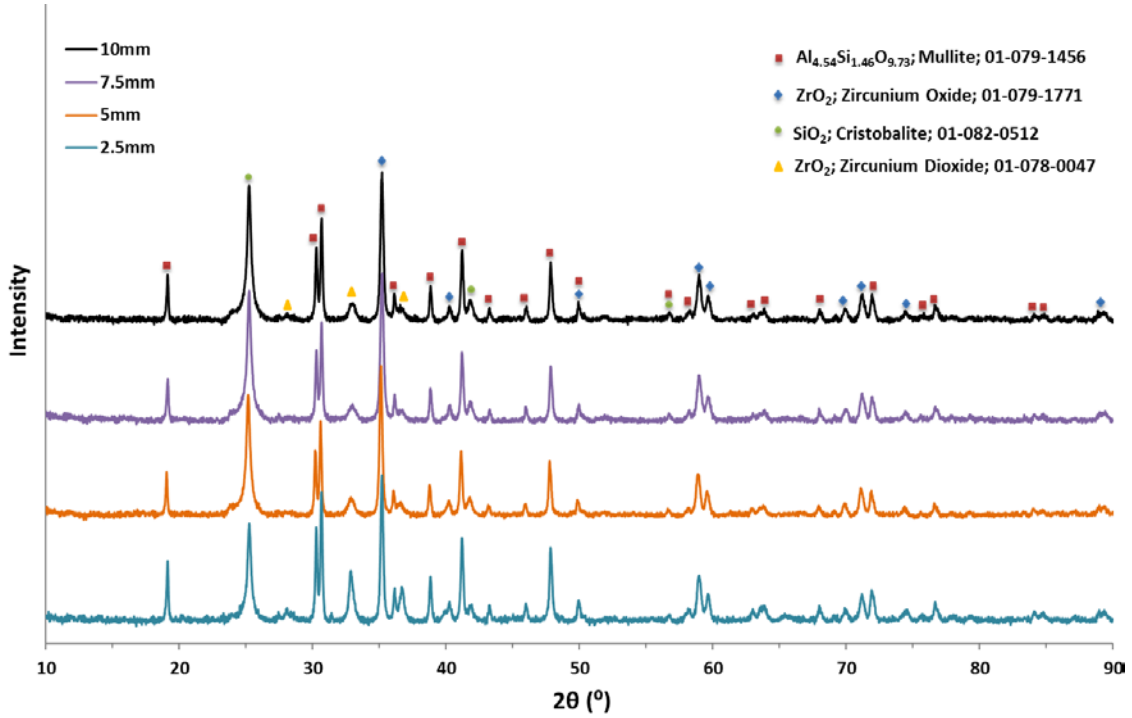

Figure 4.60: XRD patterns from Cerachem®, module 2 showing the crystallization as a function of depth.

The surface morphology of Cerachem® samples has been examined by SEM. Figure 4.61 and Figure 4.62 show secondary SEM imaging of the two modules. The outside surfaces of the fibres have an almost featureless and smooth appearance. Throughout the fibre cross-section a rougher fracture surface indicates that crystallization has taken place.

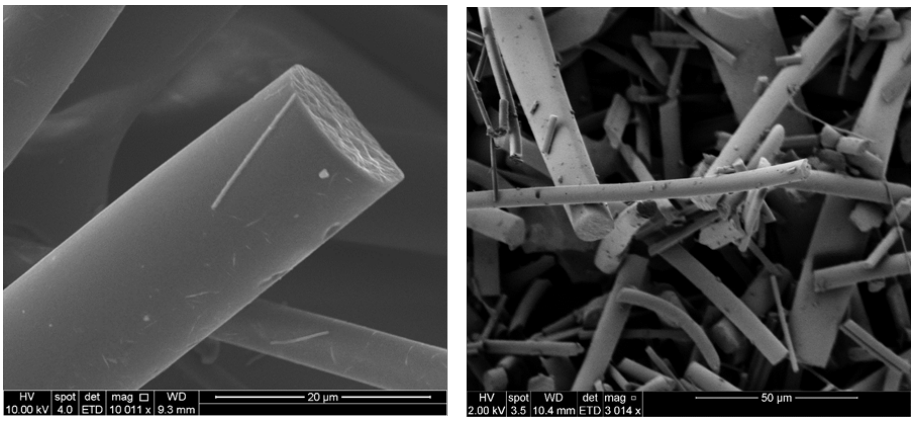

Figure 4.61: Secondary SEM imaging of Cerachem®, module 1 at the hot face.

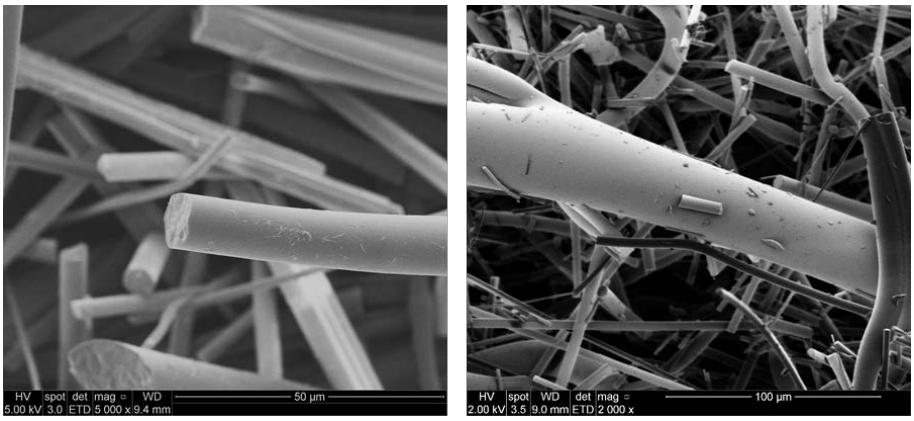

Figure 4.62: Secondary SEM imaging of Cerachem® module 2 at the hot face.

4.2.3. Thermal analysis

Differential thermal analysis was carried out to determine the crystallization behaviour of unfired Cerachem®. Figure 4.63 presents the DTA patterns gathered at 10, 20 & 40°C/minute heating rates. The primary low-temperature form of the material is a

homogeneous alumina-zirconia-silica (AZS) glass, stable up to temperatures of ca. 980-1000°C. DTA patterns show one strong exothermic peak related to the main crystallization event at 1018-1045°C which is due to the formation of mullite and zirconia (Tonnesen & Telle, 2007). A second shallow feature peak appears at around 1150°C which is probably connected with the formation of cristobalite. The result from the DTA test at the slowest rate (10°/min) shows that the exothermic crystallization peak has shifted to a lower temperature.

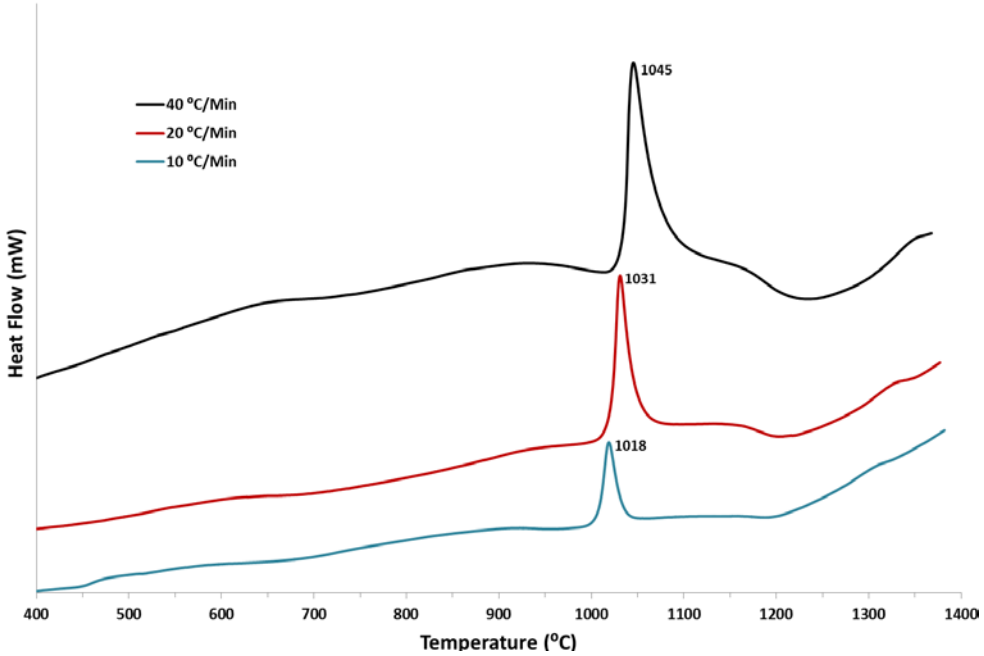

Figure 4.63: DTA analysis for unfired Cerachem® samples using different heating rates.

4.3.4. Summary

Elemental analysis of Cerachem® showed that a loss of silica occurs as a function of material depth, and is observed as a weight loss, as gaseous SiO_2 moves away from the hot face of the module samples. Investigation of the crystal structure of Cerachem® modules at various depths revealed that mullite, cristobalite and zirconia will develop.

4.4. References

Ban, T., & Okada, K. (1992). Structure refinement of mullite by the Rietveld method and a new method for estimation of chemical composition. *Journal of the American Ceramic Society, 75*(1), 227-230.

Bhagwat, M., & Ramaswamy, V. (2004). Synthesis of nanocrystalline zirconia by amorphous citrate route: structural and thermal (HTXRD) studies. *Materials Research Bulletin, 39*(11), 1627-1640.

Bondars, B., Heidemane, G., Grabis, J., Laschke, K., Boysen, H., Schneider, J., & Frey, F. (1995). Powder diffraction investigations of plasma sprayed zirconia. *Journal of Materials Science, 30*(6), 1621-1625.

Collin, G., Comes, R., Boilot, J., & Colomban, P. (1980). Crystal structure and ion-ion correlation of ion-rich β alumina type compounds I. Magnesium doped potassium rich β alumina. *Solid State Ionics, 1*(1-2), 59-68.

Cook, L. P., Roth, R. S., Parker, H. S., & Negas, T. (1977). The system K_2O-Al_2O_3-SiO_2. Part 1. Phases on the $KAlSiO_4$-$KAlO_2$ join. *American Mineralogist, 62*(11-12), 1180-1190.

Dernier, P., & Remeika, J. (1976). Structural determinations of single-crystal K β-alumina and cobalt-doped K β-alumina. *Journal of Solid State Chemistry, 17*(3), 245-253.

Ferrari, A. C., & Robertson, J. (2000). Interpretation of Raman spectra of disordered and amorphous carbon. *Physical Review B, 61*(20), 14095.

Gatta, G. D., Rotiroti, N., Ballaran, T. B., & Pavese, A. (2008). Leucite at high pressure: Elastic behavior, phase stability, and petrological implications. *American Mineralogist, 93*(10), 1588-1596. doi:10.2138/am.2008.2932

Igawa, N., & Ishii, Y. (2001). Crystal structure of metastable tetragonal zirconia up to 1473 K. *Journal of the American Ceramic Society, 84*(5), 1169-1171. doi:10.1111/j.1151-2916.2001.tb00808.x

Johnson, B. R., Kriven, W. M., & Schneider, J. (2001). Crystal structure development during devitrification of quenched mullite. *Materials Letters, 57*, 3155-3159. doi: 10.1016/S0955-2219(01)00268-0

Kissinger, H. E. (1957). Reaction kinetics in differential thermal analysis. *Analytical Chemistry, 29*(11), 1702-1706.

Kremenović, A., & Vulić, P. (2014). Disordered kalsilite $KAlSiO_4$. *Acta Crystallographica Section C: Structural Chemistry, 70*(3), 256-259.

Lacks, D. J., & Gordon, R. G. (1993). Crystal-structure calculations with distorted ions. *Physical Review B, 48*(5), 2889.

Ma, X., Ma, H., & Yang, J. (2016). Sintering Preparation and Release Properties of $K_2MgSi_3O_8$ Slow-Release Fertilizer Using Biotite Acid-Leaching Residues as Silicon Source. *Industrial and Engineering Chemistry Research, 55*(41), 10926-10931. doi:10.1021/acs.iecr.6b02991

Okada, K., Kaneda, J., Kameshima, Y., Yasumori, A., & Takei, T. (2003). Crystallization kinetics of mullite from polymeric Al_2O_3–SiO_2 xerogels. *Materials Letters*, 57(21), 3155-3159. doi: 10.1016/S0167-577X(03)00013-2

Osborn, E. F., & Muan, A. (1960). *Phase equilibrium diagrams of oxide systems*. Columbus, Ohio: American Ceramic Society with the Edward Orton Jr. Ceramic Foundation.

Seidel, S., Patzig, C., Höche, T., Krause, M., Ebert, M., Hu, Y., . . . Rüssel, C. (2016). The crystallization of $MgO–Al_2O_3–SiO_2–ZrO_2$ glass-ceramics with and without the addition of Y_2O_3–a combined STEM/XANES study. *RSC Advances*, *6*(67), 62934-62943.

Shelby, J. E. (2005). *Introduction to Glass Science and Technology* (2nd ed.). Cambridge: Royal Society of Chemistry.

Smith, J. V., & Tuttle, O. F. (1957). The nepheline-kalsilite system; Part I, X-ray data for the crystalline phases. *American Journal of Science*, *255*(4), 282-305.

Speil, S., Berkelhamer, L. H., Pask, J. A., & Davies, B. (1945). *Differential thermal analysis of clays and aluminous minerals.* (U.S. Bureau of Mines Technical Paper No. 664). Washington: U.S. Government Publishing Office.

Thermal Ceramics. (1995). *Technical aspects of ceramic fibres*. Augusta, Georgia: Thermal Ceramics Inc.

Tonnesen, T., & Telle, R. (2007). *Influence of firing temperature and time on the quantitative phase formation and recrystallization behaviour of high temperature glass fibres (AES) and refractory ceramic fibres (RCF).* (German Association of Manufacturers and Processors of High Temperature Wool).

Chapter 5

Discussion

5. Discussion

This research study aims to answer some important questions regarding the structure, thermal behaviour and chemical stability of biosoluble glass fibres in the K_2O-MgO-ZrO_2-Al_2O_3-SiO_2 system in terms of time and temperature. During this investigation, the potassium oxide losses, the phase transitions, the surface morphology of glass fibres and the factors affecting the heating atmosphere were the core research questions.

This chapter discusses the main findings as related to the principal purpose of the study. Also, other interesting findings from the results section will be discussed. All explanations are supported by the results in Chapter 4.

5.1. Thermal behaviour of Superwool XT® fibres

Due to the commercial importance of biosoluble glass fibres there are no reports in literature as to the thermal stability of compositions in the specific K_2O-MgO-ZrO_2-Al_2O_3-SiO_2 system for direct comparisons to be made here. However, data for subsystems and related systems are available. Thus, the results are discussed in comparison to the subsystems where appropriate.

The term “thermal behaviour” is used here to describe the crystallization, compositional stability and surface morphology of SWXT® fibres in terms of time and temperature. The heat treatment experiments at 850°C and 1250°C for the same firing time (up to 2160 hours) yielded different results. At lower temperature (850°C) SWXT® glass fibres are chemically stable as no elemental variations by XRF analysis were observed (Figure 4.1) and XRD disclosed that there are no alterations or phase transformations after 840 hours when disordered hexagonal kalsilite ($KAlSiO_4$) is fully formed (Figure

4.12). In contrast to ordered kalsilite, the XRD pattern of disordered hexagonal kalsilite is characterized by systematic absences of *h0l* and *hhl* reflections with *l=2n+1* (Kremenović & Vulić, 2014). These authors showed that such systematic absences result from a structure that contains substructures **a** and **b** only when they are in a ratio of 1:1 (Figure 5.1).

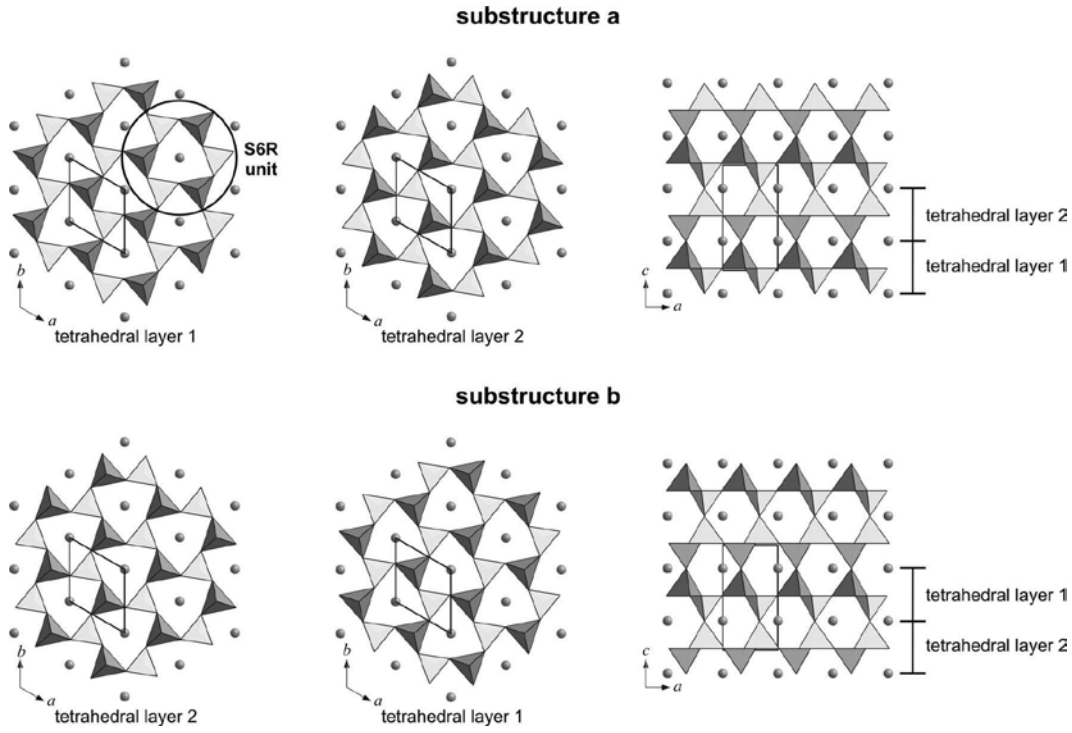

*Figure 5.1: Polyhedral representation of $KAlSiO_4$ substructures **a** and **b**. Single tetrahedral layers are shown with SiO_4 (light grey) and AlO_4 (dark grey) tetrahedra. K atoms are symbolized by grey spheres (Kremenović & Vulić, 2014).*

Hexagonal kalsilite – either in its ordered or disordered form – is reported to be stable up to approximately 950°C (Capobianco & Carpenter, 1989). Thus, the analysed phase crystallization and high elemental stability, combined with support from literature, supports the conclusion that SWXT® fibres have a high thermal stability at 850°C over prolonged heating (2160 hours).

Moreover, XRD (Figure 4.13) and XRF (Figure 4.2) investigation on SWXT® samples that have been pre-crystallized at 1200°C for 5 minutes showed that even though SWXT® fibres have transformed into glass-ceramic fibres with kalsilite formed, at low

temperature (850°C) there is no further crystal growth and all the components remain stable as a function of time (up to 2160 hours). European Patent Application EP 2213634 A1 (Boff, Jubb, & Mottram, 2010) discloses an invention relating to the effect of partial crystallization of glass fibres on their thermal properties. This patent argues that fibres which have first crystallized or at least partly crystallized will have a better performance as their shrinkage resistance will be increased. This study has shown that at 850°C the thermal behaviour – in terms of final phase assemblage and elemental stability – of glass fibres was the same for the pre-crystallized and amorphous samples.

On the other hand, structural analysis of SWXT® heat treated at 1250°C (Figure 4.23) revealed the formation of $KAlSiO_4$ and ZrO_2 crystalline phases after 168 hours and the formation of $KAlSi_2O_6$ and $KAl_{11}O_{17}$ after 840 hours of constant heat treatment. The formation of leucite starts much earlier (<72 h) when the temperature is raised to 1500°C (Figure 4.19) which shows that the development of a crystalline phase is influenced both by heating time and temperature (Comodi, Cera, Gatta, Rotiroti, & Garofani, 2010).

At the initial stage of crystallization at 1250°C disordered hexagonal kalsilite is formed which then inverts to orthorhombic kalsilite (Figure 5.2), with this transition being detectable by XRD after about 1000 h of firing. Capobianco & Carpenter (1989) obtained orthorhombic kalsilite by annealing natural hexagonal kalsilite at 1200°C in open Pt crucibles for 48 hours. These results are not contradictory, considering that the composition of SWXT® is not stoichiometric kalsilite, and that it is in the form of glass fibres with crystallization kinetics being an additional factor. In fact, in glass fibres close to stoichiometric kalsilite (KAS-5) this transition was detectable in half of the firing time compared to SWXT® (500 h), though it may occur even earlier but no experimental data are available between 24 and 500 h (Figure 4.46). Thus, this

transition can be shown to have occurred between 24 and 500 hours based on this study. Detailed crystallographic analysis of kalsilite would be needed to establish how this transition occurs in glass fibres and this is suggested for future work.

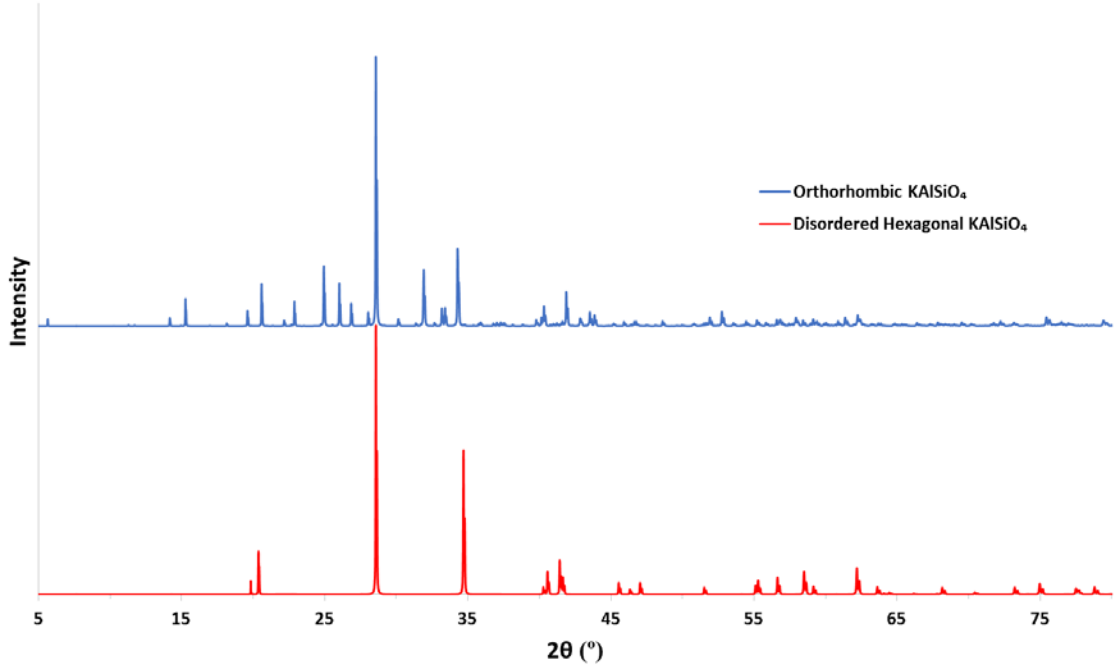

Figure 5.2: XRD patterns of disordered hexagonal $KAlSiO_4$ (Kremenović & Vulić, 2014) and orthorhombic $KAlSiO_4$ (Gregorkiewitz, Li, White, Withers, & Sobrados, 2008), for Cu Kα radiation.

The transition from hexagonal to orthorhombic kalsilite is accompanied by the formation of leucite, as observed in all XRD patterns at 1250°C for SWXT® (Figures 4.14 and 4.22 to 4.25) and melt-rig samples (Figures 4.45 to 4.48), and in accordance with Capobianco & Carpenter (1989) who observed the presence of leucite in all orthorhombic kalsilite samples. It is unclear whether hexagonal kalsilite first transforms to orthorhombic which then gradually transforms to leucite or orthorhombic kalsilite and leucite form simultaneously (Figure 5.3). The time required for these transformations depends on the starting composition; it is 1000 hours for SWXT® and 500 hours for KAS-5 (close to kalsilite stoichiometry).

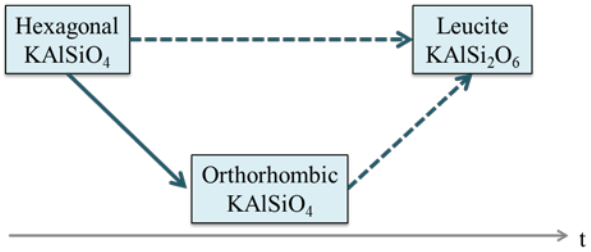

Figure 5.3: Schematic of hexagonal to orthorhombic kalsilite transition with the formation of leucite at 1250°C. Dashed arrows represent two alternative transition pathways.

XRD patterns for short firing periods at 1250°C (Figure 4.11) revealed that SWXT® partially crystallizes very rapidly, in less than one minute. Rietveld analysis (Figure 4.19) for the first long-term experiment showed that even after 2176 hours of constant heat treatment at 1250°C some amorphous phase is retained and the percentage of amorphous phase decreases linearly as a function of time. The actual values calculated for the phase contents are not reliable due to the presence of multiple phases and peak overlapping; thus, the results were used to study only the trends in the phase assemblage. Analysis of the peak area for the highest intensity peak matched by kalsilite (Figure 4.16) showed that kalsilite is disappearing and transforming into another crystalline phase which is leucite. In support of this, Rietveld analysis (Figure 5.4) shows that the percentage of leucite increases in a similar manner that the percentage of kalsilite decreases, notwithstanding the uncertainty in the calculated phase contents. The emergence of the leucite phase upon heating kalsilite was also reported by Capobianco and Carpenter (1989) at 1200°C for 48 hours, and by Gregorkiewitz et al. (2008) at 1300°C for 24 hours.

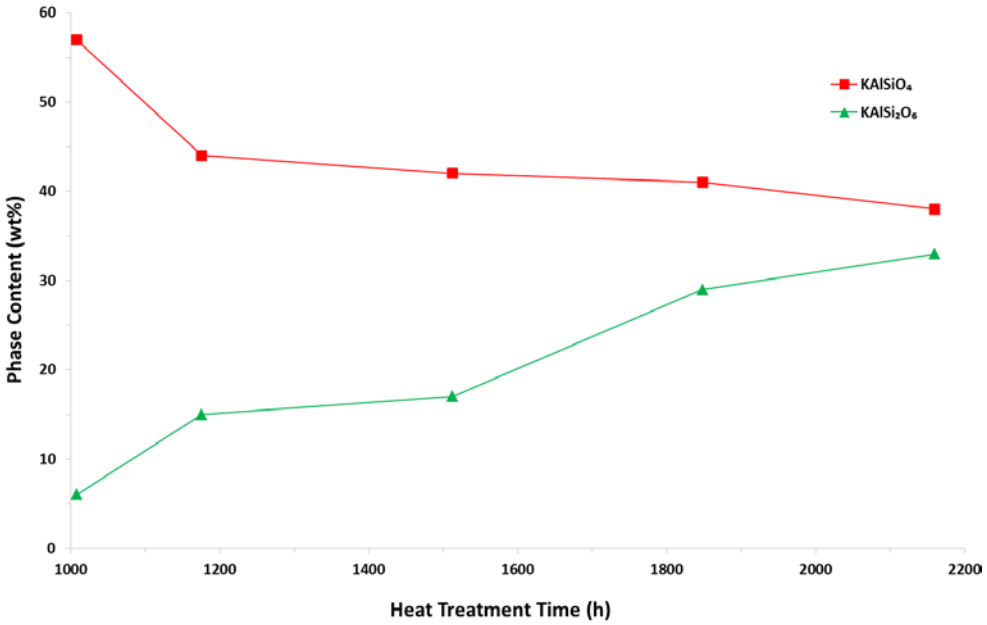

Figure 5.4: Phase content of kalsilite and leucite in SWXT® heat treated at 1250°C (1st expr) as a function of firing time, as determined by Rietveld analysis.

XRF (Figure 4.3) and EDX (Figure 4.6) analysis of heat-treated SWXT® at 1250°C showed a significant reduction in the content of K_2O as a function of time (6.8 wt% after 2160 hours). After an initial substantial loss (0-200 hours) of K_2O, the K_2O content gradually declines (200-1600 hours) and then it sharply drops again from 1600 to 2100 hours. U.S. Patent No. 8,088,701 B2 (Jubb, 2012) disclosed that glass fibres in the K_2O-Al_2O_3-SiO_2 system have the tendency to lose K_2O at elevated temperatures. The evaporation of K_2O was also reported in studies of kalsilite (Capobianco & Carpenter, 1989; Gregorkiewitz et al., 2008) and was connected with the transformation of kalsilite to leucite at high temperature and for prolonged heat treatment but the reason of this loss was not investigated.

This study shows that the thermal performance of SWXT® glass fibres deteriorates, as the surface morphology becomes rough and uneven (Figures 4.27 to 4.35) due to significant crystal growth (Tonnesen, Dietrichs, & Telle, 2005). Also, some of the SWXT® fibres heat treated for long periods display cavities (Figure 5.5). Gualtieri et al. (2009) presented similar SEM images with inner cavities, which they attributed to

crystallization, after treating man-made vitreous fibres (MMVF) ($CaO\text{-}SiO_2\text{-}MgO$) at 1300°C for 72 hours. Some untreated SWXT® fibres have pinholes (Figure 4.26) which according to the manufacturer (G. A. Jubb, personal communication, November 16, 2015) may be caused by the existence of trapped CO_2 gas during the production of the fibres but their size compared to the fibre diameter is much smaller ($\frac{d_{fibre}}{d_{pinhole}} \cong 7$).

Moreover, as depicted in Figure 5.5 after long firing (2160 hours at 1250°C) the surface of SWXT® fibres is covered with nodules, and more broken fibres exist. According to Dyson et al. (1997) nodules tend to form on fibre surfaces and work as points at which fibres will interconnect to each other. The presence of nodules and broken fibres was also observed by Gualtieri et al. (2009) in aluminosilicate and calcium magnesium silicate fibre samples heat treated at 1300°C for 72 hours. It is important to note here that the macroscopic appearance of SWXT® fibre samples changed significantly after prolonged heat treatment (800 h) at high temperature (1250°C); the samples visibly shrank and broke easily when handled as a result of the microstructural changes described above.

SEM imaging (Figure 4.26 to Figure 4.35) revealed that the significantly rougher morphology of SWXT® fibres with both core and surface crystallization after heat treatment (2160 hours at 1250°C) probably relates to the formation of $KAl_{11}O_{17}$ which is a β alumina phase (Dernier & Remeika, 1976). Chemical analysis of $K_2O\text{-}Al_2O_3$ binary mixtures (1:5) showed that potassium evaporation at high temperature (≥1400°C) leads to the development of β alumina, which is the stoichiometric 1:11 compound (Schaefer, De Kroon, & Aldinger, 1995). Potassium excess can be accommodated in the β alumina structure, $K_{1+x}Al_{11}O_{17+x/2,}$ with x values up to 0.5 being reported in literature (Iyi, Inoue, & Kimura, 1986). SWXT® fibres have very large

plate-shaped features after 1848 hours of heat treatment; these plates are more likely to be alumina plates.

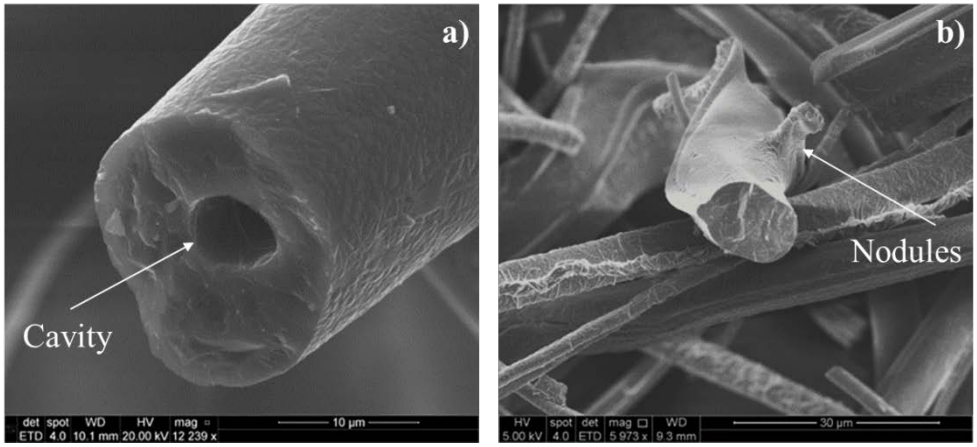

Figure 5.5: SEM secondary imaging of SWXT® fibres heat treated at 1250°C for a) 1176 hours and b) 1848 hours.

5.2. Effect of firing atmosphere on the thermal behaviour of glass fibres

The need of conducting experiments under as close to in-service conditions as possible was the rationale for a series of experiments with different sample arrangements inside the furnace (Figure 3.5 and Figure 3.6). XRF results of all the experiments with SWXT® conducted at 1250°C (Table 4.5 to 4.7) showed that there is a significant loss of K_2O – 7 wt% after 1848 hours of constant firing – as a function of time; the lost K_2O is believed to be in the form of vapours, as K_2O loss also has been measured in other potassium-bearing systems (Fedkin, Grossman, & Ghiorso, 2006; Yu, Hewins, & Wang, 2003). The concertation of potassium vapours in the furnace atmosphere is affected by the number of samples and the dimensions of the furnace.

XRD patterns (Figure 4.24 and Figure 4.25) showed that in the experiments where there was expected to be a potassium-rich atmosphere inside the furnace, the crystal growth and the development of specific crystalline phases were suppressed. Specifically,

comparing the crystallization behaviour of SWXT® samples at 1250°C for 500 and 1000 hours (Figure 4.25), for identical experimental conditions apart from the size of the furnace, the presence of leucite and potassium β alumina is lesser in the case of the small furnace, corresponding to a potassium rich atmosphere. Using the same-size furnace but varying the number of samples in it heat treated at 1250°C for 1176 to 1848 hours – it is believed changing the potassium atmosphere in the furnace – again gave rise to analogous results. The XRD peaks of leucite and potassium β alumina are less prominent in the case of the furnace with more samples (Figure 4.24), corresponding to a more potassium rich atmosphere. Thus the formation of leucite and potassium aluminium oxide appears to be suppressed by this atmosphere. Elemental analysis (Figure 4.10 and Table 4.10) of samples that were exposed to the potassium-rich environment showed that apart from the crystallization, the rate of K_2O evaporation is also suppressed. The above results indicate that the heat treatment atmosphere has a significant impact on the crystallization behaviour and the rate of potassium evaporation. Moreover, this is again evidence that the loss of potassium oxide is strongly connected with the development of leucite as in all the cases where the K_2O loss was limited, the formation of leucite was also supressed.

As discussed in several studies, different firing atmospheres can accelerate or suppress the formation of particular phases in minerals (Brindley & Lemaitre, 1987; Dubois, Murat, Amroune, Carbonneau, & Gardon, 1995; MacKenzie, 1969; MacKenzie, Meinhold, Brown, & White, 1996; Temuujin, Okada, MacKenzie, & Jadambaa, 1999). More specifically, in the case of kaolinite ($Al_2Si_2O_5(OH)_4$) a gaseous atmosphere of water or a vacuum accelerates the formation of mullite ($Al_6Si_2O_{13}$), by modifying the mullite crystallization kinetics, and conversely the presence of carbon dioxide or oxygen retards the mullite development compared to a dry atmosphere (Brindley & Lemaitre,

1987; MacKenzie, 1969). Dubois et al. (1995) showed that the presence of mullite in kaolinite samples is supressed by argon or nitrogen atmospheres. For the same system under reducing and vacuum atmospheres at 1200°C, MacKenzie et al. (1996) reported the formation of a greater amount of mullite. In all the aforementioned studies, it is pointed out that the combination of high temperature and vapours inside the furnace affects the crystallization, which is in accordance with the experimental parameters of this study where the firing atmosphere is rich in potassium and the experiments were conducted at 1250°C.

5.3. Laboratory-produced glass fibres

Systematic synthesis experiments to produce glass fibres in the ternary K_2O-Al_2O_3-SiO_2 system and the quaternary K_2O-ZrO_2-Al_2O_3-SiO_2 system were conducted. Heat treatment experiments of the resulting fibres at 1250°C to multiphase and single-phase reaction products in the kalsilite-leucite phase fields. For a short heat treatment time (24 h), all compositions formed the primary phases expected from the K_2O-Al_2O_3-SiO_2 phase diagram (Osborn & Muan, 1960), i.e. KAS-1 and KAS-2 formed leucite, KAS-3 and KAS-4 a mixture of leucite and kalsilite, and KAS-5 formed kalsilite. Prolonged firing altered the phase assemblage of some of the samples as discussed below. Samples KAS-8 and KAS-9 are compositions that lie within an experimentally unexplored region of the phase diagram, and therefore the analysis of these samples has provided new and useful information.

Elemental analysis (XRF) revealed (Table 4.17) that in sample KAS-1, which is close to the stoichiometry of leucite (SiO_2-rich) and KAS-9 and KASZ-2 (Al_2O_3-rich), no potassium loss is observed after heat treatment at 1250°C for 500 and 1000 hours.

Additionally, in sample KAS-3, the next closest material to the composition of leucite, the potassium loss was significantly lower (1.5 wt%) compared to the samples with compositions closer to the stoichiometry of kalsilite (2.7-3.6 wt%) for the same firing conditions.

Additionally, according to XRD analysis (Figures 4.41 to 4.50) KAS-1, KAS-9 and KASZ-2 after heat treatment at 1250°C for 500 and 1000 h formed only leucite without any phase transformation or development of second phases. This suggests that leucite is a stable crystalline phase in terms of time at 1250°C and this is also combined with chemical stability.

In contrast, the rest of the samples (KAS-3, KAS-4, KAS-5, KAS-8 and KASZ-1) follow the same crystallization route as SWXT® in which distinct phases develop: in the early stage of crystallization kalsilite forms, which then transforms into leucite with simultaneous formation of β alumina. This is also described in studies (Erbe & Sapieszko, 1997; Liu, Komarneni, & Roy, 1994; Y. Zhang, Lv, Chen, & Wu, 2007) which show that kalsilite is an unstable phase that probably acts as a precursor of leucite. Even for sample KAS-5, which has the kalsilite stoichiometry, leucite will form after prolonged firing. In the aforementioned studies which aimed to produce pure leucite (with silica-rich starting compositions), kalsilite crystallised first at lower temperatures (800°C) and transformed to leucite as the temperature increased (900°C). Moreover, XRD results show that after long-term (>500 h) heat treatment at 1250°C all samples investigated form leucite (at least in part depending on the composition) but the key difference is that when the starting composition is close to kalsilite this transformation will include K_2O losses.

Structural analysis of the melt-rig fibres at the leucite-kalsilite tie-line (Figure 4.40) showed that by increasing the K_2O content – moving towards kalsilite stoichiometry

samples – the time each sample needs to transform from amorphous-rich material to glass-ceramic increases. These results agree with a study (Johnson, 1979) where the effect of additives in the aluminosilicate system was examined; K_2O was found to retard crystal growth and even a small addition of K_2O had a significant effect on the amount of mullite formed.

In this work, the effect of adding ZrO_2 was also studied by comparing KAS-8 to KASZ-1 and KAS-9 to KASZ-2. KAS-8 and KAS-9 samples have no zirconia whereas KASZ-1 and KASZ-2 contain about 7 wt%. Thermal analysis disclosed (Figure 4.53) that the addition of zirconia shifts the crystallization events to higher temperatures for both cases, by 23°C for KAS-8 to KASZ-1 and by 28°C for KAS-9 to KASZ-2, which indicates that ZrO_2 increases thermal stability (Beall, 1972; Strand, 1986; Tashiro & Wada, 1963).

The addition of zirconia (1-5 wt%) to Li_2O-SiO_2-Al_2O_3-K_2O-P_2O_5 compositions was found to hamper the crystal growth of Li_2SiO_3 and $Li_2Si_2O_5$ but those experiments were conducted at low temperatures (maximum 900°C) and for short-term heat treatments (1 hour) (Fernandes, Tulyaganov, & Ferreira, 2013). This effect was also observed in another study (Apel, van't Hoen, Rheinberger, & Höland, 2007) for low zirconia contents (< 4 wt%) but the sample with the maximum percentage of ZrO_2 (4 wt%) was found to show increased crystallinity compared to the sample without ZrO_2. The present work showed that at elevated temperature (1250°C) and for long-time firing (1000 hours) increasing the ZrO_2 content will promote phase transformations and crystallization processes which implies the role of ZrO_2 as a nucleating agent.

Heat treated melt-rig samples KAS-9 and KASZ-2 did not have any structural or loss difference (Figure 5.6), with leucite being present. In the case of the samples KAS-8 and KASZ-1, with kalsilite being the main phase (Figure 5.7), the zirconia sample

(KASZ-1) had higher K_2O loss and again the amount of leucite was higher in comparison (Figure 5.7).

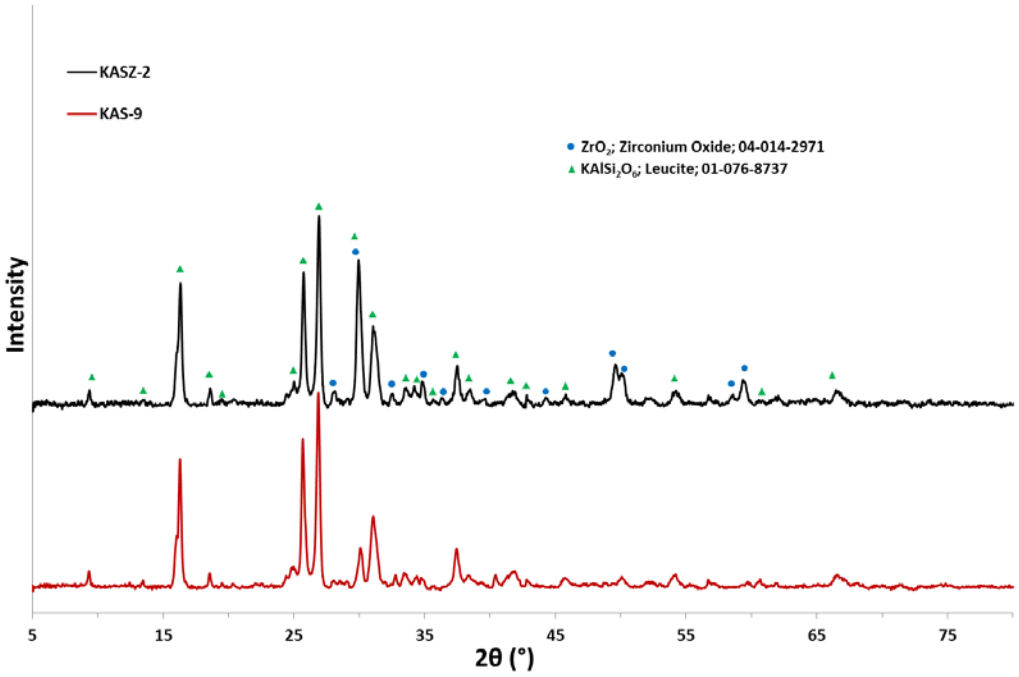

Figure 5.6: XRD patterns of heat-treated KAS-9 and KASZ-2 glass fibres at 1250°C for 1000 hours.

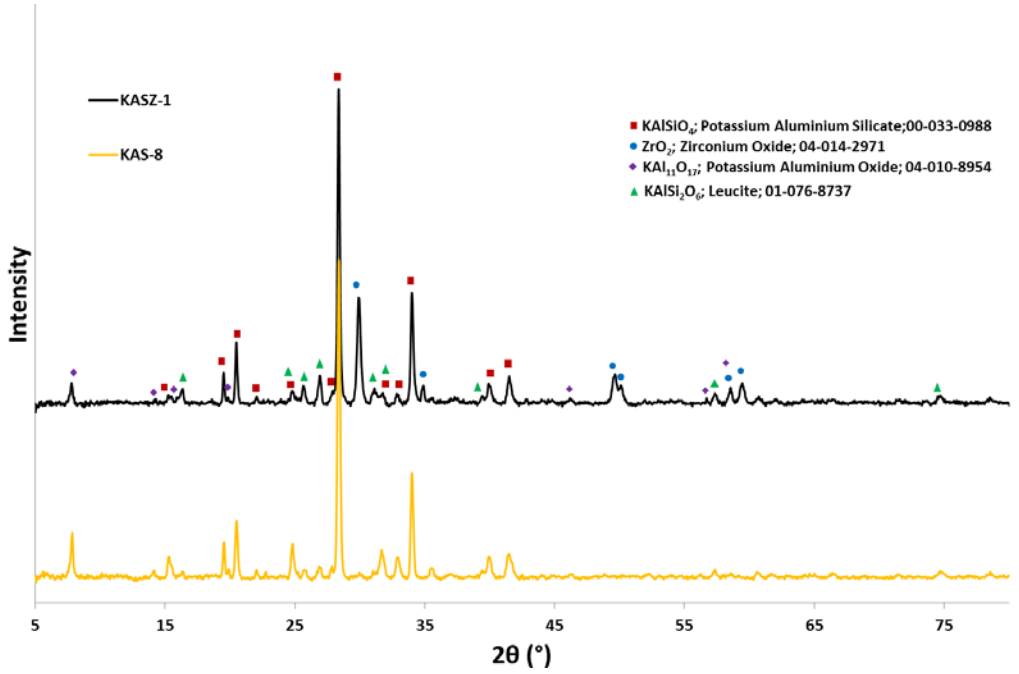

Figure 5.7: XRD patterns of heat-treated KAS-8 and KASZ-1 glass fibres at 1250°C for 1000 hours.

The role of Zr on crystallization has two aspects. It suppresses the development of β alumina as it is illustrated in Figure 5.7 where the presence of β alumina is greater for KAS-8 that does not contain ZrO_2. Accordingly, the addition of zirconia is reported to negatively affect the densification and crystal growth of alumina compared with samples without any ZrO_2 (Bunsell, 2005; Galusek et al., 2015). On the other hand, zirconia is an important nucleating agent as it is related to the formation of leucite, since KASZ-1 sample that has zirconia has also a greater amount of leucite compared with KAS-8 (Figure 5.7). Stookley (1959) reported that sub-microscopic catalysts such as ZrO_2 and TiO_2 promote the development of the principal crystalline phases and heterogeneous nucleation. Studies in the K_2O-Al_2O_3-SiO_2 system (Höland, Frank, & Rheinberger, 1995; Rouf, Hermansson, & Carlsson, 1978) disclosed that the addition of TiO_2, which has comparable effects with ZrO_2 (Kleebusch, Patzig, Höche, & Rüssel, 2016), is related to the evolution of leucite. The role of ZrO_2 on crystallization of samples in the K_2O-Al_2O_3-SiO_2 system in general could not be established within this study and this is suggested as possible future work.

KAS-9 and KASZ-2 were the only samples that produced two exothermic peaks attributed to crystallization events in DTA curves (Figure 4.54) where the first crystallization event relates to kalsilite before the main crystallization event which is the formation of leucite, as confirmed by other reports (Y. Zhang et al., 2007; Y. Zhang, Wu, Rao, & Lv, 2006). XRF analysis for both samples revealed no elemental alteration as a function of time.

Raman spectroscopy was employed to locally characterize the structure of KAS-1 to KAS-5 samples in glassy and crystallized forms. Raman spectra (Figure 4.51) for glass samples showed the presence of three sets of bands which are located in the ranges of approximately 400-525 cm^{-1}, 525-625 cm^{-1}, and 900-1200 cm^{-1}. In a recent study

(Yadav & Singh, 2015), it is reported that the broad Raman band at 900-1200 cm^{-1} is typical for aluminosilicate glasses and is related to Q_n units of the tetrahedral network. Q_n notation expresses the concertation of bridging oxygens per tetrahedron by varying the value of the subscript n. A tetrahedron fully linked into the network via four bridging oxygens is designated as Q_4 unit, while an isolated tetrahedron with no bridging oxygens is designated as a Q_0 unit. Vitreous SiO_2 is defined as consisting of 100% Q_4 units. The addition of a generic alkali oxide creates non-bridging oxygens thus decreasing the concertation of Q_4 units (Shelby, 2005). This peak at 900-1200 cm^{-1} relates to the symmetric and asymmetric stretching vibrations of bridges Si-O-(Si) and sometimes Si-O-(Al), bonds related to the AlO_4 and SiO_4 tetrahedra (Neuville & Mysen, 1996). They can involve tetrahedral units, Q_4, without non-bridging oxygens (NBO) and tetrahedra with one NBO, Q_3, (Le Losq, Neuville, Florian, Henderson, & Massiot, 2014). There is a possibility that Q_2 units are present, giving a band at 950 cm^{-1} related to $Si{-}O^-$ stretching of NBOs, but the peak is too broad for this to be discerned without deconvolution (Brawer & White, 1977; Virgo, Mysen, & Kushiro, 1980). As seen in Figure 4.51 this band shifts to lower frequencies, its intensity decreases and it becomes more asymmetric moving from sample KAS-1 ($KAlSi_2O_6$) to KAS-5 ($KAlSiO_4$) corresponding to an increase in Al_2O_3 concentration and decrease in SiO_2 concentration. The incorporation of Al^{3+} into the glass network leads to a decreased average bond strength of (Si,Al)-O, causing a decrease in the Raman shift (Bechgaard et al., 2017). Moreover, the peak centre shifts to lower wavenumbers, which would imply that the depolymerization degree of the aluminosilicate matrix increases as a result of increasing K_2O content (L. Wang, Wang, Wang, & Chou, 2016).

Shelby's (2005) mathematical model was used to calculate Q_4 and Q_3 units for KAS-1 to KAS-5 samples (Table 5.1). This model considers that only two Q_n types exist in any

alkali silicate glass. When the alkali concertation, *x*, is less than 33.3 mol% only Q_4 and Q_3 units are expected to be present and are calculated from Eq. 5.1 and Eq. 5.2, respectively.

$$Q_4 = 100 - 3x \quad 5.1$$

$$Q_3 = 2x \quad 5.2$$

Table 5.1: Theoretical calculations of Q_4 and Q_3 units using a model for binary systems (Shelby, 2005).

Sample	SiO_2 (mol%)	Al_2O_3 (mol%)	K_2O (mol%)	Q_3 (mol%)	Q_4 (mol%)
KAS-1	68.9	15.8	15.3	30.6	54.1
KAS-2	66.3	17.1	16.6	33.2	50.2
KAS-3	61.4	19.4	19.2	38.4	42.4
KAS-4	57.3	21.3	21.5	43.0	35.5
KAS-5	51.0	25.5	23.5	47.0	29.5

This model quantitatively supports the Raman evidence that Q_3 units increase and Q_4 decrease upon moving from high (KAS-1) to lower (KAS-5) SiO_2 content, signifying the depolymerization of the glass network with modifier addition. However, since this is an aluminosilicate and not silicate system, the calculated values of Q_n speciation are outside the validation of this model, as the interaction between the modifier and aluminium would affect the extent of depolymerization. Further spectroscopic analysis with the use of NMR and deconvolution of Raman spectra would be necessary to determine both Al and Si Q_n speciation and this is suggested for future work.

The Raman band at 525-625 cm^{-1} is allocated to the bending symmetric vibrations Si-O-(Si, Al) among the tetrahedra and the peak at 400-525 cm^{-1} is related to bending vibrations of $Al{-}O^-$ and $Si{-}O^-$ (McMillan & Piriou, 1983). As shown in Figure 4.51 the relative intensity of the 400-525 cm^{-1} band compared to 525-625 cm^{-1} band decreases from sample KAS-1 to KAS-5. Such a change in the relative intensity of the bands in the low-frequency region has been reported (Bechgaard et al., 2017) for alkali-alkaline

earth aluminosilicate glasses with the substitution of Al_2O_3 for SiO_2 when $[Al_2O_3] > [Na_2O]$, and was attributed to a change in the role of the alkaline earth from network modifier to charge compensation. In this work, since the $[Al_2O_3]$:$[K_2O]$ remains almost constant the observed change in the Raman spectra maybe attributable to the decrease of SiO_2 content.

Raman spectra for the KAS-1 to KAS-3 heat treated samples at 1250°C for 24 hours (Figure 4.52) confirm the presence of tetragonal leucite (Palmer, Bismayer, & Salje, 1990). Leucite is a very weak Raman scatterer that has two main intense peaks in the range of 450-550 cm^{-1} and the rest are very broad peaks in the range of 120-150 cm^{-1} and presumably represent the superposition of multiple Raman lines (Palmer et al., 1990). As confirmed by XRD, KAS-3 and KAS-4 samples form orthorhombic kalsilite while KAS-5 sample forms hexagonal kalsilite. To the best of the author's knowledge, there are no existing literature data regarding the Raman spectrum of orthorhombic kalsilite. Hexagonal kalsilite is expected to show a sharp band around 300-400 cm^{-1} and a group of low intensity bands in the range of 900-1050 cm^{-1} (Uchida, Downs, & Yang, 2006). The Raman spectrum of sample KAS-5 is not the same as that of hexagonal kalsilite. The observed modes in the ranges of about 240-260 cm^{-1}, 275-325 cm^{-1}, 350-370 cm^{-1}, 380-400 cm^{-1}, 450-470 cm^{-1}, 900-950 cm^{-1}, 1000-1050 cm^{-1} and 1070-1120 cm^{-1} for KAS-3, KAS-4 and KAS-5 cannot be identified at this stage, some or all of them are possibly attributable to orthorhombic kalsilite. Additionally, the high frequency modes 1070-1120 cm^{-1} could be related to retained aluminosilicate glass.

5.4. Transformation mechanism of kalsilite to leucite and the loss of K_2O

This study aimed to develop an understanding of the transformation mechanism of kalsilite to leucite and its connection with the loss of K_2O from SWXT® fibres. While this study revealed that kalsilite is stable for 2160 hours at temperatures of up to 850°C, structural analysis of SWXT® and melt-rig samples disclosed that kalsilite is in fact unstable at elevated temperatures (1250°C) and will transform into leucite as a function of time as also reported in literature (Capobianco & Carpenter, 1989; Gregorkiewitz et al., 2008). Combining XRD patterns with Rietveld analysis revealed that kalsilite will transform into leucite.

As mentioned above, the first evidence regarding the loss of potassium arose when SWXT® fibres were heat treated at 1250°C for prolonged times (up to 2160 hours). The first assumption was the well-known volatile character of K_2O (Yu et al., 2003) but the irregular rate of this loss indicated that further investigation was needed.

Kalsilite is less thermodynamically stable than leucite and this can be assessed using the approach of Curtis (1976), who calculated the Gibbs' free energy changes of the reactions for leucite and kalsilite (Table 5.2). Considering variation in the written formula by expressing the free energy change per gram-atom rather than per mole (this approach allows comparison of like with like in terms of numbers of bonds being broken as the framework silicate weathers) the least stable mineral is kalsilite.

Table 5.2: Weathering reactions for framework kalsilite and leucite minerals (Curtis, 1976).

Reaction	ΔG_r (kJ/mol)	ΔG_r (kJ/ gram atom)
$2KAlSiO_4+2H^++H_2O=2K^++Al_2Si_2O_5(OH)_4$	-115.25	-6.07
$2KAlSi_2O_6+2H^++H_2O=2K^++Al_2Si_2O_5(OH)_4+2SiO_2$	-88.00	-3.52

Alternatively, looking at the free energy of formation as calculated using Eq. 5.3 (Atkins & De Paula, 2013) for kalsilite and leucite, leucite is more stable in the whole temperature range of interest as shown in Figure 5.8.

$$\Delta G_T^\circ = \Delta H_{298}^\circ + \int_{298}^{T} C_p dT - T\left(\Delta S_{298}^\circ + \int_{298}^{T} \frac{C_p}{T} dT\right) \quad 5.3$$

where ΔG_T° is the Gibbs' free energy of formation at temperature T, ΔH_{298}° is the enthalpy of formation at 298 K, ΔS_{298}° is the entropy of formation at 298 K and C_p is heat capacity.

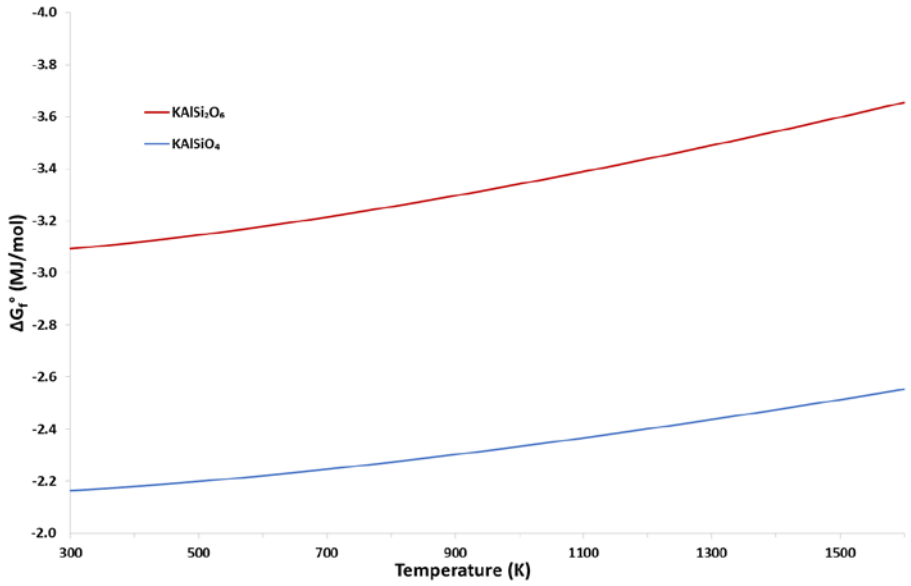

Figure 5.8: Gibbs' free energy of formation as a function of temperature, calculated using thermodynamic parameters given in Yazhenskikh, Hackb, & Müller (2011).

In this study for SWXT® (Figure 4.23) and for melt-rig samples KAS-4, KAS-5, KAS-8 and KASZ-1 XRD patterns (Figures 4.45 to 4.47) showed that kalsilite is the first phase to crystallize. Then, after prolonged heat treatment – with the exact time varying depending on composition – kalsilite transforms to leucite and loss of K_2O is also initiated.

There are two possible routes for the transformation of kalsilite to leucite in a compositional system inside the leucite-kalsilite phase fields:

The first hypothesis is that K_2O and Al_2O_3 are being ejected from kalsilite according to Eq. 5.4:

$$KAlSiO_4 \rightarrow \frac{1}{4}K_2O + \frac{1}{4}Al_2O_3 + \frac{1}{2}(KAlSi_2O_6) \quad 5.4$$

This mechanism shows that after prolonged heat treatment kalsilite will completely transform to leucite, particularly in the case of stoichiometric kalsilite. In this case some of the ejected potassium oxide will react with alumina, and the rest will evaporate according to Eq. 5.5:

$$\frac{3}{2}K_2O + \frac{11}{2}Al_2O_3 \rightarrow KAl_{11}O_{17} + K_2O \uparrow \quad 5.5$$

The formation of potassium aluminium oxide has been confirmed by XRD for all the SWXT® samples and the melt-rig samples with composition close to kalsilite, when heat treated at 1250°C.

The second hypothesis is that the transformation mechanism follows the reaction showed in Eq. 5.6:

$$KAlSiO_4 + SiO_2 \rightarrow KAlSi_2O_6 \quad 5.6$$

The second hypothesis is analogous to the crystallization mechanism of mullite as reported in literature (Huling & Messing, 1991; Tkalcec, Kurajica, & Ivankovic, 2005).

There, the first crystalline phase is spinel which reacts with the SiO_2-rich amorphous phase to form mullite ($Al_6Si_2O_{13}$) at elevated temperature (1000°C). Correspondingly, $KAlSiO_4$ would react with SiO_2 of the amorphous phase and transform to $KAlSi_2O_6$. This is consistent with XRD results presented in this study for SWXT® heat treated at 1250°C for more than 1000 hours. Phase transformation of the first crystallization product with amorphous SiO_2 from the residual glass was also reported in similar systems (Li_2O-Al_2O_3-SiO_2) where the first nucleation product is Li_2SiO_3 which develops at 650°C and then at 830°C reacts with amorphous SiO_2 to form $Li_2Si_2O_5$ (Bischoff, Eckert, Apel, Rheinberger, & Höland, 2011; P. Zhang, Li, Yang, & Xu, 2014).

The Gibbs' free energy of reaction, ΔG°_r, for the two mechanisms is shown in Figure 5.9 as a function of temperature. The first mechanism is thermodynamically not expected to take place below around 1300K (1027°C) while the second mechanism is predicted to be possible in the whole temperature range of study. Even above 1300k where both reactions are feasible the second mechanism is more favourable as the Gibbs' free energy of reaction is lower.

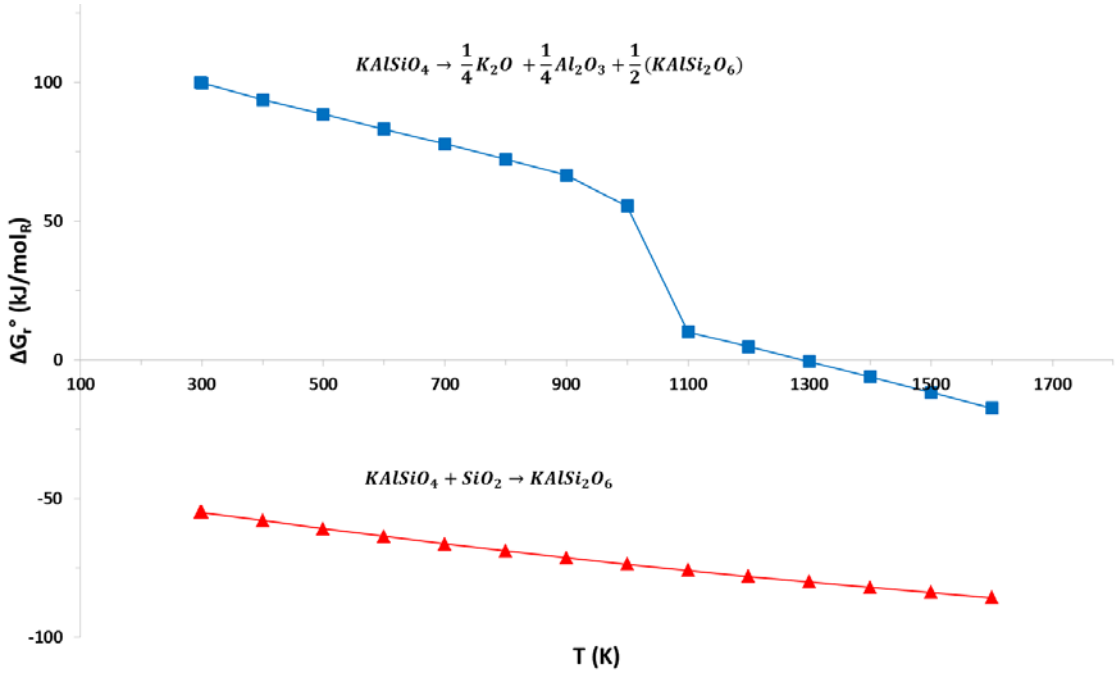

Figure 5.9: Gibbs' free energy of reaction as a function of temperature for the two transformation mechanisms, calculated using thermodynamic parameters given in Yazhenskikh, Hackb, & Müller (2011) and Stull & Prophet (1971).

Analysis of melt-rig samples with composition in the region of kalsilite and as close as possible to SWXT® – compositions with high K_2O content – supported the above hypothesis. XRF and DTA analysis showed that kalsilite will nucleate first and that at around 500 hours the development of leucite and potassium aluminium oxide is accelerating. Kalsilite will transform to leucite by reacting with SiO_2 from the amorphous phase. This reaction will create in the system an excess amount of K_2O and Al_2O_3. In addition, some of the K_2O will react with the remaining Al_2O_3 forming potassium aluminium oxide and the rest will evaporate as described in Eq. 5.5.

Both transformation mechanisms suggest that the unstable behaviour of kalsilite and the transformation to leucite are driving the K_2O loss.

The second transformation mechanism is also possible for the case of the compositions close to leucite stoichiometry (KAS-1) and richer in alumina (KAS-9 and KASZ-2). As XRF (Table 4.17) revealed these materials will not have any elemental alteration in terms of time. Again, the first crystallization product is kalsilite at low temperature

(Figure 4.43), which will react with the SiO_2 in the amorphous phase to form leucite (Eq. 5.2). The starting glass compositions are potassium deficient compared to kalsilite which may explain why there is no loss of K_2O in this case. XRD results suggest that these reactions will continue until all kalsilite transforms to leucite at elevated temperature. As studies in the formation of leucite indicate (He, Jia, Wang, & Zhou, 2011; Y. Zhang et al., 2007; Y. Zhang et al., 2006), having adequate crystallization kinetics, a metastable phase – in this case kalsilite - can form first. Indeed, Zhang et al. (2007) determined by the Kissinger method (Kissinger, 1957) that the activation energy for crystallization of kalsilite (E_a = 103 kJ/mol) is lower than that of leucite (E_a = 125 kJ/mol) for hydrothermally prepared samples.

According to Abbot (1984) orthorhombic kalsilite is more likely to be a metastable phase. Nucleation and growth kinetics can be altered by the addition of nucleating agents (Erbe & Sapieszko, 1997; Y. Zhang, Qu, Rao, Lv, & Wu, 2007; Y. Zhang et al., 2006) such as leucite nanocrystals, leading to the elimination of kalsilite as an intermediate crystallization product, and the formation of leucite at lower temperatures.

These results indicate that potassium is lost due to the instability of kalsilite at elevated temperatures; and that potassium evaporates due to its high volatility (Yu et al., 2003). Glass fibres based on the kalsilite-leucite region of the K_2O-Al_2O_3-SiO_2 system will transform into glass-ceramic fibres and the first nucleation product at low temperatures, no matter whether the composition is closer to leucite or to kalsilite, will be kalsilite. Compositions in the kalsilite region will partly form leucite at higher temperature after prolonged heat treatment – irrespective of the transformation mechanism – and the resulting excess of potassium will evaporate during the crystallization process.

To conclude, it has been shown that the metastable character of kalsilite at elevated temperatures and the stoichiometry of the starting composition together drive the loss of potassium from SWXT® and melt-rig glass fibres.

Potential strategies to minimize potassium loss could be designing a composition close to leucite thus avoiding the formation of kalsilite. Another way could be increasing the crystallization temperature by compositional modifications. Wang et al. (2016) suggests that a small addition of rare earth oxides (La_2O_3, Nd_2O_3 and Y_2O_3) to alkaline aluminosilicate glass fibres has the tendency to increase the crystallization temperature and as a result affect the thermal performance and crystallization behaviour of glass fibres. However, modifications to the system should be carefully made without negatively affecting the fiberization and the bio-solubility of glass fibres.

5.5. Cerachem® fibres

Analysis of Cerachem® in the ZrO_2-Al_2O_3-SiO_2 system showed that a loss of silica occurs as a function of material depth (from the cold to the hot face) and was measured as a weight loss by XRF (9.1 wt%). Unfortunately, the exact temperature, the environment and the duration of prolonged firing were not available due to the nature of industrial use. This has prevented useful correlations to be made with literature data, and experiments to be conducted with unfired Cerachem® under simulated operation conditions, which would have given insights into the causes of SiO_2 loss and the possible solutions. This is most likely in the form of gaseous SiO_2 that moves away from the hot face of the module samples (Figure 4.56); the cold face of the modules has the same silica content as the unfired blocks which makes silica diffusion from the hot to the cold face highly improbable. Dubois et al. (1995) observed this phenomenon,

describing a progressive ejection of silica – in a gaseous SiO or solid SiO_2 form – from mullite with increasing heat treatment temperature. Ban and Okada (1992) and Brindley and Nakahira (1959) by observing XRD patterns of mullite ($3Al_2O_3 \cdot 2SiO_2$) discovered that with increasing the heat treatment temperature, to more than 1300°C, it becomes overstoichiometric in alumina which suggests that SiO_2 content decreases without this being quantified.

Several mechanisms can be involved in the loss of silica. They can involve reduction of SiO_2 to SiO, or with water vapour or steam present they form silicic acid hydrates such as $Si(OH)_4$ or $Si_2O(OH)_6$. The vaporization of SiO_2 increases with increasing H_2 content, with increased free SiO_2, and with increased temperature (Thermal Ceramics, 1995).

XRD analysis (Figure 4.59 and 4.60) of the Cerachem® modules, showed the presence of mullite, cristobalite and zirconia. The presence of cristobalite decreases moving from the cold to the hot face, while that of mullite increases in comparison; this suggests that SiO_2 is probably lost from the cristobalite phase. Two tetragonal zirconia phases were detected, one stable (Bondars et al., 1995) and one metastable (Igawa & Ishii, 2001). The presence of the latter is more evident at the hot face.

5.6. References

Abbot, R. N. (1984). $KAlSiO_4$ stuffed derivatives of tridymite - phase-relationships. *American Mineralogist, 69*(5-6), 449-457.

Apel, E., van't Hoen, C., Rheinberger, V., & Höland, W. (2007). Influence of ZrO_2 on the crystallization and properties of lithium disilicate glass-ceramics derived from a multi-component system. *Journal of the European Ceramic Society, 27*(2), 1571-1577.

Atkins, P., & De Paula, J. (2013). *Elements of physical chemistry*. USA: Oxford University Press.

Ban, T., & Okada, K. (1992). Structure refinement of mullite by the Rietveld method and a new method for estimation of chemical composition. *Journal of the American Ceramic Society, 75*(1), 227-230.

Beall, G. H. (1972). Structure, properies and nucleaton of glass-ceramics. In L. L. Hench, & S. W. Freiman (Eds.), *Advances in Nucleation and Crystallization in Glasses* (pp. 251-261). Columbus, Ohio: American Ceramic Society.

Bechgaard, T. K., Scannell, G., Huang, L., Youngman, R. E., Mauro, J. C., & Smedskjaer, M. M. (2017). Structure of MgO/CaO sodium aluminosilicate glasses: Raman spectroscopy study. *Journal of Non-Crystalline Solids, 470*, 145-151. doi:10.1016/j.jnoncrysol.2017.05.014

Bischoff, C., Eckert, H., Apel, E., Rheinberger, V. M., & Höland, W. (2011). Phase evolution in lithium disilicate glass-ceramics based on non-stoichiometric compositions of a multi-component system: Structural studies by ^{29}Si single and double resonance solid state NMR. *Physical Chemistry Chemical Physics, 13*(10), 4540-4551. doi:10.1039/c0cp01440k

Boff, J. C., Jubb, G. A., & Mottram, R. S. (2010). *European Patent Application EP 2213634 A1*. Munich, Germany: European Patent Office.

Bondars, B., Heidemane, G., Grabis, J., Laschke, K., Boysen, H., Schneider, J., & Frey, F. (1995). Powder diffraction investigations of plasma sprayed zirconia. *Journal of Materials Science, 30*(6), 1621-1625.

Brawer, S. A., & White, W. B. (1977). Raman spectroscopic investigation of the structure of silicate glasses (II). Soda-alkaline earth-alumina ternary and quaternary glasses. *Journal of Non-Crystalline Solids, 23*(2), 261-278. doi:10.1016/0022-3093(77)90009-6

Brindley, G. W., & Lemaitre, J. (1987). Thermal, oxidation and reduction reactions of clay minerals. In A. C. D. Newman (Ed.), *Chemistry of Clays and Clay Minerals* (pp. 319-370). London: Mineralogical Society.

Brindley, G. W., & Nakahira, M. (1959). The kaolinite-mullite reaction series: II, metakaolin. *Journal of the American Ceramic Society, 42*(7), 314-318.

Bunsell, A. R. (2005). Oxide fibers for high-temperature reinforcement and insulation. *Jom, 57*(2), 48-51. doi:10.1007/s11837-005-0216-9

Capobianco, C., & Carpenter, M. (1989). Thermally induced changes in kalsilite ($KAlSiO_4$). *American Mineralogist, 74*(7-8), 797-811.

Comodi, P., Cera, F., Gatta, G. D., Rotiroti, N., & Garofani, P. (2010). The devitrification of artificial fibers: A multimethodic approach to quantify the temperature-time onset of cancerogenic crystalline phases. *Annals of Occupational Hygiene, 54*(8), 893-903. doi:10.1093/annhyg/meq056

Curtis, C. D. (1976). Chemistry of rock weathering: fundamental reactions and controls. In E. Derbyshire (Ed.), *Geomorphology and Climate* (pp. 25-57). Chichester: Wiley.

Dernier, P., & Remeika, J. (1976). Structural determinations of single-crystal K β-alumina and cobalt-doped K β-alumina. *Journal of Solid State Chemistry, 17*(3), 245-253.

Dubois, J., Murat, M., Amroune, A., Carbonneau, X., & Gardon, R. (1995). High-temperature transformation in kaolinite: the role of the crystallinity and of the firing atmosphere. *Applied Clay Science, 10*(3), 187-198. doi:10.1016/0169-1317(95)00030-8

Dyson, D. J., Butler, M. A., Hughes, R. J., Fisher, R., & Hicks, G. W. (1997). The de-vitrification of alumino-silicate ceramic fibre materials - The kinetics of the formation of different crystalline phases. *Annals of Occupational Hygiene, 41*(5), 561-590. doi:10.1016/S0003-4878(97)00013-6

Erbe, E. M., & Sapieszko, R. S. (1997). *US Patent No.5,622,551*. Washington, DC: U.S. Patent and Trademark Office.

Fedkin, A., Grossman, L., & Ghiorso, M. (2006). Vapor pressures and evaporation coefficients for melts of ferromagnesian chondrule-like compositions. *Geochimica Et Cosmochimica Acta, 70*(1), 206-223.

Fernandes, H. R., Tulyaganov, D. U., & Ferreira, J. M. (2013). The role of P_2O_5, TiO_2 and ZrO_2 as nucleating agents on microstructure and crystallization behaviour of lithium disilicate-based glass. *Journal of Materials Science, 48*(2), 765-773.

Galusek, D., Sedláček, J., Chovanec, J., & Michálková, M. (2015). The influence of MgO, Y_2O_3 and ZrO_2 additions on densification and grain growth of

submicrometre alumina sintered by SPS and HIP. *Ceramics International, 41*(8), 9692-9700. doi:10.1016/j.ceramint.2015.04.038

Gregorkiewitz, M., Li, Y., White, T. J., Withers, R. L., & Sobrados, I. (2008). The structure of "orthorhombic" $KAlSiO_4$-O1: evidence for Al–Si order from MAS NMR data combined with Rietveld refinement and electron microscopy. *The Canadian Mineralogist, 46*(6), 1511-1526.

Gualtieri, A. F., Foresti, E., Lesci, I. G., Roveri, N., Gualtieri, M. L., Dondi, M., & Zapparoli, M. (2009). The thermal transformation of Man Made Vitreous Fibers (MMVF) and safe recycling as secondary raw materials (SRM). *Journal of Hazardous Materials, 162*(2-3), 1494-1506. doi:10.1016/j.jhazmat.2008.06.066

He, P., Jia, D., Wang, M., & Zhou, Y. (2011). Thermal evolution and crystallization kinetics of potassium-based geopolymer. *Ceramics International, 37*(1), 59-63.

Höland, W., Frank, M., & Rheinberger, V. (1995). Surface crystallization of leucite in glasses. *Journal of Non-Crystalline Solids, 180*(2-3), 292-307.

Huling, J. C., & Messing, G. L. (1991). Epitactic nucleation of spinel in aluminosilicate gels and its effect on mullite crystallization. *Journal of the American Ceramic Society, 74*(10), 2374-2381.

Igawa, N., & Ishii, Y. (2001). Crystal structure of metastable tetragonal zirconia up to 1473 K. *Journal of the American Ceramic Society, 84*(5), 1169-1171. doi:10.1111/j.1151-2916.2001.tb00808.x

Iyi, N., Inoue, Z., & Kimura, S. (1986). The crystal structure of highly nonstoichiometric potassium β-alumina, $K_{1.50}Al_{11.0}O_{17.25}$. *Journal of Solid State Chemistry, 61*(1), 81-89. doi:10.1016/0022-4596(86)90008-3

Johnson, S. M. (1979). *Mullitization of kaolinite and Al_2O_3-SiO_2 mixtures.* (Unpublished master's thesis). University of California, Berkeley.

Jubb, G. A. (2012). *U.S. Patent No. 8,088,701 B2*. Washington, DC: U.S. Patent and Trademark Office.

Kissinger, H. E. (1957). Reaction kinetics in differential thermal analysis. *Analytical Chemistry, 29*(11), 1702-1706.

Kleebusch, E., Patzig, C., Höche, T., & Rüssel, C. (2016). *Effect of the concentrations of nucleating agents ZrO_2 and TiO_2 on the crystallization of Li_2O-Al_2O_3-SiO_2 glass: an X-ray diffraction and TEM investigation.* New York: Springer. doi:10.1007/s10853-016-0241-9

Kremenović, A., & Vulić, P. (2014). Disordered kalsilite $KAlSiO_4$. *Acta Crystallographica Section C: Structural Chemistry, 70*(3), 256-259.

Le Losq, C., Neuville, D. R., Florian, P., Henderson, G. S., & Massiot, D. (2014). The role of Al3+ on rheology and structural changes in sodium silicate and aluminosilicate glasses and melts. *Geochimica Et Cosmochimica Acta, 126*, 495-517. doi:10.1016/j.gca.2013.11.010

Liu, C., Komarneni, S., & Roy, R. (1994). Seeding effects on crystallization of $KAlSi_3O_8$, $RbAlSi_3O_8$, and $CsAlSi_3O_8$ gels and glasses. *Journal of the American Ceramic Society, 77*(12), 3105-3112. doi:10.1111/j.1151-2916.1994.tb04556.x

MacKenzie, K. J. D. (1969). Effects of impurities on formation of mullite from kaolonite-type minerals-1, 2, 3. *Transactions of the British Ceramic Society, 68*(3), 97-109.

MacKenzie, K. J. D., Meinhold, R. H., Brown, I. W. M., & White, G. V. (1996). The formation of mullite from kaolinite under various reaction atmospheres. *Journal of*

the European Ceramic Society, 16(2 SPEC. ISS.), 115-119. doi:10.1016/0955-2219(95)00143-3

McMillan, P., & Piriou, B. (1983). Raman spectroscopic studies of silicate and related glass structure—a review. *Bulletin De Mineralogie, 106*(5), 7-75.

Neuville, D. R., & Mysen, B. O. (1996). Role of aluminium in the silicate network: In situ, high-temperature study of glasses and melts on the join SiO_2-$NaAlO_2$. *Geochimica Et Cosmochimica Acta, 60*(10), 1727-1737. doi:10.1016/0016-7037(96)00049-X

Osborn, E. F., & Muan, A. (1960). *Phase equilibrium diagrams of oxide systems*. Columbus, Ohio: American Ceramic Society with the Edward Orton Jr. Ceramic Foundation.

Palmer, D. C., Bismayer, U., & Salje, E. K. H. (1990). Phase transitions in leucite: Order parameter behaviour and the Landau potential deduced from Raman spectroscopy and birefringence studies. *Physics and Chemistry of Minerals, 17*(3), 259-265. doi:10.1007/BF00201458

Rouf, M. A., Hermansson, L., & Carlsson, R. (1978). Crystallisation of glasses in the primary phase field of leucite in the K_2O–Al_2O_3–SiO_2 system. *Transactions of the British Ceramic Society, 77*, 36-39.

Schaefer, G. W., De Kroon, A. P., & Aldinger, F. (1995). *Effect of aluminum raw materials on the formation of potassium-beta-aluminas* doi:10.1016/0167-2738(95)00176-7

Shelby, J. E. (2005). *Introduction to Glass Science and Technology* (2nd ed.). Cambridge: Royal Society of Chemistry.

Strand, Z. (1986). *Glass-Ceramic Materials*. Amsterdam: Elsevier.

Stull, D. R., & Prophet, H. (1971). *JANAF thermochemical tables*. Washington, D.C.: U.S. Dept. of Commerce, National Bureau of Standards.

Tashiro, T., & Wada, M. (1963). Glass-ceramics crystallized with zirconia. In G. E. Rindone, & F. R. Matson (Eds.), *Advances in Glass Technology* (pp. 18-19). New York: Plenum Press.

Temuujin, J., Okada, K., MacKenzie, K. J. D., & Jadambaa, T. (1999). The effect of water vapour atmospheres on the thermal transformation of kaolinite investigated by XRD, FTIR and solid state MAS NMR. *Journal of the European Ceramic Society, 19*(1), 105-112.

Tkalcec, E., Kurajica, S., & Ivankovic, H. (2005). Diphasic aluminosilicate gels with two stage mullitization in temperature range of 1200–1300°C. *Journal of the European Ceramic Society, 25*(5), 613-626. doi:10.1016/j.jeurceramsoc.2004.02.015

Tonnesen, T., Dietrichs, P., & Telle, R. (2005). Linear shrinkage, resilience and microstructural changes in high temperature insulating wools in maximum use temperature range. *Advances in Applied Ceramics, 104*(5), 249-255. doi:10.1179/174367605X46812

Uchida, H., Downs, R. T., & Yang, H. (2006). Crystal-chemical investigation of kalsilite from San Venanzo, Italy, using single-crystal X-ray diffraction and Raman spectroscopy. *Geochimica Et Cosmochimica Acta, 70*(18), A677-A680. doi:10.1016/j.gca.2006.06.1267

Virgo, D., Mysen, B. O., & Kushiro, I. (1980). Anionic constitution of 1-atmosphere silicate melts: Implications for the structure of igneous melts. *Science, 208*(4450), 1371-1373.

Wang, L., Wang, Y., Wang, Q., & Chou, K. (2016). Raman structure Investigations of CaO-MgO-Al_2O_3-SiO_2-CrO_x and its correlation with sulfide capacity. *Metallurgical and Materials Transactions B, 47*(1), 10-15. doi:10.1007/s11663-015-0469-9

Wang, X., Liu, H., Wang, Z., Ma, Y., & Kale, G. M. (2016). Effect of rare earth oxides on the properties of bio-soluble alkaline earth silicate fibers. *Journal of Rare Earths, 34*(2), 203-207. doi:10.1016/S1002-0721(16)60015-7

Yadav, A. K., & Singh, P. (2015). A review of the structures of oxide glasses by Raman spectroscopy. *RSC Advances, 5*(83), 67583-67609.

Yazhenskikh, E., Hack, K., & Müller, M. (2011). Critical thermodynamic evaluation of oxide systems relevant to fuel ashes and slags, Part 5: Potassium oxide–alumina–silica. *CALPHAD: Computer Coupling of Phase Diagrams and Thermochemistry, 35*(1), 6-19. doi:10.1016/j.calphad.2010.10.010

Yu, Y., Hewins, R., & Wang, J. (2003). Experimental study of evaporation and isotopic mass fractionation of potassium in silicate melts. *Geochimica Et Cosmochimica Acta, 67*(4), 773-786.

Zhang, Y., Qu, C., Rao, P., Lv, M., & Wu, J. (2007). Nanocrystalline seeding effect on the crystallization of two leucite precursors. *Journal of the American Ceramic Society, 90*(8), 2390-2398.

Zhang, P., Li, X., Yang, J., & Xu, S. (2014). The crystallization and microstructure evolution of lithium disilicate-based glass-ceramic. *Journal of Non-Crystalline Solids, 392*, 26-30. doi:10.1016/j.jnoncrysol.2014.03.020

Zhang, Y., Lv, M., Chen, D., & Wu, J. (2007). Leucite crystallization kinetics with kalsilite as a transition phase. *Materials Letters, 61*(14-15), 2978-2981. doi:10.1016/j.matlet.2006.10.057

Zhang, Y., Wu, J., Rao, P., & Lv, M. (2006). Low temperature synthesis of high purity leucite. *Materials Letters, 60*(23), 2819-2823. doi:10.1016/j.matlet.2006.01.098

Chapter 6

Conclusions and Future Work

6. Conclusions and Future Work

Superwool® XT biosoluble glass fibres have been the subject of extensive research because they are of great interest for applications demanding long-term and high-temperature performance and are important for the development of new safer environmental-friendly fibres.

This chapter presents the main conclusions drawn from this research study. All the key findings and outcomes we will be summarised. Moreover, recommendations for future work based on the results of this study will be given.

6.1. Conclusions

- SWXT® crystallizes very quickly (< 1 minute) at 1250°C and after 2176 hours of constant heat treatment some amorphous phase is retained. Thus, SWXT® glass fibres after one minute of firing will be converted to glass-ceramic fibres.
- SWXT® fibres and pre-crystallized SWXT® samples (5 min, 1200°C) that were heat treated at 850°C are thermally stable as no compositional alterations or phase transformations occur after kalsilite ($KAlSiO_4$) and zirconium oxide (ZrO_2) completely develop. This phase assemblage and high compositional stability in terms of time shows that SWXT® (both pre-crystallized and amorphous) glass fibre samples have a good thermal performance as a function of time at 850°C.
- SWXT® fibres that were heat treated at 1250°C lost K_2O as a function of time, and crystallization. The first crystallization products are $KAlSiO_4$ and ZrO_2 (168 hours) and then $KAlSi_2O_6$ and $KAl_{11}O_{17}$ develop after 800 hours of constant heat treatment. Kalsilite is disappearing and transforming into leucite with increasing

firing time. In addition, this study shows that SWXT® macroscopically shrinks and the surface morphology of the fibres becomes rough and uneven, negatively affecting the thermal performance of the product.

- Heat treatment experiments demonstrated that the firing atmosphere parameters, such as concertation of potassium vapours and therefore number of samples inside the furnace and dimensions of the furnace, will affect the crystallization behaviour and the rate of K_2O volatilization. Furthermore, the loss of potassium oxide is strongly connected with the development of leucite as in all the cases where K_2O loss was limited, due to increase of potassium vapours, the formation of this phase was also supressed.
- Experiments with melt-rig glass fibres in the ternary K_2O-Al_2O_3-SiO_2 system and the quaternary K_2O-ZrO_2-Al_2O_3-SiO_2 system revealed that leucite is a stable crystalline phase in terms of time at elevated temperature in contrast with kalsilite that is an unstable phase which probably behaves as an intermediate precursor of leucite. Samples with kalsilite being the main phase appear to lose K_2O after prolonged firing (1000 hours) dissimilarly with samples with leucite being the main phase in which no compositional alteration was detected.
- Finally, two hypotheses were presented regarding the phase transformation of kalsilite to leucite and the evaporation of K_2O. In the first one, K_2O and Al_2O_3 are ejected from unstable kalsilite resulting in a more stable phase which is leucite. Part of the ejected K_2O reacts with Al_2O_3 to form a new phase, potassium aluminium oxide ($KAl_{11}O_{17}$), and the rest of the K_2O evaporates. In the second hypothesis, unstable kalsilite reacts with silica from an amorphous phase – taking into consideration that the material is a glass-ceramic – to form a more stable phase

which is leucite. In this case some of the excess K_2O evaporates and some reacts with Al_2O_3 to form $KAl_{11}O_{17}$.

In both hypothetical cases the crystallization process, and more specifically the unstable behaviour of kalsilite, drives the loss of potassium and the development of leucite and potassium aluminium oxide. Compositions with kalsilite being the main phase will partly form leucite as a final product after prolonged heat treatment and will lose potassium oxide during the crystallization process.

6.2. Future work

There are several lines of research arising from this work which should be pursued.

1. Building an understanding on the unstable behaviour of kalsilite at elevated temperatures. It is very important to understand the reason of the unstable behaviour of kalsilite and the connection with time and temperature.
2. Study of the kinetics as the reaction mechanism and the activation energies of all the phase transformations should be determined. The activation energies of kalsilite crystallization and leucite crystallization via kalsilite can be determined to explore this transformation mechanism further.
3. Regarding the heating atmosphere and its effect on the crystallization process and the rate of K_2O loss, heat treatment experiments at various temperatures with potassium atmosphere inside the furnace should provide greater differences in K_2O evaporation content to identify in detail the changes due to potassium oxide effects.

4. Heat treatment experiments with bulk glass and glass fibres to understand how the surface area to volume ratio of SWXT® is affecting the development of specific crystalline phases and the evaporation of K_2O.
5. A secondary line of research, which follows from chapter 4, is to investigate the strong anomaly before the main exothermic peak in DTA traces of melt-rig samples (Figure 4.52 and Figure 4.53).
6. As discussed in Chapter 2 (Section 2.4.7.), modifications of key elements of SWXT® composition could be examined. For instance, the challenges faced by the addition of rare earth oxides on the crystallization behaviour of biosoluble glass fibres can be determined.
7. Detailed structural analysis of glass compositions on the leucite-kalsilite tie-line with the use of NMR and Raman spectroscopy could be used to investigate the Al and Si Q_n speciation.
8. Finally, the role of ZrO_2 in K_2O-Al_2O_3-SiO_2 systems could be explored to build an understanding on the nucleating effect in terms of temperature and composition.